Experimental Investigation of Ignition under High Altitude Conditions with and w/o Effusion Cooling Interaction

Zur Erlangung des akademischen Grades eines

Doktors der Ingenieurwissenschaften (Dr.-Ing.)

von der KIT-Fakultät für Chemieingenieurwesen und Verfahrenstechnik
des Karlsruher Instituts für Technologie (KIT)

genehmigte

Dissertation

von

Dipl.-Ing. Alexios-Dionysios Martinos

aus Athen (Griechenland)

Tag der mündlichen Prüfung	07.09.2023
Erstgutachter:	Prof. Dr.-Ing. Nikolaos Zarzalis
Zweitgutachter:	Prof. Dr. sc. techn. Thomas Koch

Dedicated to my wife and my family

Acknowledgement

I express my sincere gratitude to my doctor-father, Prof. Dr.-Ing. Nikolaos Zarzalis, whose expertise and immense knowledge guided me throughout this research activity. He was always willful to conduct a scientific discussion about the already obtained results or new ideas.

Besides my doctor-father, I would like to thank my supervisor Dr.-Ing. Stefan Harth, for his motivation and patience after a vast number of meetings repeatedly discussing the results and finding the optimum solutions to the every-day problems that arise in the life of research.

My special thanks to my colleagues at the EBI group for their cooperation all these years. I am immensely grateful to Dr.-Ing. Alexandra Loukou for motivating me to proceed every time after a failure. Dipl.-Ing. Thomas Christou for our countless hours of coding and scientific discussion, which converted to a strong friendship. Last but not least, Dipl.-Ing. Petros Vlavakis, with whom we connected through our shared passion for music and sports, and without even noticing it, I became his best man.

My wife, Despoina, has been tremendously supportive of me throughout this challenging process. She makes me so happy in my private life, which helped me become a balanced person, compensating for all this stress from our hectic everyday life. Thank you for sharing your dreams with me.

Finally, I would like to thank my family. Mom and Dad, thank you for the continuous support, encouragement, love, and the “do whatever makes you

happy" attitude you have given to me from the first day of my life. My brother, thank you for always being my role model and my inspiration.

Abstract

A rare though catastrophic event might occur during the operation of a jet engine, referred to as a flameout. It denotes the engine failure due to the extinction of the flame within the combustion chamber (see Section 2.6). Following a flameout event, the engine should be restarted while the subsequent spooling-up of its main shaft reinsures the safe operation. Due to the inherent safety implications during the flight, the jet engine's high-altitude relight capability is essential for developing the next-generation combustion chambers. Therefore, the investigation of this process constitutes the focus of this research activity.

The high-altitude relight capability is a challenging process from an engineering perspective since the imposed operating conditions (low pressure and temperature) lead to poor atomization, low degree of evaporation, and slow reaction rate of the vaporized fuel. Typically, engineers deal with the conflict of interest between safety and harmful emissions. Undoubtedly, a better understanding of the high-altitude relight process would significantly reduce the design iterations, aiding in developing new combustion chambers meeting the ambitious targets and regulations set by the EASA (European Union Aviation Safety Agency) and FAA (Federal Aviation Administration). For this research activity, a rectangular, one-sector RQL (Rich-Quench-Lean) combustion chamber was employed for experimental investigations under high altitude conditions. The combustion chamber design is modular, so experiments for two configurations, i.e., without and with effusion cooling holes, are feasible. The fuel injection and the ignition system are representative of the ones used in commercial aviation.

The experimental investigation has been carried out at the ISCAR (**I**gnition under **S**ub atmospheric **C**onditions - **A**ltitude **R**elight) rig, developed at the Engler-Bunter Institute. The ISCAR rig constitutes one of the few test facilities globally facilitating low pressure and temperature conditions for flowing kerosene-air mixtures.

The present experimental investigation enhances the understanding/knowledge of the jet engine's altitude relight process. The latter, albeit inextricably linked with flight safety, is not a well-understood process to date. This research focuses on determining how varying imposed high-altitude conditions influence the ignition probability, the minimum fuel-to-air ratio (FAR), and the ignition timing for a successful ignition event. In addition, the unsteady flame kernel generation and propagation were analyzed by high-speed imaging recording. An in-house image processing code was developed and employed to derive quantitative spatial information and identify overall trends among ignition sequences for the same or different operating conditions. Particular attention has been given to the hot gases' displacement within the combustion chamber, significantly affecting the ignition process.

The global operating conditions (combustor pressure and air inlet temperature) and the pressure drop across the nozzle and the liners were maintained coequal depending on the operating condition to achieve comparability between the investigated configurations (liners without and with effusion cooling). Results showed that pressure and temperature affect the ignition process, with the latter being less prominent due to the substantially limited temperature variations, compared to pressure, in the investigated test matrix. In both configurations, the minimum FAR increased as long as the combustion chamber's operating

conditions became adverse, indicating that the performance of the airblast atomizer under high altitude conditions deteriorated, causing poor ignition. The latter is overcome by creating a richer fuel-air mixture in the primary zone. Moreover, the air injected through the effusion cooling holes near the spark seems to create favorable conditions for ignition since the configuration with effusion cooling exhibited higher ignitability, especially at higher simulated altitudes.

Furthermore, RANS (Reynolds-Averaged Navier-Stokes) simulations have been carried out for different operating conditions to support the high-altitude relight experimental investigation. Based on these results, essential flow characteristics, such as the formation of the recirculation zone and the residence time in the primary zone, have been revealed.

The acquired results of the aforementioned experimental campaign indicated that the atomization quality constitutes one of the most influential ignition performance parameters. Poor atomization's quality directly affects the evaporation process and subsequently generates variations of the local fuel-to-air ratio, which, if skewed towards leaner mixtures, affects the ignition process detrimentally. The imposed operating conditions hamper the performance of an airblast atomizer, leading to a low-quality spray with ligaments and non-spherical particles. Therefore, all measurements in this investigation have been conducted with the shadowgraphy measurement technique, which is advantageous compared to the typical PDA (Phase Doppler Anemometry) approach when dealing with the abovementioned spray features.

This investigation focuses on generating a database concerning the atomization process of airblast atomizers under sub-atmospheric conditions with kerosene

Jet A-1, which, to the best of the author's knowledge, has not been reported in the literature before. The effect of the main physical phenomena governing atomization, such as thermodynamic and fluid dynamics, was captured. Results showed the effect of air temperature and pressure, ALR (Air to Liquid Ratio), and air velocity on the SMD (Sauter Mean Diameter) and droplet distribution for kerosene Jet A-1 and water. The obtained results constitute the basis for deriving more universal models, which predict the SMD under different imposed operating conditions. Moreover, measurements of the atomization's quality for both configurations, with and without effusion cooling, revealed different spay behavior that confirms the latter's higher ignitability than the former.

Furthermore, the influence of the igniter's location on the ignition performance has been investigated. Two-phase flow simulations using as inputs the experimentally acquired spray's SMD and the droplet distribution have been conducted in the SOPRANO EU Project frame. Three different locations were discerned, and their high-altitude performance has been compared with each other and the nominal location. Results showed that the ignition probability is very sensitive to the igniter's location. Subsequently, the tracking algorithm was employed to give insight into the interaction of the hot gases' displacement with the imposed flow field.

In realistic configurations, the ignition failure is not strictly correlated with the flame kernel generation but is attributed to the subsequent flame development. The latter pertains to the reaction rate, the atomization's quality, and the spark region's instantaneous flow field. The residence time of the mixture should exceed the reaction and evaporation time scales to ensure a stable flame. However, the combustion chamber's employed airflow causes a conflict of interest

between the evaporation rate and the residence time. At constant global operating conditions, increased airflow passing through the nozzle, on the one hand, improves the atomization's quality, but on the other hand, reduces the residence time significantly. The effect of increasing the airflow rate in the primary zone has been investigated in three simulated altitudes, and results indicated that the effect of residence time grows immensely with adverse conditions. Finally, one of the developed features of the tracking algorithm is calculating the hot gases' velocity. Results showed a good agreement with the cold-flow simulations, under similar imposed conditions, to both magnitude and direction.

Structure of the dissertation:

Chapter 2 - Theoretical background: A brief introduction of the general conservation equations for laminar and turbulent flows, which constitute the foundation of numerical flow modeling of the gas phase, is carried out. Particular reference is given to the statistical description of turbulent flows found in most technical devices. Moreover, the fundamentals of the combustion process are introduced, while attention is given to the phenomenology of laminar and turbulent premixed flames as well as spray combustion and flame stabilization. Furthermore, a thorough explanation and a literature review of the ignition process, which constitutes the core of this research activity, are given. Finally, particular attention is given to the parameters influencing spray atomization, a process inextricably linked with ignition.

Chapter 3 - Experimental Method: The main components of the high-altitude relight test facility are presented, along with a thorough description of the com-

bustion chamber developed in this research activity frame. Moreover, the complete measurement plan for the ignition as well as spray investigations is defined. This chapter focuses on developing, validating, and implementing the measurement techniques employed to characterize the ignition and atomization processes under high-altitude conditions fully. The development of an advanced image processing code for tracking the displacement of the flame's luminosity center within the combustion chamber and the shadowgraphy measurement technique are presented in detail.

Chapter 4 - Numerical Method: The generated flow field, obtained by RANS simulations for different operating conditions, is presented. Firstly, a brief introduction of the numerical setup, such as the generated mesh and the boundary conditions, is given. Subsequently, two different approaches for estimating the mixture's residence time in the primary zone, which appears dominant for the ignition process, are defined.

Chapter 5 - Results and Discussion: The high-altitude relight capability of the two different employed configurations (with and without effusion cooling) are compared. More specifically, results concerning the ignition probability with constant fuel mass flow, the minimum FAR determination for a successful ignition event, and the ignition timing are presented. Furthermore, high-speed recordings of the unsteady flame kernel generation and propagation have been obtained and thoroughly analyzed. Moreover, the spray measurements under high-altitude conditions are presented, and their outcome is linked with the ignition measurement. Furthermore, particular interest has been given to the effect of the atomization's quality and the residence time, which have a counter effect on the ignition process. Finally, the hot gases' displacement has been

thoroughly analyzed by employing the developed tracking algorithm. The obtained results have been compared with the CFD predictions of the carrier's velocity under similar operating conditions.

The dissertation concluded with a summary of the key outcomes obtained throughout this experimental investigation and suggestions for further research.

Zusammenfassung

Während des Betriebs eines Triebwerks kann ein seltenes, aber schwerwiegendes Ereignis eintreten, das gewöhnlich als Flameout bezeichnet wird. Er bezeichnet den Ausfall des Triebwerks aufgrund des Löschens der Flamme in der Brennkammer (siehe Abschnitt 2.6). Nach einem Flameout sollte das Triebwerk neu gestartet werden, wobei der anschließende Hochlauf der Hauptwelle den sicheren Betrieb wiederherstellt. Aufgrund der inhärenten Sicherheitsaspekte während des Fluges, ist die Fähigkeit des Triebwerks in großer Höhe wieder zu zünden, für die Entwicklung von Brennkammern der nächsten Generation, von wesentlicher Bedeutung. Daher steht die Untersuchung dieses Prozesses im Mittelpunkt dieser Forschungsarbeit.

Das Wiederanzünden in großer Höhe ist aus technischer Sicht eine Herausforderung, da die vorgegebenen Betriebsbedingungen (niedriger Druck und niedrige Temperatur) zu einer schlechten Zerstäubung, einem geringen Verdampfungsgrad und einer langsamen Reaktionsgeschwindigkeit des verdampften Kraftstoffs führen. In der Regel müssen sich die Ingenieure mit dem Interessenkonflikt zwischen Sicherheit und Schadstoffemissionen auseinandersetzen. Ein besseres Verständnis des Prozesses der Wiederzündung in großer Höhe würde zweifellos die Anzahl der Entwurfsiterationen erheblich reduzieren und die Entwicklung neuer Brennkammern unterstützen, die den ehrgeizigen Zielen und Vorschriften der EASA (European Union Aviation Safety Agency) und der FAA (Federal Aviation Administration) entsprechen. Für diese Forschungsarbeit wurde eine rechteckige, einsektorige RQL (Rich-Quench-Lean) -Brennkammer für experimentelle Untersuchungen in großer Höhe eingesetzt.

Die Brennkammer ist modular aufgebaut, so dass Versuche für zwei Konfigurationen, d.h. ohne und mit Effusionskühlungslöchern, möglich sind. Die Düse und das Zündsystem sind repräsentativ für die in der kommerziellen Luftfahrt verwendeten Systeme.

Die experimentelle Untersuchung wurde an der ISCAR-Anlage (Ignition under Subatmospheric Conditions - Altitude Relight) durchgeführt, die am Engler-Bunter-Institut entwickelt wurde. Die ISCAR-Anlage ist eine der wenigen Versuchsanlagen weltweit, die niedrige Druck- und Temperaturbedingungen für strömende Kerosin-Luft-Gemische ermöglicht.

Die vorliegende experimentelle Untersuchung trägt dazu bei, das Verständnis und die Kenntnisse über den Prozess der Wiederzündung des Triebwerks in der Höhe zu verbessern. Dieser Prozess, der zwar untrennbar mit der Flugsicherheit verbunden ist, ist bis heute nicht gut verstanden worden. Im Mittelpunkt dieser Forschungsarbeit steht die Frage, wie die Zündwahrscheinlichkeit, das Mindest-Brennstoff-Luft-Verhältnis und der Zündzeitpunkt für eine erfolgreiche Zündung durch unterschiedliche Höhenbedingungen beeinflusst werden. Zusätzlich wurden die instationäre Flammenkernbildung und -ausbreitung durch Hochgeschwindigkeitsaufnahmen analysiert. Ein interner Bildverarbeitungscode wurde entwickelt und eingesetzt, um quantitative räumliche Informationen abzuleiten und allgemeine Trends zwischen Zündsequenzen bei gleichen oder unterschiedlichen Betriebsbedingungen zu erkennen. Besonderes Augenmerk wurde auf die Verteilung der heißen Gase in der Brennkammer gelegt, die den Zündvorgang erheblich zu beeinflussen scheint.

Die globalen Betriebsbedingungen (Brennkammerdruck und Lufteintrittstemperatur) und der Druckverlust über die Düse und die Liners wurden in Abhängigkeit von den Betriebsbedingungen gleich gehalten, um eine Vergleichbarkeit zwischen den untersuchten Konfigurationen (Liner ohne und mit Effusionskühlung) zu erreichen. Die Ergebnisse zeigten, dass sowohl Druck als auch Temperatur den Zündprozess beeinflussen, wobei letztere aufgrund der im Vergleich zum Druck wesentlich geringeren Temperaturschwankungen in der untersuchten Testmatrix weniger ausgeprägt ist. Bei beiden Konfigurationen nahm die Mindest-FAR zu, je ungünstiger die Betriebsbedingungen in der Brennkammer wurden, was darauf hindeutet, dass sich die Leistung des Luftstrahlzerstäubers unter Höhenbedingungen verschlechterte, was zu einer schlechten Zündung führte. Letzteres wird durch die Erzeugung eines fetteren Kraftstoff-Luft-Gemisches in der Primärzone überwunden. Darüber hinaus scheint die durch die Effusionskühlungslöcher in der Nähe des Funkens eingespritzte Luft günstige Bedingungen für den Zündvorgang zu schaffen, da die Konfiguration mit Effusionskühlung eine höhere Zündfähigkeit aufwies, insbesondere in größeren simulierten Höhen.

Darüber hinaus wurden RANS-Simulationen (Reynolds-Averaged Navier-Stokes) für verschiedene Betriebsbedingungen durchgeführt, um die experimentelle Untersuchung des Wiederanzündens in großer Höhe zu unterstützen. Auf der Grundlage dieser Ergebnisse wurden wesentliche Strömungsmerkmale ermittelt, wie die Bildung der Rezirkulationszone und die Verweilzeit in der Primärzone.

Die Ergebnisse der oben erwähnten Versuchskampagne zeigten, dass die Qualität der Zerstäubung einer der einflussreichsten Parameter für die Zündleis-

tung ist. Eine schlechte Qualität der Zerstäubung wirkt sich direkt auf den Verdampfungsprozess aus und erzeugt in der Folge Schwankungen des lokalen Kraftstoff-Luft-Verhältnisses, die, wenn sie in Richtung magerer Gemische verschoben werden, den Zündprozess nachteilig beeinflussen. Die auferlegten Betriebsbedingungen beeinträchtigen die Leistung eines Airblast-Zerstäubers und führen zu einem minderwertigen Spray mit Ligamenten und nicht-sphärischen Partikeln. Daher wurden alle Messungen in dieser Untersuchung mit der Shadowgraphy-Messtechnik durchgeführt, die im Vergleich zur typischen PDA-Methode (Phase Doppler Anemometry) vorteilhaft ist, wenn es um die oben genannten Spraymerkmale geht.

Diese Untersuchung konzentriert sich auf die Erstellung einer Datenbank über den Zerstäubungsprozess von Airblast-Zerstäubern unter subatmosphärischen Bedingungen mit Kerosin Jet A-1, über den nach dem Wissen des Autors in der Literatur bisher nicht berichtet wurde. Die Auswirkungen der wichtigsten physikalischen Phänomene, die die Zerstäubung bestimmen, wie z. B. Thermodynamik und Fluiddynamik, wurden erfasst. Die Ergebnisse zeigten den Einfluss von Lufttemperatur und -druck, ALR (Air to Liquid Ratio) und Luftgeschwindigkeit auf den SMD (Sauter Mean Diameter) und die Tröpfchen Verteilung sowohl für Kerosin Jet A-1 als auch für Wasser. Die erzielten Ergebnisse bilden die Grundlage für die Ableitung universellerer Modelle, die den SMD unter verschiedenen Betriebsbedingungen vorhersagen. Darüber hinaus ergaben Messungen der Zerstäubungsqualität für beide Konfigurationen, mit und ohne Effusionskühlung, ein unterschiedliches Spray-Verhalten, das die höhere Entzündbarkeit der letzteren bestätigt.

Außerdem wurde der Einfluss der Position des Zünders auf die Zündleistung untersucht. Im Rahmen des EU-Projekts SOPRANO wurden zweiphasige

Strömungssimulationen durchgeführt, bei denen die experimentell ermittelten SMD-Werte des Sprays und die Tröpfchen Verteilung als Eingaben verwendet wurden. Es wurden drei verschiedene Standorte unterschieden, deren Leistung in großer Höhe miteinander und mit dem Nennstandort verglichen wurde. Die Ergebnisse zeigten, dass die Zündwahrscheinlichkeit sehr empfindlich auf den Standort des Zünders reagiert. Anschließend wurde der Tracking-Algorithmus eingesetzt, um einen Einblick in die Wechselwirkung zwischen der Verschiebung der heißen Gase und dem immanenten Strömungsfeld zu erhalten.

In realistischen Konfigurationen ist das Scheitern der Zündung nicht strikt mit der Flammenkernbildung korreliert, sondern wird auf die nachfolgende Flammenentwicklung zurückgeführt. Letztere hängt von der Reaktionsgeschwindigkeit, der Qualität der Zerstäubung und dem momentanen Strömungsfeld in der Funkenregion ab. Die Verweilzeit des Gemisches sollte die Reaktions- und Verdampfungszeitskala überschreiten, um eine stabile Flamme zu gewährleisten. Der in der Brennkammer verwendete Luftstrom verursacht jedoch einen Interessenkonflikt zwischen der Verdampfungsrate und der Verweilzeit. Bei konstanten globalen Betriebsbedingungen verbessert ein erhöhter Luftstrom durch die Düse einerseits die Qualität der Zerstäubung, reduziert aber andererseits die Verweilzeit erheblich. Die Auswirkung einer Erhöhung des Luftdurchsatzes in der Primärzone wurde in drei simulierten Höhenlagen untersucht, und die Ergebnisse zeigten, dass die Auswirkung der Verweilzeit bei ungünstigen Bedingungen immens zunimmt. Schließlich ist eines der entwickelten Merkmale des Tracking-Algorithmus die Berechnung der Geschwindigkeit der heißen Gase. Die Ergebnisse zeigten eine gute Übereinstimmung mit den Simulationen der kalten Strömung unter ähnlichen Bedingungen, sowohl hinsichtlich der Größe als auch der Richtung.

Gliederung der Dissertation:

Kapitel 2 - Theoretical background: Eine kurze Einführung in die allgemeinen Erhaltungsgleichungen für laminare und turbulente Strömungen erfolgt, die die Grundlage für die numerische Strömungsmodellierung der Gasphase bilden. Insbesondere wird auf die statistische Beschreibung turbulenter Strömungen eingegangen, wie sie in den meisten technischen Geräten vorkommen. Darüber hinaus werden die Grundlagen des Verbrennungsprozesses eingeführt, wobei die Phänomenologie laminarer und turbulenter vorgemischter Flammen sowie die Sprayverbrennung und Flammenstabilisierung behandelt werden. Außerdem wird der Zündprozess, der den Kern dieser Forschungsarbeit bildet, eingehend erläutert und eine Literaturübersicht angegeben. Besondere Aufmerksamkeit wird schließlich den Parametern gewidmet, die die Zerstäubung des Sprays beeinflussen, ein Prozess, der untrennbar mit der Zündung verbunden ist.

Kapitel 3 - Experimental Method: Die Hauptkomponenten der Höhenversuchsanlage und eine ausführliche Beschreibung der in diesem Forschungsrahmen entwickelten Brennkammer werden vorgestellt. Darüber hinaus wird der komplette Messungsplan für die Zünd- und Sprayuntersuchungen definiert. Dieses Kapitel konzentriert sich auf die Entwicklung, Validierung und Implementierung der Messverfahren, die zur vollständigen Charakterisierung der Zünd- und Zerstäubungsprozesse unter Höhenbedingungen eingesetzt werden. Die Entwicklung eines fortschrittlichen Bildverarbeitungscodes zur Verfolgung der Verschiebung des Leuchtkraftzentrums der Flamme in der Brennkammer und die Shadowgraphy-Messtechnik werden im Detail vorgestellt.

Kapitel 4 - Numerical Method: Das durch RANS-Simulationen für verschiedene Betriebsbedingungen erzeugte Strömungsfeld wird vorgestellt. Zunächst wird eine kurze Einführung in den numerischen Aufbau, wie das erzeugte Netz und die Randbedingungen, gegeben. Anschließend werden zwei verschiedene Ansätze zur Abschätzung der Verweilzeit des Gemischs in der Primärzone, die für den Zündvorgang dominant erscheint, definiert.

Kapitel 5 - Results and Discussion: Die Höhenwiederzündfähigkeit der beiden verschiedenen eingesetzten Konfigurationen (mit und ohne Effusionskühlung) wird verglichen. Im Einzelnen werden Ergebnisse zur Zündwahrscheinlichkeit bei konstantem Brennstoffmassenstrom, zur Bestimmung der Mindest-FAR für ein erfolgreiches Zündereignis und zum Zündzeitpunkt vorgestellt. Außerdem wurden Hochgeschwindigkeitsaufnahmen der instationären Flammenkernbildung und -ausbreitung gewonnen und eingehend analysiert. Darüber hinaus werden die Spraymessungen unter Höhenbedingungen vorgestellt und deren Ergebnisse mit der Zündmessung verknüpft. Von besonderem Interesse sind auch die Auswirkungen der Qualität der Zerstäubung und der Verweilzeit, die sich auf den Zündprozess gegenläufig auswirken. Schließlich wurde die Verlagerung der Heißgase mit Hilfe des entwickelten Tracking-Algorithmus gründlich analysiert. Die erzielten Ergebnisse wurden mit den CFD-Vorhersagen für die Geschwindigkeit des Mediums unter ähnlichen Betriebsbedingungen verglichen.

Die Dissertation schließt sich mit einer Zusammenfassung der wichtigsten Ergebnisse dieser experimentellen Untersuchung und Vorschlägen für weitere Forschungsarbeiten.

Contents

List of Figures

List of Tables

Nomenclature

A	Cross Sectional Area	m^2
A	Pre-exponential Coefficient	s^{-1}
a	Thermal Diffusivity	m^2s^{-1}
B_M	Spalding Mass Transfer Number	-
c	Overall Concentration	$kmolm^{-3}$
$\dot{c}$	Molecular Flux	$kmolm^{-2}\ s^{-1}$
C_D	Drag Coefficient	-
Cp	Specific Heat Capacity with p=constant	$Jkg^{-1}\ K^{-1}$
C_V	Specific Heat Capacity with V=constant	$Jkg^{-1}\ K^{-1}$
C_j	Droplet Density Number of j^{th} Segment	$numberm^{-3}$
ΔD	Droplet Class Interval	-
d_0	Jet Port Radius	m
d_q	Quenching Distance	m
D	Diameter	m^2
D	Diffusion Coefficient	$m^2\ s^{-1}$
$\dot{D}$	Flux of the Angular Momentum	$kg\ m^2s^{-2}$
D_p	Diameter of the Prefilmer	m

D_h	Double of the Annular Discharge Slot	m
E	Energy	J
E_A	Activation Energy	$Jmol^{-1}$
f	Discrete Particle Number Distribution	-
f	Frequency	Hz
f_a	Continuous Particle Number Distribution	-
F	Flammability Factor	-
F	Force	N
G	Group Combustion Number	-
Δh_c	Specific Heat of Combustion	$J\ kg^{-1}$
h	Convective Heat Transfer Coefficient	$W\ m^{-2}\ K^{-1}$
h	Height	m
h	Specific Enthalpy	$J\ Kg^{-1}$
h^0	Formation Enthalpy	$J\ Kg^{-1}$
$\dot{I}$	Flux of the Axial Momentum	$kgms^{-2}$
I	Luminosity	-
In	Total Intensity of the Binary Image	-
k_i	Arrhenius Constant	-
k	Chain Production/Consumption Rate	s^{-1}
k	Thermal Conductivity	$W\ m^{-1}\ K^{-1}$

k	Turbulent Kinetic Energy	$m^2\ s^{-2}$
K	Evaporation Constant	-
K	Flame Stretch	s^{-1}
l_0	Integral Length Scale	m
l	Length Scale	m
L	Length	m
L_M	Markstein Length	m
L_C	Characteristic Length	m
L_{cc}	Length of the Main Combustion Chamber	m
H_{cc}	Height of the Main Combustion Chamber	m
W_{cc}	Width of the main Combustion Chamber	m
m	Mass	kg
$\dot{m}$	Mass Flow	kgs^{-1}
$\dot{m}''$	Mass Flux	$kgs^{-1}\ m^{-2}$
M_{rel}	Relative Mass Flow	-
M_i	Molecular Mass	$kgmol^{-1}$
n_i	Number of Moles	kmol
$\vec{n}$	Normal Vector	-
n	Overall Reaction Order	-
n	Droplet Number Density	m^{-3}

n_d	Number of Droplets	-
N	Number of Flame Particles	-
N_{att}	Number of Attempts	-
N_i	Number of Droplets	-
N_k	Number of Species in a Mixture	-
p	Pressure	N m^{-2}
P	Probability	-
q	Rossin-Rammler Parameter	-
$\dot{q}$	Heat Release or Loss per Unit Time	W
Q	Fraction of total volume	-
Q	Thermal Energy Release	J $kmol^{-1}$
$r_{l,0}$	Droplet Radius in Reference Conditions	m
r	Radial Coordinate	-
r	Radius	m
R	Specific Gas Constant	J Kg^{-1} K^{-1}
R	Universal Gas Constant	JK^{-1} mol^{-1}
R_{ij}	Reynolds Stress Tensor	Kg m^{-1} s^{-2}
R_0	Radius of the Burner Exit	m
R_c	Droplet Cloud Radius	m
R_b	Radius of Pre-heating Zone	m

sw	Statistical Weight	-
s_n	Standard Deviation	-
Sc	Schmidt Number	-
S_L	Laminar Flame Speed	ms^{-1}
S_T	Turbulent Flame Speed	ms^{-1}
S_D	Displacement Speed	ms^{-1}
S_{ij}	Deformation Tensor	s^{-1}
S	Source Term	-
ΔT_c	Temperature Rise due to Combustion	K
t	Time Step of Image Acquisition	m
t	Time	s
t_{ch}	Chemical Delay time	s
t_i	Ignition Delay time	s
t_{ph}	Physical Delay time	s
T	Temperature	K
u'	Root Mean Square Velocity Fluctuation Component	ms^{-1}
$\tilde{u}$	Velocity Fluctuation Component	ms^{-1}
u_0	Fuel Jet Velocity	ms^{-1}
u_j	Velocity Component in Direction j	ms^{-1}
$d\overline{Vol}$	Droplet Volume Fraction	-

v_{ki}^{f}	Stoichiometric Coefficients (Forward Reaction)	kmol
v_{ki}^{b}	Stoichiometric Coefficients (Backward Reaction)	kmol
v	Volume	m^3
v_j	Volume of j^{th} Segment	m^3
v	Kinematic Viscosity	$m^2\ s^{-1}$
V	Volume	m^3
$\dot{V}$	Volumetric Flow	$m^3\ s^{-1}$
w	Tangential Velocity	ms^{-1}
x	Coordinate in x Direction	m
x	Flame Length	m
x	Flame's Luminosity Center coordinate x Direction	m
X	Rossin-Rammler Parameter	-
X_k	Species k	-
y	Coordinate in y Direction	m
y	Flame's Luminosity Center coordinate y Direction	m
Y	Mass Fraction	$kg\ kg^{-1}$

Greek

a	Thermal Diffusivity	m^2s^{-1}
β	Zeldovic Number	-

δ_{ij}	Kronecker Delta	-
δ_{χ}	Flame Front Deformation	m
δ	Flame Thickness	m
δ_{v}	Pre-heating Zone Thickness	m
δ_{R}	Reaction Zone Thickness	m
ε	Dissipation Rate	$m^2\ s^{-3}$
ζ	Normally Distributed Rando Number	-
η	Kolmogorov Length Scale	m
θ	Specific Volume	m^3kg^{-1}
κ	Specific Heat Capacity	$m^2K^{-1}\ s^{-2}$
κ	Wavenumber	-
λ	Air Number	-
λ	Heat Conductivity	$W\ m^{-2}K^{-1}$
λ	Wavelength	nm
μ	Dynamic Viscosity	$kgm^{-1}s^{-1}$
μ_t	Turbulent Viscosity	m^2s^{-1}
ξ	Mixture fraction	-
ρ	Density	kgm^{-3}
σ	Surface Tension	Nm^{-1}
σ_{ij}	Stress Tensor	$kgm^{-1}s^{-2}$

τ	Residence Time	s
τ	Time Scale	s
φ	Conserved Variable	-
Φ	Equivalence Ratio	-
Φ_0	Overall Equivalence Ratio	-
$\dot{\omega}_k$	Production Rate	s^{-1}
$\dot{\omega}_F$	Fuel Degradation Rate	$kgs^{-1}\ m^{-3}$

Acronyms

AC	Alternating Current
AIT	Auto-ignition Temperature
ALETHO	ALgorithm for imagE processing and Tracking of tHe Object's displacement
AFR	Air to Fuel Ratio
ALR	Air to Liquid Ratio
AMR	Adaptive Mesh Refinement
ATA	Atmospheric Test Rig
CAD	Computer Aided Design
CCD	Charge-Coupled Device
CFD	Computational Fluid Dynamics

Da	Damköhler Number
DC	Direct Current
DNS	Direct Numerical Simulations
DOF	Depth of Field
EASA	European Union Aviation Safety Agency
FAA	Federal Aviation Administration
FAR	Fuel to Air Ratio
FFT	Fast Fourier Transformation
Fo	Fourier Number
IRZ	Inner Recirculation Zone
ISCAR	Ignition under Sub atmospheric Conditions - Altitude Relight
Ka	Karlovitz Number
KIT	Karlsruhe Institute of Technology
Le	Lewis Number
LES	Large Eddy Simulation
Ma	Markstein Number
MIE	Minimum Ignition energy
MMD	Mass Mean Diameter
NR	Normalization Radius
NTC	Negative Temperature Coefficient

NTC Negative Temperature Coefficient

Nu Nusselt Number

Oh Ohnesorge Number

ORZ Outer Recirculation Zone

PDA Phase Doppler Anemometry

PTU Programmable Timing Unit

Pr Prandtl Number

RANS Reynolds Averaged Navier Stokes

Re Reynolds Number

RMS Root Mean Square

RQL Rich Quench Lean

RSM Reynolds Stress Model

SBES Stress Blended Eddy Simulation

Sc Schmidt Number

SL Minimum Slope

SMD Sauter Mean Diameter

SOPRANO SOot Processes and Radiation in Aeronautical inNOvative combustors

SST Shear Stress Transport

UDF User Defined Function

We	Weber Number

Subscripts

0	Initial Conditions
a	Air
abs	Absolute
act	Total Air with Effusion Cooling
$artf$	Total Air with Effusion Cooling
at	Total Air w/o Effusion Cooling
b	Backward Reaction
b	Burnt
br	Border
br	Chain Branching Reaction
$char$	Characteristic
$crit$	Critical Conditions
cc	Combustion Chamber
d	Property of Droplet
$diff$	Diffusion
DOF	Depth of Field
e	Chemical

e	Evaporation
eff	Effective
f	Forward Reaction
fl	Flame
fp	Flame particle
F	Fuel Property
gl	Global
i	Diameter Class of the Discrete Distribution
ign	Ignition
ind	Induction
inv	Inviscid
k	Species
ker	Flame kernel
kin	Kinetic
l	Liquid
ls	Loss
$norm$	Normalized Conditions
nzl	Nozzle
n	Normal Component
p	Prefilmer

pmz	Primary Zone
pt	Particle Tracking
q	Quenching
r	Release
ref	Conditions at Reference Operating Conditions
rel	Relative Conditions
R	Rayleigh
R	Reaction
$Real$	Realistic Value
s	Spark
sec	Secondary Air
st	Stoichiometric Conditions
t	Tangential Component
tot	Total
tr	Chain Termination Reaction
$turb$	Turbulent Conditions
u	Unburnt
w	Water

1 Introduction

The design of modern combustors has been challenging for engineers due to the conflict of interest among emission standards, flame stability, and the jet engine's relighting process. Future commercial aviation trends include concepts with reduced combustor size and lean burning to counter harmful emissions such as nitrous oxides (NO_x) and carbon monoxide (CO). Both designs could adversely affect the combustor's performance during a high-altitude relight. The high-altitude relight capability of an aircraft engine is one of the requirements for an engine's successful certification due to the inherent safety implications [1,2]; thus, it is a critical area of research. The high-altitude relight of a jet engine is a complex process influenced by physical and chemical phenomena, such as chemical kinetics, fluid mechanics, atomization, and fuel evaporation. The complexity of the phenomena governing the ignition process affects the reliability of predicting its behavior. A description of the chain of events during the engine's high altitude relight based on Mosbach et al. [3] can be given as follows:

Kerosene Jet-A1 is injected into the chamber. The spark igniter deposits energy at a rate of a few Hz, producing plasma spheres, subsequently transported by the incoming mixture in specific flow directions dependent on the highly turbulent flow field's instantaneous conditions. The order of magnitude of the plasma's initial temperature is several thousand degrees but decreases rapidly. Reactions are then initiated, and the ignition kernel has been generated. The formation of a stable flame depends strongly on the subsequent development of the flame kernel. Several parameters influence this sequence of events, and

probably the most important are the flow field, the local fuel to air ratio, the droplet sizes, and the ignition energy. Several investigations on the ignition of spray flames have been reported in the literature, evaluating the influence of various parameters on the ignition process under well-defined experimental conditions [4–10]. However, experiments under realistic conditions of an altitude relight are scarce [11–15].

Full-scale engine tests under relight conditions are challenging from a technical and economic perspective, while the instrumentation possibilities are usually limited. The simulation tools for two-phase combustible mixtures are computationally expensive, still under development, and require experimental validation. Non-expensive models that predict the flame propagation following the spark ignition are valuable in assisting engineers during the combustors' early design [16,17]. For this investigation, a one-sector combustion chamber with broad optical access has been employed for experimental investigations at high altitude relight conditions.

This research activity aims to determine the ignition capability of a realistic jet engine's combustion chamber configuration under high-altitude conditions, thus improving the understanding/knowledge of the relevant phenomena. Furthermore, the applicability of existing correlations that describe the high-altitude relight capability, such as the one based on the loading parameter θ [18] (see Eq. (1.1)), will be investigated.

$$\theta = \frac{P_{cc}^{1.75} V_{cc} e^{\left(T_{cc}/300\right)}}{\dot{m}_{a,cc}} \tag{1.1}$$

According to Lefebvre (see Eq. (1.1)), the jet engine's relight depends on the thermodynamic conditions (pressure P_{cc}, temperature T_{cc}), the geometry (volume V_{cc}), as well as the required residence time to accelerate the engine expressed by the air mass flow $\dot{m}_{a,cc}$ through the combustion chamber. The fact that the loading number is not dimensionless implies that the underlying physics governing the ignition process is not well understood, and further investigation should be conducted to capture the effect of other parameters that potentially contribute to the prediction of the high altitude relight process and are not considered in Eq. (1.1).

2 Theoretical background

2.1 Basic Equations in Fluid Dynamic

The differential formulation of a scalar quantity can be applied to the mass, energy, and momentum conservation equations, and it is written as follows:

$$\frac{\partial \rho\varphi}{\partial t} + \frac{\partial(\rho\varphi u_j)}{\partial x_j} = \frac{\partial}{\partial x_j}\Gamma\frac{\partial \phi}{\partial x_j} + S \tag{2.1}$$

The first term on the left side of the equation denotes the rate of change of the variable Φ in the control volume V_C, while the second term describes the convective transport. More specifically, ρ denotes the density of the fluid, t time and u_j the j-th component of the velocity The transport equation's right side describes the cause of the change due to the diffusion term (1st term) and the source term (2nd term).

2.1.1 Mass Balance

The mass balance can be derived by the balance equation of a conserved variable using the aforementioned approach by replacing $\varphi = 1$ [19].

$$\frac{\partial \rho}{\partial t} + \frac{\partial(\rho u_j)}{\partial x_j} = 0 \tag{2.2}$$

Eq. (2.2) states that for an enclosed system, the change of mass in time is equal to the inflow and outflow through the boundary surface. In other words, the sum of the masses maintains constant over time. The first term of the equation describes the local, volume-related mass flow storage, while the second term

is equal to the volume-related mass flow entering and leaving the boundary surface.

The balance equation for a species k can be written as follows:

$$\frac{\partial(\rho Y_k)}{\partial t} + \frac{\partial(\rho u_i Y_k)}{\partial x_i} = -\frac{\partial j^{d,k}}{\partial x_i} + \dot{\omega}_k \tag{2.3}$$

with $\dot{\omega}_k$ the production rate of species k, where $k = 1, \dots N$. In addition, $j^{d,k}$ is the diffusive flux calculated according to Fick's law as follows:

$$j_i^{d,k} = -\rho D_k \frac{\partial Y_k}{\partial x_i} \tag{2.4}$$

where D_k is the diffusion coefficient for a species k. The ratio of kinematic viscosity (momentum diffusion) to mass diffusion defines the dimensionless Schmidt-number as follows:

$$Sc_k = \frac{\mu}{\rho D_k} \tag{2.5}$$

Therefore, Eq. (2.4) may be written:

$$j_i^{d,k} = -\frac{\mu}{Sc_k} \frac{\partial Y_k}{\partial x_i} \tag{2.6}$$

2.1.2 Energy Balance

Heat transfer processes in a reactive flow can be described by the energy balance. According to the first law of thermodynamics, the internal energy of a system changes through the transport of heat and work performed into the system. The balance equation of the specific enthalpy h gives consequently:

$$\frac{\partial(\rho h)}{\partial t}+\frac{\partial(\rho u_i h)}{\partial x_i}=\frac{Dp}{Dt}-\frac{\partial {j_i}^q}{\partial x_i}+\tau_{ij}\frac{\partial u_i}{\partial x_j}+\dot{q}_R \tag{2.7}$$

The specific enthalpy of a mixture is determined by the specific enthalpy of each component of the mixture as follows:

$$\mathrm{h}=\sum_k^{N_k} Y_k h_k \tag{2.8}$$

The gas phase during the altitude relight process can be considered as ideal gas due to the low pressures that are present. Thus, the specific enthalpy of the ideal gases may be written:

$$h_k=h_k^0(T_{ref})+\int_{T_{ref}}^{T} C_{p,k}dT \tag{2.9}$$

The heat flux density ${j_i}^q$ is calculated by the sum of the conduction heat flux and mass diffusive heat flux as follows:

$${j_i}^q=-\lambda\frac{\partial T}{\partial x_i}+\sum_i^{N_k} h_k j_i^{d,k} \tag{2.10}$$

where λ is the thermal conductivity. By considering the dimensionless Prandtl number $Pr={}^{\mu C_p}/_{\lambda}$, which describes the analogy between momentum and thermal diffusivity, and Eq. (2.6), Eq. (2.10) yields:

$${j_i}^q=-\frac{\mu}{Pr}\left[C_p\frac{\partial h}{\partial x_i}+\sum_i^{N_k}\left(\frac{Pr}{Sc_k}-1\right)h_k\frac{\partial Y_k}{\partial x_i}\right] \tag{2.11}$$

2.1.3 Momentum Balance

The momentum balance (Navier-Stokes equations) is derived by the second Newton's axiom, which states that the momentum change is equal to the forces acting on the control volume over time. The forces, which can affect the momentum, are surface forces such as pressure, shear stresses, or body forces such as gravity and electromagnetic forces. Subsequently, the momentum balance related to a compressible Newtonian fluid is the following [20]:

$$\frac{\partial(\rho u_i)}{\partial t} + \frac{\partial(\rho u_i u_j)}{\partial x_j} = -\frac{\partial p}{\partial x_j} + \frac{\partial \tau_{ij}}{\partial x_j} + f_i \tag{2.12}$$

where p stands for the static pressure, i and j denote the direction of action and the reference surface respectively, and f_i represents a body force (e.g., weight). The viscous stress tensor of a Newtonian fluid can be described as follows:

$$\tau_{ij} = 2\mu \left[S_{ij} - \frac{1}{3}\left(\frac{\partial u_i}{\partial x_j}\right)\delta_{ij} \right] \tag{2.13}$$

where μ is the dynamic viscosity, which varies significantly during combustion, due to the very high temperature gradients, while constituting the proportionality constant between the shear stress and the shear rate. In addition, S_{ij} is the strain rate tensor, which can be calculated as follows:

$$S_{ij} = \frac{1}{2}\left(\frac{\partial u_i}{\partial x_j} + \frac{\partial u_j}{\partial x_i}\right) \tag{2.14}$$

with δ_{ij} denoting a function, which is called Kronecker delta:

$$\delta_{ij} = \begin{cases} 1, & if\ i = j \\ 0, & if\ i \neq j \end{cases} \tag{2.15}$$

2.2 Turbulent Flows

The usual approach in fluid mechanics is to distinguish between laminar and turbulent flows. In most technical applications, the flow is turbulent underlying that instead of a smooth flow in parallel streamlines (laminar flows), a chaotic, unsteady, three-dimensional flowing motion governs the flow field. The latter lies in the turbulence's ability to enhance the reactant mixture's mass consumption rate, which subsequently increases the energy release rate and, therefore, the engine's specific (related to volume) power generation. Turbulence consists of temporal and spatial fluctuations in the flow field. The dimensionless number describing the transition from laminar to turbulent flows is called the Reynolds number [21,22]. It compares whether the destabilizing inertial forces are more significant than the stabilizing viscous forces and can be defined as follows.

$$Re = \frac{u \cdot l_{char}}{\nu} \tag{2.16}$$

where u denotes the mean velocity of the flow field, l_{char} a characteristic geometrical dimension, and ν is the kinematic viscosity. At high Reynolds-Number, the inertial forces dominate the viscous forces, so the flow tends to be unstable indicating turbulence. At low Reynolds-Number viscous forces dominate the fluid motion, and the flow becomes laminar [23].

2.2.1 Statistical Description of Turbulent Flows

2.2.1.1 Reynolds Average

Turbulence pertains to chaotic behavior, which can be described statistically by decomposing any instantaneous quantity ϕ into its time-averaged and fluctuating values $\bar{\phi}$ and $\tilde{\phi}$, according to Eq. (2.17).

$$\phi = \bar{\phi} + \tilde{\phi};\ \ \phi' = \sqrt{\overline{\tilde{\phi}^2}} \tag{2.17}$$

where ϕ' denotes the Root Mean Square (RMS) of the fluctuating component.

$$\bar{\phi}(x_i, t) = \lim_{T\to\infty} \frac{1}{T} \int_{t_0}^{t_0+T} \varphi \, dt \tag{2.18}$$

The variable T denotes the period over which the conserved variable will be approximated, with the mean value of the fluctuating component being:

$$\bar{\tilde{\phi}} = \frac{1}{T} \int (\phi - \bar{\phi}) dt = \bar{\phi} - \bar{\phi} = 0 \tag{2.19}$$

Applying the Eq. (2.17), Eq. (2.18) and Eq. (2.19) to the mass and momentum conservation equations Eq.(2.2) & Eq.(2.12) respectively, yields the Reynolds-Averaged-Navier-Stokes (RANS) equations for an incompressible flow, as follows [24] :

$$\rho \frac{\partial \bar{u}_i}{\partial x_i} = 0 \tag{2.20}$$

$$\rho \left(\frac{\partial \bar{u}_i}{\partial t} + \frac{\partial \overline{u_i u_j}}{\partial x_j} \right) = -\frac{\partial \bar{p}}{\partial x_i} + \frac{\partial}{\partial x_j} \bar{\tau}_{ij} \tag{2.21}$$

Through the decomposition of the velocity from Eq. (2.17) and Eq. (2.19), the following are valid:

$$\bar{u}_i = \overline{\bar{u}_i + \tilde{u}_i} = \bar{u}_i \tag{2.22}$$

$$\overline{u_i u_j} = \overline{(\bar{u}_i + \tilde{u}_i)(\bar{u}_j + \tilde{u}_j)} = \bar{u}_i \bar{u}_j + \overline{\tilde{u}_i \tilde{u}_j} \tag{2.23}$$

Hence, from Eq. (2.22 & 2.23), Eq. (2.21) may be written as follows:

$$\rho\left(\frac{\partial \bar{u}_i}{\partial t} + \frac{\partial \overline{u_i u_j}}{\partial x_j}\right) = -\frac{\partial \bar{p}}{\partial x_i} + \frac{\partial}{\partial x_j}\bar{\tau}_{ij} + \frac{\partial}{\partial x_j}\left(-\rho\overline{\tilde{u}_i \tilde{u}_j}\right) \tag{2.24}$$

The last term of the right-hand side arises from the non-linearity of the convective term, according to Eq. (2.23). The so-called Reynolds stress tensor is the only term of Eq. (2.24), which contains information concerning the turbulent fluctuations of the flow and constitutes an additional unknown, raised by the averaging process, creating a closure problem. Thus, different turbulence models need to be employed to derive additional equations for solving the RANS equations' closure (see Section 2.2.3).

2.2.2 Energy Cascade Process

A turbulent flow is composed of a broad spectrum of turbulent eddies sizes. Each eddy is characterized by a length scale l, velocity $u(l)$ and a timescale $t(l) = l/u(l)$ [25]. The large eddies, which depend on the geometrical dimensions, carrying the turbulent kinetic energy major part, are characterized by the integral length scale l_0 and the velocity scale $u(l_0) = u'$. Subsequently, from Eq. (2.38), $u' = u(l_0) = (2k/3)^{1/2} = \sqrt{\frac{1}{3} \cdot \left(\overline{\tilde{u}_x^2} + \overline{\tilde{u}_y^2} + \overline{\tilde{u}_z^2}\right)}$ is derived, denoting the RMS of the fluctuating velocity where k is the turbulent kinetic energy.

The large interacting eddies disintegrate continuously into smaller eddies until the Kolmogorov length is reached, where dissipation of the turbulent kinetic energy into heat takes place. This mechanism is the so-called energy cascade process [26]. The rate of the turbulent kinetic energy extracted from the mean flow can be described by the following equation:

$$\Pi = -\overline{\tilde{u}_\iota \cdot \tilde{u}_J} \cdot S_{ij} \tag{2.25}$$

Since $S_{ij} \sim {u'}/{l_0}$ and $\tilde{u}_i \sim u'$ it applies $\Pi \sim \frac{u'^3}{l_0}$.

For high Re_t, most of the energy cascade's dissipation is contained in the Kolmogorov scale, and may be written as follows:

$$\varepsilon = 2\nu\overline{\tilde{S}_{\iota J} \cdot \tilde{S}_{\iota J}} \sim \nu \frac{u_\eta^2}{\eta^2} \tag{2.26}$$

where η denotes the Kolmogorov length scale. It is conspicuous that the dissipation grows with the gradient of the velocity. Moreover, to achieve the dynamic balance, Π should be in the order of ε, in other words $\Pi \sim \varepsilon$. The latter implies that there is no energy storage at any intermittent condition, and the same energy, which has been extracted, will be eventually dissipated.

Furthermore, the Reynolds number based on the smallest Eddy should be introduced.

$$Re_\eta = \frac{u_\eta \cdot \eta}{\nu} \sim 1 \tag{2.27}$$

According to the first Kolmogorov Hypothesis on local similarity, under sufficiently high Reynolds numbers, the statistics of the small scale turbulent have

a universal form, which is uniquely determined by the viscosity v and the dissipation ε. Thus, a dimensional analysis derives the so-called Kolmogorov scales:

Length scale

The Eq. (2.26) based on the Kolmogorov length scale yields:

$$\eta^2 \sim \frac{v u_n^2}{\varepsilon} \tag{2.28}$$

By substituting u_η from Eq. (2.27) to Eq. (2.28), the following applies:

$$\eta \sim \left(\frac{v^3}{\varepsilon}\right)^{1/4} \tag{2.29}$$

Velocity scale

$$u_\eta \sim (\varepsilon v)^{1/4} \tag{2.30}$$

Time scale

$$\tau_\eta \sim \left(\frac{v}{\varepsilon}\right)^{1/2} \tag{2.31}$$

The Kolmogorov scale can be also related with the system scale (associated with the large eddies), by taking in to account the proportionality $\Pi \sim \varepsilon$ and assuming high Re_t.

$$\frac{u'^3}{l} \sim v \frac{u_\eta^2}{\eta^2} \overset{(2.27)}{\approx} \frac{v^3}{\eta^4} \tag{2.32}$$

Hence, solving Eq. (2.32) based on the η/l_0 yields:

$$\frac{\eta}{l_0} \sim Re_t^{-\frac{3}{4}} \tag{2.33}$$

where $Re_t = {u' l_0}/{\nu}$ is associated with the large eddy scale. It is evident that as the Reynolds number increases, the separation of the largest and the smallest eddies increases as well.

In Figure 2.1, the turbulent kinetic energy distribution spectrum concerning wavenumber (κ) is illustrated. The turbulent kinetic energy production process takes place through the large eddies, whose kinetic energy has been extracted by the mean flow. The large structures' unstable nature leads to a continuous transfer of kinetic energy towards smaller structures. Once the turbulent structures are in the Kolmogorov length scale order, the kinetic energy is dissipated to heat. The total turbulent kinetic energy may be written as follows:

$$k = \int_0^\infty E(\kappa) d\kappa \tag{2.34}$$

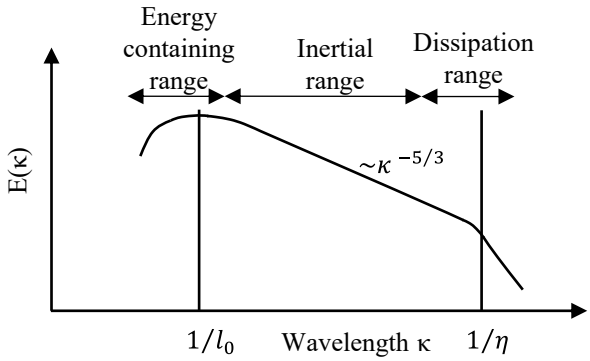

Figure 2.1 Distribution of turbulent kinetic energy spectrum [27]

Another length scale whose physical meaning is not as plain as the Kolmogorov or the large scale is the so-called Taylor microscale λ. It constitutes an intermediate scale, which is smaller than the integral scale and larger than the Kolmogorov scale. Within this intermediate zone is essential to define an additional subrange, the so-called inertial subrange, which lies between $l_{EI} > l > l_{DI}$, as shown in Figure 2.2. The l_{EI} length scale describes the declamation point from which eddies become isotropic. In addition, l_{DI} corresponds to the limit from which the viscous effect becomes dominant on the eddy dynamic. The Taylor length scale is defined based on the turbulent energy dissipation per unit mass for isotropic turbulence as follows [28]:

$$\varepsilon = 15\nu\overline{\tilde{S}_{ij}\tilde{S}_{ij}} \tag{2.35}$$

$$\lambda \sim \sqrt{15\frac{\nu}{\varepsilon}u'} \tag{2.36}$$

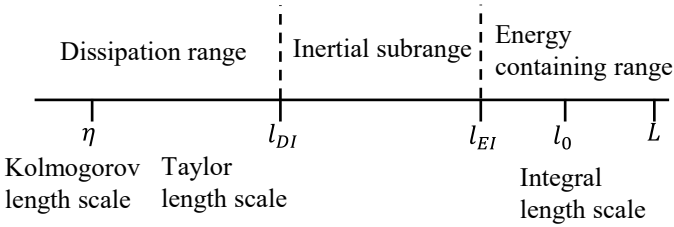

Figure 2.2: Turbulence length scales [25]

2.2.3 Modeling of the Reynolds Stresses

As mentioned afore (see Section 2.2.1.1), the new quantity (i.e., Reynolds stress tensor) arising from the averaging imposes a closure problem for solving the equation. Different approaches address the modeling of the Reynolds

stresses. One of the most common ways is to apply the eddy (or turbulent) viscosity assumption to model the Reynolds-Stress tensor, the so-called Boussinesq hypothesis [29].

$$R_{ij} = -\rho\overline{\tilde{u}_i\tilde{u}_j} = \mu_t\left(\frac{\partial\bar{u}_i}{\partial x_j} + \frac{\partial\bar{u}_j}{\partial x_i}\right) - \frac{2}{3}\rho k\delta_{ij} \tag{2.37}$$

where k is the turbulent kinetic energy, which may be written as follows:

$$\mathrm{k} = \frac{1}{2}\overline{\tilde{u}_i\tilde{u}_i} \tag{2.38}$$

and defines the energy contained in the turbulent velocity fluctuations. The proportionality factor μ_t denotes the turbulent viscosity related to the vortex structure of turbulent flows. In contrast to the laminar viscosity, the turbulent viscosity is not a substance quantity but rather depends on the local flow conditions. The turbulent viscosity is unknown, so it needs to be modeled. The modeling approximation consists of zero-, one-, two-or higher-order equation models, by which the turbulent viscosity is determined. One of the most commonly two-equation models used in the RANS simulation context is the k-ε model [30–32]. Launder and Sharma later proposed the most widely used k-ε model to simulate mean flow characteristics under turbulent conditions, with optimized parameters, the so-called standard k-ε model [33]. In this model, the following correlation is applied:

$$\mu_t = \rho C_\mu \frac{k^2}{\varepsilon} \tag{2.39}$$

where C_μ is a constant (see Table 2.1). Subsequently, the two transport equations for both variables are derived as follows:

k-Equation

$$\frac{\partial(\rho k)}{\partial t} + \frac{\partial(\rho k\overline{u_i})}{\partial x_i} = \frac{\partial}{\partial x_j}\left[\left(\mu + \frac{\mu_t}{Pr_k}\right)\frac{\partial k}{\partial x_j}\right] + P_k - \rho\varepsilon \tag{2.40}$$

ε-Equation

$$\frac{\partial(\rho\varepsilon)}{\partial t} + \frac{\partial(\rho\varepsilon\overline{u_i})}{\partial x_i} = \frac{\partial}{\partial x_j}\left[\left(\mu + \frac{\mu_t}{Pr_\varepsilon}\right)\frac{\partial \varepsilon}{\partial x_j}\right] + C_{\varepsilon 1}P_k\frac{\varepsilon}{k} - \rho C_{\varepsilon 2}\frac{\varepsilon^2}{k} \tag{2.41}$$

where Pr is the turbulent Prandtl number and the term P_k denotes the production of the turbulent kinetic energy and may be written:

$$P_k = -\rho\overline{\tilde{u}_i\tilde{u}_j}\frac{\partial \bar{u}_i}{\partial x_j} \tag{2.42}$$

C_μ [−]	$C_{\varepsilon 1}$ [−]	$C_{\varepsilon 2}$ [−]	Pr_k [−]	Pr_ε [−]
0.09	1.44	1.92	1.0	1.3

Table 2.1: Coefficients of k-ε model [33].

Another commonly employed two-equation model, which constitutes a closure for the RANS equations, is the k-ω model. It is based on the hypothesis that the specific rate of dissipation ω is characteristic of all the turbulent motions [34]. Thus, the transport equation for the specific rate of dissipation can be derived:

k-*Equation*

$$\frac{\partial(\rho k)}{\partial t} + \frac{\partial(\rho k\overline{u_i})}{\partial x_i} = \rho P_k - \beta^*\rho k + \frac{\partial}{\partial x_j}\left[\left(\mu + \sigma^*\frac{\rho k}{\omega}\right)\frac{\partial k}{\partial x_j}\right] \tag{2.43}$$

ω-*Equation*

$$\frac{\partial(\rho\omega)}{\partial t}+\frac{\partial(\rho\omega\overline{u_i})}{\partial x_i} = \frac{\alpha\omega}{k}P_k-\beta\rho\omega^2+\frac{\partial}{\partial x_j}\left[\left(\mu+\sigma\frac{\rho k}{\omega}\right)\frac{\partial\omega}{\partial x_j}\right] + \sigma_d\frac{\rho}{\omega}\frac{\partial k}{\partial x_j}\frac{\partial\omega}{\partial x_j} \tag{2.44}$$

where $\alpha, \beta, \sigma, \sigma^*, \sigma_d$ are closure coefficients, which have been reported in the literature [35]. A different approach, which does not consider isentropic turbulent viscosity and determines the Reynolds stresses by the transport equation of each stress component, is the Reynolds-stress-model (RSM) [25].

Applying the aforementioned Reynolds averaging to the balance equations of species and energy leads to the following correlations, respectively:

$$\frac{\partial(\rho\overline{Y_k})}{\partial t}+\frac{\partial(\rho\overline{u_i}\overline{Y_k})}{\partial x_i}=-\frac{\partial}{\partial x_i}\left(\rho\overline{D_k}\frac{\overline{\partial Y_k}}{\partial x_i}+\rho\overline{\tilde{u}_i\tilde{Y}_k}\right)+\overline{\dot{\omega}_k} \tag{2.45}$$

$$\frac{\partial(\rho h)}{\partial t}+\frac{\partial(\rho\overline{u_i}\overline{h})}{\partial x_i}=\frac{D\bar{p}}{Dt}-\frac{\partial}{\partial x_i}\left(\overline{j_i^q}-\rho\overline{\tilde{u}_i\tilde{h}}\right)+\overline{\tau_{ij}\frac{\partial u_i}{\partial x_j}}+\overline{\dot{q}_R} \tag{2.46}$$

where the Reynolds fluxes $\rho\overline{\tilde{u}_i\tilde{Y}_k}$ and $\rho\overline{\tilde{u}_i\tilde{h}}$ are modelled analogously to the Reynolds stresses (see Eq. (2.37)

2.3 Combustion

A basic understanding of the combustion processes is essential for the analysis of the ignition process. This subsection summarizes the theory of combustion

with attention to laminar and turbulent premixed flames and droplet combustion. In general, the chemical reaction where fuel conversion into products and heat takes place is the so-called combustion process. One of the most important parameters describing the combustion process is the combustible mixture's composition, expressed by the ratio between the oxidizer and the fuel. Depending on this ratio, three different categories arise. There is just as much oxidizer as required for the fuel's total consumption in the case of stoichiometric mixtures. Under these conditions, the necessary amount of air can be determined directly by the chemical reaction of the combustion stoichiometry as follows:

$$C_a\, H_b + \left(a + \frac{b}{4}\right)(O_2 + 3.76N_2) \rightarrow aCO_2 + \frac{b}{2}H_2O + 3.76\left(a + \frac{b}{4}\right)N_2 \tag{2.47}$$

where a, b denote the stoichiometric coefficients. In addition, the N_2 is considered an inert gas, and subsequently, the same number of moles exist in both educts and products. When the amount of air provided is greater than the required one for combustion, apart from the main products, i.e., water, carbon dioxide, and inert nitrogen, there is a remaining oxygen percentage. This is the so-called "lean" combustion. On the other hand, if the combustion process takes place with a lack of oxygen, incomplete combustion products are formed, such as carbon monoxide, hydrogen, and unburned hydrocarbons. The latter is the so-called "rich" combustion. For a quantitative description of the combustion stoichiometry, the so-called air number or air ratio λ is used.

$$\lambda = \frac{AFR}{AFR_{st}} = \frac{\left(\frac{m_a}{m_F}\right)}{\left(\frac{m_a}{m_F}\right)_{st}} \tag{2.48}$$

In a wide range of applications, the so-called equivalence ratio φ is used, which is expressed by the following correlation:

$$\varphi = \frac{1}{\lambda} = \frac{FAR}{FAR_{st}} = \frac{\left(\frac{m_F}{m_a}\right)}{\left(\frac{m_F}{m_a}\right)_{st}} \tag{2.49}$$

Eq. (2.47) constitutes the global reaction, albeit, in reality, a chemical reaction consists of several elementary reactions, which include numerous elementary steps and intermediate products. The elementary reactions can occur concurrently and compete with each other [36,37]. The reaction mechanism is the system of the elementary equations, which describes the global reaction.

$$\sum_{k=1}^{N_k} v_{ki}^{f} X_k \rightleftharpoons \sum_{k=1}^{N_k} v_{ki}^{b} X_k \,, with\ i = 1 - N_r \tag{2.50}$$

where v_{ki}^{f} and v_{ki}^{b} are the stoichiometric coefficients of the species k for the forward and backward reaction of the i^{th} elementary reaction, respectively. In addition, X_k represents the species k. The production rate $\dot{\omega}_k$ of a species k can be calculated by the following correlations.

$$\dot{\omega}_k = \sum_{k=1}^{N_k} v_{ki} r_i \tag{2.51}$$

$$v_{ki} = \left(v_{ki}^{f} - v_{ki}^{b}\right) \tag{2.52}$$

where r_i denotes the reaction velocity for the forward and backward reaction of the i^{th} elementary reaction, which can be determined as follows:

$$r_i = k_i^f \prod_{k=1}^{N_k} [X_k] v_{ki}^f - k_i^b \prod_{k=1}^{N_k} [X_k] v_{ki}^b w \tag{2.53}$$

with k_i being the reaction rate coefficients and $[X_k]$ the molar concentration (i.e., [kmol/m^3]) of species k. The former depends on the collision rate of the molecules expressing the probability that an impact will cause the molecules to react. Based on the collision theory the following expression for the reaction rate coefficients can be derived [38,39].

$$k_i = A_i T^B e^{-\frac{E_A}{RT}} \tag{2.54}$$

where A_i is the pre-exponential factor, which is constant for each chemical reaction. T is the temperature, R the universal gas constant and E_A the activation energy of the reaction.

2.3.1 Laminar Premixed Flames

Laminar premixed flames are commonly utilized in various practical operations, especially in small devices with low residence time where high heat release rates are desired. Despite their widespread use, understanding turbulent flames can be significantly enhanced through prior knowledge of laminar flames. It is evident that the same physical processes govern both laminar and turbulent flows, leading to the development of turbulent flame theories based on the structure of laminar flames. In the analysis of laminar flames, particular emphasis is placed on the laminar flame speed as it determines essential flame features such as stabilization and shape. More specifically, the laminar flame speed S_L corresponds to the velocity of the incoming gas v_0 normal to the stationary flame front (see Figure 2.3).

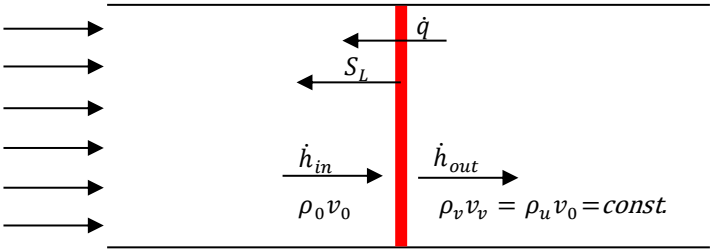

Figure 2.3: Schematic representation of the laminar flame front

In Figure 2.4, the temperature profile of the corresponding laminar flame, approximated by linearization, is illustrated [40]. The flow is considered without losses. Linear approaches describe heat and mass transfer. The linear rise's width constitutes the flame thickness $\delta = \delta_v + \delta_R$, where δ_v and δ_R denote the pre-heating and reaction zones' thickness, respectively. One-dimensional simulations can determine the flame thickness from the linearization of the steepest temperature gradient as follows [41]:

$$\delta = \frac{T_b - T_u}{max\left(\frac{\partial T}{\partial x}\right)} \tag{2.55}$$

where T_b and T_u are the temperatures of the burnt and unburnt gases, respectively. According to the thermal theory of Mallard and Le Chatelier [42], the transition from the preheating zone to the reaction zone is defined as the point of imminent ignition after a temperature rise of ΔT_v. However, there are no adequate means to determine an ignition temperature. The enthalpy necessary to reach the ignition temperature is transferred, due to the temperature gradient, from the reaction zone to the preheating zone by heat conduction, whose direction is against the flow (see Figure 2.4), yielding the following correlation:

$$\rho_0 S_L C_p \Delta T_v = \lambda \frac{\Delta T_R}{\delta_R} \tag{2.56}$$

The following correlation applies for the flame thickness:

$$\delta = \delta_v + \delta_R = \frac{a}{S_L}\frac{\Delta T}{\Delta T_v} \sim \frac{a}{S_L} \tag{2.57}$$

The detailed derivation of Eq. (2.57) has been thoroughly described in the literature [38].
The enthalpy balance in the reaction zone can express the thickness of the flame front, which constitutes an unknown, by considering the following assumptions [38] :

1. One dimensional, constant area, steady flow problem.
2. Viscous shear work, thermal radiation, kinetic and potential energy are negligible.
3. Constant pressure.
4. The Lewis number Le, which determines the ratio of the thermal diffusivity to the mass diffusivity, i.e. $Le = \frac{a}{D} = \frac{\lambda}{\rho D C_p}$, is unity.
5. Single step exothermic reaction.
6. Complete consumption of the fuel at the flame.

$$\rho_0 S_L C_p \Delta T = -\Delta h_c \delta \dot{\omega}_F \tag{2.58}$$

where $\dot{\omega}_F$ denotes the fuel's volumetric degradation rate Δh_c denotes the heat of combustion, which based on the single step stoichiometry $1\ kg\ fuel + x\ kg\ air \rightarrow (1+x)\ kg\ products$ becomes $\Delta h_c = (1+x)\ C_p \Delta T$. The following correlation for the flame thickness is derived:

$$\delta = \frac{1}{(1+x)} \frac{-\rho_0}{\underbrace{\dot{\omega}_F}_{\tau_R}} S_L \tag{2.59}$$

The dimensional analysis expresses the thickness of the flame with the local characteristic chemical reaction time τ_R. Thus, the combination of Eq. (2.57) and Eq. (2.59) yields the laminar burning velocity:

$$S_L = \left[a(1+x) \frac{-\dot{\omega}_F}{\underbrace{\rho_0}_{\tau_R^{-1}}} \frac{\Delta T}{\Delta T_v} \right]^{\frac{1}{2}} \sim \sqrt{\frac{a}{\tau_R}} \tag{2.60}$$

The temperature ratio requires the estimation of the ignition temperature, which is a theoretical value and cannot be determined.

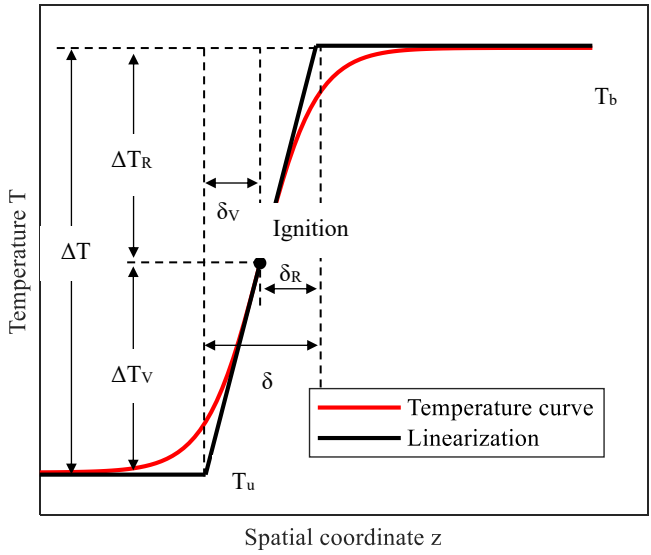

Figure 2.4: Schematic representation of the one-dimensional thermal theory in laminar planar premixed flames

2.3.2 Flame stretch

The so-called flame stretch is an additional parameter originally introduced by Karlovitz [43,44] and affects the laminar burning velocity. The stretch is caused by a non-uniform flow, to which the flame is subjected when propagating or area changes caused by the curvature effects. It can even extinguish the flame since it distracts energy from the flame front. The general definition of the flame stretch describes the logarithmic change of area A in time and is expressed as follows:

$$K \equiv \frac{1}{A}\frac{d}{dt}A \tag{2.61}$$

where $A(t)$ is any area element of the flame surface undergoing a different stretch according to the local flow conditions (see Figure 2.5). The change in time of each area element $A(t + \Delta t)$ depends on their absolute velocity $\vec{w}$ [40,45,46].

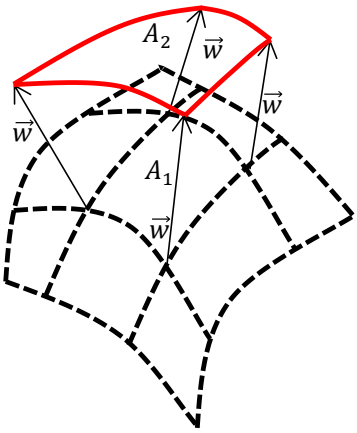

Figure 2.5: Different area elements of the flame's surface move with their corresponding velocity, leading to an increased surface area

The surface's absolute velocity can be split into its components $\vec{w} = \vec{w}_t + \vec{w}_n$, which denote the tangential and normal velocity, respectively [40].

$$K = \frac{1}{A}\lim_{\Delta t \to 0}\frac{A(t+\Delta t) - A(t)}{\Delta t} = \underbrace{\nabla_t \cdot \vec{w}_t}_{\substack{total\\ tangential\\ stretch}} + \underbrace{(\vec{w}\cdot\vec{n})\nabla\cdot\vec{n}}_{\substack{total\\ normal\\ stretch}} \tag{2.62}$$

where $\nabla_t \cdot \vec{w}_t$ refers to the tangential divergence of the surface's velocity w tangential component. Since the flame front propagates only in the normal direction, the tangential component can be caused only by the fluid's movement, and more specifically, by the tangential component $\vec{u}_t$ of the fluid's velocity. Therefore, the following applies:

$$\vec{w}_t = \vec{u}_t \tag{2.63}$$

The last term of Eq. (2.62) contains the divergence of the surface normal vector $\nabla \cdot \vec{n}$, which constitutes the mean curvature of a three-dimensional surface. Therefore, it is possible to determine the difference between the stretching parts caused by the fluid and those caused by the flame curvature.

Another frequently formulation used to determine the flame's stretching is based on the so-called displacement speed S_d, which is defined as the relative velocity of the flame's surface to the fluid velocity $\vec{u}$ [47] as follows:

$$S_d = (\vec{w} - \vec{u}) \cdot \vec{n} \tag{2.64}$$

By combining Eq. (2.63) and Eq. (2.64), Eq. (2.62) may be written:

$$K = \underbrace{\nabla_t \cdot \vec{u}_t}_{K_t} + \overbrace{(\vec{u}\cdot\vec{n})\nabla\cdot\vec{n} + S_d}^{K_n}\nabla\cdot\vec{n} \tag{2.65}$$

It is conspicuous that the two-leading mechanisms of the flame stretch concerning the flame surface are the tangential stretching and the movement in the

normal direction of the curved surface. The tangential velocity $\vec{u}_t$ pulls the planar flame apart whereas the positively curved flame moves normal to itself with the total velocity $(\vec{u} \cdot \vec{n}) + S_d$ leading to an increase of the flame surface.

The effect of an increased stretch-induced into the flame speed is not deterministic. Subsequently, the Lewis-number Le, which determines how the flame reacts when exposed to stretch, is introduced. More specifically, it compares how fast the heat is conducted away compared to the diffusion of the reactants towards the flame.

$$Le \equiv \frac{a}{D} \tag{2.66}$$

where a is the thermal diffusivity and D the diffusion coefficient of the deficient species. Relative to the equivalence ratio Φ the deficient species is fuel ($\Phi < 1$) or oxygen O_2 ($\Phi > 1$). The maximum unstretched flame speed $S^0_{L,max}$ is achieved in planar flames approximately at the stoichiometric conditions ($\Phi \approx 1$). For stretched and curved flames, when $Le > 1$, i.e., $a > D$ [41,48], the heat flux $\nabla \cdot \vec{q}$ diffuses faster than the reactants $\nabla \cdot \vec{j}$. If the flame is positively curved ($\nabla \cdot \vec{n} > 0$) the heat flux is defocused and the heat loss is greater compared to a planar flame, which leads to a corresponding lower local flame speed. In contrast, when the flame has negative curvature ($\nabla \cdot \vec{n} < 0$) the heat flux is focused, and as a result the heat conducted away is less compared to the planar plane, leading to a higher local flame speed. If $Le < 1$, i.e., $a < D$ the local flame speed's determination depends on the preferential diffusion. When the flame has positive curvature, the mass flux is focused in a smaller area, which leads to a shifting of the local flame speed towards higher values if the diffusion coefficient of the deficient species is greater than the one of the abundant species. One the other hand, if the abundant species' coefficient is greater

than the deficient species' corresponding, the local flame speed decreases. With a negative curvature the mass flux is defocused, which leads to a spread of the faster species to a larger area. If the oxygen is less mobile than the fuel $D_F > D_{O_2}$, leaner conditions are created locally and richer on the contrary. Therefore, the fresh gases' equivalence ratio determines whether this is beneficial for the local flame speed or vice versa [49].

The linear Markstein model with a first-order Taylor expansion gives a simplified approach for quantifying the effect caused by a low stretch on the flame speed [50].

$$S_L(K) \approx S_L^0 + \left.\frac{\partial S_L}{\partial K}\right|_K (K - 0) \tag{2.67}$$

The Markstein length L_M describes the effect of the stretch on the flame speed as follows:

$$\mathrm{L}_M \equiv -\frac{\partial S_L}{\partial K} \tag{2.68}$$

By introducing the unstretched flame thickness δ^0 and dividing with the unstretched burning velocity, Eq. (2.67) yields [51]:

$$\frac{S_L(K)}{S_L^0} \approx 1 - \frac{\mathrm{L}_M}{\delta^0}\frac{K\delta^0}{S_L^0} \tag{2.69}$$

where $\frac{\mathrm{L}_M}{\delta^0}$ constitutes the so-called Markstein number M_a, and the $\frac{K\delta^0}{S_L^0}$ denotes the Karlovitz number K_a ending up into the following linear relationship, which describes how a low-intensity stretch controls the laminar burning velocity.

$$\frac{S_L(K)}{S_L^0} \approx 1 - \mathrm{M}_a \mathrm{K}_a \tag{2.70}$$

Several experimental studies have been reported in the literature concerning the determination of the laminar burning velocity. A detailed review was compiled by Egolfopoulos et al. [52], which contains the current state of knowledge on the influence of stretch on the burning velocity of spherical flames. In addition, the reviews of Daguat et al. [53] and Ranzi et al. [54] contain a summary of the experimental investigations regarding the laminar burning velocities of hydrocarbon-based fuels.

More specifically, experiments determining the laminar burning velocity of the kerosene Jet-A-1, which is the most common aviation fuel, are scarce. Vukadinovic et al. [55] and Chong and Hochgreb [56] investigated the laminar burning velocity of the Jet-A-1 under high pressure and temperature, respectively, with varied equivalence ratios. Furthermore, Kumar et al. [57] and Hui and Sung [58] investigated Jet-A also under high temperature and pressure. Honnet et al. [59], following the correlation proposed by Brandley et al. [60] , obtained under atmospheric conditions with equivalence ratio $\Phi = 1.1$, a laminar burning velocity 0.4 m/s. Under high altitude conditions (low pressure and temperature), the laminar burning velocity is a theoretical value due to the liquid phase's presence. However, it constitutes a mixture's reactivity indication.

2.3.3 Turbulent Premixed Flames

In section 2.3.1, it was shown that the laminar burning velocity is a function of the thermodynamic state and the composition of the mixture. In the turbulent premixed flames, the flame front is also affected by the flow field. According

to the simplified assumption of Damköhler [61], in the case of large-scale turbulence, the turbulent eddies are larger than the flame thickness δ of the flame front. The turbulent structures deform the flame front, which increases the surface area. The turbulent flame is essentially considered as a wrinkled laminar flame, depicted in Figure 2.6. Therefore, the basic phenomena of diffusion, convection, and chemical reactions have similar characteristics in laminar and turbulent flames. Thus, according to Eq. (2.71), the turbulent flame speed can be determined relative to the laminar burning velocity.

$$\frac{S_T}{S_L} = \frac{A_T}{A_L} \tag{2.71}$$

where A_T denotes the instantaneous area of the laminar flame contained in a duct with a constant area A_L. Damköhler correlated the increase of the area in a turbulent wrinkled flame with the increase of the fluctuating velocity's RMS u' of the unburned gas upstream of the turbulent flame front., as follows [62].

$$\frac{A_T}{A_L} = 1 + \frac{u'}{S_L} \overset{2.71}{\Rightarrow} S_T = S_L + u' \tag{2.72}$$

The statistical description of a turbulent premixed flames is based on the dimensional analysis and the following assumptions:

- Homogeneous turbulence indicating that the flow's statistical properties are identical at every point of the flow field.
- Isotropic flow filed, which expresses no directional dependence of the local statistical quantities.
- Statistically steady quantities of the turbulent flow.

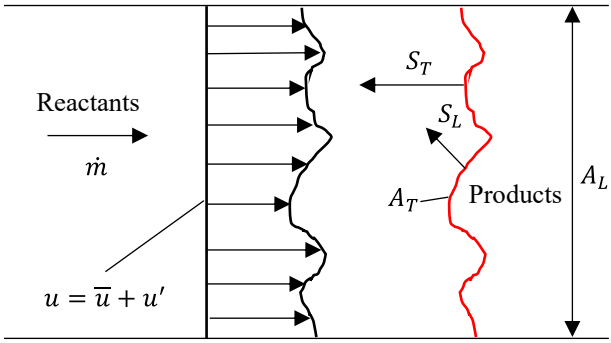

Figure 2.6: Schematic illustration of a turbulent premixed flame in a constant area duct

The ratio of the fluctuating velocity's RMS u' to the laminar burning velocity S_L indicates the increase of the surface area due to the folding effect. In Figure 2.7, a vortex with the integral length scale l_0, which comes in contact with the flame front, is illustrated. The lifetime (until it is burned) of this vortex corresponds to $t_w = \frac{l_0}{S_L}$, which is large enough to deform the flame front during the combustion process. This deformation is defined as the characteristic vortex velocity multiplied with the vortex lifetime:

$$\delta x = u' \frac{l_0}{S_L} \tag{2.73}$$

A significant folding occurs when the deflection of the flame front, calculated by Eq. (2.73), is greater than the flame thickness δ (see Eq. (2.57)), which yields:

$$u' \frac{l_0}{S_L} \gg \frac{a}{S_L} \rightarrow \frac{u' l_0}{a} \gg 1 \tag{2.74}$$

Assuming that $Pr = a/v = 1$, so that the thermal diffusivity a is equal with the kinematic viscosity v, Eq. (2.74) may be written as follows:

$$Re_t \gg 1 \tag{2.75}$$

where Re_t corresponds to the turbulent Reynolds number.

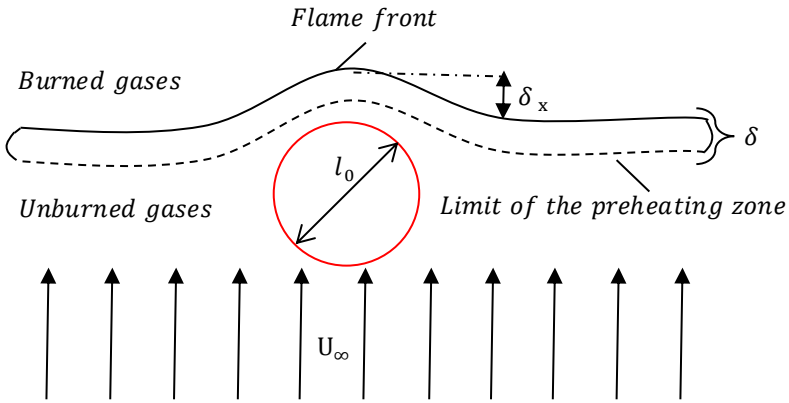

Figure 2.7: Effect of a turbulence structure on the folding of the flame front, modified [63]

The structure and the characteristics of a turbulent premixed flame depend highly on the interaction between the chemical reactions and the turbulent structures (different time and length scales). Damköhler (Da) and Karlovitz (Ka) are two dimensionless numbers determining this interaction. The turbulent Da number expresses the turbulent flow's characteristic time scale to the chemical reaction's characteristic time scale.

$$Da = \frac{\tau_t}{\tau_R} \tag{2.76}$$

The turbulent time scale is determined by the time scale of the large eddies, which as it was mention above has a corresponding integral length scale of l_0.

The turbulent Da number with respect to the characteristic chemical time scale is derived as follows:

$$\tau_R = \frac{\delta}{S_L} \rightarrow Da = \frac{l_0}{u'}\frac{S_L}{\delta} \tag{2.77}$$

In Da≫1, the reaction rate is substantially faster than the rate of turbulent mixing. Therefore, the flame structure depends on the latter. In contrast (Da≪1), the flame is affected mainly by reaction kinetics.

The Ka number expresses the ratio of the characteristic time scale of the chemical reaction τ_R to the characteristic time scale of the smallest turbulent structures τ_η, which correspond to the Kolmogorov length scale. The Ka number indicates the probability of Kolmogorov's length scales penetration disrupting the flame structure.

$$Ka = \frac{\tau_R}{\tau_\eta} \tag{2.78}$$

which, can be also expressed in terms of length scale ratios as follows:

$$Ka = \left(\frac{\delta}{\eta}\right)^2 \tag{2.79}$$

The turbulence effect on the flame's structure can be determined by comparing the flame thickness of the corresponding laminar premixed flame with the characteristic length scales of the turbulent flow (in both integral and Kolmogorov scales).

The phenomena mentioned above are illustrated in Figure 2.8. The axes of the so-called Borghi diagram [64] express the magnitude of the turbulent length scale and intensity concerning their corresponding laminar flame values. It is

conspicuous that it consists of four distinct boundary lines, which define five characteristic regimes of premixed flames. Each regime characterizes the different interaction between the chemical kinetic and the turbulent flow, which leads to variation in the flame's structure.

Laminar flame regime

The line $Re_t = 1$ delimits this regime, where the turbulence intensity is relatively weak. The latter leads to a flame, which has the characteristics of a laminar premixed flame, whose flame front is not deformed.

Wrinkled flamelets

In the case of a flame thickness, which is smaller than the Kolmogorov scale, i.e., $\delta < \eta$ or Ka<1, the effect of turbulence is described as *wrinkling* of a laminar premixed flame and the turbulent diffusion becomes an essential factor concerning the transfer phenomena.

Thin reaction zone

In this regime (Da> 1, Ka>1), the flame front is thicker than the smallest eddies $\delta > \eta$. Subsequently, the turbulent structures penetrate the flame front and alter the flame's internal structure [63].

Well-stirred reactor zone

In this case (Da<1, Ka>1), even the largest turbulent structures are smaller than the flame front thickness. Subsequently, several vortex classes can penetrate the flame. In the preheating zone (see Figure 2.3), the heat and the mass transfer rates enhance, which leads to a considerable increase in its thickness.

Practically, the flame front's well-defined concept is not apparent, and the flow field behaves as a well-stirred reactor[1]. In this regime, an empirical correlation of the turbulent flame speed can be derived. Analogous with the laminar burning velocity from Eq. (2.60), the following applies for the turbulent flame speed:

$$S_T \sim \sqrt{\frac{a_t}{\tau_R}} \sim \sqrt{\frac{u' l_0}{\tau_R}} \tag{2.80}$$

where a_t corresponds to the turbulent thermal diffusivity. The ratio of the turbulent to the laminar flame speed, considering $Pr = 1$, can be expressed as follows:

$$\frac{S_T}{S_L} \sim \sqrt{\frac{a_t}{a}} \sim \sqrt{\frac{u' l_0}{a}} = \sqrt{Re_t} \tag{2.81}$$

So far, correlations for the determination of the turbulent burning velocity in the flamelet regime (see Eq. (2.72)) and the well-stirred reactor (see Eq. (2.81)) have been examined. According to Schmid [65] a correlation in the transition regime can be also derived [66].

[1] The well-stirred reactor constitutes an ideal device, in which the instantaneous mixing of the reactants is feasible. Subsequently the thermochemical-behavior of the system is determined solely by the chemical kinetics.

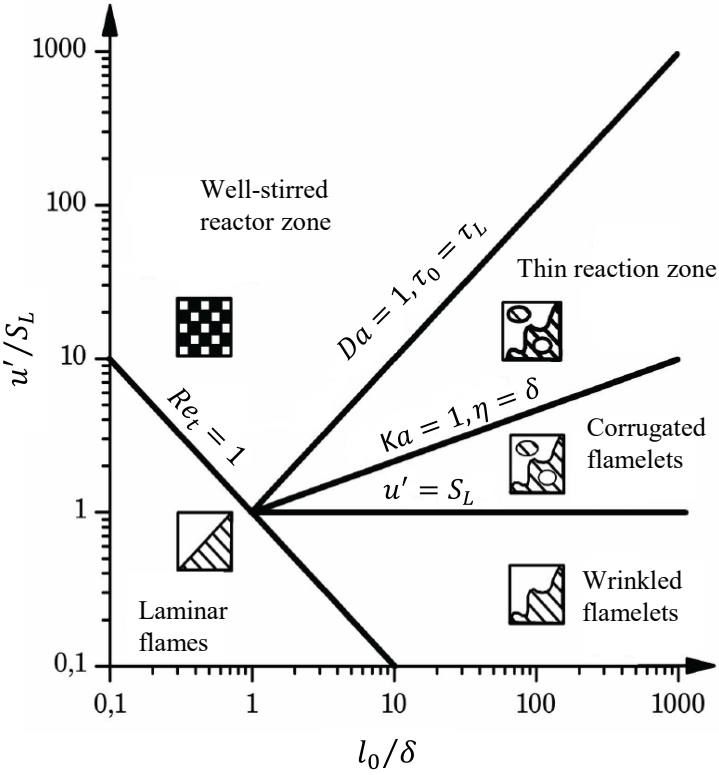

Figure 2.8: Borghi diagram for premixed turbulent combustion [67]

The gradient of the straight line, which separates the laminar form the turbulent regime can be determined by replacing the thermal diffusivity according to Eq. (2.57):

$$\frac{u' l_0}{a} = Re_t \rightarrow \frac{u' l_0}{\delta S_L} = Re_t \rightarrow \frac{u'}{S_L} = Re_t \left(\frac{l_0}{\delta}\right)^{-1} \tag{2.82}$$

The Ka number can be introduced by employing Eq. (2.33), which then yields:

$$\frac{u'}{S_L} = Ka^{2/3}\left(\frac{l_0}{\delta}\right)^{1/3} \tag{2.83}$$

With respect to Da number taken from Eq. (2.77) the following applies:

$$\frac{u'}{S_L} = \frac{1}{Da}\frac{l_0}{\delta} \tag{2.84}$$

2.3.4 Droplet combustion

The combustion of a liquid's fuel single isolated droplet exposed in an oxidizer environment is the prerequisite to understanding the spray combustion process, which appears in most technical devices. It constitutes a complex process containing several physicochemical phenomena [68]. In Figure 2.9, the schematic illustration of an isolated droplet in a steady-state condition, quiescent atmosphere, and without the effect of thermal buoyancy is depicted. The temperature gradient from the flame's surface to the droplet's surface enhances the heat transfer from the gas to the liquid phase. As a result, the liquid phase's evaporation process is initiated, and the produced fuel vapor diffuses radially outwards. In the regions of a stoichiometric mixture, the chemical reactions are activated, leading to a diffusion flame, which has a spherical shape surrounding the droplet [69,70].

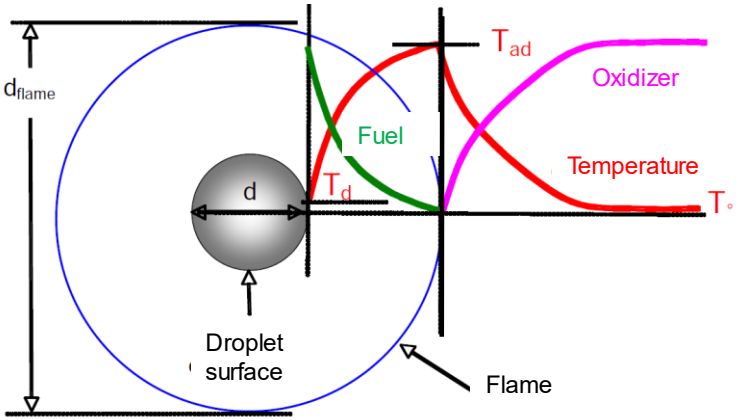

Figure 2.9: Combustion of a single isolated droplet, modified [71]

2.3.4.1 Evaporation process

The evaporation process can be characterized by the momentum, mass, and heat transfer phenomena. It highly depends on the gas phase's global operating conditions (pressure and temperature) and on liquid properties including fuel volatility, temperature, and liquid droplet diameter and the droplets' slip velocity with the gas phase. A comprehensive determination of evaporation is a very complicated and computationally expensive process, which requires the simultaneous solution of the momentum, heat, and mass balance equations in a turbulent, two-phase environment. This modeling should account for several parameters, such as the turbulent mixing, the primary and secondary atomization, and the impact of droplets on the walls. Therefore, various simplified approaches have been developed for characterizing the evaporation process, with the most prominent of them being the d^2 law [71].

The d^2 law is based on the heat, and mass balance equations, but with the following assumptions:

1. Spherical symmetry is considered, which leads to a one-dimensional analysis of the heat and mass transfer.
2. No spray effect. Each droplet is considered isolated, while there is no interaction between the droplets.
3. No effect of Soret, Dufour, and radiation phenomena.
4. One-component fuel, where even if the fuel is a mixture, is treated as a homogeneous medium with specific physical properties.
5. Uniform droplet temperature, the heat transfer phenomena due to conduction in the liquid phase, are negligible.
6. Saturation vapor pressure on the droplet surface.
7. Quasi-stationary conditions of the gas phase.
8. Constant transport properties of the gas phase.

In Figure 2.10, an example of the evaporation process of a spherical droplet is illustrated. The process comprises two phases. In the first phase (transient process), the droplet's temperature rises, leading to the gradual evaporation of the liquid phase and the saturation of the droplet's surface with vapor. As long as the vapor concentration in the environment is lower than that on the droplet's surface (concentration gradient), vapors diffuse radially, promoting the evaporation process. After a sufficient time has passed, the second phase (stationary process) is initiated, achieving equilibrium. The droplet's temperature remains constant in this phase, and the entire heat input evaporated the liquid phase.

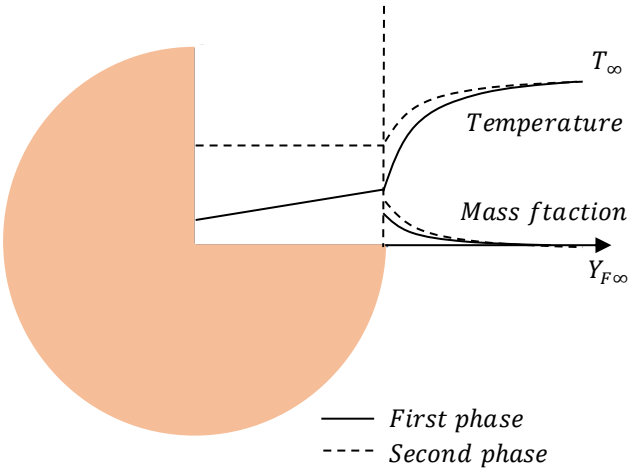

Figure 2.10: Example of droplet evaporation process, temperature and mass fractions, modified [72]

The mass balance in the differential spherical element depicted in Figure 2.11 yields [72,73]:

$$\overset{stat=0}{\overbrace{\frac{\partial \dot{m}}{\partial t}}} + \dot{m}(r+dr) - \dot{m}(r) = 0 \tag{2.85}$$

$$\dot{m}(r) + \frac{\partial \dot{m}}{\partial r}\partial r - \dot{m}(r) = 0 \rightarrow \frac{\partial \dot{m}}{\partial r} = 0 \overset{yields}{\longrightarrow} \dot{m}(r) = constant \tag{2.86}$$

On the droplet surface, the mass flow of the fuel can be written as follows:

$$\dot{m}_{rd} = 4\pi r_d^2 \rho U_{r_d} = \dot{m}_F = \dot{m} \tag{2.87}$$

The balance equation of the liquid phase assuming steady state conditions yields:

$$\dot{m}_F'' = \dot{m}'' Y_F - \rho D \frac{\partial Y_F}{\partial r} \tag{2.88}$$

In other words, Eq. (2.88) indicates the balance equation of the liquid fuel, where Netto flux = convection + diffusion and $\dot{m}_F''$ denotes the mass flux $\left[\frac{kg_F}{s}\frac{1}{m^2}\right]$ of fuel. The Eq. (2.88) can be written concerning the mass flow of the liquid phase by multiplying both sides with the known surface area of the sphere $4\pi r^2$, which yields:

$$\dot{m} = \dot{m} Y_F - \rho D 4\pi r^2 \frac{\partial Y_F}{\partial r} \tag{2.89}$$

By integrating Eq. (2.89) from the surface of the droplet r_d to the environment r_∞, where $Y_{F,\infty}$=0, the following equation can be derived:

$$\frac{\dot{m}}{4\pi\rho D}\frac{1}{r_d} = \ln\left(1 + \frac{Y_{F,d}}{1 - Y_{F,d}}\right) \tag{2.90}$$

where $\frac{Y_{F,d}}{1-Y_{F,d}} = B_M$, which denotes the so-called Spalding mass transport number, while $Y_{F,d}$ denotes the fuel mass fraction at the droplet's surface. Subsequently Eq. (2.90) can be written as follows:

$$\frac{\dot{m}}{4\pi\rho D}\frac{1}{r_d} = \ln(1 + B_M) \tag{2.91}$$

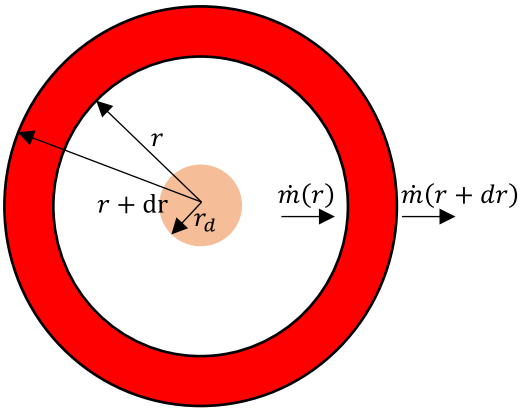

Figure 2.11: Mass balance in a differential spherical element

An increase of B_M enhances the rate of evaporation of the liquid phase. The evaporation process leads to a continuous decrease in the droplet's mass and, therefore, its diameter. The change in the droplet's diameter due to the evaporation process can be determined, by assuming $Le = 1$, as follows:

$$\dot{m} = -\rho_F \frac{d}{dt}\left(\frac{\pi d^3}{6}\right) \tag{2.92}$$

$$Le = 1 \xrightarrow{yields} \frac{\lambda}{\rho C_p}\frac{1}{D} \approx 1 \tag{2.93}$$

Therefore, by combining Eq. (2.92) & Eq. (2.93), Eq. (2.91) yields:

$$-\frac{\rho_F \frac{d}{dt}\left(\frac{\pi d^3}{6}\right)}{2\pi \frac{\lambda}{C_p}}\frac{1}{d} = \ln(1 + B_M) \tag{2.94}$$

$$\frac{d}{dt}(d^2) = \underbrace{-\frac{8\lambda}{C_p\rho_F}\ln(1+B_M)}_{K=Evaporation\ constant} \tag{2.95}$$

$$\int_{d_0^2}^{d^2(t)} d(d^2) = -K\,dt \tag{2.96}$$

$$d^2(t) - d_0^2 = -K\,dt \tag{2.97}$$

From Eq. (2.97), if the droplet diameter $d(t) = 0$, then the total time of evaporation can be determined as follows:

$$t_d = \frac{d_0^2}{K} \tag{2.98}$$

Therefore, the surface of the droplet changes linearly with time, and this phenomenon, illustrated in Figure 2.12, is known as the d^2 law [71].

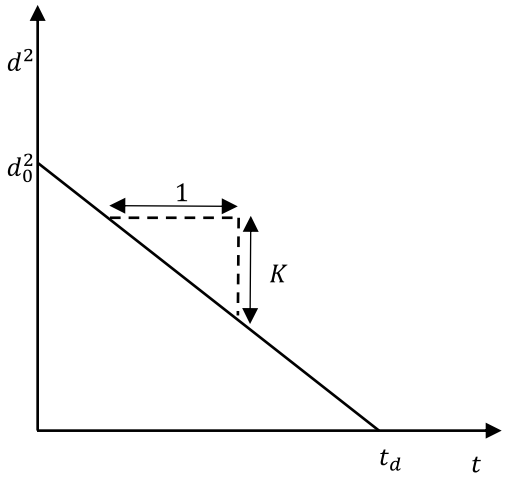

Figure 2.12: Time of droplet evaporation with respect to its initial diameter- d^2 law

2.3.5 Combustion of droplets cloud

In most technical applications, the fuel is introduced into the combustion chamber in the form of a spray. The latter has been excessively reviewed in the past by Sirignano [74], Annamalai [75], Jenny [76], and Faeth [77,78]. Spray combustion cannot be considered as the sum of individual droplet flames (Section 2.3.4) [79], instead of as non-isolated combustion of droplets, the so-called spray combustion [80–82]. In the case of a sufficiently large distance between the droplets of the cloud and a high rate of mass entrainment of the oxidizer, the combustion of the droplet cloud can be treated as an isolated droplet combustion process. On the contrary, the short distance of the droplets and the limited amount of mass entrainment also limit the concentration of the produced fuel vapor, leading to local cooling of the region surrounding each droplet, and the ignition of the mixture within the cloud is not feasible. In this case, multiple diffusion flames surrounding groups of droplets, the so-called internal group combustion, may appear, or a flame in the external boundaries of droplets cloud, the so-called external group combustion.

In Figure 2.13, the change in the flame's morphology concerning the varied characteristics of the droplet cloud is illustrated [83]. The total droplets' number increases from the left to the right, decreasing the distance between the droplets. In the case of a considerable distance between the droplets, individual diffusion flames surround the droplets (see Figure 2.13 (a)). In Figure 2.13 (b), it is evident that the increased number of droplets results in the onset of spherical diffusion flames surrounding the droplets that are located near the boundaries of the cloud, while the produced fuel vapor of the remaining droplets creates an internal flame whose location is depicted in red in Figure 2.13 (b). In Figure 2.13 (c), the number of droplets has been sufficiently increased so

that the evaporation process occurs in the complete volume of the cloud. The produced fuel vapors diffuse outwards, meet the oxidizer, and create a flame located outside of the boundaries of the droplets cloud.

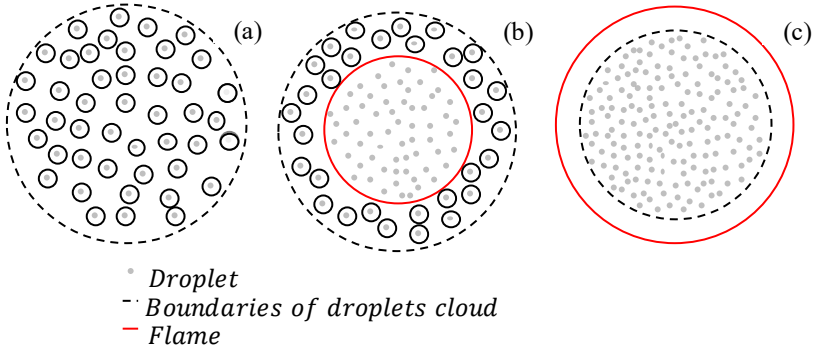

Figure 2.13: Group combustion of liquid spherical droplets, modified [83]

The group consideration of spray combustion has been investigated in the past. Chiu et all. [83] derived the so-called group combustion number G, which describes the mode of combustion and can be defined as follows:

$$G = 4\pi\lambda r_{l,0} n \frac{\left(1 + 0.276 Re_d^{\frac{1}{2}} Sc^{\frac{1}{3}}\right) R_b^2}{\rho D C_p} \tag{2.99}$$

where $r_{l,0}$ is the radius of the liquid droplet at a reference state, n the droplet number density, and R_b the radius of the preheating zone. For $G < 10^{-2}$, the isolated-droplet combustion mode occurs (see Figure 2.13 (a)), while with $10^{-2} < G < 10^{-1}$ the internal group combustion takes place (see Figure 2.13 (b)). Moreover, for $G > 1$, the external group combustion occurs (see Figure 2.13 (c)), and for $G > 10^2$, the evaporated fuel comes from the droplets, which

lie in a thin layer at the surface of the droplets cloud (external sheath group combustion).

2.3.6 Flame stabilization by an inner recirculation zone (IRZ)

The prerequisite for flame stabilization is the flow velocity equal and opposite to the flame speed. Therefore, increasing the latter is beneficial to realizing a wide stability range. For highly turbulent cases, Eq. (2.81) indicates that the turbulent flame speed can be increased by increasing the laminar flame speed or increasing the turbulent velocity fluctuation. The recirculation of exhaust gases (see Figure 2.14) heats the incoming fresh mixture, thus enhancing the laminar burning velocity of the mixture (function of temperature – see Eq. (2.60)). Moreover, the recirculation zone causes large shear stresses that generate turbulence. Flame stabilization through IRZ has been widely employed in jet engines and constitutes the method of flame stabilization of this research activity.

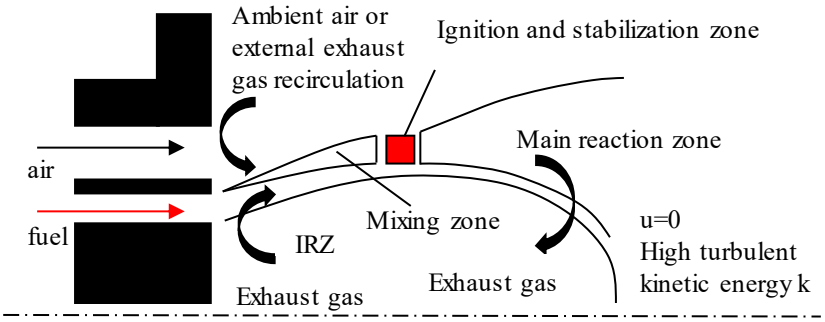

Figure 2.14: Flame stabilization through swirl [84]

In a swirling flow, a fluid element rotates around the symmetry axis with a tangential velocity w. The solution of the Navier-Stokes equation provides the radial distribution of the tangential component for an incompressible flow. For steady-state and frictionless conditions, the Navier-Stokes equation in the tangential direction can be reduced to the Euler differential equation [85,85].

$$\frac{\partial^2 w}{\partial r^2} + \frac{1}{r}\frac{\partial w}{\partial r} - \frac{w}{r^2} = 0 \tag{2.100}$$

As shown in Figure 2.15, the tangential velocity profile can be well reproduced by the Rankine vortex. The fluid is characterized by a free vortex for a large radius, where the tangential velocity is inversely proportional to the radius $\sim\frac{1}{r}$. Therefore, for a small radius ($r \to 0$), the tangential velocity would rise to an infinite value with the shear rate's subsequent increase. Thanks to nature, this undesirable condition at a small radius is avoided, and the fluid rotates as a rigid body, the so-called forced vortex, where the tangential velocity is proportional with the radius $w{\sim}r$. Thus, the tangential velocity decreases linearly towards smaller radii and reaches zero value on the combustions chamber's centerline (see Figure 2.15). The characterization as mentioned above of fluid's motion is known as Rankine vortex and may be written as follows [86]:

$$w(r) = w_1\left(\frac{r_1}{r}\right)^m \; with \; \begin{cases} m = -1 \;\; for \;\; 0 \le r \le r_1 \\ m = 1 \;\; for \;\; r \ge r_1 \end{cases} \tag{2.101}$$

The exponent m has been investigated in the past, and results showed that it depends on the swirl generator' design. According to these investigations, the exponent m varies from -0.2 to -0.6 [87,88].

Moreover, the balances of forces on a moving along a circular path fluid element with a tangential velocity w, by disregarding the gravitational effect in the radial direction yields:

$$\frac{w^2}{r} = \frac{1}{\rho}\frac{\partial p}{\partial r} \tag{2.102}$$

By combing Eq. (2.101) and Eq. (2.102) in the region of the free and forced vortex, the following applies respectively:

$$\underbrace{p(r) = p_1 + \frac{\rho}{2} w_1^2 r_1^2 \left(\frac{1}{r_1^2} - \frac{1}{r^2}\right)}_{Free\ vortex} \tag{2.103}$$

$$\underbrace{p(r) = p_1 + \frac{\rho}{2}\frac{w_1^2}{r_1^2}(r^2 - r_1^2)}_{Forced\ vortex} \tag{2.104}$$

In Figure 2.15, it is evident that the maximum of the tangential velocity when the swirl jet enters the combustion chamber is shifted to a bigger radius $r_1 < r_2$ and together with the conservation of the angular momentum $D_1 = D_2$ yield:

$$r_1 w_1 = r_2 w_2 \tag{2.105}$$

According to Eq. (2.105), $w_1 > w_2$ and this combined with Eq. (2.104) leads to the following correlation:

$$p_1 - \frac{1}{2}\rho w_1^2 < p_2 - \frac{1}{2}\rho w_2^2 \tag{2.106}$$

The latter indicates that the swirled jet undergoes vortex breakdown due to the positive pressure gradient, and the flow is reversed, creating a negative velocity region, which was aforementioned as IRZ.

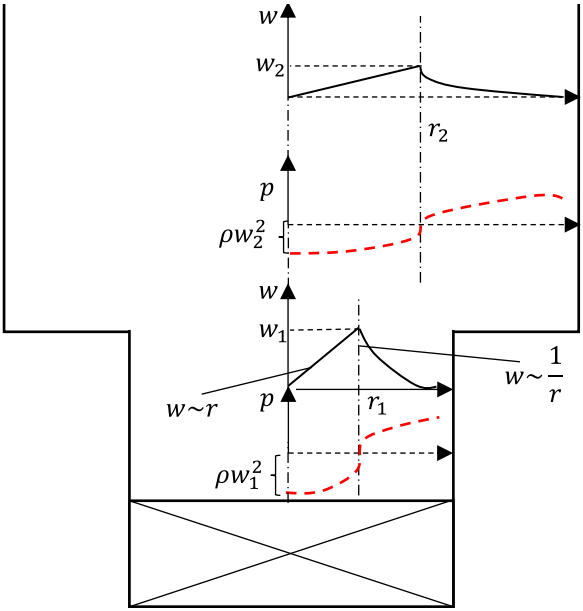

Figure 2.15: Tangential velocity and static pressure profiles in a Rankine vortex

The swirl number characterizes the strength of the swirl flow [89]. It represents the ratio of the angular momentum's flux to the corresponding axial one, multiplied with a characteristic length, in this case, the radius of the burner exit creating the following dimensionless number:

$$S = \frac{\dot{D}}{\dot{I} R_0} \tag{2.107}$$

with

$$\dot{D} = 2\pi \int_0^R \rho u w r^2 dr \tag{2.108}$$

$$\dot{I} = 2\pi \int_0^R (p + \rho u^2 r) dr \tag{2.109}$$

A low swirl number indicates that the axial momentum compared to the angular momentum is higher, which prevents the formation of the inner recirculation zone. As shown in Figure 2.16, at swirls numbers higher than 0.5, the positive pressure gradient on the axis is sufficient to generate the recirculation zone on and near the center axis of the combustion chamber.

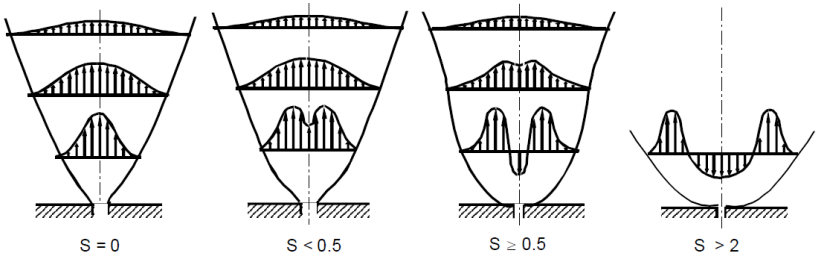

Figure 2.16: Swirled free jet development at increasing swirl number [90]

2.4 Ignition

The ignition process is the transition from the unreacted or slowly reacting mixture to a fast oxidation reaction and is achieved by adding heat into the flammable mixture (thermal ignition) or production of free radicals (chemical chain ignition), benefiting the branching chain reactions. Energy delivery into the system in terms of heat can be highly localized or distributed into the whole mass, raising the evolution rate of the exothermic reactions. Ignition is crucial process in numerous practical systems such as industrial furnaces, boilers, gas turbines, and spark-ignition engines. Moreover, the ignition process is highly dependent on the thermodynamic conditions (pressure and temperature), flow field (air velocity and turbulence intensity), mixing (Fuel to Air Ratio), spray

characteristics (SMD), and the energy imposed on the system (MIE). The focus of this research activity is the analysis of ignition processes at combustors for aero engines. A successful ignition event can be described, instead of a single-step mechanism, as a sequence of the following events according to Lefebvre [91]:

1. The flame kernel generation by a spark discharge needs to have sufficient size and enough heat to survive in the imposed conditions (properties of the flow field, global operating conditions).
2. Propagation of the flame kernel towards the fuel injector with the subsequent flame stabilization in a single burner.
3. The so-called light round [92] expresses the flame's spread to all the burners of an annular combustion chamber, typical of the ones employed in the aviation industry.
4. Heat release generation, capable of accelerating the spool of the engine up to the desired operational speed.

A failure of any step mentioned above could be detrimental to igniting one sector and the combustion chamber's subsequent light round. The failure modes of both steps have been investigated, for both liquid and gaseous mixtures, by laminar flame simulations [93,94], Direct Numerical Simulations (DNS) [95–99], and experiments in academic burners [6,100,101].

This research activity focuses on the first two steps of the ignition sequence. The survival of the flame kernel indicates that the heat release rate produced by the spark exceeds the rate of heat loss by turbulent diffusion, heat conduction with the walls of the chamber, and radiation. Therefore, the fuel-to-air ratio, the size (energy duration) of the spark, and the flow field characteristics

in the spark plug's region govern the success or failure of the first step by dictating the mixture's reactivity and the heat losses from the kernel, respectively.

The second step is governed by all the parameters beneficial for the flame's stabilization, such as the flow field, the fuel-to-air ratio, and the global operating conditions. Usually, low-velocity regions, higher pressure and temperature, and conditions close to stoichiometry promote flame stabilization and the ignition event's subsequent success. Moreover, the location of the spark plug plays an essential role since it determines whether the flame kernel will be sucked (upstream propagation) towards the primary zone or swept away (downstream propagation), which could be favorable or detrimental to the ignition process (see Section 5) respectively.

Usually, ignition is divided into two categories, explained thoroughly in Sections 2.4.2 and Section 2.4.3, auto-ignition (or self-ignition) and forced ignition, either for gaseous or liquid fuels, respectively.

2.4.1 Chain reactions

The chain reactions are used as a precursor for the detailed description of the ignition processes. The combustion process is usually initiated with the formation of free radicals, which mark the beginning of different reactions that lead to the formation of the combustion's products. The chain reactions constitute fundamental chemical reactions, which are determined by a considerable range of reaction rate constants and can be complementary or competitive. The formation or destruction of free radicals governs the total reaction rate because free radicals are highly reactive chemical compounds that promote the

reaction's evolution. The following elementary steps can describe the chain reactions.

1. *Chain-initiation*: The formation of free radicals from stable molecules
2. *Chain-propagation*: Reaction of a free radical with a stable molecule leads to the formation of another stable molecule and free radical that continues the reaction chain. The number of free radicals is maintained constant, but their chemical composition changes.
3. *Chain-branching*: Reaction of a free radical with a stable chemical compound leads to the formation of more free radicals than the ones entering the step. Therefore, chain-branching reactions promote the reaction rate increase compared to the corresponding one if the mechanism contained only chain-propagation reactions.
4. *Chain-termination*: Recombination of two or more free radicals leads to the formation of a stable chemical compound. Thus, the number of available free radicals reduces.

2.4.2 Auto-ignition

Auto-ignition is encountered in the compression ignition engines (diesel engines), where the oxidizer is already at a high temperature and pressure for a chemical reaction to proceed. Auto-ignition occurs without the assistance of any external source [4,62] and is usually away from stoichiometric conditions Information concerning this phenomenon is crucial for engineers designing any combustion system. On the one hand, it leads to undesirable events, such as knocking behavior in an Otto engine, industrial fires, or explosions, while on the other hand, controlled auto-ignition is critical for the proper operation of diesel engines. The prerequisite for auto-ignition is the temperature rise of

the mixture, which can be achieved by placing the mixture in a hot environment or by imposed adiabatic compression. Therefore, the continuously increasing temperature of the mixture increases the heat production rate, and auto-ignition takes place when the heat release is larger than the heat losses from the reaction volume. The auto-ignition characteristics are influenced by several parameters, such as the equivalence ratio of the mixture, pressure, mixing quality, and the chemical structure of the fuel. Auto-ignition temperature (AIT) is defined as the minimum temperature at which a fuel spontaneously ignites. To determine the auto-ignition temperature methods relying on the visual observation of the flame, pressure and temperature recordings and the mixture's chemical composition's sudden change have been proposed. It depends highly on the concentration of the reactants, the global operating conditions, and the fuel's nature. Several experimental investigations concerning the auto-ignition temperature of various gaseous fuels, such as hydrogen [102,103], methane [104–108], ethane [109], propane [110], n-butane [111], as well as liquid fuels [4] such as n-heptane [112], aircraft type fuels at elevated pressures [113], have been reported in the literature.

The AIT depends strongly on the chemical structure (molecular weight, branched or linear connection, average carbon chain length) of the fuel. As shown in Figure 2.17, hydrocarbons with low molecular weight exhibit a limited auto-ignition capability due to their chemical bonding structures. Hydrocarbon molecules of lower molar mass contain fewer carbon-carbon bonds, which are the weakest to break, initiating the chain reaction, compared to the carbon-hydrogen bond. For instance, the energy required to break the C-H bond of methane is around 439 kJ/mol^{-1}, and the C-C bond of larger hydrocarbons is from 305 to 320 kJ/mol^{-1} [114].

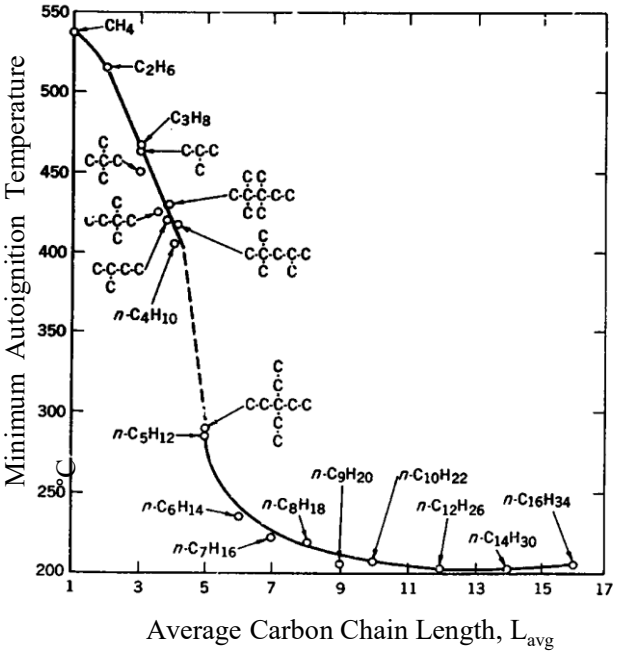

Figure 2.17: Auto-ignition temperatures of hydrocarbons/air mixtures with respect to the average carbon chain length [115]

2.4.2.1 Thermal ignition

The first qualitative analyses of the thermal ignition process were conducted by Semenov [116] and Frank-Kamenetskii [117]. The thermal ignition theory is based on the energy balance between the heat release from the single exothermic reaction and the heat losses from the combustion volume to the vessel walls, without considering the details of the chain reactions. If the heat release is greater than the heat loss, the mixture is ignited. Therefore, according to the thermal ignition's theory, the following applies:

$$\dot{q}_R = A c_F^n V e^{\left(-E_A/RT\right)} Q \tag{2.110}$$

where $\dot{q}_R$ is the heat released due to chemical reaction per unit time, A is the pre-exponential coefficient, c_F the concentration of the fuel, V the vessel's volume, n is the overall reaction order, and Q the heat generated by the reaction [62,118].

$$\dot{q}_{ls} = hA(T - T_0) \tag{2.111}$$

where $\dot{q}_{ls}$ denotes the heat loss to the vessel walls, h is the convective heat transfer coefficient, A the surface area of the walls of the vessel, T the temperature of the flammable gaseous mixture, and T_0 the temperature of the walls. In this case, the overall conservation of energy may be written as follows:

$$C_v \rho V \frac{dT}{dt} = \dot{q}_R - \dot{q}_{ls} \tag{2.112}$$

where C_V denotes the specific volume heat capacity, ρ is the mean density and V the volume of the vessel.

There is a critical point ($\dot{q}_R = \dot{q}_{ls}$) in which a small temperature perturbation could either lead to an ignition (positive temperature perturbation) or return in the initial condition (negative temperature perturbation). The analytical solution of Eq. (2.112) in the critical point has been rigorously described in the literature [62,118]. By assuming that the overall reaction order is $n = 2$ for common hydrocarbons and that the mean molar density can be written concerning pressure $c_F^n \sim (P/RT)^2$, the following applies:

$$\ln\left(\frac{P_C}{T_0^2}\right) = \frac{E_A}{2RT_0} + C \tag{2.113}$$

The Semenov equation indicates that an increase in the system pressure leads to an ignition event, which takes place at a lower temperature [119,120].

The AIT is also influenced by the fuel concentration, where experimental investigations have shown that there is an optimum fuel concentration attributed to the lowest AIT, and usually, this concentration is far from the stoichiometric one [121]. Different experimental investigations studied the dependency of the AIT on the equivalence ratio [122], where instead of an optimum value, it was revealed that with increased equivalence ratio, AIT decreases. Moreover, the vessel's size and global operating conditions play an essential role in the AIT of different fuels, indicating that increasing the test vessel's size decreases AIT [119,123].

The majority of the studies correlate the auto-ignition behavior in terms of the so-called ignition delay time. This parameter determines the time interval between the combustible mixture's formation and the onset of the flame.

$$t_i = Ae^{\left(E_A/_{RT}\right)}[Fuel]^m[Oxygen]^n \tag{2.114}$$

where A, m, n are experimental constants.

In gaseous fuels, the ignition delay time represents the time until the uniform gaseous mixture is ignited, which highly depends on the chain reactions and heat release that determine auto-ignition. This time interval is usually described as chemical ignition delay t_{ch} and for gaseous mixtures applies $t_i = t_{ch}$. In liquid fuels, the ignition delay time is influenced by additional parameters such as atomization, evaporation, and mixing times [4]. The parameters mentioned above constitute the so-called physical delay time t_{ph}, representing the mixture's preparation time before any chemical activity. Therefore, for

spray ignition applies $t_i = t_{ch} + t_{ph}$, while the physical or the chemical delay time may govern the auto-ignition process in different applications. Several parameters, such as temperature, fuel and oxygen concentration, droplet diameter, and equivalence ratio, influence the ignition delay time and have been excessively investigated in the past. The effect of pressure on the ignition delay time of gaseous fuels such as methane and propane [124] as well as for liquid fuels such as n-heptane and cetane [125] is of great practical interest due to the continuing trend towards engines, which operate with higher pressure ratios. According to the experimental investigations, an increase in pressure decreases the ignition delay time significantly. Concerning the effect of equivalence ratio, there is a lack of consistency among different authors, especially for liquid fuels. Some of them observed experimentally no effect [126,127], whereas others found a strong effect [113,124], indicating that ignition delay time decreases until an optimum value and then increases again by increasing equivalence ratio [128]. The latter has also been shown by numerical studies [129,130]. Measurements have shown that an increase in oxygen concentration decreases ignition delay time for both gaseous (propane) and liquid (JET A-1) fuels [113]. Furthermore, the auto-ignition characteristics of a multicomponent fuel are sensitive to the initial mass fraction of the volatile component [131], where adding a small portion of a volatile component is beneficial for the ignitability of non-volatile fuels.

2.4.2.2 Chemical chain ignition

The thermal ignition theory describes ignition as a single-step process, which is not precise, at least for the majority of the fuels' chemical reactions, where several intermediate reactions take place (Section 2.4.1). For a successful auto-

ignition in the case of chemical chain ignition, the production rate of the chain branching reactions k_{br} should be higher than their consumption rate k_{tr} through chain termination reactions [62,116,132,133]. Subsequently, if this condition is fulfilled, the total reaction rate is accelerated, and the ignition delay time can be written as follows:

$$t_i = \frac{const}{k_{br} - k_{tr}} \tag{2.115}$$

2.4.2.3 Cool flames

The cool flames constitute a unique phenomenon that occurs during the oxidation of the majority of hydrocarbons. The latter is related to the fact that the hydrocarbons' chemical reaction rate first increases and then decreases by increasing the system's temperature. Although it is counterintuitive, the cool flame becomes weaker with the temperature increase over a range, depending on the fuel's nature and the global operating conditions. A further temperature increase leads to the transition from the weak reaction to the subsequent hot ignition, where the cool flame acts as a precursor. The name cool flames refers to the fact that the heat released from these reactions is limited due to the low amount of radical and ionized species [134–137].

Hydrocarbons' oxidation reactions exhibit a complex kinetic behavior because they involve kinetic mechanisms that vary depending on the system's temperature. Three different mechanisms can be identified:

1. Low-temperature oxidation reactions
2. Intermediate temperature oxidation reactions
3. High-temperature oxidation reactions

The boundary regions that define each oxidation region depend on the system pressure. As mentioned afore (see Section 2.4.1), the free radical's production and destruction mechanisms determine the hydrocarbon's oxidation. As shown in Figure 2.18, except for very high temperature above 1200K, where the alkyl radical (R) decomposes, leading to the production of smaller hydrocarbon fragments with high reactivity forming final products, the reaction is initiated by the so-called H-abstraction from the alkene (RH) by oxygen molecules form an alkyl (R), and hydroperoxyl radical OOH. At low temperature (500-600K), the system evolution towards ignition is governed by the low-temperature branching sequence, where alkyl radicals react rapidly with oxygen molecules and form peroxyalkyl (RO_2). Subsequently, the peroxyalkyl forms peroxide species and small radicals out of several reactions, which react with alkane molecules by metatheses, and alkyl radicals are regenerated. The leading chain carriers in this chain propagation are the hydroxyl radicals (OH).

Alkyl radicals can isomerize to hydroperoxyl alkyl radicals (QOOH), and an addition of another O_2 to QOOH forms O_2QOOH, whose formation is crucial because an O-OH bond is involved, which breaks easily and leads to the formation of two radicals. The multiplication of the radicals is called a degenerated branching reaction and induces an exponential acceleration of the reaction rate leading to an acceleration of the overall fuel's consumption rate and heat release. The subsequent temperature rise reverses the reaction path ($\underbrace{RO_2 \overset{a}{\leftrightarrow} R + O_2 \overset{b}{\rightarrow} olefin + HO_2}_{a \rightarrow b\ with\ increased\ temperature}$) to the benefit of the slow, non-branching thermoneutral HO_2 propagation instead of fast exothermic OH chain branching, which reduces the overall reaction rate. Therefore, the steady increase in

decomposition rates of RO_2 and the subsequent HO_2 accumulation with a temperature increase is the main cause of the appearance of the so-called Negative Temperature Coefficient (NTC). The NTC is a distinctive feature of the majority of hydrocarbons, in which, albeit counterintuitive, the global reaction rate decreases with temperature within a specified temperature zone in the transition of low to intermediate temperature oxidation.

In Figure 2.19, the ignition delay calculation conducted with the Aachen mechanism (80 m% n-decane and 20 m% trimethyl benzene)[59] is illustrated. The analysis has been performed with Matlab Cantera 2.4.0 Toolbox and depicts the characteristic behavior of the hydrocarbons' NTC during the transition from low to intermediate temperature oxidation. Initially, the reactivity of the mixture exhibits an increasing trend, represented by an ignition delay reduction, until approximately 660 K (end of the low-temperature oxidation mechanism). An increase in temperature switches to a non-branching reaction pathway and subsequently causes the reduction of the fuel's consumption rate. Therefore, the overall reactivity of the mixture decreases, indicated by the increase in the ignition delay. At around 800 K, the high-temperature oxidation is activated, and as a result, the fuel's consumption rate increases leading to faster ignition delays.

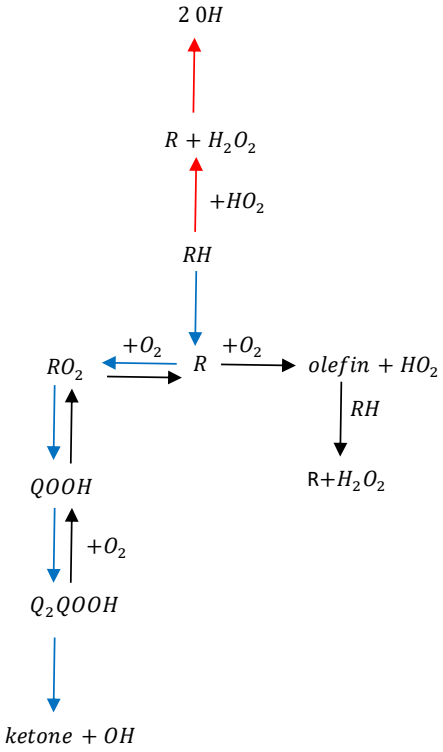

Figure 2.18: Schematic representation of the primary oxidation reaction of hydrocarbons for high (red), intermediate (black), low (blue) temperature.

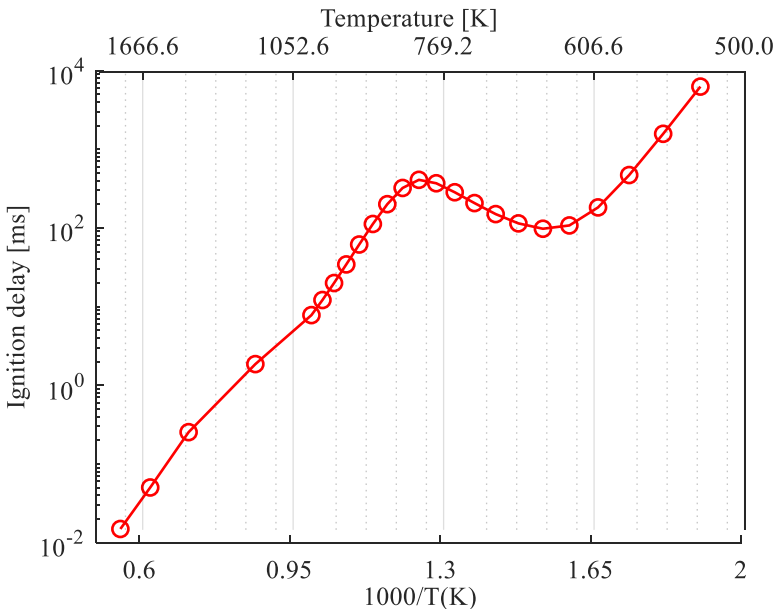

Figure 2.19: Typical S-curve of the hydrocarbons' ignition delay time in the transition from the low to intermediate temperature oxidation - 0.64 bar, FAR_{ref} (see Table 3.1) - Aachen mechanism 80 m% n-decane and 20 m% trimethyl benzene [59]

The cool flames and the NTC are connected with the so-called two-stage ignition observed in most hydrocarbons. The typical behavior of a two-stage ignition process is illustrated in Figure 2.20. The first ignition stage is initiated by a moderate increase of the system heat release and, therefore, the temperature. At this point, the ignition process is governed by the chain branching reactions, and for some time (induction period), the temperature maintains constant until the rate of heat release is equal to the rate of heat losses. Subsequently, the temperature rises steeply.

Further increase of the temperature provides the shift from branching to non-branching reaction pathway and subsequently the NTC behavior. Following

this event, the overall reactivity of the mixture is very low. After a certain time, a second rapid reaction occurs at a higher temperature, leading to the total fuel consumption (transition to hot ignition).

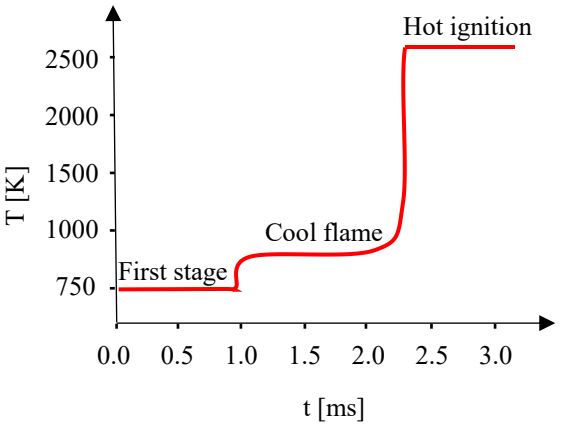

Figure 2.20: Typical temporal evolution of temperature during ignition of a hydrocarbon at a specific pressure and intermediate temperature [138]

2.4.3 Forced ignition

The second category is the so-called forced ignition existing in the aircraft engines and constitutes this research activity's focus. The initial state in forced ignition is in a chemically frozen state. Thus, it requires energy deposition, which rises temperature sufficiently high, fast, and in a range wide enough to initiate the combustion process and subsequently generate a self-sustaining flame. Usually, forced ignition is described with the so-called Minimum Ignition Energy (MIE), representing the minimum amount of energy required to ignite a flammable mixture of vapor, gas, or dust clouds. The theoretical anal-

ysis of the minimum ignition energy is based on the assumption that the transient heat source (electric spark, plasma jet, laser, heated surface) heats the ignition volume to such an extent that the energy released from this volume exceeds the heat losses extracted from it [73].

$$Heat\ released\ by\ combustion > Heat\ transport\ by\ conduction$$

This condition leads to the determination of a critical radius, which has to be attained for a self-sustained flame and the following applies:

$$\dot{q}_R v_{crit} \geq \dot{Q}_{ls} \tag{2.116}$$

where $\dot{q}_R$ denotes the heat release from the combustion. By considering the following assumptions:

1. Stationary process.
2. Uniform temperature of the ignition volume, equal to the adiabatic flame temperature.
3. Heat losses only occur due to heat conduction.
4. Single-phase, premixed stoichiometric conditions.
5. The heat source delivers energy used to heat the ignition volume to the adiabatic temperature and is considered without losses.

Eq. (2.116) may be written as follows:

$$-\dot{\omega}_F \Delta h_c \, 4/3\pi \, R_{crit}^3 \geq -\lambda 4\pi R_{crit}^2 \left.\frac{dT}{dr}\right|_{R_{crit}} \tag{2.117}$$

where $\dot{\omega}_F$ denotes the mass flux of fuel based on the volume and has a negative sign due to the fuel's consumption, Δh_c is the heat of combustion and R_{crit} is the critical radius.

By integrating the right part of the inequality (see Eq. (2.117)) with boundaries $T(R_{crit}) = T_{exh}$ and $T(\infty) = T_0$ (see Figure 2.21) yields:

$$-\dot{\omega}_F \Delta h_c \, 1/3 \, R_{crit} \geq -\lambda \frac{T_{exh} - T_0}{R_{crit}} \tag{2.118}$$

Thus, the critical radius, may be written as follows:

$$R_{crit}^2 \geq \frac{3\lambda(T_{exh} - T_0)}{-\dot{\omega}_F \Delta h_c} \tag{2.119}$$

By considering Eq. (2.60) and the heat of combustion of 1 kg fuel that raises the temperature of $(1 + x)$ kg of products, $\Delta h_c = (1 + x)\, C_p(T_{exh} - T_0)$ (Section 2.3.1), yields the following expression assuming $\frac{\Delta T}{\Delta T_v} = 2$:

$$R_{crit} = \sqrt{6} \frac{a}{S_L} \tag{2.120}$$

Eq. (2.120) can be expressed by the critical Fo-number as follows:

$$\frac{1}{6} = \frac{a^2}{S_L^2} \frac{1}{R_{crit}^2} = \frac{\frac{a}{S_L^2}}{\frac{R_{crit}^2}{a}} = \frac{\tau_{ign}(R_{crit,} T_{o,} p_{o)})}{\tau_{diff}} = Fo_{crit} \tag{2.121}$$

Therefore, Eq. (2.121) implies that a successful ignition event in the critical regime requires a $Fo_{ign} < Fo_{ctit}$.

The minimum ignition energy denotes the required heat to raise the temperature of a spherical volume of gas with radius R_{crit}, from T_0 to T_{exh}, and it is determined as follows:

$$MIE = m_{crit} C_p (T_{exh} - T_0) = \rho_{exh} \, 4/3\pi \, R_{crit}^3 C_p (T_{exh} - T_0) \tag{2.122}$$

By substituting Eq. (2.120) to Eq. (2.122) and the density of the exhaust gases ρ_{exh} with the ideal gas equation, the following correlation is derived:

$$MIE = 61.6\left(\frac{C_p}{R_{exh}}\right)\left(\frac{T_{exh}-T_0}{T_{exh}}\right)\left(\frac{a}{S_L}\right)^3 p \qquad (2.123)$$

Different correlations concerning MIE have been proposed in the literature [114,139], while most of them lead to higher predicted values than the experiments. It has been experimentally observed that forced ignition is not successful if the electrode's distance does not exceed a minimum value, the so-called quenching distance d_q. In the case of a distance smaller than the minimum, the heat losses from the mixture to the electrodes hamper the generation of a self-sustained flame. Therefore, higher ignition energy should be delivered into the system to compensate for these losses. The quenching distance constitutes a different physical quantity than the critical diameter $d_{crit} = 2R_{crit}$, albeit some of the authors consider that both parameters are equivalent [140] .

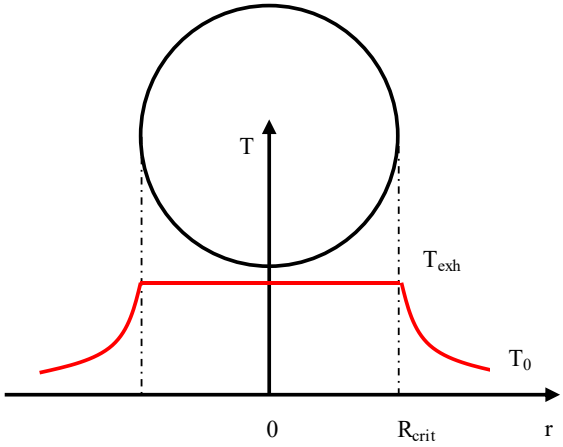

Figure 2.21: Critical radius for a self-sustaining flame propagation

The model by Brutscher [141] employs a detailed reaction mechanism and neglects physical and chemical effects with different time scales in a one-dimensional, unsteady combustion process of quiescent methane-air mixtures. The user initiates the numerical solution by defining several input variables, such as the energy density (a well-defined energy source applied in the energy equation), the geometry (shape, radius), and the external source's duration. The numerical simulation outcome is successful or unsuccessful ignition events detected by the temperature and oxygen concentration profiles. For instance, for a given geometry and duration of the external source, an ignition event is successful if the heat release of combustion exceeds the heat losses through diffusive transport.

As shown in Figure 2.22, the ignition process can be divided into three distinctive regimes. The critical regime (low energy input radius and short durations) is described by Eq. (2.121), while the induction-controlled regime ($\tau_{ign} = 10\tau_s$) is characterized by a constant Fo-number ($Fo_{ign} = 0.01$), independent of the user's input variables (geometry and duration of the external source). It is conspicuous that in the induction-controlled regime, the ignition time and the time of external energy input take place at different time scales, and thus the two processes can be decoupled. The supplied energy suddenly heats the defined ignition volume, and ignition occurs after the induction period (ignition delay time). Due to the constant Fo-number, a further increase of the energy input radius increases the induction period, thus the corresponding temperature that the gas should be warmed up, and therefore the required energy input.

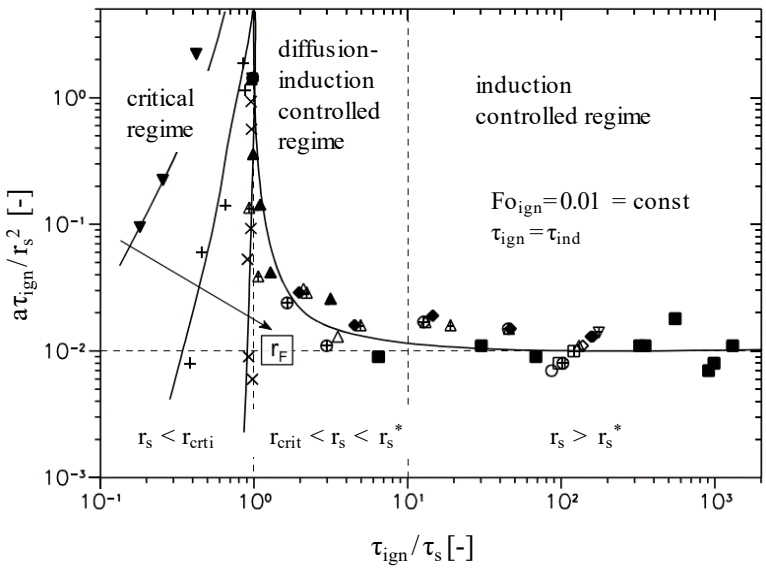

Figure 2.22: Classification of ignition process with non-dimensional parameters [141]

In the induction-controlled regime the following applies:

$$\tau_{ign} \approx \tau_{ind} = Ae^{\frac{B}{T_G}} \tag{2.124}$$

where A, B are numerical constants. Subsequently, the minimum gas temperature is determined as follows:

$$T_G = B\left[\ln\left(\frac{Fo_{ign}r_s^2}{aA}\right)\right]^{-1} \; with \; Fo_{ign} \approx 0.01 \tag{2.125}$$

where T_G denotes the minimum gas temperature, raised by the external source, which ensures a successful ignition event. Therefore, the minimum ignition energy in the induction-controlled regime is defined as follows:

$$E_{ign,sph} = \int_{T_0}^{T_G(r_s,\tau_s)} \frac{4}{3}\pi r_s^3 \rho_G(T) C_{p,G}(T) dT \tag{2.126}$$

With smaller radii or larger heating times, it is not valid to decouple the energy input processes by the external source and the ignition process, while strong cooling effects by conduction and diffusion govern the latter. In the diffusion-induction controlled regime, the minimum ignition energy criterion is that ignition occurs directly after the heat release ($\tau_{ign} = \tau_s$). A correlation that allows the estimation of the radius beyond which the diffusive transport process, during the heating period of the external energy input, cannot be neglected, yields:

$$r_s^* \approx \sqrt{10^{-3} a \tau_s} \tag{2.127}$$

In this regime, the ignition energy densities increase compared to the induction-controlled regime, and according to Eq. (2.127), this increase occurs in larger radii, the longer the energy input is.

2.4.3.1 Minimum ignition energy of gaseous mixtures

The MIE of premixed gaseous mixtures for both quiescent and flowing mixtures has been extensively studied both experimentally [140,142–148] and numerically [149–151] and review by Mastorakos [152]. Experimental results have shown a cubic relationship of MIE with the quenching distance [140] for methane and propane, whereas others reported $MIE \sim d_q^{2.5}$ for different fuels [153]. Measurements have shown that a higher initial temperature leads to a lower MIE for both flowing [144] and quiescent mixtures [154], whereas the dependency with pressure appears to be $MIE \sim P^{-n}$, where n varies from 1 to 2 [144,155] depending on high-velocity flow or quiescent mixtures. The MIE

is obtained with an optimum electrode gap, equal to the quenching distance [140,142,144,155], which, as mentioned afore, is large enough to compensate for the heat losses to the electrodes. Additionally, an optimum spark duration [156] is long enough to account for the early losses created by shockwaves and short enough to prevent high heat dissipation.

Moreover, increasing turbulent intensity causes an increase in the turbulent diffusion, which increases the heat losses from the flame kernel, and subsequently, a successful ignition event requires more energy [157,158]. Three different turbulent regimes affecting MIE differently, can be identified. The region of low turbulence in which the effect of turbulent intensity is mild and an increase in the integral length scale causes a reduction of MIE. The region of high turbulence in which turbulent intensity is quite apparent while increasing the integral length increases MIE. Finally, the transition between both regions has been detected at $u'/S_L = 2$ [140], where the integral length does not affect MIE, which depends solely on the u'.

The effect of equivalence ratio on MIE exhibits different behavior for quiescent and flowing mixtures. As shown in Figure 2.23, the optimum equivalence ratio is shifted towards rich mixtures for higher hydrocarbons in quiescent mixtures.

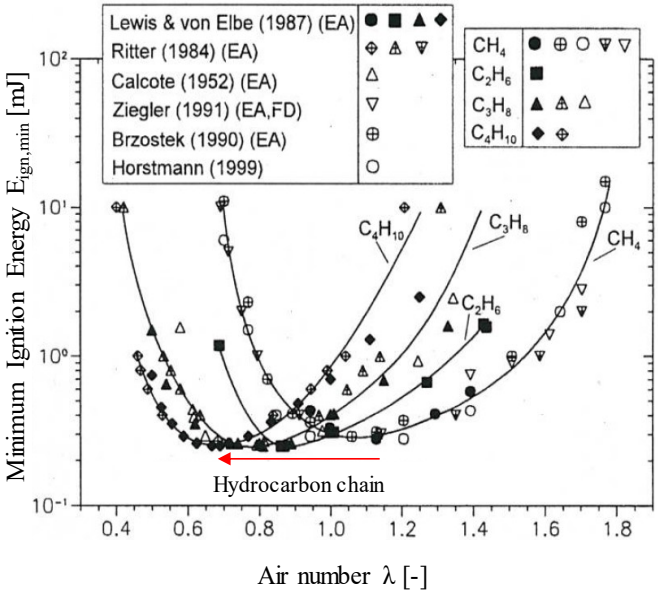

Figure 2.23: MIE with respect to air number for different hydrocarbons in quiescent mixtures [141]

This shift is attributed to preferential diffusion processes during the generation of the flame kernel [155]. At first, the flame kernel expansion occurs due to the heat transfer from the exhausted gases to the fresh gases. Subsequently, from the expansion's opposite direction, fuel and oxidizer reach the kernel with their corresponding molecular fluxes $\dot{c}_F$ and $\dot{c}_{O_2}$, respectively, and the preferential diffusion takes place as follows:

1. If the mixture is rich (see the blue point in Figure 2.24), and the hydrocarbon is heavier than the oxidizer (i.e., C_4H_{10} where $D_{C_4H_{10}} < D_{O_2}$), then oxidizer reaches the flame kernel faster than the fuel. The latter

leads to leaner conditions (green arrow) towards stoichiometric conditions, which increases the laminar burning velocity and therefore reduces the minimum ignition energy (see Eq. (2.123)). In contrast (red arrow), if the oxidizer is heavier than the hydrocarbon (i.e., CH_4 where $D_{CH_4} > D_{O_2}$), it leads to even richer conditions, which reduces the laminar burning velocity and increases the minimum ignition energy.

2. If the mixture is lean, on the one hand, for higher hydrocarbons, oxygen reaches faster the ignition kernel, which leads to even leaner conditions and subsequently higher minimum ignition energy. On the other hand, for small hydrocarbons, the shift in richer mixture reduces the minimum ignition energy.

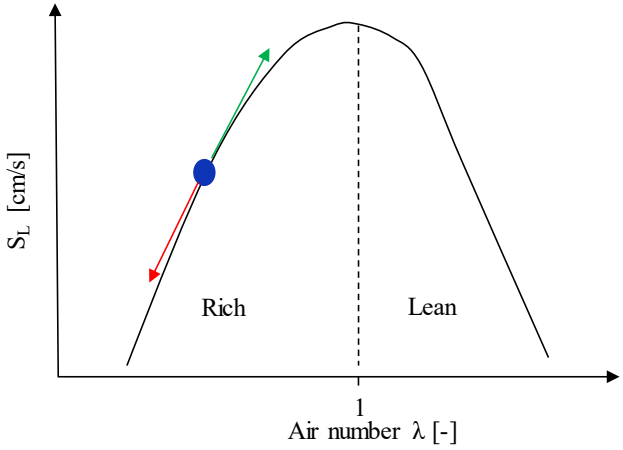

Figure 2.24: Laminar burning velocity with respect to air number

However, the effect of preferential molecular diffusion is not evident in flowing mixtures. According to Ballal and Lefebvre, the transport processes are

accelerated to such an extent that the preferential molecular diffusion is as not dominant as in quiescent mixtures [142].

The turbulence involves an additional complexity in the forced ignition of turbulent gaseous mixtures compared to the corresponding quiescent mixtures. With turbulence, the ignition process becomes highly probabilistic due to the inherent irregularities and instabilities imposed in the spark region. Therefore, under these conditions, the quantities representing ignition rarely constitute absolute values. Thus, usually, MIE corresponds to the energy such that 50% of the ignition trials are successful [4]. Several realistic configurations employ turbulent non-premixed configurations, imposing randomness on the ignition process, due to the arising mixture fraction fluctuation [159]. The stochastic behavior of the ignition process can be quantified with the following probabilities:

1. F – Flammability Factor: Represents the probability of finding a flammable mixture in the region of the spark and is defined as follows [159]: $F = \int_{\xi_{lean}}^{\xi_{rich}} P(n)d(n)$, where ξ_{lean}, ξ_{rich} represent the lean and rich flammability limits in terms of the mixture fraction ξ, $P(n)$ denotes the probability density function of the mixture fraction.
2. P_{ker}: Represents the probability of a successful flame kernel generation.
3. P_{ign}: Represents the probability of a successful ignition event (flame kernel generation and propagation).

Concerning the first phase of the ignition process (flame kernel generation), experiments [5,6] have shown that P_{ker} may be lower than F, while $P_{ign} < P_{ker}$ indicating that excessive strain rate may quench the flame kernel and that

the knowledge of the local mixture fraction, albeit it constitutes a very essential information, is not sufficient to characterize the ignition behavior.

The second and third phase of the ignition process contains the so-called flame kernel propagation and the subsequent burner stabilization, which has been studied for methane mixtures [5], indicating localized quenching of the flame kernel, even if existing within a flammable recirculation zone [6]. A significant experimental observation is that the ignition probability is higher when the spark is initiated in regions with flow velocity, promoting an upstream flame propagation. Measurements in jet flames revealed the optimum locations concerning the exit of the nozzle [100], while the speed that the flame propagates upstream has also been investigated and constitutes essential information for numerical model validation [160,161].

Simplified models have been reported in the literature, addressing the ignition process of quiescent gaseous mixtures [162–164] in terms of ignition energy. Several simplifications, such as negligible heat losses to the electrodes and single-step reaction mechanism, have led to an unsatisfactory agreement with the corresponding experiments [165,166]. However, numerical models provide insight into the underlying physicochemical processes during ignition by resolving all species' spatial and temporal profiles and temperatures.

2.4.3.2 Forced ignition of spray flames

Several factors distinguish spray ignition from gaseous flame ignition. The most prominent parameters are the droplet size distribution, the spatial distribution of droplets in the spark region, fuel volatility, and the degree of pre-

evaporation. Similar to gaseous mixtures, turbulence, and non-premixing impose a stochastic behavior in spray ignition during the first ignition stage (kernel generation). However, igniting heterogeneous mixtures entails higher minimum ignition energy than the homogeneous ones. The difference pertains to the additional energy required for droplet evaporation [167–169].

Additionally, the lean flammability limits during spray ignition can be extended [170]. The latter occurs due to the droplets' non-uniform dispersion, which leads to local inhomogeneity of the overall equivalence ratio. Thus, a phenomenological overall rich mixture may result in an unsuccessful ignition event, attributed to incomplete evaporation, which creates a less favorable equivalence ratio than the overall one and vice versa. The minimum ignition energy of quiescent and flowing heterogeneous mixtures has been reviewed by Aggarwal [4]. Experimental and numerical investigations of spay ignition induced by an external source have been reported in the literature for both quiescent [171] and flowing sprays [8]. The quiescent spray configurations have been extensively studied and used to validate numerical models because several complications arising from the convective effects and the imposed turbulence are neglected. A comparison between quiescent and flowing mixtures, as expected, revealed that the laminar forced convection increases the ignition kernel's heat loss rate, and thus, the required spark energy increases.

Experiments for an overall equivalence ratio (liquid + fuel vapor) $\Phi_0 \leq 1$ have shown that an increase in SMD increases MIE under atmospheric [4,99,172,173] and sub-atmospheric conditions [15]. Under these conditions, MIE increases monotonically as the fuel volatility reduces, the degree of fuel's pre-evaporation reduces, and as the sub-stoichiometric Φ_0 decreases [8,15,174]. Additionally, MIE decreases as pressure [15,171] and temperature

[15] increase. Measurements have revealed an optimum equivalence ratio [175], while for a certain equivalence ratio, optimum droplet size can be found [170], and this behavior has also been captured numerically [176]. Moreover, the optimum spark duration increases with larger droplets and higher flow velocities. Similar to the ignition of gaseous mixtures, turbulence intensity increases MIE. An important observation is that for different fuels, the optimum SMD ranges between 10-30 μm [4]. Moreover, Ballal and Lefebvre derived a model that accounts for flowing heterogeneous mixtures, turbulence, and the effect of convection [8].

The second phase of ignition (flame propagation) in sprays involves additional complications compared to the ignition of gaseous mixtures and has been studied fundamentally in laminar systems [177] and experimentally for uniform monodispersed quiescent mixtures [178,179]. The flame propagation speed in uniform sprays strongly depends on the overall equivalence ratio, the size of the droplets, and the degree of pre-evaporation, compared to the premixed laminar flame, which is only a function of the FAR. Flame propagation in uniform sprays is a highly complex phenomenon that depends highly on the amount of fuel vapor in the inter-droplet space, which depending on the imposed inhomogeneity, might promote flame propagation. Neophytou et al. [180] related this phenomenon to the spray's group number (see Eq. (2.99)), where the flame front travels from droplet to droplet, igniting diffusion flames surrounding each droplet [181].

In general, the droplets' presence reduces the flame's propagation speed compared to a pre-vaporized case, attributed to the time required for the evaporation process. On the one hand, larger droplets reduce the propagation speed, especially in overall lean equivalence ratios, at which incomplete evaporation

acts detrimentally in flame propagation due to the shift of the fuel vapor to air ratio towards lower values. On the other hand, rich overall equivalence ratios and large droplets, though under these conditions, may approach stoichiometric conditions, promoting the flame speed increase. However, experimental and numerical investigations regarding turbulent flame propagation in sprays are scarce, and this area needs further research.

Similar to the ignition in gaseous mixtures, the flame kernel generation is necessary but not sufficient for a successful ignition event in spray ignition. The flame kernel propagation and the subsequent burner stabilization have been studied experimentally, and results have been reported in the literature for single and multiple spark events using n-heptane [7]. Results have shown that with a single spark, P_{ign} increases if the spark is deposited in regions with an overall equivalence ratio within the flammability limits, small SMD, and velocity field that facilitates the convection of the flame kernel towards the recirculation zone. With multiple sparks, the optimum position of spark deposition appears to be the axial location concerning the nozzle's exit, which maximizes the probability of the spark's penetration in the recirculation zone.

2.4.4 Ignition modeling

The ignition process of aircraft [182–184] and laboratory scale [185,186] combustion chambers have been investigated with fully reactive LES. It is a promising approach, quite effective on a detailed representation of a single spark event. The latter is, however, insufficient for the numerical investigation of a jet engine's combustion chamber. Several sparks are required to complete the ignition process (each spark event takes place in a different instantaneous flow field and fuel distribution), which involves the heating up of the spark plug,

the fuel evaporation, and the subsequent flame propagation. Therefore, the numerical simulation assigns a physical time up to several seconds, unfeasible with the current resources, and fully reactive LES fails to provide a statistical description of this stochastic phenomenon.

Non-expensive, low-order models [16,17] that predict the flame propagation following the spark ignition are valuable despite their expected inaccuracy due to the introduction of relevant assumptions that may lead to a physical inconsistency. These models are based on performing a single cold-flow CFD simulation (either RANS or LES). These simulations provide a quick assessment of whether each spark delivered at a specific location would be potentially a successful ignition event or not. The Karlovitz number of each grid (i.e., flame particle) Ka_{fp} determines whether the flame will propagate and spread in the dedicated mesh's neighboring grids and is calculated as follows:

$$Ka_{fp} = 0.157\left(v\frac{{u_p'}^3}{L_{turb}}\right)^{0.5}\frac{1}{S_{L,p}^2} \tag{2.128}$$

2.5 Spray atomization

The atomization process decomposes a bulk fluid into small particles, dispersing them into the gaseous phase (oxidizer). It constitutes the first step of the liquid's fuel combustion process. The combustion evolution rate depends highly on the mass and heat transfer phenomena, such as the molecular diffusivity and evaporation rate, respectively. The physical phenomena governing the latter mentioned processes rely on atomization quality. The atomization process aims to increase the liquid's surface area, enhancing the mass and heat transfer rate and the mixing rate of the fuel with the oxidizer [187].

Moreover, the evaporation rate of the atomized fuel is inextricably linked with the droplet's surface because the ratio of surface area to volume varies inversely proportional to the droplet's diameter. Therefore, a reduced droplet diameter would increase the mass of evaporation per volume unit. For that reason, in the conventional systems of liquid fuel combustion, the production of small droplets is essential because it enhances the evaporation rate and the combustion rate.

2.5.1 Classification of atomizers

The atomizers are classified according to the type of energy they employ for atomization [187,188], either by exploiting of the liquid's kinetic energy or mechanical energy applied by vibrating or rotating devices, or the exchange of momentum of a high-velocity gas with the liquid phase. The first category includes the so-called pressure atomizers. They are related to the capillary breakup of a jet or liquid sheet injected from the nozzle under high pressure and velocity. The liquid mass flow that passes through the pressure atomizer is proportional to the pressure difference's square root. Therefore, the quality of atomization depends on the system and liquid pressure.

The second category is related to the centrifugal forces acting on the liquid. An electrical motor drives a disk or a cup [189]. The atomizer's centrifugal energy is transmitted to the liquid, which leads to the liquid discharge at a very high-speed relative to the gas phase and disintegration. The centrifugal energy of the atomizer is transmitted to the liquid, which leads to its discharge at very high-speeds and disintegration. The quality of atomization depends on the rotational speed of the disk.

The third category involves the twin fluid atomizers, which use the shear stress caused by the exchange of momentum in the gas-liquid interface. The twin fluid category is subdivided into Air-Assist atomizer and airblast atomizers. The difference between both configurations lies in the fact that the former category uses relatively small quantities at very high velocities (sonic velocities). On the contrary, the latter employs considerable quantities of air at lower velocities [188]. The most prominent advantages of the airblast atomizers are the relatively fine spray produced without requiring high fuel pressure and the low soot combustion due to the uniform FAR production within the combustion chamber.

In this research activity, a hybrid pre-filming airblast atomizer representative of the ones used in commercial aviation is employed. In Figure 2.25 and Figure 2.26, the working principle is illustrated. A pressure atomizer injects fuel, and a significant proportion impacts into the walls of the pre-filmer, creating a thin, continuous liquid film and simultaneously generated prior atomization of the fuel. Providing a minimum atomization quality appears to be of great importance to countereffect the pure performance of an airblast atomizer associated with low cranking speeds [190]. Therefore, this is beneficial to fast relight in a flameout event, which is critical for flight safety. The interaction of the liquid's free surface with the airflow stream forces the liquid to the lip of the pre-filmer, where the air stream that has penetrated through the swirling channels disintegrates the liquid film to ligaments and fine droplets.

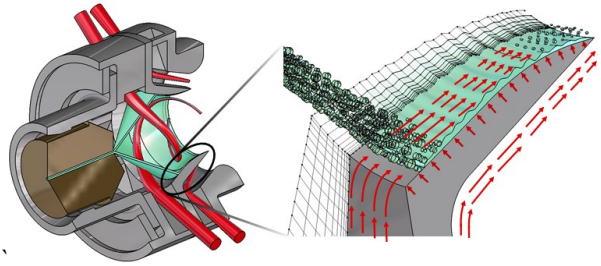

Figure 2.25: Overview of a pre-filming airblast atomizer - CAD TU Darmstadt

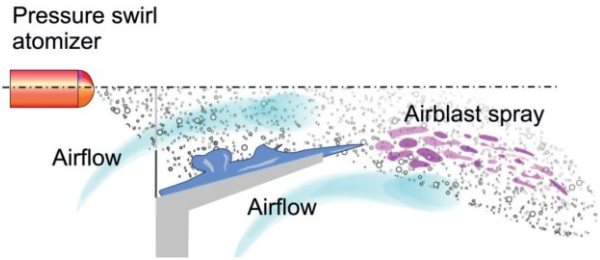

Figure 2.26: Pre-filming airblast atomizer detailed working principle [190]

2.5.2 Mechanisms of liquid atomization

The atomization process is usually divided into two distinct stages. The primary atomization, where the fuel stream splits into shreds and ligaments, and the secondary atomization, in which the already created droplets from the primary atomization are further disintegrated into smaller droplets. The spray's final formation is determined by the atomizer's internal geometry and the air's and fuel's properties [187].

2.5.2.1 Single Droplet mechanism

The most important physical properties governing the single droplet mechanism are the kinematic viscosity and the surface tension of the fuel [191], which constitutes the magnitude of the liquid's resistance to any imposed change in its surface by holding the liquid molecules together. The relative velocity between the gas phase and the droplet generates aerodynamic forces, which tend to deform the droplet. The breakup of the droplet occurs when the aerodynamic forces exceed the stabilizing.

Generally, surface tension is related to the contractive tendency that allows the deformation by an external force. The fluid molecules within the droplet are attracted to each other in all directions due to cohesion, and no net force is acting on them. At the liquid to the gas interface, molecules are subject to forces inward to the droplet and along the edges but not towards the other side. Therefore, the surface tension generates pressure, stabilizing the droplet and maintaining its surface in conjunction. This pressure is derived by balancing the normal stresses over the surface and the subsequent integration concerning the curvature surface, as shown in Figure 2.27. The resulting pressure difference in the interface of the gas and liquid phases is described by the Young-Laplace equation as follows:

$$\Delta p = p_2 - p_1 = \sigma \nabla \cdot n = \sigma \left(\frac{1}{r_{min}} + \frac{1}{r_{max}} \right) \tag{2.129}$$

where Δp denotes the pressure difference of the interior and exterior side of the droplet, σ the surface tension, $\nabla \cdot n$ the divergence of the normal vector of surface inter-phase, denoting the droplet's curvature r.

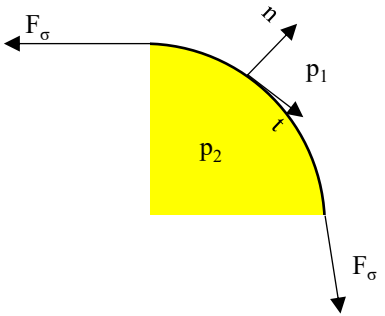

Figure 2.27: Force balance on the interphase of droplet with the gas phase

In the case of droplet deformation, the pressure distribution across the surface alters, leading to either an equilibrium between the external aerodynamic forces with the internal stabilizing forces (i.e., surface tension and viscosity) or a potential droplet breakup. For a spherical droplet with diameter d suspended in the air, Eq. (2.129) can be reformulated as follows:

$$p_\sigma = \frac{4\sigma}{d} \tag{2.130}$$

The droplet will not break up as long as the air pressure p_a does not exceed the stabilizing pressure p_σ at any point of the droplet's surface. If the stabilizing pressure does not compensate for an appreciable increase of the air pressure, the droplet disintegrates into smaller. Therefore, the droplet's disintegration is initiated when the shear stress caused by the aerodynamic resistance equal the surface tension forces, as shown in the following correlation:

$$C_D \frac{\pi d^2}{4} \frac{1}{2} \rho_a U_{rel}^2 = \pi d \sigma \tag{2.131}$$

where C_D denotes the drag coefficient, U_{rel} is the relative velocity of between the droplet and the air.

Three dimensionless numbers can describe the phenomena governing atomization. The Reynolds number (Re_d) of the droplet, the Weber number (We), and the Ohnesorge number (Oh). To determine the critical droplet size at which the aerodynamic forces exceed the stabilizing forces (see Eq. (2.131)) and the droplet breakup takes place, the critical Weber number is used:

$$We_{crit} = \frac{\rho_\alpha U_{rel}^2 d}{\sigma} = \frac{8}{C_D} \tag{2.132}$$

Additionally, several studies have employed this correlation to determine the limiting relative velocity at which the droplet breaks up. Two different droplet breakup modes have been detected in the literature [192,193] depending on whether the droplet is subjected to steady acceleration or sudden exposure to the gas phase's high-velocity. Therefore, two critical Weber numbers have been reported. For low viscosity liquid droplets subjected to free fall $We_{crit} = 22$ [188], while for low viscosity droplets suddenly exposed to high-velocity air stream $We_{crit} = 12$ [192,193].

The effect of viscosity is apparent on the droplet breakup mechanism, promoting droplet stabilization. It can be described by the Oh number, which represents the ratio of the internal viscosity forces to the interfacial surface tension forces, as follows:

$$Oh = \frac{We^{1/2}}{Re_d} = \left[\frac{\rho_\alpha U_{rel}^2 d}{\sigma_d}\right]^{1/2} \left[\frac{v_d}{U_{rel} d}\right] \tag{2.133}$$

where the subscript d denotes a droplet's property. Additionally, in the calculation of the Re_d number, the kinematic viscosity of the liquid is used.

The critical Weber number is expressed concerning the kinematic viscosity as follows [188]:

$$We^*_{crit} = We_{crit}\,[1 + f(Oh)] \tag{2.134}$$

Different correlations have been proposed in the literature, such as for $Oh < 10$, suggesting that an increase of the kinematic viscosity delays the droplet breakup by increasing the actual Weber number [194]

$$We^*_{crit} = We_{crit} + 1.077Oh^{1.6} \tag{2.135}$$

High-speed recordings have revealed three different modes of droplet deformation depending on the flow pattern surrounding them [192]:

- *Lenticular deformation* (see Figure 2.28 (a)): The droplet is flattened, and the formation of an ellipsoid shape is obtained. Further deformation leads to a torus shape that gets stretched and disintegrated into smaller droplets.
- *Cigar-shaped deformation* (see Figure 2.28 (b)): The droplet is elongated, and a cylindrical shape or ligament is obtained, which subsequently breaks up into smaller droplets.
- *Bulgby deformation* (see Figure 2.28 (c)): Local deformation of the droplet's surface forms bulges and protuberances that eventually are detached by the initial droplet.

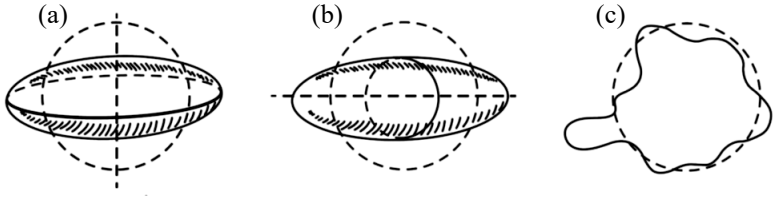

Figure 2.28: Different modes of the droplet's deformation [188]

The effect of the Weber and Ohnesorge number on the breakup mechanism is concluded in Figure 2.29 and Figure 2.30. For low Weber and Ohnesorge, different levels of deformation are present. However, by increasing the Weber number, the deformation of a droplet is enhanced until the shift in a different breakup mode, while for higher Ohnesorge number, the deformation region takes place at a higher Weber number.

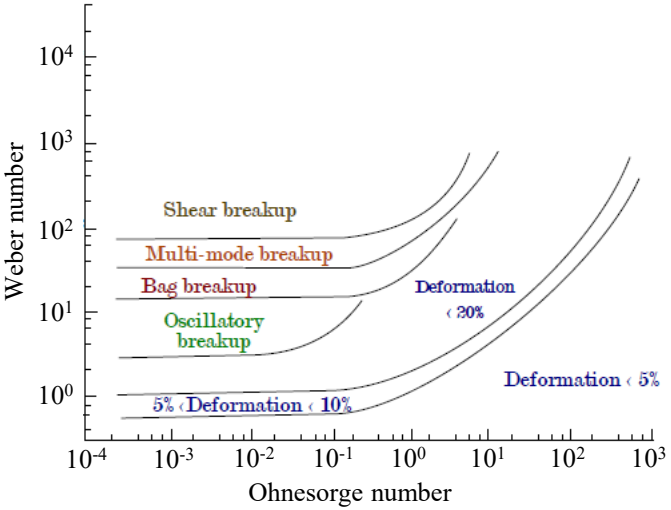

Figure 2.29: Droplet breakup regime map [195]

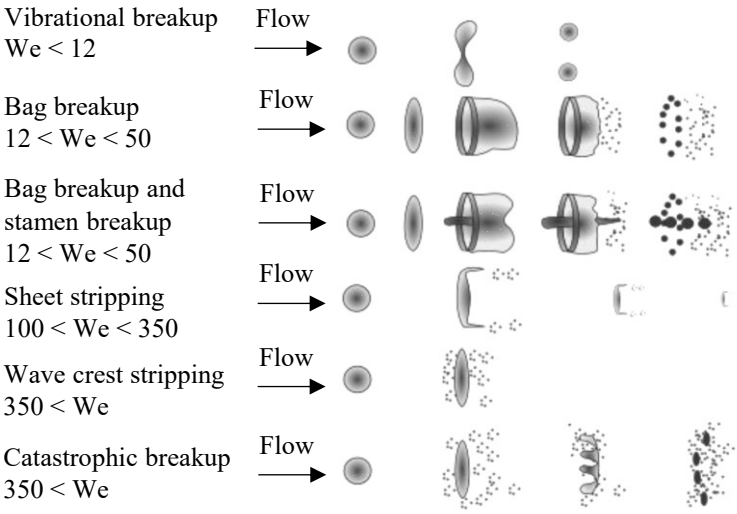

Figure 2.30: Modes of droplet breakup [196]

2.5.2.2 Atomization of liquid films and flat sheets

Compared to the single droplet mechanism, atomization of liquid jets and films expose much more complicated behavior, while several phenomena are involved. However, similar to the breakup of a single droplet, the development and the propagation of waves on the liquid's surface induce loss of stability, and subsequently, the so-called liquid breakup [187]. Several experimental studies induced small perturbances classified as internal and external on the liquid surface. The perturbances are generated by the liquid swirling in the former category, the liquid expansion due to the imposed pressure drop, or the atomizer's potential vibrations. The latter is described by the interaction of the liquid with the surroundings (i.e., aerodynamic forces). Mathematical solutions that reveal the effect of the imposed vibration on the breakup mechanism and

their experimental validation in orifices with low discharge velocities have been reported in the literature [187,197].

Three different mechanisms of liquid jet disintegration have been identified [187]. The first one is related to axisymmetric waves generated by jet velocities of 1 m/s, while the second one is caused by asymmetric waves (usually denoted as “first wind-induced atomization”) apply for jet velocities of the order of 10 m/s. Moreover, for velocities up to 100 m/s, the aerodynamic forces caused the liquid jet disintegration, generated by the high relative velocity between the jet and the surroundings. A fourth mechanism has been identified and reported in the literature [198], denoting that the effect of turbulence and the aerodynamic forces are predominant for the atomization process (“turbulent breakup”). Figure 2.31 and Figure 2.32 show the jet breakup map and the different jet disintegration mechanisms, respectively.

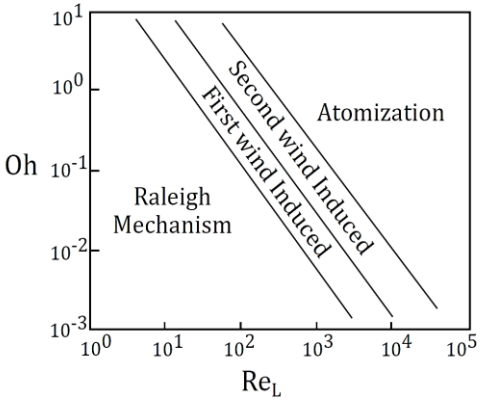

Figure 2.31: Jet breakup regime [199]

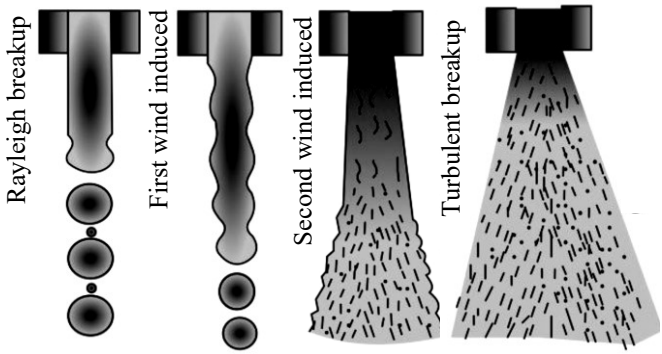

Figure 2.32: Different jet breakup modes [198]

Rayleigh studied the disintegration of liquid jets at low velocities in a vacuum [197,197], which is known as the Rayleigh mechanism. It is characterized by the formation of large droplets of reasonably uniform size, and the obtained droplet diameter is predicted according to the following correlation:

$$D \geq 1.436d \tag{2.136}$$

where D is the droplet diameter, and d denoted the orifice diameter. Furthermore, according to the Rayleigh's study, the hydrodynamic instabilities are initiated by wavelengths higher than the perimeter of the jet, while the wavelength at which the jet becomes unstable is defined as follows:

$$\lambda = 4.51d \tag{2.137}$$

Weber [200] showed that surface tension damp wavelengths with magnitude less than a minimum value, whereas greater magnitudes enhance their effects on the droplet breakup. As shown in these experiments, the damping effects

due to the increased velocity tend to increase the optimum wavelength described by Eq. (2.137), while the following correlation for the mean droplet size produced by a liquid jet was derived:

$$\frac{D}{d} = 1.436(1 + 3 \cdot Oh)^{1/6} \tag{2.138}$$

In the first wind-induced breakup regime, the surface tension effect is enhanced due to the higher relative velocity between the gas and the liquid phase, hence accelerating the breakup process. The jet breakup occurs many jet diameters downstream of the nozzle's exit, while the obtained droplet diameter D is in the magnitude of the orifice diameter d [188].

For higher relative velocities, the second wind-induced breakup is attained. The droplet production is caused by the unstable growth of short-wavelength waves acting on the surface of the jet. The obtained droplet diameter is smaller than the orifice diameter d. Moreover, the turbulent breakup process (atomization) completely disrupts the jet, specifically at the nozzle's exit, producing relatively small droplet diameters.

The discharge velocity of the liquid affects the disintegration of a liquid sheet primarily. The lack of stability due to the acting waves on the interface between the continuous and discontinuous phases leads to a liquid sheet's breakup into droplets. According to the liquid's discharge velocity, three different modes of sheet disruption are identified and are illustrated in Figure 2.33 [187]:

1. Attributed to a discharge velocity in the order of magnitude of a few meters per second by increasing the distance downstream of the atomization edge, the liquid film becomes thinner. Subsequently, in the

region with the sufficiently thin area, perforations are developed, and ligaments, prone to loss of stability, disintegrate further into droplets.

2. For higher discharge velocities, annular as well as circumferential waves with direction longitudinal to the velocity of the sheet create disturbances that disintegrate the sheet into annuli and the subsequent droplet formation.
3. For discharge velocities, up to 100 m/s, the flat sheet disintegrates directly into droplets caused by short-wavelength disturbances with high amplitude, enhancing the loss of stability.

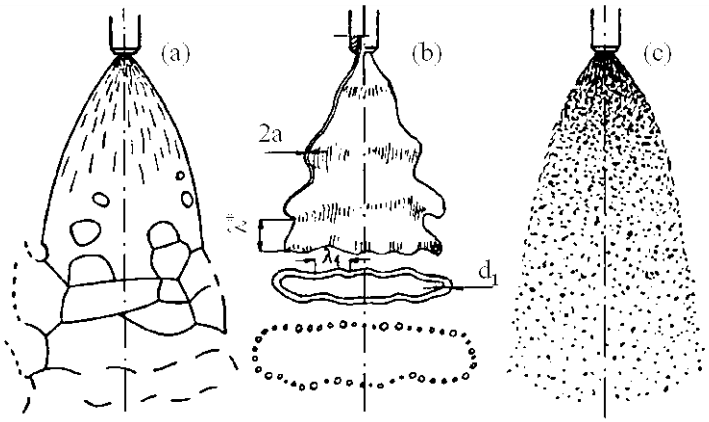

Figure 2.33: Different modes of sheet disintegration: a) Perforation: b) Wave phenomena: c) Atomization [187]

Rizk and Lefebvre studied the film thickness's effect on an airblast atomizer's atomization quality [201] excessively. They found that high viscosity fluids with high flow rates lead to thicker films, whereas for thinner liquid films, the produced droplets exhibit smaller Sauter Mean Diameter (SMD) (see Section 2.5.3) so that $SMD \sim t^{0.4}$, where t denotes the film thickness. Furthermore,

Geperth et al. investigated the effect of the liquid's physical properties, air velocity, atomizing edge thickness, pre-filming length, and liquid film flow rate, revealing that the first two parameters dominate the primary atomization. Albeit the parameters mentioned before undoubtedly influence the ligament formation, they do not exhibit significant influence on the mean droplet diameter [202].

2.5.3 Spray characterization

The majority of technical devices (i.e., atomizers) produce sprays consisting of a wide range of droplet diameters due to the atomization process's stochastic nature that pertains to the different breakup mechanisms. Therefore, the produced spray is treated as a spectrum of droplet sizes described by characteristic mean values. Usually, the spray distribution is plotted as a histogram, in which the abscissa represents the different droplet diameter class, which is defined by an interval denoted as Dd, against the number of droplets, or the volume of the spray, contained in each different class. As shown in Figure 2.34, by employing the spay volume, the resulting distribution is skewed to the right due to the large droplet's (d^3) weighting effect. If ΔD tends to zero, the discrete particle distribution is converted to the so-called continuous particle number distribution, known as frequency distribution.

The discrete and continuous particle number distribution may be written as follows:

$$f[D] = \frac{\Delta \overline{n}_i}{\Delta D_i} = \frac{(\Delta n_i / \Delta D_i)}{\sum_i^m \Delta n_i} \tag{2.139}$$

$$f_a(D) = \frac{d\bar{n}}{dD} = \frac{(dn/dD)}{\int_0^\infty (dn/dD)dD} \tag{2.140}$$

where $\Delta\bar{n}_i$ and $d\bar{n}$ denote the number of droplets in a given range, calculated as the ratio of the number of droplets in each class to the total number of droplets. Converting the particle number distribution into the volume (or mass) distribution requires the following relation:

$$\frac{d\overline{Vol}}{dD} \sim D^3 \frac{d\bar{n}}{dD} \tag{2.141}$$

where $d\overline{Vol}$ represents the volume fraction of the droplets contained in a particular range.

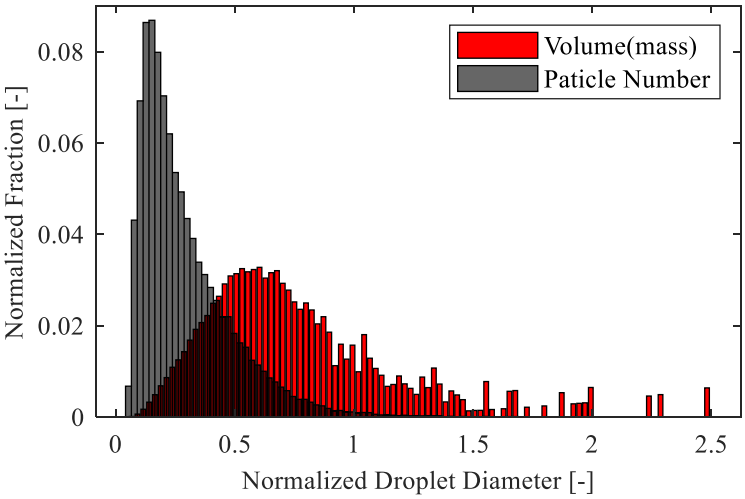

Figure 2.34: Example of droplet size histogram extracted by experimental data

The integral of the frequency distribution, or in other words the cumulative distribution (see Figure 2.35), represents the percentage of the droplets with a specific feature and is usually employed to extract spray characteristics.

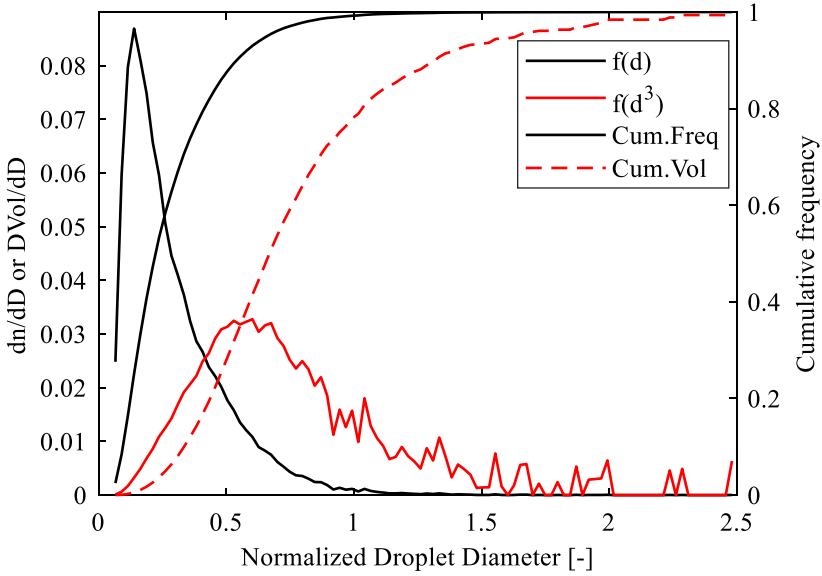

Figure 2.35: Example of **d**roplet frequency distribution curve extracted by the same experimental data as in Figure 2.34

The cost and complexity of conducting an experimental investigation have turned the scientific community to derive and employ mathematical functions, which simulate the droplet distribution's shape. Usually, the experimentally obtained results validate the aforementioned mathematical models, subsequently used as an input for numerical simulations. Several distributions have been proposed in the past, mostly based on probability density functions and empirical correlations [188]. The Rosin-Rammler distribution constitutes the

most widely employed expression to predict the droplet size distribution. It is also known as Weibull distribution and may be written as follows:

$$Q = 1 - e^{-(D/X)^q} \tag{2.142}$$

where Q denotes the fraction of the total volume contained in droplets with a diameter less than D, while X and q are the two parameters that adjust the distribution according to the requirements. The q parameter represents the droplet diameter's dispersion and is obtained as the slope of the curve in Figure 2.36. Higher values lead to a more uniform distribution. The X parameter is representative diameter given by the value D, which solves the following equation:

$$1 - Q = e^{-1} \tag{2.143}$$

yielding $Q = 0.632$. Therefore, 63.2% of the total liquid volume is composed of droplets whose diameter is less than X. One of the advantages of employing this correlation rather than its simplicity pertains to the possible extrapolation of the data into the range of fine droplets, in which the existing measurement techniques tend to be imprecise. However, it is not capable of predicting multiple peaks if existing.

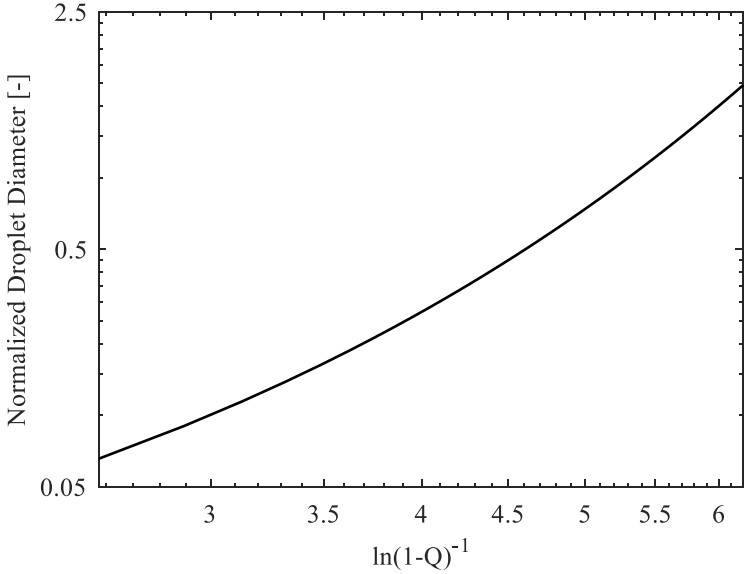

Figure 2.36: Typical Rosin-Rammler Plot extracted by the same experimental data as in Figure 2.34

A modified version of the Rosin-Rammler distribution has been reported in the literature [203] and seems to fit better the experimentally obtained distributions, particularly in the range of large droplets (see Figure 2.37). The following equation describes the so-called "Modified Rosin-Rammler Distribution":

$$Q = 1 - e^{-\left(\frac{\ln(D)}{\ln(X)}\right)^{q}} \tag{2.144}$$

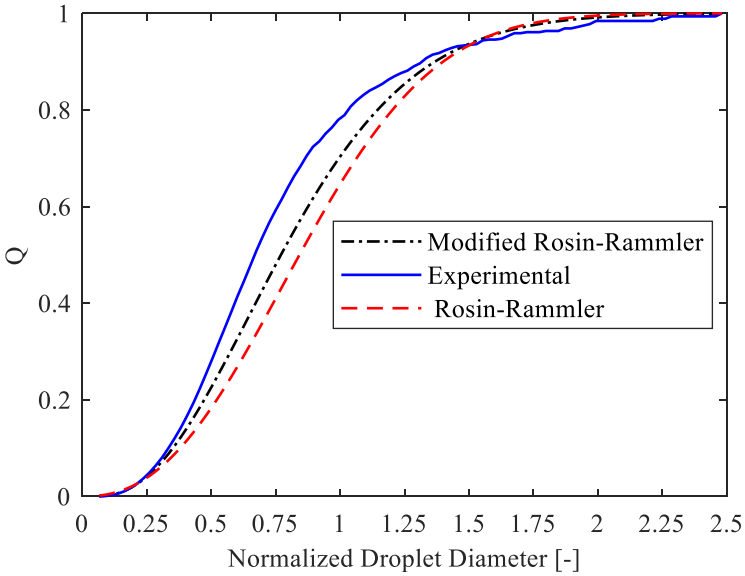

Figure 2.37: Comparison of the experimental with the Rosin-Rammler cumulative distributions (same experimental data as in as in Figure 2.34)

Usually, different characteristic diameters are selected to describe the distributions. They constitute statistical values, which describe a specific feature of the spray (i.e., diameter, surface, and volume of droplets) depending on the selection of the a and b, according to the following correlation:

$$D_{ab} = \left[\frac{\int_{D_{min}}^{D_{max}} D^a \frac{dn}{dD} dD}{\int_{D_{min}}^{D_{max}} D^b \frac{dn}{dD} dD}\right]^{\frac{1}{a-b}} \tag{2.145}$$

For disperse distributions applies the following:

$$D_{ab} = \left[\frac{\sum D^a N_i}{\sum D^b N_i}\right]^{\frac{1}{a-b}} \tag{2.146}$$

where N_i denotes the number of droplets with diameter D contained in the diameter class of the discrete distribution with index i.

In Table 2.2, the diameters that are commonly used together with their primary application are illustrated.

a	b	Symbol	Name	Applications
1	0	D_{10}	Length	Comparison of disperse systems
2	0	D_{20}	Surface area	Absorption or vaporization
3	0	D_{30}	Volume	Volumetric phenomena
2	1	D_{21}	Surface area-length	Droplet disintegration
3	1	D_{31}	Volume-length	Evaporation, combustion
3	2	D_{32}	SMD	Mass/heat transfer, combustion
4	3	D_{43}	De Brouckere's mass	Combustion

Table 2.2: Mean drop diameters

Several parameters have been reported in the literature used to define the existing distribution functions, and probably the most prominent of them are the following:

- $D_{0.1}$: 10% of the total liquid volume consists of droplets with smaller diameters.
- $D_{0.5}$: 50% of the total liquid volume consists of droplets with smaller diameters, usually denoted as Mass Mean Diameter (MMD).
- $D_{0.632}$: 63.2% of the total liquid volume consists of droplets with smaller diameters, and it constitutes one of the two parameters determining the Rosin-Rammler distribution.

- $D_{0.9}$: 90% of the total liquid volume consists of droplets with smaller diameters.
- D_{peak}: The droplet diameter attributed to the highest detection frequency.

2.6 High altitude relight conditions

During a flight, a rare, though detrimental phenomenon can occur. The extinction of the flame in the combustion chamber is defined as a flameout event. Several parameters, such as fuel starvation, compressor stall, ingestion of ice, or a mechanical failure, can cause this event. The jet engine's high altitude relight is determined as the restart and the subsequent proper spool-up of its shaft. The operating conditions in the case of a flameout event are adverse for the combustion process, as illustrated in Figure 2.38. An increase in the altitude deteriorates the combustor entry conditions, while low temperature and pressure hamper several crucial mechanisms governing the combustion process, such as reaction rate and atomization quality. The latter also affects the evaporation rate while, as mentioned afore (Section 2.3.4.1), bigger droplets exhibit a slower evaporation rate. The evaporation of the fuel is also limited by the low temperature of the gas and liquid phases.

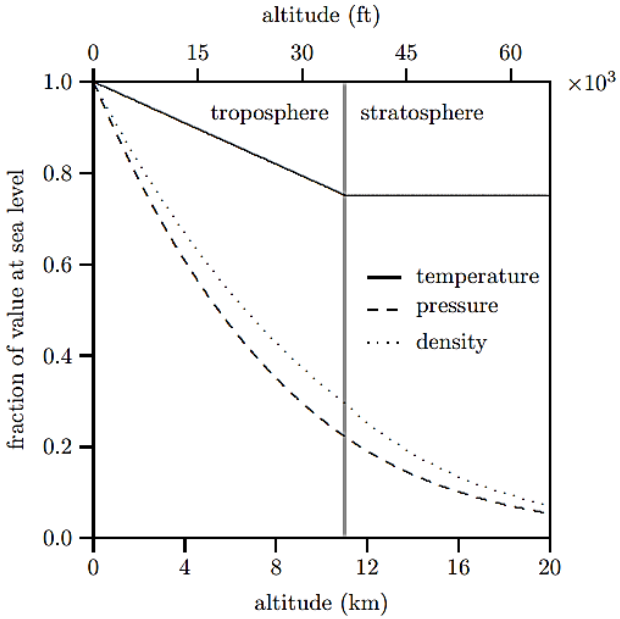

Figure 2.38: Global operating conditions as a function of altitude [204]

Due to the inherent safety implications, the relight process draws considerable attention from the early design stages. According to the Federal and European Aviation Agencies, the engine manufacturers have to provide the so-called relight envelope [1,205], containing information such as the altitude and the Mach number, at which the relight of the jet engine is feasible. Depending on the altitude and the Mach number, the relight process is classified as windmill and starter assist restart, as shown in Figure 2.39. The former is attributed to higher Mach numbers, and the latter is required to aid the compressor in achieving a sufficient rotational speed.

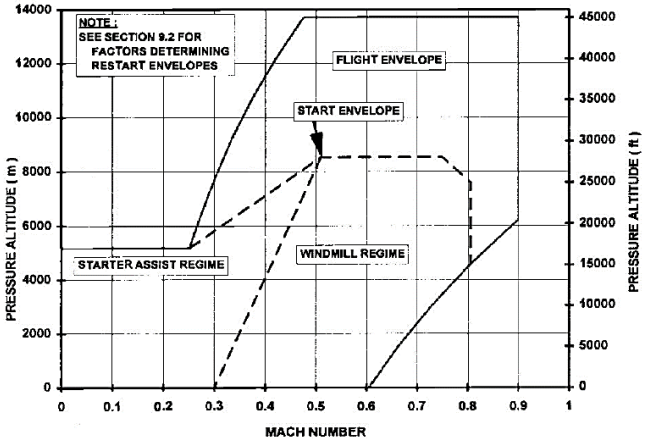

Figure 2.39: Relight envelope [206]

As mentioned afore, the high-altitude relight capability is a crucial process for flight safety. It constitutes a dominant factor for each jet engine's design since several compromises are made to ensure a fast and successful re-ignition and the subsequent proper-spool up of the engine's main shaft. However, due to the complexity associated with realizing the high-altitude conditions in a laboratory environment, the experimental investigations reported in the literature are scarce. Laboratory scaled experiments of simplified configurations [12,15] have been conducted to account for the high complexity created in technical or semi-technical configurations. The latter arises from the heterogeneous flow, which generates remarkable fluctuations of the local equivalence ratio (liquid and vapor) and the instantaneous flow field (turbulent characteristics) at the instant of the spark. Therefore, experimental results obtained with realistic configurations fail to produce a database that does not apply only to each examined case. The MIE evaluation under well-defined conditions promotes the

enhancement of understanding/knowledge concerning the ignition process parameters. Results indicate that MIE for a successful ignition event decreases with fast chemical kinetics, improved atomization quality, low airflow rates, and volatile fuels, consistent with the measurement under atmospheric conditions (see 2.4.3.2). However, the measured value deviates significantly from the corresponding predicted one by the theory [8], and this might lie in additional effects, such as the heat loss in the spark electrodes. Knowledge of the parameters affecting MIE could lead to extended spark plug life and significantly reduce the maintenance time intervals.

Nevertheless, in real engines, the energy delivered by the spark plug consistently exceeds by a significant factor the MIE obtained experimentally. Therefore, whether an ignition attempt is successful does not pertain to the flame's kernel generation but to parameters that promote or not the subsequent flame development. Experimental investigations under high-altitude conditions in realistic configurations have revealed that the flow field and the effective equivalence ratio (fuel vapor) constitute the dominant factors concerning the ignition process [3,11,14,207,207]. Results indicate that a rapid upstream propagation of the flame kernel towards the nozzle increases the probability of successfully igniting. The latter depends highly on the generated cold-flow, whose prior knowledge is crucial for the ignition evolution since it determines the optimum igniter's location. Moreover, the ignition sequence's high-speed recordings showed that the flame's kernel luminosity decreases rapidly after its initiation until it recovers strongly before the stable burning configuration. Finally, with increased altitude, variations of the local FAR, raised by the lower evaporation rate, hamper the ignition process, which requires a higher amount of injected fuel.

3 Experimental Method

This investigation focuses on generating an engine's high altitude relight database (see Figure 3.1) for kerosene Jet-A1-air mixtures. The reported experimental results in the literature are scarce. More specifically, within this research activity scope, a rectangular, single-injection RQL combustion chamber has been developed to investigate the high altitude relight capability of two configurations, with and without effusion cooling. Moreover, the operating conditions have been selected and realized to cover a wide range of thermodynamic conditions that a real engine might encounter in a potential flameout event during the flight. In the frame of this research activity, novel techniques have been developed, such as tracking the flame's luminosity center (see Section 3.4.1) to enhance the understating/knowledge of the relevant phenomena governing the high altitude relight of a jet engine.

The complete engine's relight database is enriched with a thorough spray investigation under high altitude relight conditions with kerosene Jet A-1, which is unique to the best of the author's knowledge. The experimental investigation has been conducted using the shadowgraphy measurement technique, an optical laser technique suitable for non-spherical droplet detection.

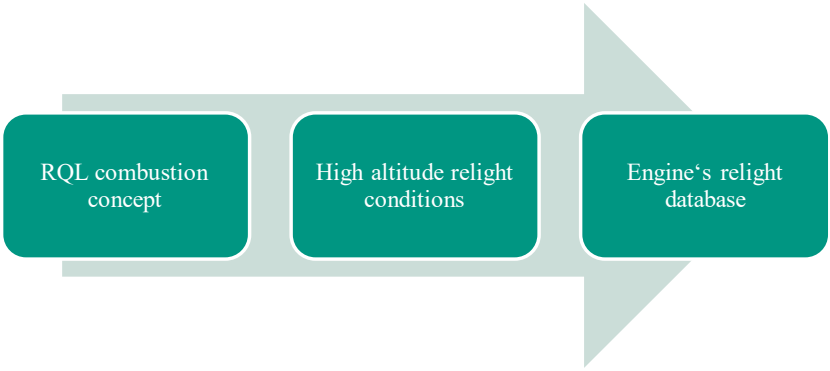

Figure 3.1: Research Objectives

3.1 High altitude test facility

The experiments of this research activity were conducted at the ISCAR (“Ignition under Sub atmospheric Conditions- Altitude Relight”) rig, which was designed and manufactured at the Engler-Bunte-Institute of Karlsruhe Institute of Technology (KIT). It is capable of generating low pressure and temperature conditions for flowing kerosene-air mixtures. The turbulence influence on spark ignition was studied previously at the ISCAR rig by Majcherczyk et al. [12]. The simplified picture of the rig is shown in Figure 3.2 and the corresponding schematic diagram in Figure 3.3.

The combustion chamber’s flow and low pressure are produced by a set of eight parallel ejectors, which are vacuum devices and can be switched on and off independently. The pressure is regulated through pressure reducer 3 (PR3) in Figure 3.3. The cold air is generated through the expansion of compressed air in two small automotive turbochargers. The turbine’s exit temperature de-

pends on the turbine pressure ratio and can be regulated by inlet turbine pressure through pressure reducer 1 (PR1) in Figure 3.3. The excess of cold air is used to cool down the walls of the incoming flow. This additional cooling allows maintaining a constant ignition chamber temperature even at low volume flows and at a lower temperature range. The test rig's practical operating temperature and pressure range is -20°C to ambient temperature and 0.4 bar to atmospheric, respectively.

The ignition chamber's air mass flow is regulated through regulating valve 1 (RV1), as is shown in Figure 3.3. The linear dependency of the mass flux from the suction pressure enforces a further regulation through a bypass system, through pressure reducer 2 and regulating valve 2 (PR2), (RV2). Thus, the combustion chamber's mass flux and pressure are regulated independently of the linear ejector characteristic curve.

The fuel (kerosene Jet-A1) is supplied from a pressure vessel pushed out by a piston. The fuel's temperature is expected to be a few degrees lower than the room temperature due to the exposure of the fuel pipes to the cold air during the experimental trial. As shown in Figure 3.3, kerosene passes through a series of valves. A solenoid valve connected with the afterburner's ionization sensor ensures the test rig's safe operation by preventing the injection of kerosene into the combustion chamber in case of a flameout event in the afterburner.

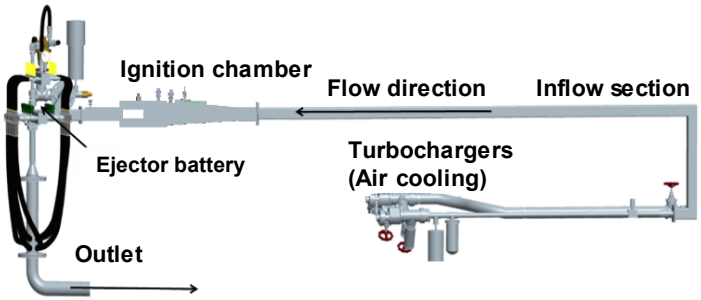

Figure 3.2: Simplified overview of ISCAR test rig

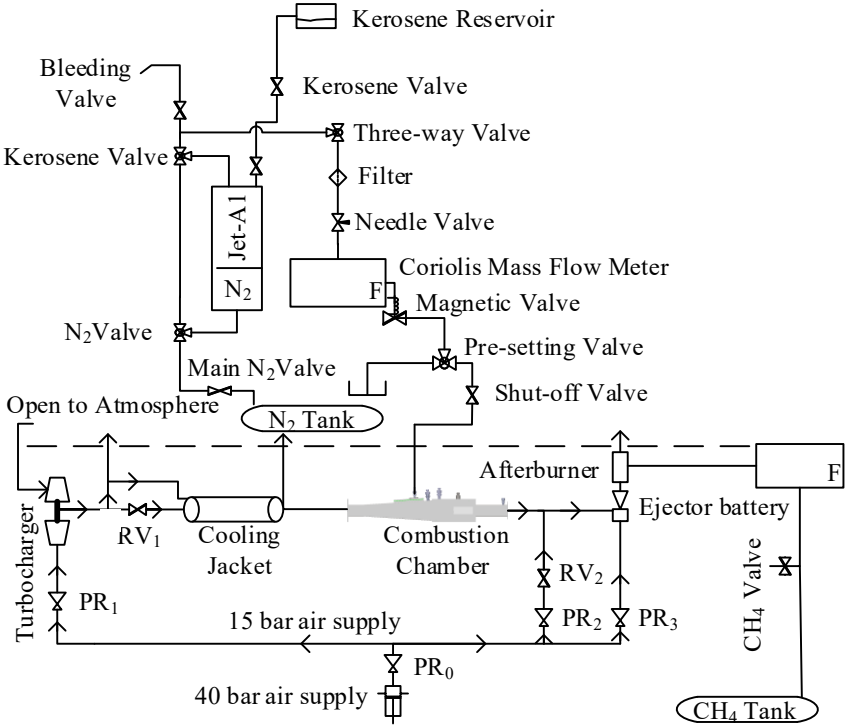

Figure 3.3: Detailed schematic diagram of ISCAR test rig

3.1.1 Combustion chamber layout

A single injection RQL (Rich-Quench-Lean) combustion chamber has been designed and manufactured in the scope of this research activity. The employed combustion concept was introduced in the early 80s [208] and used as a strategy for NO_x reduction, primarily from stationary gas turbines Later, in the early 90s, NASA integrated the RQL combustion concept as a part of High-Speed Civil Transportation (HSCT) [209,210]. It holds a significant market share compared to different staged combustion concepts in commercial aviation. The main reason for this predilection of the aviation industry towards the RQL combustion concept lies in the following considerations:

1. Reliable and smooth ignition on the ground as well as under high attitude conditions (safety considerations).
2. Wide stability limits (overall performance).
3. Exit temperature distribution is regulated to prevent any excessive damage to the blades of the turbine
4. Low NO_x and smoke emissions
5. Ability to operate with fuels with complex and varying compositions

As shown in Figure 3.4, an RQL combustion chamber employs a staged combustion concept. The fuel-rich primary zone enhances the flame's stability to the high concentration of hydrocarbon radical species. Moreover, it favors NO_x emissions, primarily due to the lack of oxygen in the rich zone combined with a low temperature in the lean zone. In Figure 3.5, the influence of the staged combustion concept on the formation of NO_x is depicted. Operating the combustion chamber close to stoichiometric conditions induces maximum NO_x for-

mation. The emanating effluent from the primary zone comprises partially oxidized hydrocarbons, hydrogen, and carbon monoxide. Therefore, it requires further processing to be exhausted, and the effluent is imposed to a transition zone known as the quick quench zone. A substantial amount of secondary area is injected into the combustion chamber through the dilution zone, oxidizing the high concentrations of carbon monoxide and intermediate hydrocarbon species. Subsequently, prior to the combustor's exit, the last zone, known as the lean zone, is generated. In this zone, NO_x formation is prevented due to the low temperature. The quick-quench zone's design is one of the significant challenges determining the RQL concept's performance. The effluent exiting the primary zone should be mixed with the injected air rapidly to prevent near stoichiometric conditions that increase the combustion temperature and lead to the formation of nitrogen oxides.

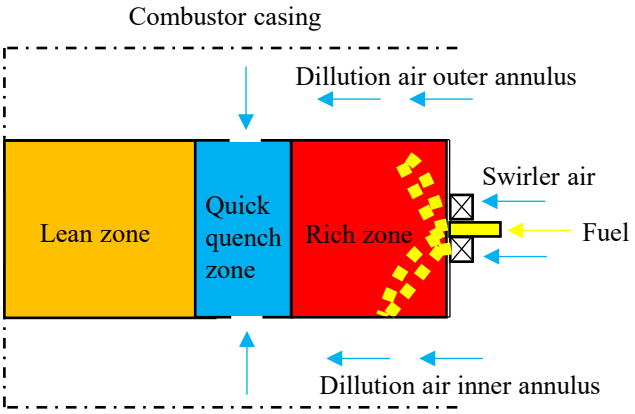

Figure 3.4: RQL combustion concept

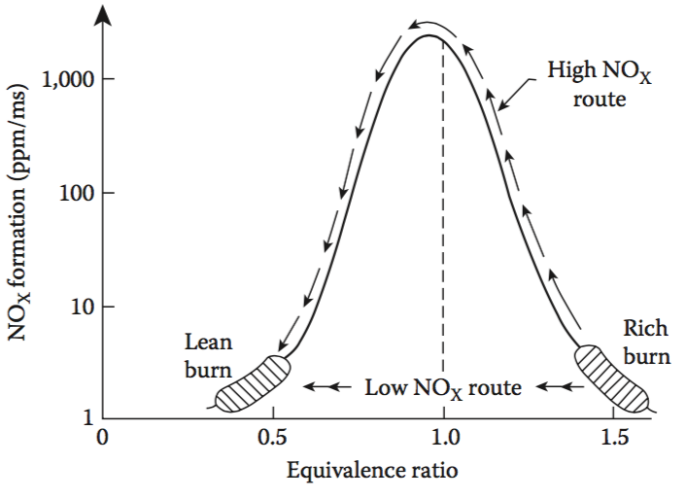

Figure 3.5: Influence of staged combustion concept on the NO_x production [91]

The ignition process's characterization has been conducted with a rectangular shape, single injection RQL combustion chamber, developed at Engler-Bunte Institute (Figure 3.6). As shown in Figure 3.7, it constitutes a realistic RQL configuration, where the flowing air at the end of the pre-diffuser splits into three regimes: the inner and outer annulus and subsequently through the dilution holes, which have a staggered configuration, in the quick-quench zone, and through the nozzle, which is used for mixing and atomization purposes. In Figure 3.8, the RQL combustion chamber integrated into the ISCAR rig, along with the testing hardware, is illustrated.

The modular approach in the combustion chamber design enables the testing of different liners, with or without effusion cooling, variable size and number of dilution holes, and studying the influence of the spark plug location of the

ignition process. Moreover, it provides broad optical access via quartz windows, and thus the high-speed recording of the unsteady flame kernel generation and propagation is feasible.

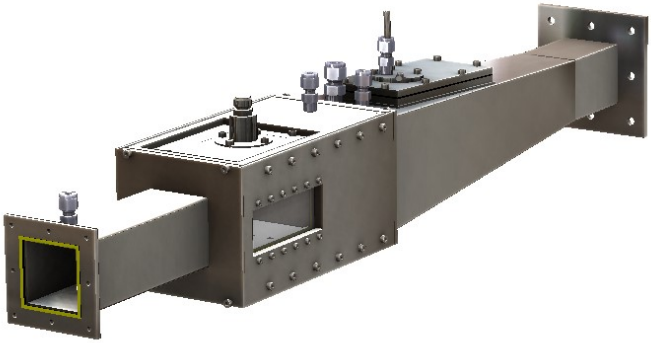

Figure 3.6: CAD overview of the RQL combustion chamber

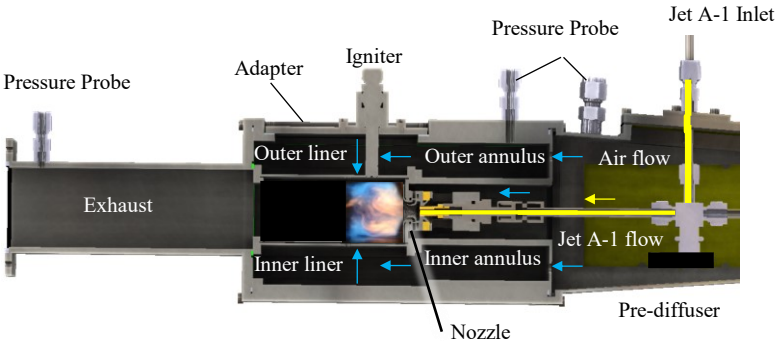

Figure 3.7: Cross section of the RQL combustion chamber – yellow arrow (kerosene Jet A-1 flow), cyan arrow (airflow)

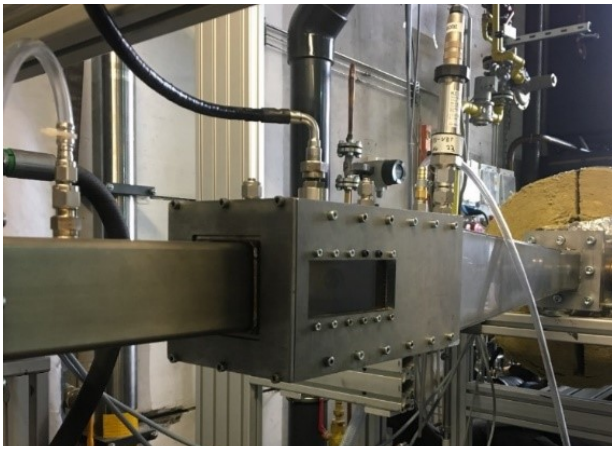

Figure 3.8: RQL Combustion chamber mounted on the ISCAR test rig

The experimental investigation has been conducted with realistic ignition and injection systems, representative of the ones employed in commercial aviation, to enhance the investigation's technical relevance. In Figure 3.9, a simplified view of the flow field generated by the swirler is depicted. The swirled jet undergoes vortex breakdown due to the presence of a positive pressure gradient on the swirler axis, leading to negative axial velocities around the centerline of the combustor, forming a strong IRZ (see Section 2.3.6). Furthermore, the ignition device consists of a commercial spark plug whose location is illustrated in Figure 3.9. The spark plug is flush mounted at the outer liner's inner surface and contains s series of cooling holes, which protects the material and prevents as much as possible fuel accumulation at the surface of the igniter that is detrimental to its performance.

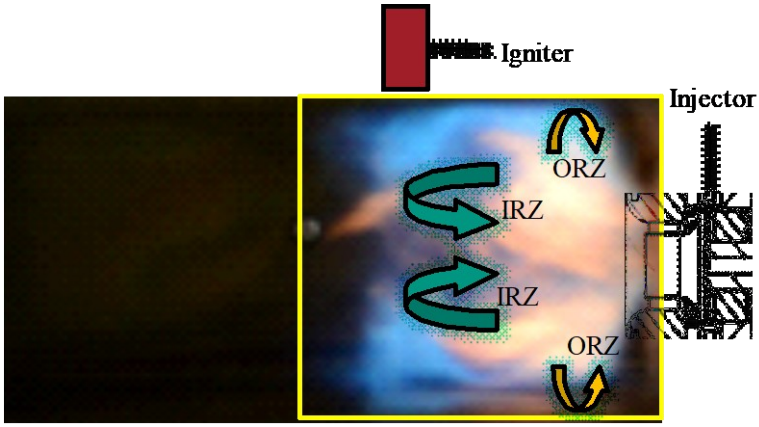

Figure 3.9: Swirler's flow field together with the hardware of the combustion chamber; yellow rectangular represents the interrogation window of the high-speed camera

The ignition exciter's pin connection is illustrated in Figure 3.10. It operates with a combined power supply of Alternating current (AC) and Direct current (DC), generating sparks at a rate of approximately 7 Hz. The impedance of the AC has been simulated with a circuit consisting of an inductor (L1) and resistance (R1). The latter prevents any potential damage to the ignition exciter. The histogram shown in Figure 3.11 has been obtained experimentally out of seven individual experiments. A Si-photodiode was acquiring the voltage amplitude in time, obtained by continuously sparking for 10 seconds. Subsequently, a Matlab code was employed to perform the statistical analysis.

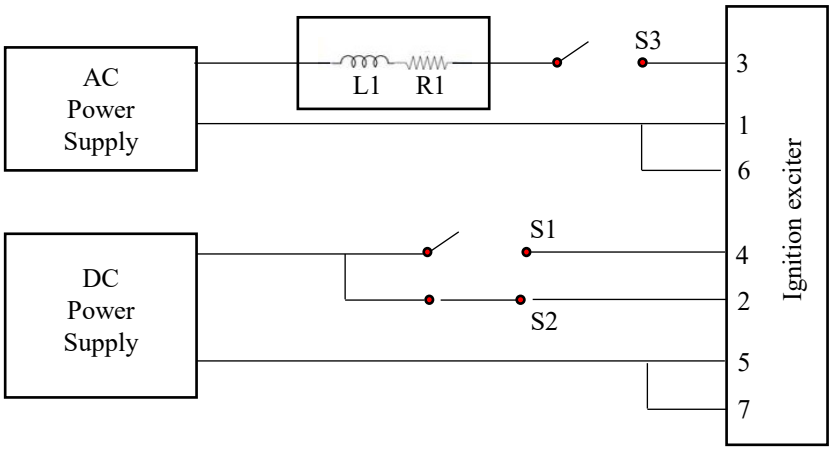

Figure 3.10: Input power supply of the employed ignition exciter

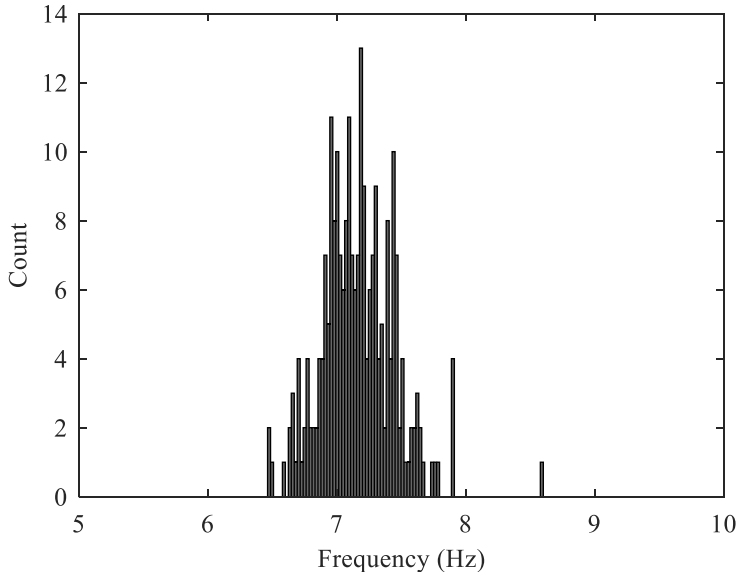

Figure 3.11: Spark frequency, histogram extracted by seven individual measurements

The combustion chamber's commissioning was conducted in a dedicated atmospheric test rig, developed in the frame of this research activity. Initially, the ATA (Atmospheric Test Rig) rig, shown in Figure 3.14, was employed for leakages tests and detailed effective area measurements to determine the exact split of the flow among the different regimes (i.e., nozzle, liners, cooling holes of the igniter). The effective area was calculated with the following equation, whose detailed derivation is explained in Appendix A.1:

$$A_{eff} = \frac{\dot{m}\sqrt{T_1/p_0}}{\left(\frac{p_1}{p_0}\right)^{\frac{1}{\kappa}}\sqrt{\frac{2\kappa}{\kappa-1}\frac{p_1}{p_0}\left[1-\left(\frac{p_1}{p_0}\right)^{\frac{\kappa-1}{\kappa}}\right]}} \tag{3.1}$$

Configuration without effusion cooling

In this configuration (see Figure 3.12), the detailed effective measurements revealed roughly a 30% through the nozzle to 70% dilution zone air split, while the following applies $\dot{m}_{sec} = 2.5 \cdot \dot{m}_{nzl}$.

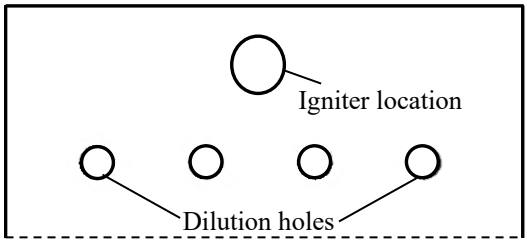

Figure 3.12: Liners without effusion cooling

Configuration with effusion cooling

Effusion cooling in gas turbine combustion chamber constitutes an advanced concept to reduce the wall temperature, and it is currently state of the art for cooling the liners and the turbine blades [211]. The liners with effusion cooling (see Figure 3.13) have been carefully engineered to meet the test facility's operating range margin. The additional air required for cooling, while maintaining the global operating conditions constant, applies $\dot{m}_{act} = 1.6 \cdot \dot{m}_{at}$.

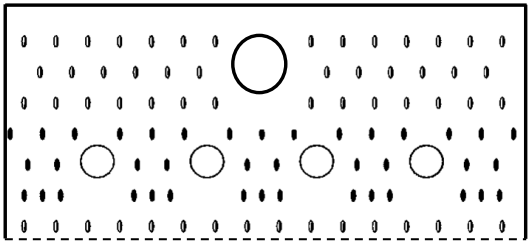

Figure 3.13: Liners with effusion cooling

After having determined the exact flow split, preliminary tests on flame stabilization under atmospheric conditions were conducted. The latter indicated successful ignition events and subsequent flame stabilization in a wide range of operating conditions. A representative flame shape obtained under atmospheric conditions is illustrated in Figure 3.15.

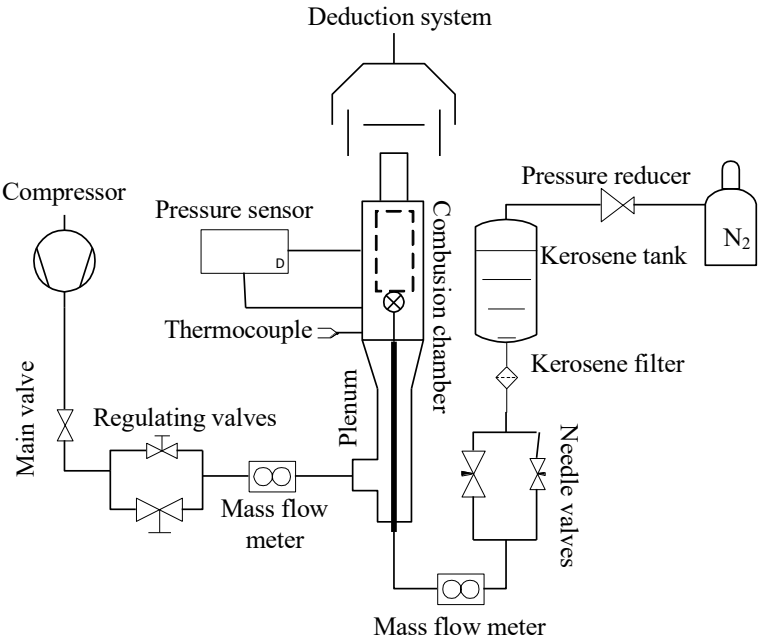

Figure 3.14: Schematic representation of the atmospheric test rig

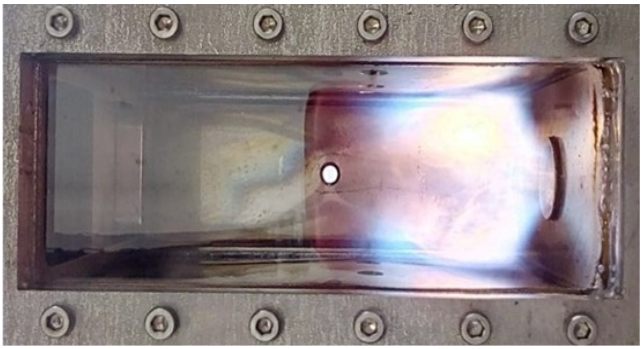

Figure 3.15: Flame shape obtained under atmospheric conditions

In addition, LBO (Lean Blow Out) measurements have been conducted under atmospheric conditions [212]. The fuel's mass flow rate was reduced, following a successful ignition event, until the flame's extinction was captured. In Figure 3.16, LBO_{nozzle} and $LBO_{total\ combustor}$ represent the stable and unstable regimes based on the air that passes through the injector and the total amount of air (injector + dilution), respectively. It is conspicuous that an increase of pressure drop widens the stable regime, and the reason is the better performance of the airblast atomizer at higher air mass flows.

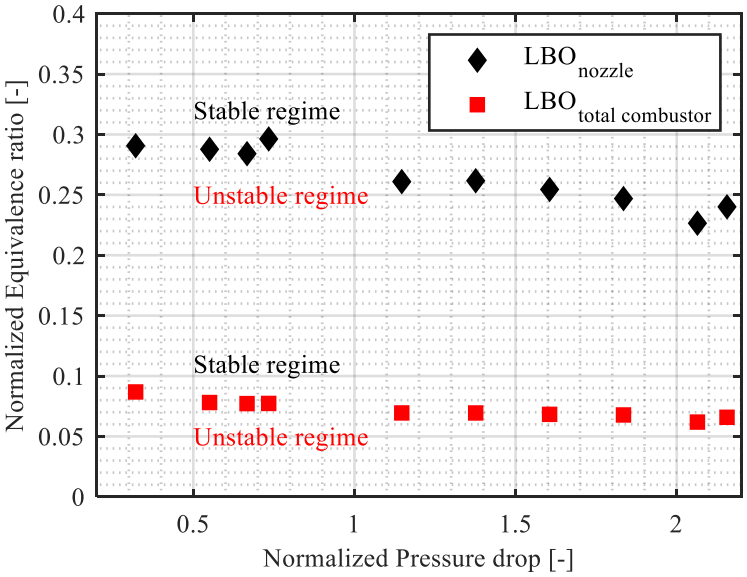

Figure 3.16: Lean Blow Out measurements (1 bar, 20°C)

3.1.2 Operating conditions

The test matrix in Table 3.1 consists of 12 different operating conditions, which cover a wide range that an engine could encounter in a potential flame-out event at high altitudes as well as in the ground during a hot but also a cold day. As shown in Table 3.1, the global conditions of the 0.64 bar operating point have been selected as the reference operating conditions so that the complete test matrix is normalized according to them.

Nr. [-]	P_3 [bar]	T_3/T_{ref} [-]	FAR/FAR_{ref} [-]	$\Delta p_{nozzle}/\Delta p_{nozzle,ref}$ [-]
1	1.00	1.103	0.681	0.954
2	1.00	0.948	0.562	1.200
3	0.67	0.948	0.824	1.252
4	0.65	1.003	0.867	1.197
5	0.65	0.948	0.890	1.233
6	0.64	1.000	1.000	1.000
7	0.55	0.948	0.962	1.357
8	0.54	0.977	1.062	1.206
9	0.54	0.948	1.024	1.243
10	0.53	0.974	1.143	1.087
11	0.44	0.948	1.229	1.316
12	0.43	0.948	1.333	1.169

Table 3.1: Ignition test matrix-fuel mass flow constant for each operating condition

The laminar burning velocity is a mixture's property (see Section 2.3.1), indicating its reactivity under imposed operating conditions. As shown in Figure

3.17, a preliminary investigation of the test matrix's laminar burning velocity revealed four different "reactivity classes". It is evident that with increased simulated altitude, the predicted laminar burning velocity decreases, indicating a lower mixture's reactivity. The Aachen mechanism and 80 m% n-decane and 20 m% trimethyl benzene is employed [59], and the analysis is performed with Matlab Cantera 2.4.0 Toolbox.

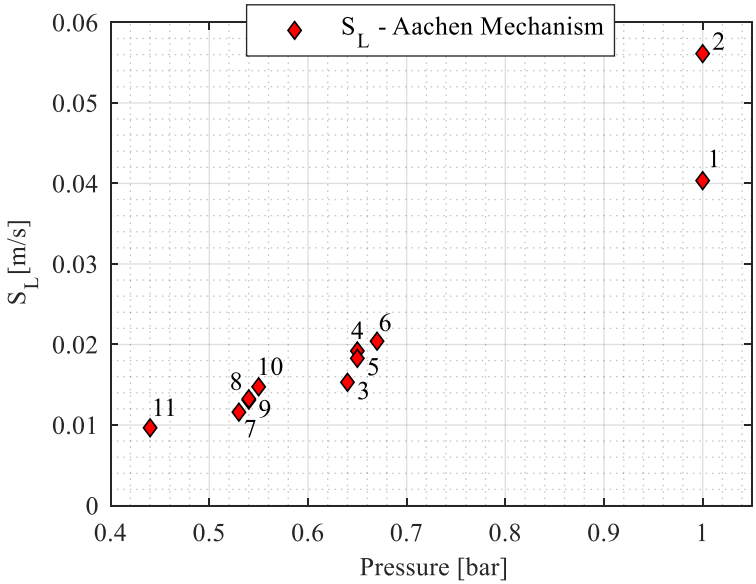

Figure 3.17: Laminar burning velocity calculation of the high-altitude conditions with Cantera – Aachen Mechanism – numbers assigned according to Table 3.1 – no convergence for operating condition Nr.12

Comparability for both configurations (with and without effusion cooling) is attained since they are exposed in the same operating conditions, maintaining the same pressure drop across the nozzle, following the same experimental procedure, which consists of three distinctive phases:

Preparation:

- Set air mass flux, temperature, and pressure
- Reach steady-state conditions

Light on:

- Start and stabilize the fuel flow
- Start the igniter
- Light on-event (producing spark for 10 sec)
- Successful or unsuccessful ignition event

Shut down:

- Turn off the igniter
- Purging of the remaining kerosene from the pipe

3.2 High-altitude relight capability

The so-called high altitude relight capability includes, aside from the ignition probability map, the determination of the minimum FAR (Fuel to Air Ratio) for each operating condition of the test matrix (see Table 3.1). To create the ignition probability map, only one experiment for each operating condition is inadequate. At this stage, statistics were compromised by the experimental time needed for the realization of the global operating conditions (low pressure and temperature) and the actual measurement, which was particularly time-consuming. Four ignition attempts per different operating conditions were performed by maintaining a fixed fuel mass flow and considered an optimum

value that fulfills the experimental objectives. Therefore, the ignition probability is obtained by the following correlation:

$$P_{ign} = \frac{number\ of\ successful\ ignition\ events}{Total\ number\ of\ \ attempts} \tag{3.2}$$

The minimum FAR was measured for $P_{ign} = 25\%$ (configuration without effusion cooling) and $P_{ign} = 100\%$ (both configurations) and a direct comparison is presented in Section 5.2.

3.3 Ignition timing

In the frame of this research activity, ignition timing is defined as the time interval between the first spark and the flame's onset. Since the spark power is maintained constant, ignition timing might be influenced by the liquid and gas phase's thermophysical properties, the SMD and the volatility of the liquid fuel, and subsequently the local effective equivalence ratio [213]. A Si-photodiode (Thorlabs PDA36A-EC), triggered by the ignition exciter, was used to detect the ignition timing. As shown in Figure 3.18, the Si-photodiode was placed perpendicular to the combustion chamber facing its optical access. LabView monitored the photodiode's electrical signal during an experimental trial. The latter was used as an input in a dedicated Matlab code, which yielded, aside from the ignition timing, the spark frequency and duration, and the number of sparks required for each successful ignition trial.

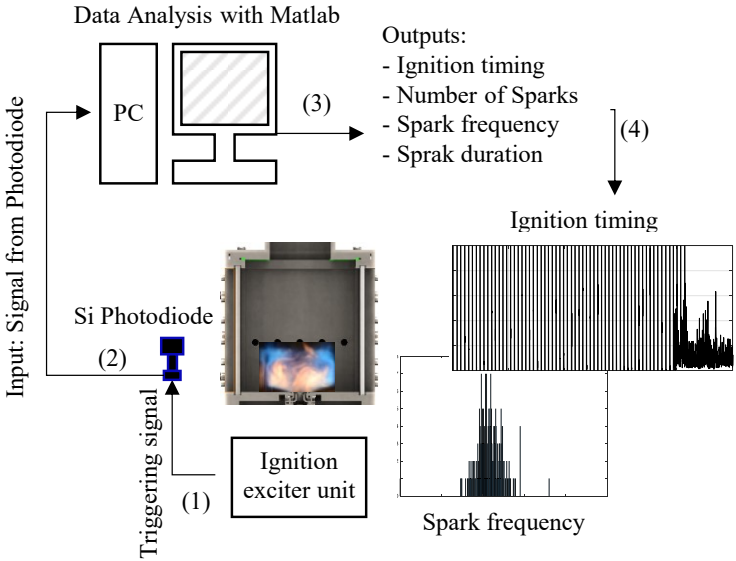

Figure 3.18: Schematic representation of the experimental method for the ignition timing detection

3.4 High-speed imaging recording

It has been previously reported in the literature that the convection of the flame kernel by the imposed flow field plays a dominant role in the evolution of the ignition process [14]. Therefore, in this investigation, a high-speed video camera (LaVision HighSpeedStar 5) was employed to record the broad-band emissions generated during the unsteady flame kernel generation and propagation. As shown in Figure 3.19, the camera was arranged perpendicular to the flow direction, providing imaging at a repetition rate of 1500 Hz.

3.4.1 Development of an in-house image processing code

Several experimental investigations have employed high-speed imaging recording for qualitative evaluation of the ignition process [214]. However, this research activity systematically extracts quantitative spatial and temporal information from the flame's visualization. Therefore, an in-house advanced image-processing code using Matlab was developed in the frame of this research activity. A simplified block diagram of the code is integrated into Figure 3.19. It uses as input the grayscale images obtained by the high-speed camera, and subsequently, to highlight the details and the boundaries, each image is filtered with Gaussian kernel and intensity enhancement. The third step pertains to each image's segmentation by employing maximum intercluster variance, a self-adaptive threshold determination method known as Otsu's method [215]. The binarization converts the grayscale image, where each pixel lies within the range of 0 (black) to 255 (white), to values of 0 (no flame particle) to 1 (flame particles).

Moreover, the image processing code employs its boundary trace algorithm, which defines the height and the length of the flame at each time step. Due to the ignition process's probabilistic nature, it is essential to study the mean behavior. Thus, the ALETHO (**AL**gorithm for imag**E** processing and **T**racking of t**H**e **O**bject's displacement) algorithm post-processes single ignition trials as well as average behaviors of the ignition evolution for a specific set of operating conditions. It constitutes a handy tool to compare the ignition sequence of the same or different imposed operating conditions and identify characteristic behaviors and overall trends.

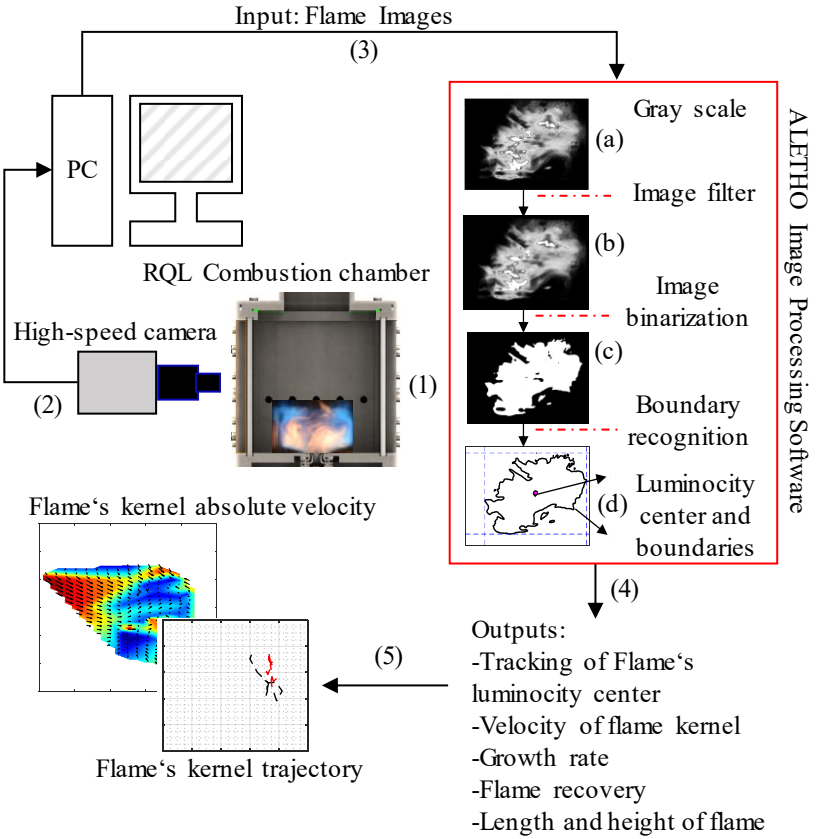

Figure 3.19: Schematic representation of the high-speed imaging recording and the dedicated post-processing

3.4.1.1 Total intensity variation of flame particles

The total intensity variation of particles that the ALETHO algorithm identifies as flame particles provide an appraisal of the combustion activity during an

ignition trial. Further evaluation of these data extracts the influence of the different simulated altitudes on the timescale of ignition success or failure, also capturing the behavior of the following stable burning configuration. In Figure 3.20, a representative binarized image in a specific time step of the ignition recording is illustrated. $In_{max} = a \cdot b$ is defined as the maximum image intensity observed if the interrogation window is completely covered with flame particles (white color). In contrast, no combustion activity corresponds to $In_{min} = 0$, whereas in any other case, the total intensity of flame particles is calculated as follows:

$$In_{image} = \sum_{i=0}^{a} \sum_{j=0}^{b} n_{pixels}\big|_{pixel=1} \tag{3.3}$$

where and a and b represent the length and the height of the camera's interrogation window, respectively, while n_{pixels} denote the number of pixels that the algorithm has identified as flame particles.

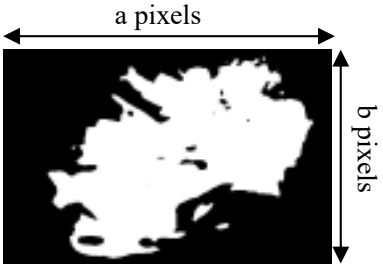

Figure 3.20: Total intensity variation extracted by the image processing code

3.4.1.2 Flame trajectory

Trajectory plots of the flame's motion have been derived and evaluated to compare the ignition evolution process of successful and unsuccessful ignition events. The flame tracking algorithm integrated into the ALETHO algorithm is employed to generate the flame's trajectory plots for single as well as for multiple high-speed recordings of the ignition attempts. The flame's luminosity center is extracted via the grayscale image using the following weighting method:

$$x = \frac{\sum_{i=1}^{N} x_i I(x_i, y_i)}{I(x_i, y_i)}$$
$$y = \frac{\sum_{i=1}^{N} y_i I(x_i, y_i)}{I(x_i, y_i)} \tag{3.4}$$

where x and y denote the resulting horizontal and vertical coordinates of the flame's luminosity center; i is the index of each pixel of the N number of identified pixels identified as flame particles; x_i and y_i are the horizontal and vertical coordinates of each pixel located within the flame region, and $I(x_i, y_i)$ is the corresponding luminosity of the coordinates x_i and y_i extracted by the grayscale image.

By adjusting the camera's recording frequency, a known time interval between each acquired image was defined. Therefore, the flame tracking algorithm calculates the axial, the radial, and the absolute velocity vector and magnitude by the known displacement of the flame's luminosity center within a known time difference as follows:

$$U_x = \frac{x_{k+1} - x_k}{t_{k+1} - t_k}$$
$$U_y = \frac{y_{k+1} - y_k}{t_{k+1} - t_k} \tag{3.5}$$

where t_k denotes the k[th] time step of the image acquisition. Hence, the magnitude of the velocity is calculated as follows:

$$U_{tot} = \sqrt{U_x^2 + U_y^2} \tag{3.6}$$

The ALETHO algorithm calculates and plots the arrows that represent the directional component of U_x and U_y at the Cartesian coordinates assigned to x and y.

3.5 Spray measurements with shadowgraphy

3.5.1 Principle of the measurement technique

The experimental investigation concerning the spray characterization was conducted with a planar image velocimetry system, as shown in Figure 3.21. The shadowgraphy measurement technique lies in the pulsating backlight illumination of the droplets, capturing their contours shadows in the focal plane via a high-speed camera coupled with a long-distance microscope. In Figure 3.21, the shadowgraphy set-up is illustrated. It is evident that the light source is aligned with the detection system, and the measurement plane is placed in between them. The illumination system consists of a Litron laser doubled pulse Nd: YAG laser (Neodym Yttrium Aluminum Garnet laser) and a high-efficiency diffuser. The laser beam has a wavelength of λ=532 nm, with maximum frequency of 15 Hz and a duration of 10 ns. A PTU (Programmable Timing

Unit) controls the laser pulse by synchronizing the trigger signal with the camera's aperture control system. Furthermore, the laser emits two pulses, usually denoted as pulse A and B, occurring with a specified user duration dt. Thus, the velocity component's calculation is feasible by cross-correlating the change of position of the already identified droplets in both captured images [216]. The laser beam passes through the high-efficiency diffuser, impacting the fluorescent dye plate, which results in an incoherent light at a wavelength of 574-580 nm. Subsequently, the converted light beam is transported through the optical fiber to the diffuser head, where it expands and focuses at the distance of maximum light intensity, about 400 mm.

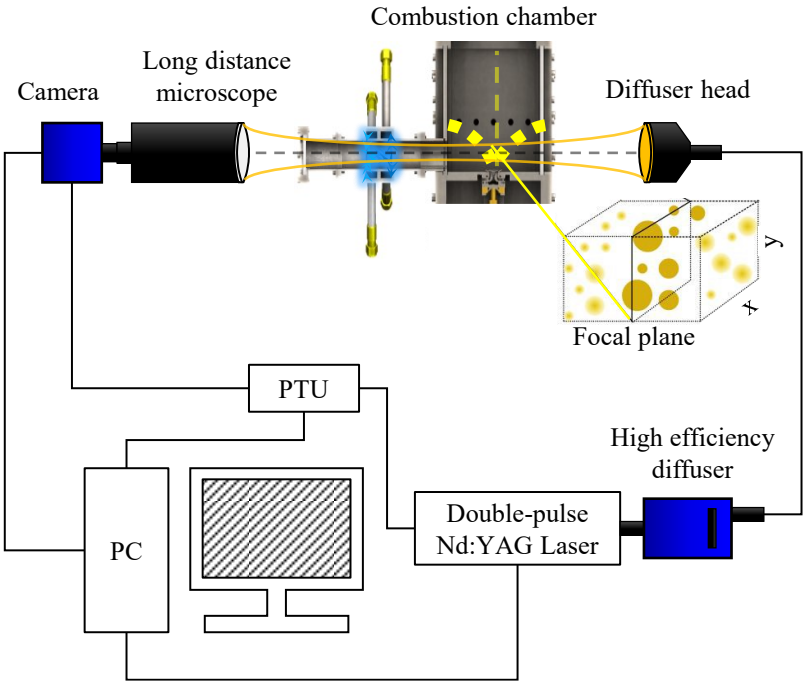

Figure 3.21: Shadowgraph imaging set-up for spray characterization

A four-megapixel CCD camera coupled with a mirror-based long-distance microscope (Maksutov Cassegrain Catadioptric) is used as a detection system. In Figure 3.22, the working principle of the long-distance microscope is illustrated. The light penetrates the front correcting lens, and it is directly refracted in the rear section of the microscope, the so-called primary mirror. Subsequently, the light is reflected in the secondary mirror, which is mounted in the front section, and it passes through a tube, supported in the central hole of the primary mirror, to the prism. Therefore, the image, which reached the axial port of the camera, is enlarged. This type of long-distance microscope is suitable for measuring particles from 5 to 100 µm.

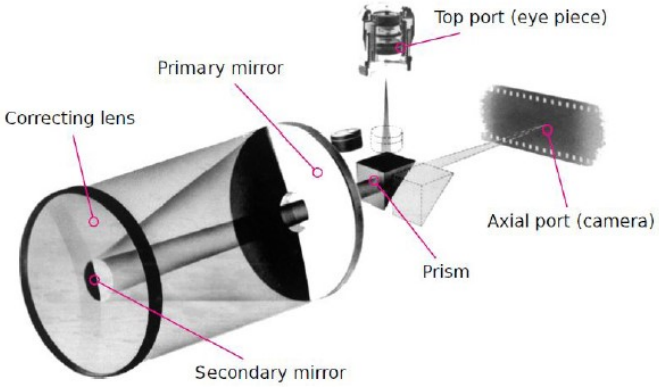

Figure 3.22: Working principle of the long distance microscope [216]

In order to scale the acquired image, the plate presented in Figure 3.23 is used. In this plate, a distance of 5 mm is divided into 200 lines, with the smallest distance between lines being 25 µm. The scaling plate has to be mounted in the

field of view of the long distance microscope and the camera has to be focused on the calibration plate [216].

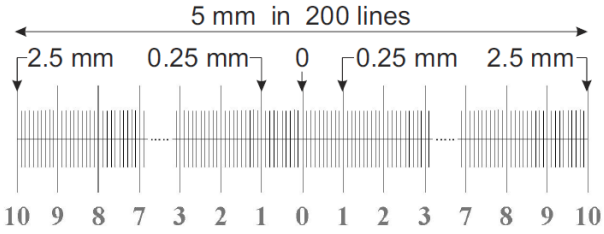

Figure 3.23: Image scaling, convert pixels in distance (mm or µm) [216]

3.5.2 Image preprocessing-Particle detection

The objective of image preprocessing is to normalize the brightness (intensity) of the image. Depending on the illumination intensity, images may have a different overall intensity and variable local intensity. Particles located far outside the focal plane remain as diffuse shadows on the image, and the image's brightness is locally changed. The so-called normalization process is to level out the entire image's local intensity to a reference value of 100%. The latter is achieved by applying a strict sliding maximum, which expresses the search radius in pixels, and according to this value, the software automatically creates a reference image (see Figure 3.24). The local intensity of the actual raw image is then divided by the reference one's respective intensity, leading to a new locally normalized image, which can be further processed.

In Figure 3.24, the effect of different normalization radius settings is depicted. If the raw image is normalized with a single value of the total intensity (red curve), the various local intensities are not easily distinguished, and the diffuse

particles are not resolved. It is apparent, especially when small diffuse structures are near big particles, where the low intensity of this region would be identified as a large structure, which adds an error in the prediction of spray characteristics. The reduction of the normalization radius (blue and green curves) enhances the small-scale features' intensity.

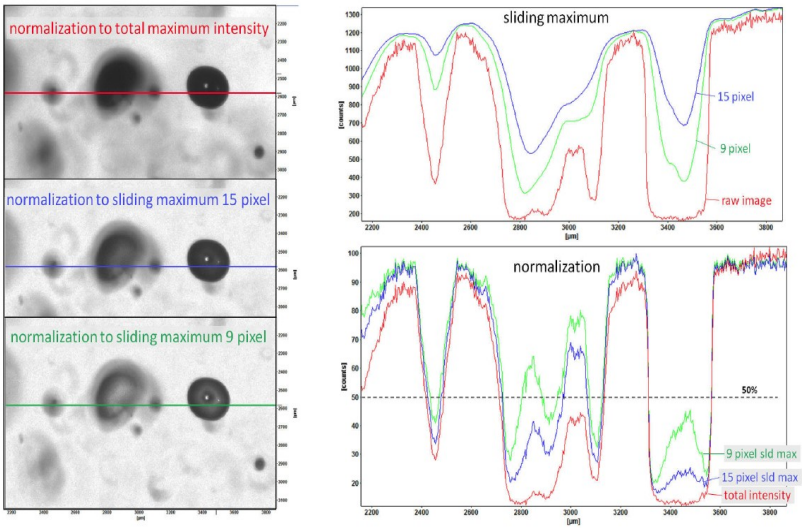

Figure 3.24: Normalization with sliding maximum [216]

As mentioned afore, after the normalization process, each image contains bright regions (i.e., 100% relative intensity) and dark regions (i.e., 0% relative intensity). The so-called binarization threshold determines the percentage of relative intensity, which separates black and white. Moreover, two additional parameters are defined prior to the post-processing through the ParticleMaster software [216]. The minimum shadow area, accounting for any potential noise in the signal, determines a minimum area in pixels considered a droplet. The

second parameter restricts the droplet image to a certain sharpness of the shadow. As shown in Figure 3.25, the gradient of the gray values of the droplet's contours is used as a validation criterion, while a minimum slope should be set. The better the droplet's focus, the higher the detected slope.

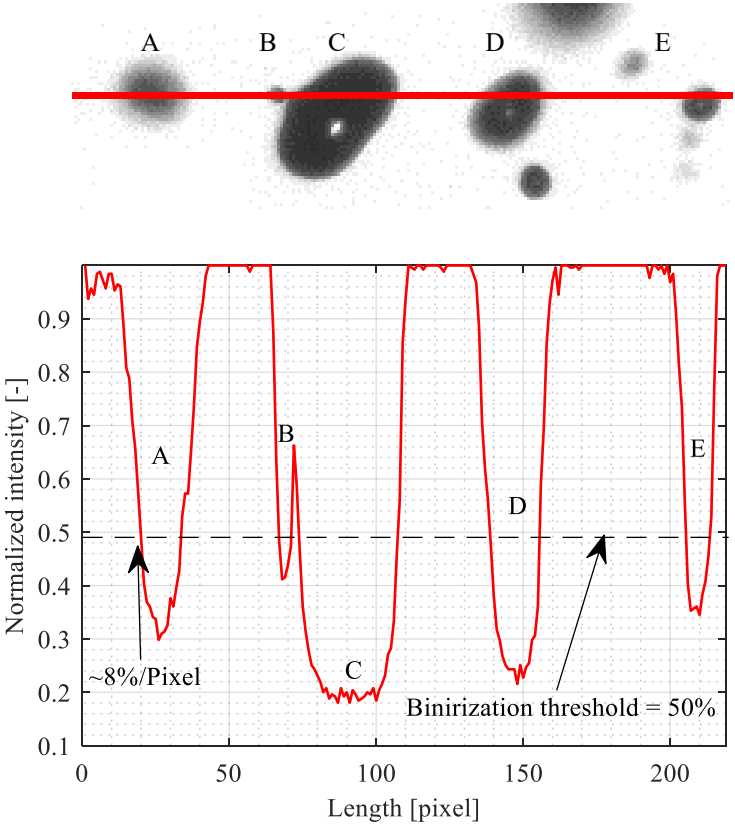

Figure 3.25: Intensity slope at the particle rim, extracted by experimental data

For a given set of the parameters mentioned above, the calculation of the droplet diameter is feasible. As shown in Figure 3.26, the particle area (red area) is defined as the area surrounded by the already detected particle rim (blue curve). Moreover, for the final calculation, an equivalent diameter is introduced, defined as a spherical droplet area, equal to the particle area detected by the software.

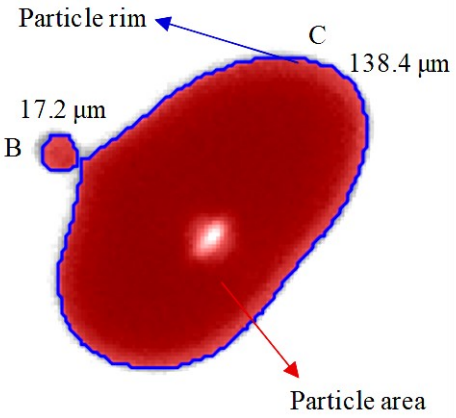

Figure 3.26: Measurement of the droplet diameter

Furthermore, by fitting an ellipse to the particle area, the software, as shown in Figure 3.27 with yellow color, is capable of detecting the long and the short axis of the non-spherical particles and their corresponding excentricity. Finally, the coordinates of the centroid are detected, and all these parameters, together with the droplet velocity information (see Section 3.5.4), the orientation of the long axis, the statistical weight (see Section 3.5.3), are stored in the so-called Particle list, whose post-processing will be extensively discussed in Section.

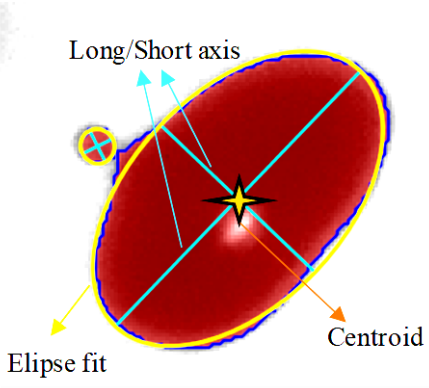

Figure 3.27: Complete droplet identification

3.5.3 Statistical weight correction

There is a particular bias of the shadowgraphy system related to the particle size, affecting the obtained statistical information, such as the mean diameters. The ParticelMaster software, to prevent errors in each particle's statistical contribution to all particles' ensemble, treats this bias carefully. Without the statistical weight correction, the software tends to detect larger droplet more frequently, regardless of the number density (particles/m^3). The software introduces two compensation corrections to achieve a size-independent measurement. The border effect, where larger droplets intersect the image's border more frequently, leading to the reduction of their effective area of detection and, subsequently, their probability to be detected, as shown in Figure 3.28. The statistical weight to compensate for the border effect, assuming spherical droplets, may be written as follows:

$$sw_{br} = \frac{w \cdot h}{(w-d)(h-d)} \tag{3.7}$$

where w and h represent the interrogation window's width and height, respectively, and d is the droplet diameter. This value is inversely proportional to the probability of detecting a droplet, biased by the border, and it is always greater than 100% and increases with increased droplet diameter.

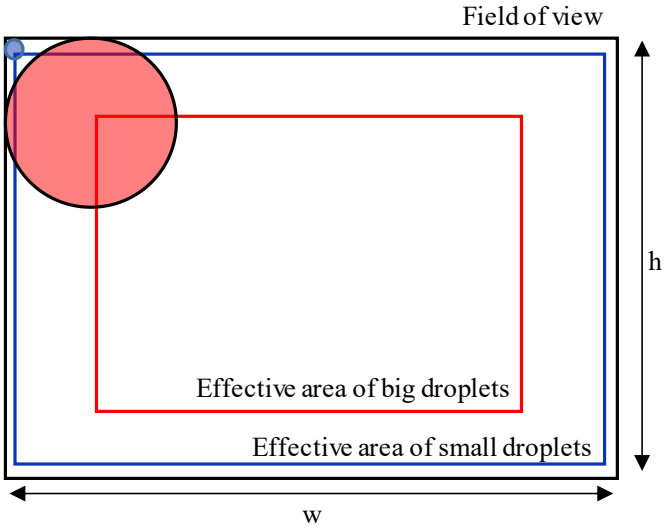

Figure 3.28: Border correction related to the effective area of detection, [216] modified

The second correction is related to the deeper sample of volume that a large droplet is detected compared to the small structures. Therefore, the detection probability of a large droplet increases, and the statistical weight based on the Depth of Field (DOF) is employed. As shown in Figure 3.29, initially, without the DOF correction, the depth of the detection volume is proportional to the

droplet diameter. This statistical weight related to the depth of field is expressed relative to reference particle size $d_{ref} = 100\,\mu m$, and is calculated according to the following equation:

$$sw_{DOF} = \frac{d_{ref}}{d} \tag{3.8}$$

In Figure 3.29, an example of a DOF statistical weight correction is illustrated. More specifically, a uniform distribution of two different particle size classes is depicted. Without the DOF correction, the number of detected large droplets is greater than the counted small droplets, which favors of a size-dependent measurement. By applying the correction, the small droplets are counted twice (i.e., $sw_{DOF} = 2$), whereas only half of the large droplets are counted (i.e., $sw_{DOF} = 0.5$), and thus the statistical biased towards large droplets is compensated.

The total statistical weight is then calculated as the statistical weight product based on border correction and the statistical weight based on the depth of field. Both corrections represent the reciprocal of droplet probability detection in the corresponding case and may be written as follows:

$$sw = sw_{br} \cdot sw_{DOF} = \frac{1}{P_{br}} \frac{1}{P_{DOF}} \tag{3.9}$$

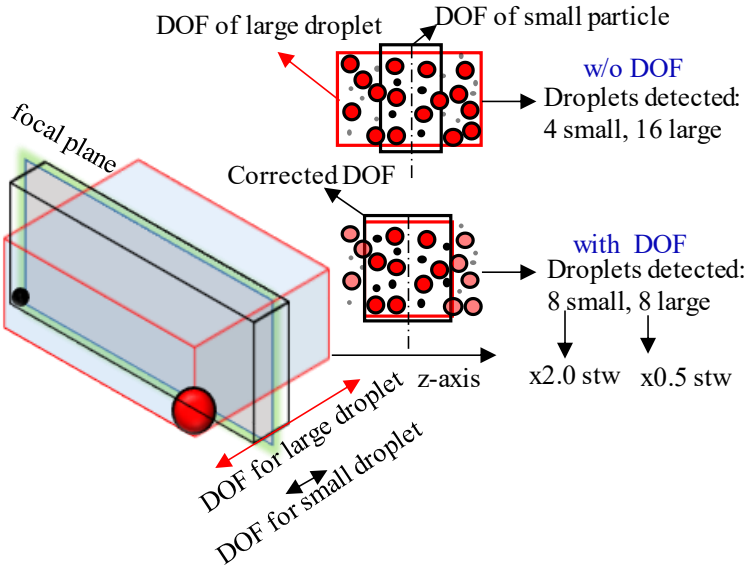

Figure 3.29: DOF for two different particle size together with a statistical weight example [216] modified

3.5.4 Droplet velocity calculation

As mentioned before, the double pulse laser emits two pulses with a known predefined time interval in between them. Therefore, two consecutive frames with a short time difference are acquired, referred to as frames A and B. Thus, the droplet velocity calculation is feasible. The particle algorithm cross-correlates both images with the particle list to identify droplets that should be treated as siblings, whose velocity is calculated by the displacement of their centroid within a known time difference. Two droplets to be considered as siblings

should satisfy several matching parameters, such as the maximum size deviation between droplets in both frames, an estimated velocity vector, and a velocity variation range.

In Figure 3.30, the droplet referred to as 1, with a known droplet centroid, is detected in frame A. Setting an estimated velocity vector in the algorithm, the center of the searching area for sibling droplets in the second frame is transferred in location 2. Three droplets, A, B, and C, have been identified as sibling droplets with this center. The maximum size deviation is employed at this stage, and droplet C is rejected due to the larger size deviation with particle 1. Subsequently, the velocity variation defines the boundaries of the searching area, referred to as 3 in Figure 3.30, where it is evident that the centroid of particle B is out of bounds. Consequently, particle A is the sibling particle of particle 1, and the velocity is calculated from the known displacement of the droplet within a specific time interval. If more than one droplet with an acceptable size deviation is detected within the searching area, the chosen particle will be the one with the minimum size deviation. In this research activity, the estimated velocity vector was chosen to be $(-1:1)u_{ref}$, the velocity range ± 1.25 m/s, and the maximum size deviation of 25%.

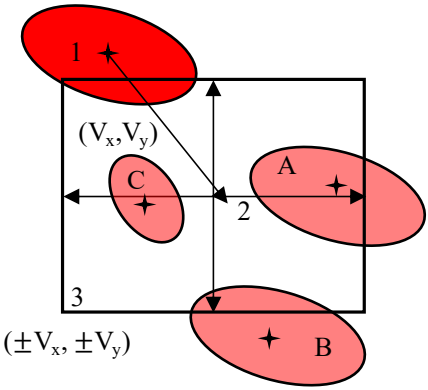

Figure 3.30: Example of velocity computation, [216] modified

3.5.5 Validation of shadowgraphy measurement technique

In most technical applications, the spray is characterized by broad droplet diameter distributions. However, to calibrate all the employed components and validate the measurement technique, a device capable of producing a well-defined monodispersed droplet chain was used. Therefore, the commercial droplet generator of FMP Technology GmbH was employed, whose operation has been thoroughly described in the literature[217,218]. It consists of a single orifice, where a piezo actuator triggered by a frequency generator stimulates the liquid's Rayleigh breakup. As shown in Figure 3.31, the liquid is supplied by a continuously pressurized vessel to prevent any undesirable pressure fluctuation, and a mass flow controller adjusted the water's mass flow rate. Subsequently, the jet velocity was calculated by the continuity equation, and for a known jet velocity and an applied frequency, instabilities of the liquid stream were produced, whose wavelength is calculated according to the following correlation:

$$\lambda = \frac{u}{f} \tag{3.10}$$

where u denotes the jet velocity and f is the frequency of the produced disturbances.

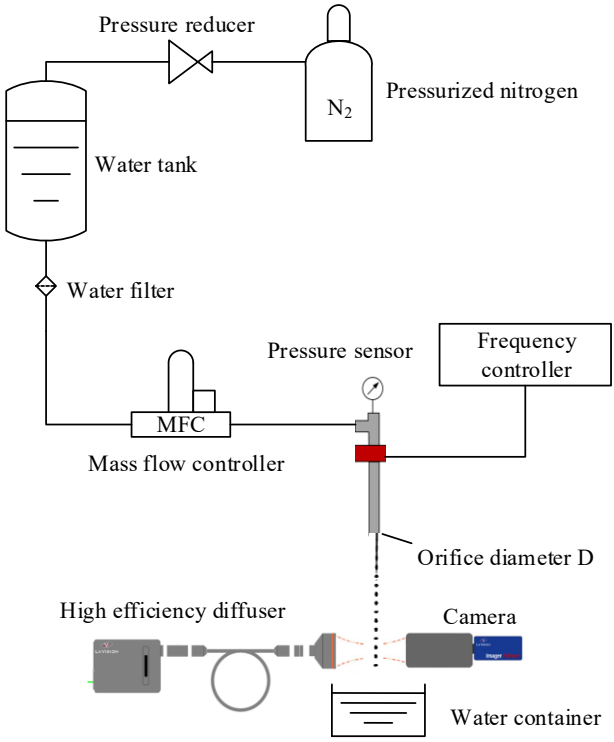

Figure 3.31: Schematic representation of the experimental setup.

If the frequency is not within a specific range (i.e., $\frac{0.3u}{\pi D} < f < \frac{0.9u}{\pi D}$, where D is the orifice's diameter) leads to producing a non-equally sized and spaced droplets, with no clear distribution, as shown in Figure 3.32.

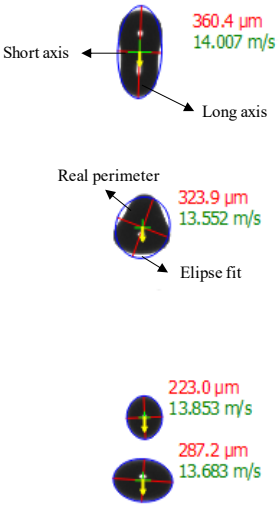

Figure 3.32: Droplet chain with no equal sized and spaced droplets

However, with a careful selection of the disturbances' frequency, the produced droplet chain consists of equally sized and spaced droplets, as shown in Figure 3.33. According to the Rayleigh instability for the jet breakup, the following equation applies [219]:

$$\frac{\pi}{6} D^3 = \pi \left(\frac{d}{2}\right)^2 \lambda \tag{3.11}$$

which implies that the droplet's volume is equal to the volume of a cylindrical jet with radius d (the orifice diameter) and length the wavelength λ. According to Eq. (2.137) and Eq. (3.11), the droplet diameter $D_{R,inv}$ may be written as follows:

$$D_{R,inv} \approx 1.896 \cdot d \tag{3.12}$$

The droplet generator manufacturer stated that the size of the produced droplet formed by an inviscid jet breakup is almost twice the orifice diameter [217,218], so the comparison of the obtained experimental results with Eq. (3.12) should fulfill the requirements for the validation of the measurement technique.

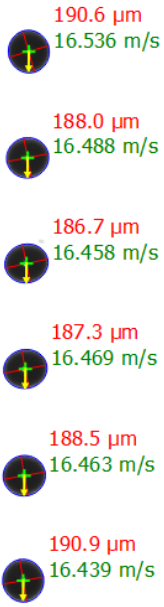

Figure 3.33: Droplet chain with equal sized and spaced droplets, d=100 µm – f=34.250 kHz – m_dot$_w$= 0.418 kg/h

In Table 3.2, the mean diameter D_{10} and the SMD D_{32} measured with the shadowgraphy system are compared with the expected diameter. The similarity between the mean diameter and the SMD indicates that most of the produced droplets were identical.

D_{10} $[\mu m]$	D_{32} $[\mu m]$	$D_{R,inv}$ $[\mu m]$
189.90	190.90	189.60

Table 3.2: Comparison table of the mean diameters

3.5.5.1 Optical access

Due to the nature of the current experimental investigation, i.e., realizing the global operating conditions (low pressure and temperature) and safety protocols (operating with atomized kerosene JET A-1), the combustion chamber was not open into the atmosphere. Moreover, the employed airblast atomizer created a spray with a certain angle, which, combined with the abovementioned geometrical constraints, established one of the fundamental difficulties faced during the experimental campaign. The difficulty pertained to spray impingement on the glass during the measurement. The latter was forming a liquid film on the surface of the window's glass. The shadowgraphy system appeared to be extremely sensitive to this condition as the presence of liquid film or even a low number of droplets on top of the glass's surface promoted light refraction due to the dispersion effect. Therefore, a significant distortion of the image quality was apparent, detrimental to the droplet's proper sizing and characterization. A thorough investigation of the image's quality effect on spray characterization has been reported in the literature [196].

Having decided that the new design's main feature would involve an extension of the combustion chamber, avoiding the spray impingement, at least in the region of interest (primary zone), several design concepts were evaluated. However, two were chosen for manufacturing, while both had their advantages and disadvantages. In Figure 3.34, an overview of concept No.1 is illustrated.

One of the conceptual benefits of this design was the manufacturing of the extension without compromising the combustion chamber's optical access, which enabled measuring in various locations across the combustion chamber. Moreover, employing this concept required the same glasses used for the combustion tests, which reduced the assembly's cost.

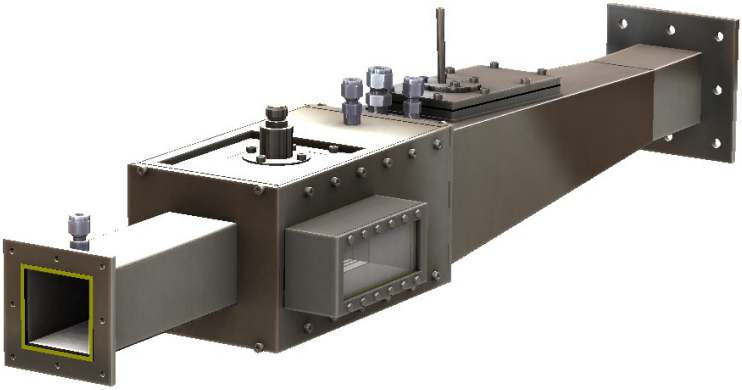

Figure 3.34: CAD overview of the concept design No.1

In Figure 3.35, a cross-section (top view) of design concept No.1 is illustrated. The assembly consists of a frame, used as a dummy, placed in the position previously engaged by the glass, the extension, the glass placed in a new position, and a set of long screws and sealings to connect all the components.

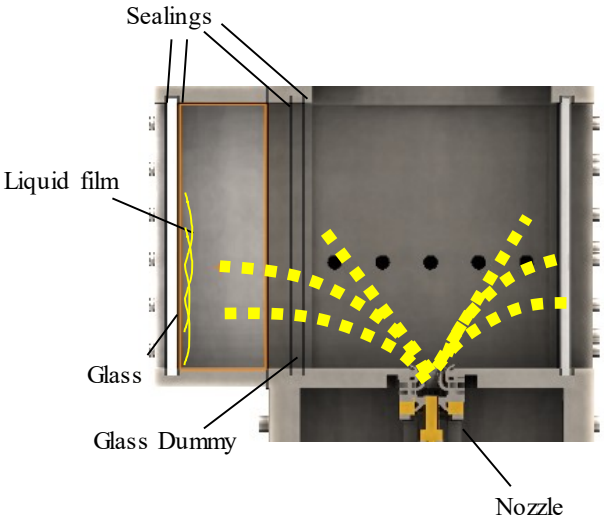

Figure 3.35: Cross section (top view) of the combustion chamber with concept No.1

Testing concept No.1 showed a considerable improvement in the image's quality obtained in the first experiments. Nevertheless, this was not a long-lasting situation. By running a series of experiments, kerosene was accumulating in the chamber's extension, while some of it was inevitably impinging on the glass, albeit there was no direct contact of the spray in the region of interest.

An advanced optical access was developed to prevent spray impingement in the glass (see Figure 3.36). The concept's drawback was the reduction of the optical access, reducing the spatial spray characterization to specific locations.

Figure 3.36: CAD overview of the concept design No.2

As shown in Figure 3.37, the advanced optical access constitutes a cylindrical extension mounted in a metallic adapter placed in the position prior engaged by the glass. It consists of the so-called suction-flush chamber, a set of O-rings, and new glasses with a cylindrical shape. In the suction-flush chamber, a certain amount of air was introduced by the blowing side of a pump (second duct) and directly extracted by the suction side (first duct), building an air barrier and preventing the impingement of the droplets and any liquid fuel accumulation.

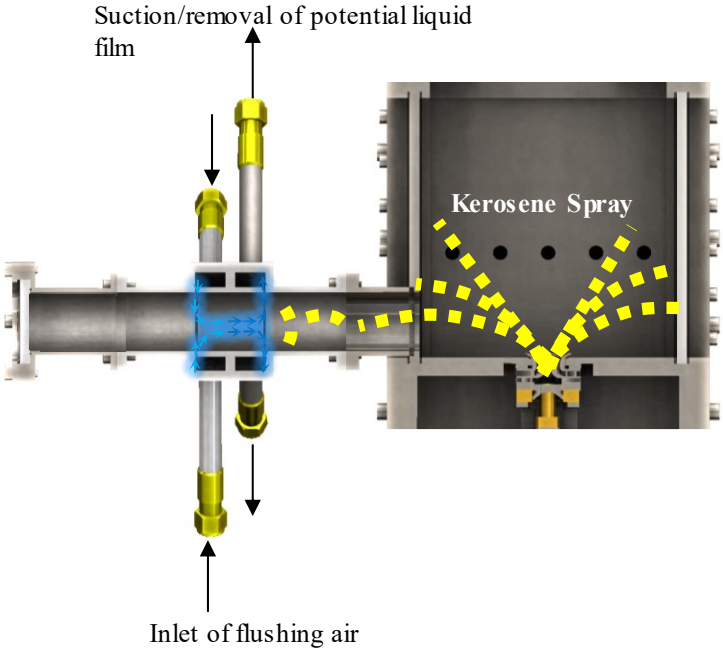

Figure 3.37 Cross section (top view) of the combustion chamber with concept No.2

In Figure 3.38, a simplified overview of the selected measurement locations is illustrated. The nozzle's exit and the spark region were chosen as important locations. The shape of the extension introduced an additional constraint, especially when measuring at the former location. Thus, the measurement area (red color) was shifted $0.019L_{cc}$ in the axial direction to compensate for the inherent reduction of the optical access on the cylinder's edges. Measuring spay characteristics in the igniter (blue color) region requires a second metallic adapter, in which the advanced optical access could be mounted shifted for $0.214L_{cc}$ in the axial direction and $0.086H_{cc}$ in the radial.

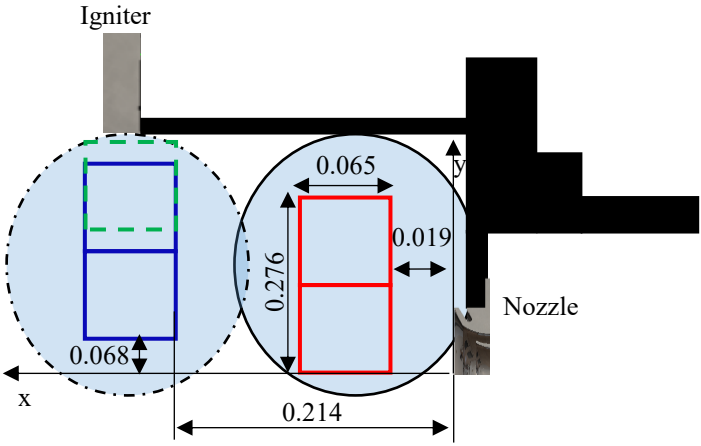

Figure 3.38: Simplified overview of the measurement locations together with the coordinate system – distances in x and y axes normalized with L_{cc} and H_{cc}, respectively

3.5.6 Measurement plan

To the best of the author's knowledge, most experimental investigations regarding spray characteristics of kerosene JET A-1 have been conducted under ambient or high-pressure conditions [220–223]. The effect of high altitude conditions (low temperature and pressure) on atomization's quality has been investigated using water as fuel [224]. This experimental investigation focused on generating a non-existing database concerning a pre-filming airblast atomizer's spray characteristic under high altitude conditions with kerosene JET A-1. More specifically, a thorough, isolated parameter variation, experimental investigation regarding the influence of the global operating conditions (pressure, temperature, ALR) and liquid properties (surface tension, viscosity) has been conducted. Concerning the test matrixes, the following has to be taken into consideration:

- $\mathbf{T_{norm} = T/ T_{ref}}$: T_{ref} corresponds to the ignition test matrix's reference temperature (see Table 3.1).
- $\mathbf{ALR_{norm} = ALR/ ALR_{ref}}$: ALR_{ref} corresponds to the reference ALR of the current experimental investigation (spray characterization).
- $\mathbf{U_{norm,air} = U/ U_{ref}}$: U_{ref} corresponds the current experimental investigation's reference bulk velocity at the exit of the nozzle (spray characterization).
- $\mathbf{(\Delta p/p)_{norm} = (\Delta p/p) / (\Delta p/p)_{ref}}$: where $(\Delta p/p)_{ref}$ corresponds to the reference pressure drop across the nozzle of the ignition test matrix (see Table 3.1).

3.5.6.1 Influence of air velocity

As mentioned before, modern civil aircraft engines employ pre-filming airblast atomizers, whose operation is governed by the momentum's exchange between the air and the liquid stream. Therefore, higher air kinetic energy leads to better atomization quality. After adjusting the thermodynamic conditions (pressure, temperature) within the combustion chamber, and while the effective area of the nozzle has been measured (see Section 3.1.1), the determination of the corresponding mass flow penetrating the combustion chamber is feasible. Subsequently, the air bulk velocity at the exit of the nozzle is derived as follows:

$$U_{air} = \frac{\dot{m}_{air,nzl}}{\rho_{air} A_{eff,nzl}} \tag{3.13}$$

P [bar]	T_{norm} [-]	ALR_{norm} [-]	$U_{norm,air}$ [-]	$(\Delta p/p)_{norm}$ [-]
Influence of Air Velocity				
0.64	1.003	1.00	0.70	0.35
			0.90	0.59
			1.00	0.72
			1.20	1.04
			1.60	1.81

Table 3.3: Measurement matrix - Air velocity influence on SMD, at the exit of the nozzle

3.5.6.2 Influence of global operating conditions

The system's temperature was maintained constant throughout the measurements with kerosene JET-A1. A temperature variation was decided not to be included in the scope of this research activity. With even lower temperatures than the selected, already cold one, technical issues occurred. This temperature was the lowest possible that the compressed nitrogen impinging in the glass could maintain a state without ice accumulation, which substantially reduced the quality of the obtained image. Moreover, the literature has reported that a limited variation is insufficient to detect the temperature's impact on the atomization's quality, albeit a 20 to 40°C difference is imposed [222]. Therefore, this requires extended cooling time intervals in the already long experimental time, affecting the quality of the research activity [196]. Thus, the focus has been given to the influence of pressure, as shown in Table 3.4. By adjusting

the motive fluid pressure (see Section 3.1) on the ejectors, the pressure variation lies in the practical operating range during a relight event, from 0.43 bar to 0.9 bar.

P [bar]	T_{norm} [-]	ALR_{norm} [-]	$U_{norm,air}$ [-]	$(\Delta p/p)_{norm}$ [-]
Influence of Air Pressure				
0.90 0.80 0.64 0.50 0.43	1.003	1.00	1.20	1.04

Table 3.4: Measurement matrix - Air pressure influence on SMD, at the exit of the nozzle

Moreover, to investigate the effect of We=const on SMD, additional measurements have been performed and the obtained experimental results have been compared with predictions of existing correlations. In these measurements, the pressure of the system and subsequently the air density was varying (see Table 3.6), and simultaneously the Weber number (see Eq. (3.14)) was maintained constant by adjusting the air bulk velocity U_{air}. Therefore, the following applies:

$$We^* = \frac{\rho_{air} U_{air}^2 L_c}{\sigma_l} \tag{3.14}$$

where L_c denotes the prefilmer's diameter, U_{air} the air bulk velocity, and σ_l the fuel's surface tension. In this research activity, the properties of kerosene Jet A-1 have been extracted according to Rachner [225] as follows:

$$\rho_l = c_1 + c_2 T + \frac{c_3 T}{c_4 - T} \tag{3.15}$$

$$\sigma_l = c_1 (c_2 - T)^{c_3} \tag{3.16}$$

$$\mu_l = c_1 \rho_l^{1/3} e^{c_2 \rho / T} \tag{3.17}$$

Variable	c_1	c_2	c_3	c_4
Density	1032.27	-0.70767104	-9488.259	733
Surface Tension	1.550388E^{-5}	684.2	1.2222	-
Dynamic Viscosity	2.196E^{-6}	1.555332	-	-

Table 3.5: Jet A-1 properties coefficients [225]

P [bar]	T_{norm} [-]	ALR_{norm} [-]	$U_{norm,air}$ [-]	$(\Delta p/p)_{norm}$ [-]
Influence of We=const				
0.90	1.003	1.00	1.16	0.97
0.64			1.38	1.39
0.43			1.60	2.00

Table 3.6: Measurement matrix – Influence of We=const on SMD

3.5.6.3 Influence of ALR

As shown in Table 3.7, the effect of ALR on spray characteristics has also been investigated. For specified operating conditions, ALR varied by adjusting the amount of fuel injected into the chamber with all the other parameters maintained constant. As illustrated before (see Section 3.1.1), ALR variation was achieved with the needle valves placed before the mass flow meter.

P [bar]	T_{norm} [-]	ALR_{norm} [-]	$U_{norm,air}$ [-]	$(\Delta p/p)_{norm}$ [-]
Influence of ALR				
0.64	1.003	0.50 0.60 1.00 1.50 2.00	1.20	1.04

Table 3.7: Measurement matrix - ALR influence on SMD, at the exit of the nozzle

3.5.6.4 Influence of fluid properties

The fluid's properties effect (surface tension, viscosity) on the atomization process has also been captured. Therefore, in this experimental section, water was used as the atomization liquid. As shown in Table 3.8, a velocity variation has been performed and the results have been compared to the corresponding obtained with Kerosene Jet A-1. For water measurements the selected temperature of the combustion system was increased (i.e., $1.048*T_{ref}$) to prevent any potential icing of the fuel's pipelines.

P [bar]	T_{norm} [-]	ALR_{norm} [-]	$U_{norm,air}$ [-]	$(\Delta p/p)_{norm}$ [-]
Influence of Fluid properties (Water)				
0.64	1.048	1.00	1.00 1.20 1.60	0.69 0.99 1.74

Table 3.8: Measurement matrix - Fluid influence on SMD, at the exit of the nozzle

3.5.6.5 Influence of air velocity - igniter region

As mentioned before, measurements have also been performed close to the igniter location (see Figure 3.38). At this region, the effect of air velocity variation on spray characteristics has been investigated. Subsequently, the obtained results were compared with the corresponding at the nozzle's exit. Moreover, to provide insights regarding the different ignition performance revealed by the two configurations [226] (see Section 5.1 & 5.2), measurements with effusion cooling have been included and compared with the corresponding without effusion cooling close to the liner.

P [bar]	T_{norm} [-]	ALR_{norm} [-]	$U_{norm,air}$ [-]	$(\Delta p/p)_{norm}$ [-]
Influence of Air Velocity				
0.64	1.03	1.00	0.70	0.35
			1.00	0.59
			1.60	1.04

Table 3.9: Measurement matrix - Air velocity influence on SMD, close to the igniter location

3.6 SMD correlations for pre-filming airblast atomizers

Several correlations predicting the SMD of a pre-filming airblast atomizer have been reported in the literature. The majority of them constitute empirical correlations due to the inherent complexity of the atomization processes' relevant phenomena. They express the relationship between the SMD and parameters that appear to have a pronounced contribution to spray characteristics,

such as the gas and liquid properties, the flow conditions, and the airblast atomizer's geometry. The experimental results obtained in this research activity have been compared with the most recent and well-known correlations derived for pre-filming airblast atomizers, though under atmospheric or high-pressure conditions. The first equation has been proposed by Rizkalla and Lefebvre [222], in which the authors derived SMD as a sum of two parameters.

$$SMD = A\left[3.33 \cdot 10^{-3} \frac{\left(\sigma_l \rho_l D_p\right)^{0.5}}{\rho_a U_a} + 0.13A\left(\frac{\mu_l^2}{\sigma_l \rho_l}\right)^{0.425} D_p^{0.575}\right] \quad (3.18)$$

where $A = \left(1 + \frac{1}{ALR}\right)$, and D_p denotes the diameter of the prefilmer. It is evident that the first term of the sum is governed by the fuel's surface tension and the air momentum (Weber number), while the second term by the fuel's viscosity (Ohnesorge number).

The second correlation has been proposed by Jasuja [223], who also employed the light scattering method, derived a similar equation with Eq. (3.18), and tried to decouple the geometry of the atomizer from the prediction of the SMD.

$$SMD = 10^{-3} A\left[\frac{(\sigma_l \rho_l)^{0.5}}{\rho_a U_a} + 0.06\left(\frac{\mu_l^2}{\sigma_l \rho_a}\right)^{0.425}\right] \quad (3.19)$$

El-Shanawany and Lefebvre [220] derived the following correlation by employing the forward scattering monochromatic light:

$$SMD = D_h A\left[0.33\left(\frac{\sigma_l}{\rho_a {U_a}^2 D_P}\right)^{0.6}\left(\frac{\rho_l}{\rho_a}\right)^{0.1} + 0.068\left(\frac{{\mu_l}^2}{\sigma \rho_l D_p}\right)^{0.5}\right] \quad (3.20)$$

where D_h denotes the double of the annular discharge slot [220].

The already described correlations have been compared with the SMD extracted by the experimental results. The reason lies in evaluating whether the already existing correlations apply under high altitude conditions.

In the experimental procedure, each recording consists of 400 double images, in which depending on the applied post-processing parameters (see Section 3.5.2), the software detects the corresponding droplets and provides the following raw data:

1. X and Y position of each droplet within the measurement area
2. Diameter of each droplet
3. Velocity of each droplet (see Section 3.5.4)
4. Statistical weight for each droplet (see Section 3.5.3)

The dedicated software calculates the SMD according to the following equation [216]:

$$D_{32} = \frac{\sum_{i=1}^{N} D_i^3 sw_i}{\sum_{i=1}^{N} D_i^2 sw_i} \tag{3.21}$$

This correlation accounts for the inherent bias of the system to detect large droplets with higher frequency. However, several issues arise by employing this correlation that does not resolve the produced spray structure. The most prominent features are the assumption of spray uniform dispersion and the nature of the shadowgraphy measurement technique. The former has no relevance to the examined configuration due to the spray's hollow cone structure, which implies high dependence of the SMD on each droplet's radial location. This feature is treated by introducing each droplet's distance r_i relative to the nozzle's middle axis. Therefore, weighting the equation with the radial distance focuses the SMD calculation in locations with higher droplet density, and

hence any potential noise produced by scattered droplets is filtered. The latter lies in the differences that have been reported in the literature [227] when measuring with spatial (shadowgraphy) or temporal (PDA- Phase Doppler Anemometry) measurement techniques. Employing the spatial approach implies that the number of droplets located within the measurement area depends on their residence time, which is inversely proportional to each particle's velocity. Hence, particles with high velocity are underestimated, and this feature is being treated by weighting the SMD correlation with the droplet velocity U_i, as follows:

$$D_{32,r,u} = \frac{\sum_{i=1}^{N} D_i^3 sw_i r_i U_i}{\sum_{i=1}^{N} D_i^2 sw_i r_i U_i} \tag{3.22}$$

A second approach, which takes into account the non-homogeneity of the particle distribution, is derived. It is depicted in Figure 3.39 and involves the following steps:

1. Discretization of the measurement area into N segments with defined length, height, and depth.
2. Calculation of each segement's D_{32} according to Eq. (3.21).
3. Final calculation according to Eq. (3.23).

$$D_{32,r,u} = \frac{\sum_{j=1}^{N} C_j v_j D_{32,j}}{\sum_{j=1}^{N} C_j v_j} = \frac{\sum_{j=1}^{N} n_{d,j} D_{32,j}}{\sum_{j=1}^{N} n_{d,j}} \tag{3.23}$$

where C_j is the droplet density [number of droplet/m^3], v_j is the measurement volume assuming unit depth. Subsequently, $n_{d,j}$ denotes the number of droplets detected in the jth segment.

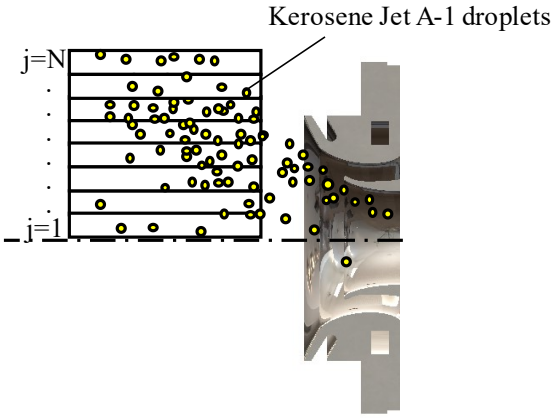

Figure 3.39: Interpretation of the global SMD

3.7 Parametric analysis

As highlighted before (see Section 3.5.2), the post-processing parameters have a pronounced impact on the droplet's identification. A different combination of these parameters (NR-Normalization Radius and SL-minimum Slope) might shift the software's focus to large structures located close to the focal plane when employing small NR (i.e., 15) and a strict minimum slope (i.e., 7%) or vice versa. Subsequently, the SMD and the number of detected droplets might vary substantially, albeit the same operating conditions are imposed. A thorough investigation of identification errors by employing different parameters revealed that it is unfeasible to derive a global optimum combination [196]. In Figure 3.40, a schematic representation of the parametric analysis conducted in this research activity is illustrated.

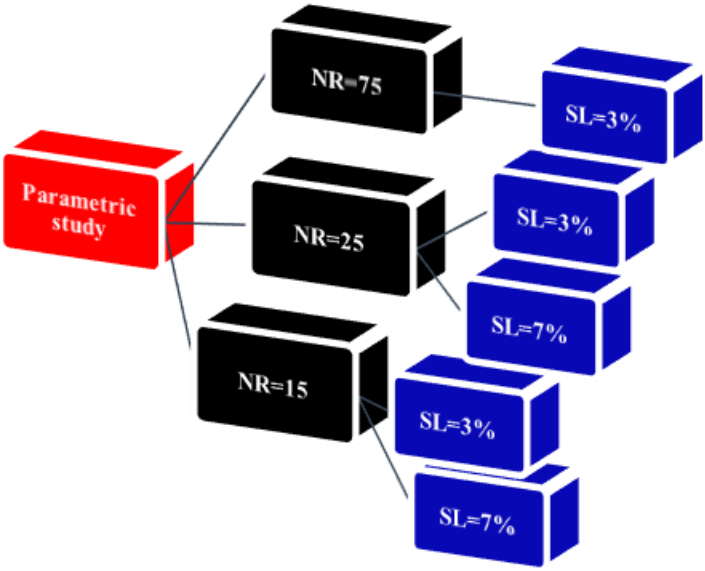

Figure 3.40: Parametric study used for particle identification [196]

Subsequently, the final SMD value for a single trial under specific operating conditions has been derived by averaging each parametric combination's SMD to eliminate the post-processing effect on the final value. Additionally, more than two trials have been carried out in each operating condition, and statistical analysis has been applied to calculate the 95% confidence interval for all the conducted attempts with all the post-processing parameters [228]. The latter may be written as follows:

$$CI_{95} = 1.96 \frac{s_n}{\sqrt{N_{att}}} \tag{3.24}$$

where s_n is the standard deviation of all measurement trials, and N_{att} the number of attempts.

4 Numerical Method

The flow field itself influences the ignition process of a jet engine's combustion chamber. Therefore, the knowledge of the flow pattern within the combustion chamber is of great importance.

CFD (Computational Fluid Dynamics) simulations have been conducted in this research activity, and detailed results have been reported in the literature [229]. Here, only the results that reveal the overview of the generated flow field and the residence time distribution within the combustion chamber, supporting the results obtained during the experimental investigation (see Section 5), are presented.

The CFD simulations were performed with the commercial software ANSYS FLUENT, while RANS (Reynolds-Averaged Navier-Stokes) simulations for different performance conditions have been performed. This numerical investigation aims to reveal the turbulent characteristics and residence time distribution's essential features within the combustion chamber's primary zone.

4.1 Numerical setup

In Figure 4.1, the dedicated model for mesh generation is illustrated. This model represents the extracted, from the CAD model, fluid volume. As mentioned before, the RQL concept is fulfilled with the following steps:

1. The air for the rich primary zone is supplied through the *Inner Nozzle* zone.

2. The *Outer* and *Inner Inlets* consist of a series of holes, acting as a Carnot diffuser, integrated into the combustion system to adjust the liner's desired pressure drop.
3. The secondary air is injected into the combustion chamber through the *igniter cooling holes* and the *dilution hole*s, which exhibit a staggered configuration.
4. The exhaust gases are exiting the combustion chamber through the duct, denoted as the system's *outle*t.

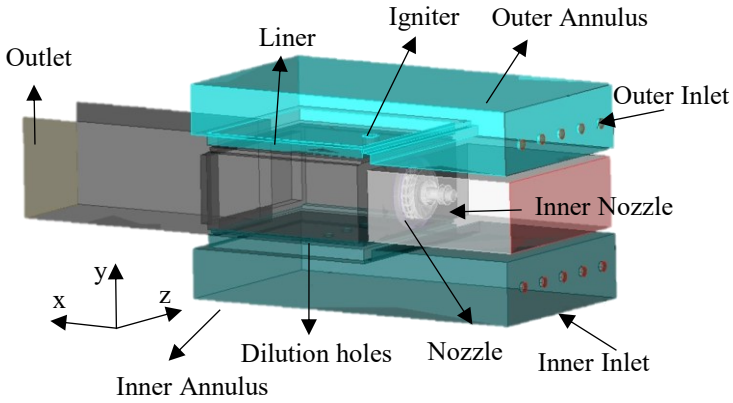

Figure 4.1: Numerical model prepared for the mesh generation

Figure 4.2 depicts the normalized dimensions used to define the locations of interest throughout the CFD simulations. More specifically, L_{cc}, H_{cc} and W_{cc} denote the length, the height, and the width of the main combustion chamber, respectively. The origin of the coordinate system is set in the middle plane at the exit of the nozzle. Furthermore, an adaptive mesh refinement at the regions exhibiting large gradients has been implemented to reduce the simulations' computational cost. The combustion chamber's primary zone constitutes the

first area of interest, which arises from the expected creation of recirculation zones, acting beneficially to the ignition evolution. Moreover, regions with complex geometry and fast-changing properties, such as the swirler, the igniter, and the dilution holes, have been treated with an increased grid density.

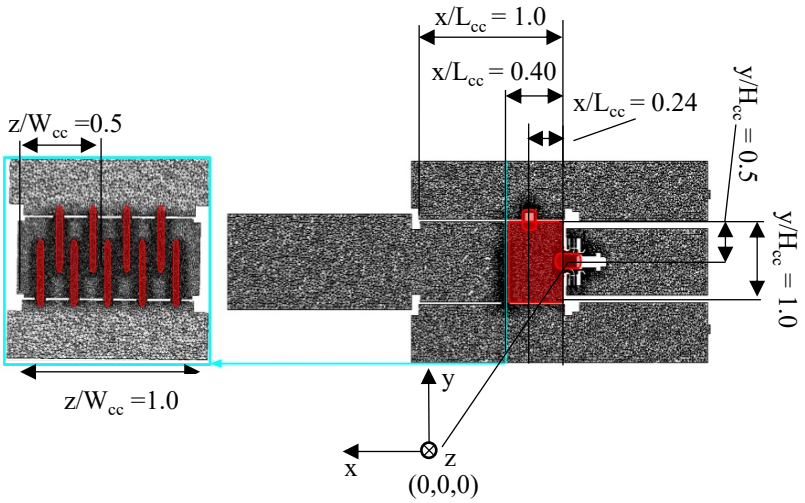

Figure 4.2: Adaptive mesh refinement in the regions of interest – Mesh generation in ICEM CFD

4.2 Generated flow field

In Table 4.1, the high-altitude conditions tested in the CFD simulations are illustrated. The cold case denotes the operating condition, which supports the experimental investigation related to the influence of the igniter's location on the ignition process (see Section 5.4). *Case 1*, *Case 2*, and *Case 3* constitute operating conditions with the same thermodynamic conditions (pressure and temperature), exhibiting different performance data related to the air load. It is

conspicuous that from *Case 3* to *Case 1*, the total amount of air, thus the amount of air passing through the nozzle, increases. The latter exhibits a double effect on the ignition evolution since it improves atomization quality, because of the increase in air velocity (see Section 5.3.1), but it also significantly decreases the residence time in the primary zone. Both parameters have a countereffect on the ignition process. The aim is to reveal which one is dominant under certain imposed operating conditions that have been experimentally investigated in the frame of this research activity (see Section 5.5).

Global Conditions	*Cold case*	*Case 1*	*Case 2*	*Case 3*
p [bar]	0.43	0.64	0.64	0.64
T_{norm}	0.948	1	1	1
$\dot{m}_{tot,norm}$	0.489	1	0.894	0.519
$\dot{m}_{nzl,norm}/\dot{m}_{tot,case\ 1}$	0.138	0.283	0.254	0.146

Table 4.1: High-altitude operating conditions tested in CFD simulations – Normalized values with respect to Case 1

As shown in Figure 4.3, the main features of the generated flow field pertain to the generation of a strong Inner Recirculation (IRZ)) zone. As mentioned before (see Section 2.3.6), the swirled jet undergoes vortex breakdown due to the presence of a positive pressure gradient on the swirler axis, which leads to negative axial velocities around the centerline of the combustion chamber (see Figure 4.4). Moreover, the jet emanating from the swirler is not symmetrical due to its interaction with the igniter's cooling air. Additionally, since the annuli's air velocity is low, the air jet injected in the combustion chamber from the dilution zone exhibits vertical penetration.

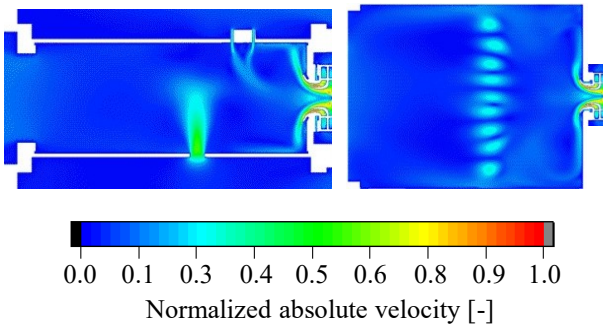

Figure 4.3: Normalized total velocity (Cold Case) – 0.43 bar, 0.948*T_{ref} – left side: y-x planes at z/W_c=0.0 – right side: x-z planed at y/H_c=0.0 – Normalized values over the maximum axial velocity detected under the imposed conditions – flow direction from right to left

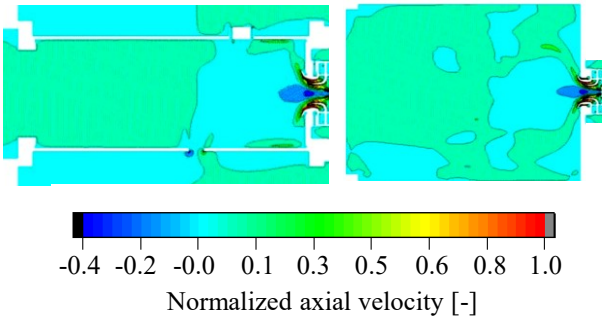

Figure 4.4: Normalized axial velocity (Cold Case) – 0.43 bar, 0.948*T_{ref} – left side: y-x planes at z/W_c=0.0 – right side: x-z planed at y/H_c=0.0 – Normalized values over the maximum axial velocity detected under the imposed conditions – flow direction from right to left

Likewise, in Figure 4.5, the normalized total velocity contour is illustrated. *Case 1* and *Case 2* exhibit a similar flow field, while in *Case 3*, the generated flow field appears to be different.

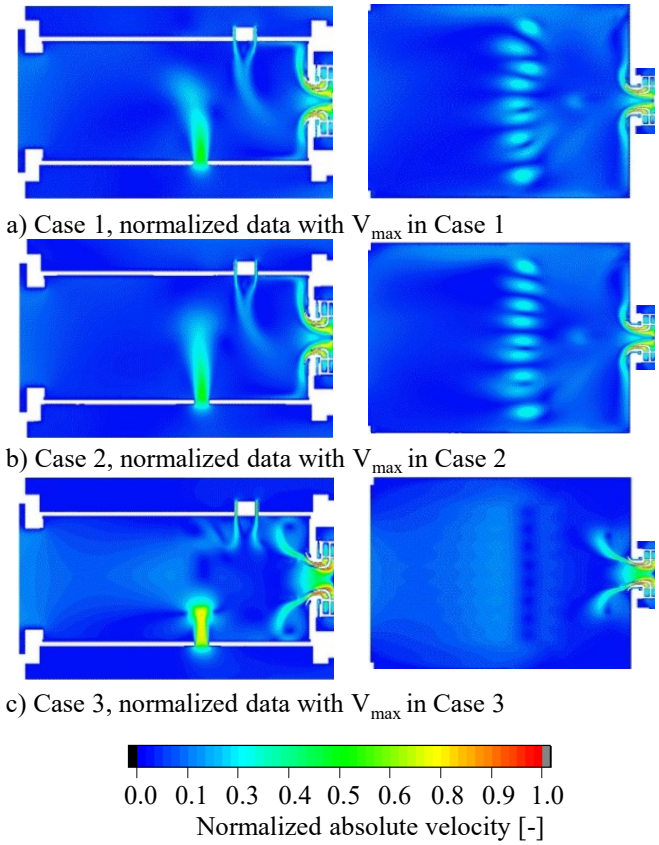

Figure 4.5: Normalized total velocity – 0.64 bar, T_{ref} – left side: y-x planes at z/W_c=0.0 – right side: x-z planed at y/H_c=0.0 – Normalized values over the maximum total velocity detected in each case

In Figure 4.6, a closer look at the normalized axial velocity in the primary zone is depicted. The position and the shape of the IRZ depend on the fluid velocity at the inlet of the swirler. In *Case 1* (see Figure 4.6 (a)) and *Case 2* (see Figure 4.6 (b)), the IRZ has been developed successfully from the outlet of the swirler to downstream in the primary zone. However, in *Case 3* (see Figure 4.6 (c)),

the IRZ is shifted close to x/L_{cc}=0.197. It is evident that with a decreased fluid velocity at the inlet of the swirler, IRZ becomes less intense. The latter was also observed in the work of Blesigner [230], where the Re-number influence on the recirculation intensity was investigated with LES.

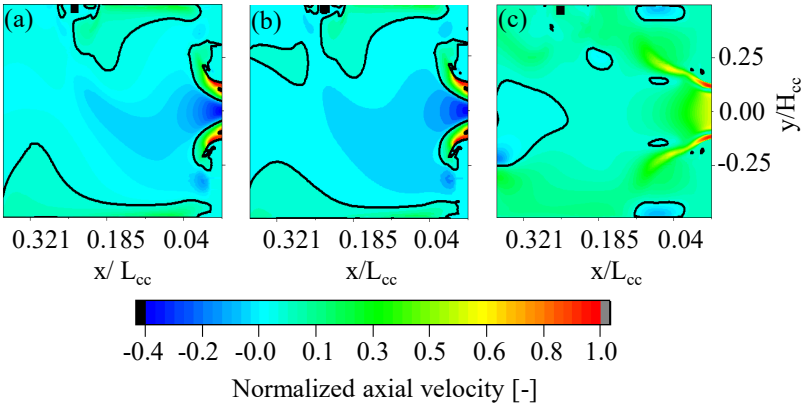

Figure 4.6: Normalized total velocity – 0.64 bar, T_{ref} – y-x planes at z/W_c=0. – a) Case 1, b) Case 2, c) Case 3 – Black rectangular represents the position of the spark plug - Black isoline represents zero axial velocity - Normalized values over the maximum axial velocity detected in each case

4.3 Modeling of residence time

The residence time of the mixture in the primary zone is decisive for the ignition process's evolution. For a successful ignition event, the residence time should exceed the total ignition delay time (physical and chemical, see Section 2.4.2) to ensure that the heat release is sufficient for the chemical reaction to proceed and subsequently to sustain the flame [231].

An estimation of the maximum residence time is given for a perfectly stirred volume as follows:

$$\tau = \frac{V}{\dot{V}} \tag{4.1}$$

where V represents the primary zone's volume, and $\dot{V}$ the air volumetric flow, which penetrates in the primary zone. In the frame of this research activity, two numerical methods have been employed to extract the reactant's mean residence time of in the primary zone, the particle tracking method and the transport equation.

4.3.1 Transport equations

According to the definition of the scalar transport (see Eq. (2.1)) for incompressible flow at steady-state conditions, a calculation of the residence time is feasible and may be written as follows:

$$\frac{\partial}{\partial x_j}\rho\tau u_i = \frac{\partial}{\partial x_j}\Gamma\frac{\partial\tau}{\partial x_j} + \rho \tag{4.2}$$

Further information concerning the solution of Eq. (4.2), such as the UDF (User Defined Function) employed to calculate density ρ as the source term [229], and the boundary conditions [232], have been reported in the literature.

4.3.2 Particle tracking

The model of the discrete particle is applied to identify the trajectories of the fluid particles. In the Langrangian approach, massless particles are introduced that travel along the flow path with the velocity of the flow. The residence time of these particles is determined by the integration of the following equation:

$$\tau_{pt} = \int_0^s \frac{1}{u(s)}ds \tag{4.3}$$

were $u(s)$ is the velocity of the tracking particle along the traveling path-s.

The random walk model (see Figure 4.7) is used to predict the dispersion of particles imposed by the instantaneous turbulent velocity fluctuations. Therefore, the velocity is defined as follows:

$$u = \bar{u} + u' \tag{4.4}$$

The fluctuation component's RMS velocity u' is a function partially constant over a time interval, defined by the characteristic lifetime of the eddy. In the two-equation models, assuming isotropic turbulence, u' is calculated as a function of the local kinetic energy k and a normally distributed random number ζ, which yields:

$$u' = \zeta \sqrt{\frac{2}{3}k} \tag{4.5}$$

The time interval of a particle interaction with a turbulent eddy is evaluated as follows:

$$t_l = 2C_L \frac{k}{\varepsilon} \tag{4.6}$$

where C_L denotes a time constant, whose value for the k-ε turbulence model is set to 0.15. Detailed information have been reported in the literature [229].

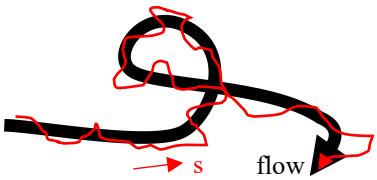

Figure 4.7: Simplified overview of the implemented random walk

5 Results and Discussion

5.1 High altitude relight capability without effusion cooling

5.1.1 High altitude relight probability

According to Section 3.2, the high altitude relight capability of this investigation was carried out initially with a constant fuel mass flow, the same for each operating condition of the test matrix (see Table 3.1).

In Figure 5.1, the height of each bar demonstrates the ignition probability concerning pressure and normalized temperature. An increase in the simulated altitude influences the likelihood of a successful ignition event. Low pressure and temperature conditions hamper several essential mechanisms governing the relight process. Fuel atomization and chemical reaction rate constitute the most prominent and detrimentally affected by high altitude conditions. The general trend indicates a reduction in ignition probability as long as the operating conditions become adverse. The pressure effect is more apparent than the imposed by temperature within the practical operating range of a relight event. The latter is related to the limited substantial relative variations of temperature obtainable.

More specifically, for the first two points in Figure 5.1, the pressure in the ignition chamber is atmospheric, and the measured ignition probability is 100% for both operating conditions despite the relative temperature reduction of 14%. Moreover, the ignition probability decreases from 100% at 1 bar (4

out of 4) to 50% at 0.55-0.53 bar in the lower pressure range. The transition to the lowest pressure range at 0.44-0.43 bar (approximately 20% pressure reduction) leads to a further 25% reduction of the ignition probability.

Despite the limited relative variations, the temperature's effect is apparent within the moderate pressure range of 0.67-0.64 bar. A temperature reduction of approximately 5% decreases the ignition probability by 25%.

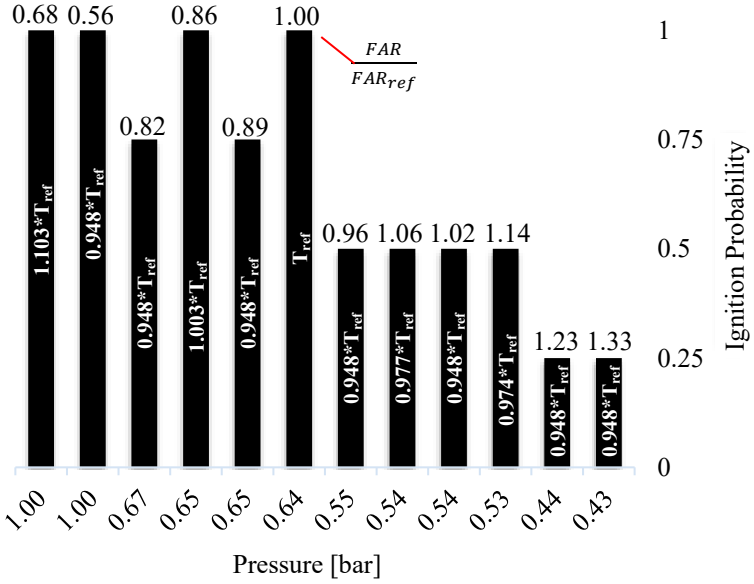

Figure 5.1: Ignition probability with constant fuel mass flow with respect to pressure and normalized temperature [226]

5.1.2 Minimum Fuel to Air Ratio determination

As mentioned afore, the high altitude relight experiments were performed with a constant fuel mass flow. It is also essential to investigate the effect of pressure and temperature on the minimum FAR for a potential successful ignition event.

The fuel quantity has been gradually reduced with a defined step for each operating condition, starting from the constant fuel mass flow of the prior investigation. The minimum FAR was determined using the amount of fuel of the step in which at least one successful event out of four (25% ignition probability) was detected.

In Figure 5.2, the red curve represents the minimum FAR corresponding to 25% ignition probability. The general trend indicates an increase in the minimum FAR with increased altitude. The trend of the minimum FAR confirms earlier studies showing similar behavior. There is a sequence of events explaining the latter behavior. The airblast atomizer performs poorly under low-pressure conditions due to the low air density. The latter leads to large droplets, which, combined with low temperature, significantly reduces the evaporation rate. The variation of the local FAR, formed by the fuel vapor in the spark region, results in a leaner mixture, which is overcome by injecting more fuel relative to the air with increased altitude.

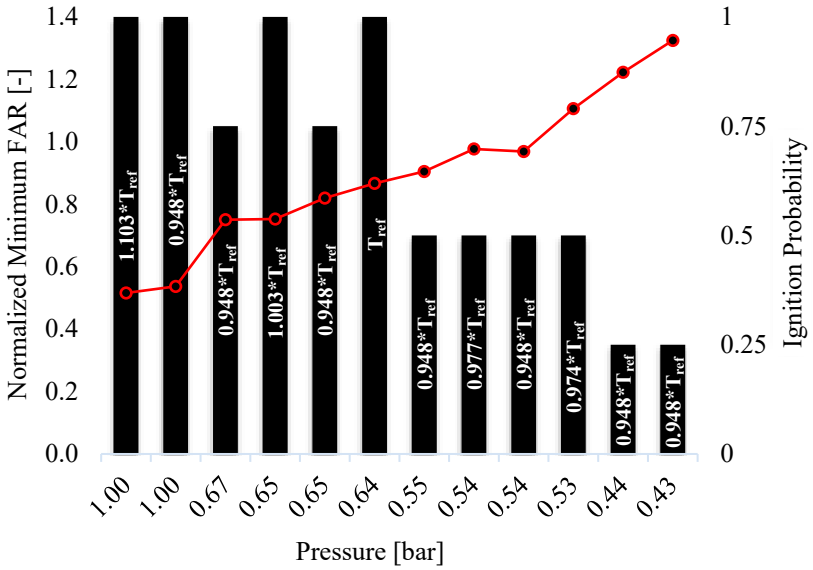

Figure 5.2: Normalized minimum FAR (red curve) with respect to pressure and normalized temperature [226]

5.1.3 Ignition timing measurements

As mentioned in Section 3.3, ignition timing constitutes the time interval between the first spark and the onset of the flame. The effect of the global operating conditions on ignition timing has been investigated. Each equally distributed peak represents an individual spark in Figure 5.3, Figure 5.4, and Figure 5.5. As stated above, the ignition probability decreases as long as the operating conditions become more adverse within the combustion chamber. The latter implies that less successful ignition events were detected within the first 10 seconds, indicating that the ignition timing increases with increased simulated altitude. However, ignition has a rather stochastic nature and depends strongly

on the probability of finding a flammable mixture in the spark region. As shown in Figure 5.4 and Figure 5.5, the ignition timing of a successful ignition event at 0.64 bar was longer than 0.44 bar, albeit this was the only successful event for the latter condition within the first 10 seconds. Moreover, low altitude conditions produced yellow flames (high level of soot emitted) associated with high amplitude voltage captured by the photodiode. In contrast, more bluish flames are generated as long as the simulated altitude increases.

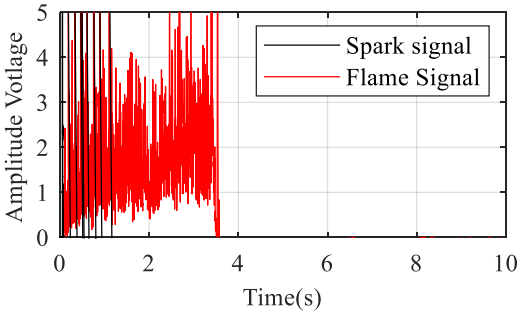

Figure 5.3: Ignition timing – 1 bar and 1.103*T_{ref} [226]

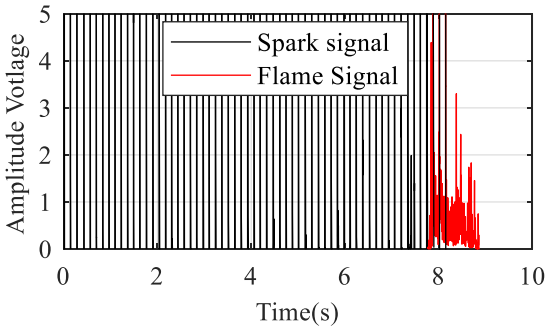

Figure 5.4: Ignition timing – 0.64 bar and T_{ref} [226]

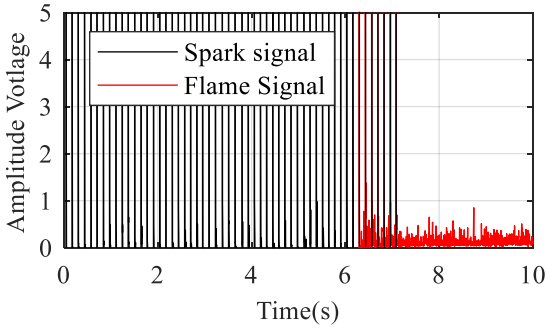

Figure 5.5: Ignition timing – 0.44 bar and 0.948*T_{ref} [226]

5.1.4 High-speed imaging recording

As mentioned in Section 3.4, a high-speed video camera was employed to record the unsteady flame kernel generation and propagation. The camera was arranged perpendicular to the flow direction, providing flame luminosity images at a repetition rate of 1500 Hz. Figure 5.6 illustrates a successful ignition sequence of the reference operating condition, while Figure 5.7 depicts two sparks that led to unsuccessful ignition events.

The progress of the ignition process can be summarized as follows:

- The first frame of the recording at 0 ms shows a bright kernel produced by the plasma emission and propagates upstream towards the nozzle.
- The light emission from the flame kernel decays rapidly, and a weak emission from the kernel persists into the following two frames up to 20 ms.
- A dark period appears in the following 15 ms, which shows no visible evidence of any combustion activity. This ignition delay may contain

the droplet evaporation process or a shift in the emission wavelength beyond the detection range [207].

- At 50 ms, the flame radiation reappears.
- At 68 ms, it moves in the inner recirculation (IRZ) zone.
- Then the flame volume increases and covers the lower part of the chamber at 78 ms.
- Due to the further increase of the flame volume, a stable burning configuration is observed at 159 ms.

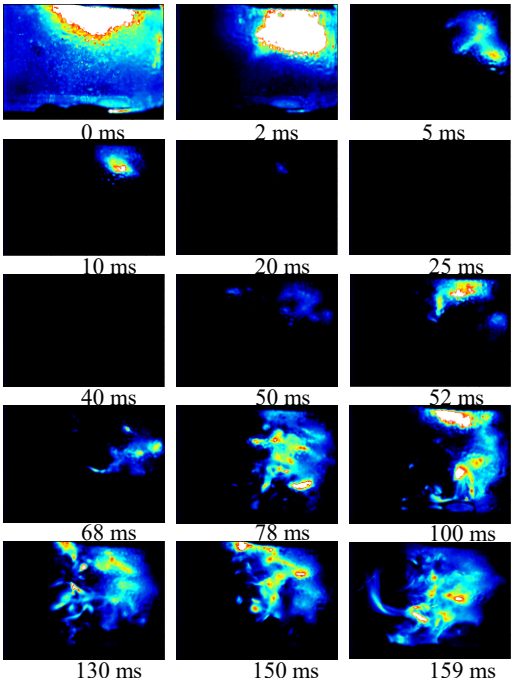

Figure 5.6: Ignition sequence, reference-operating condition at 1500 Hz, flow direction from right to left [226]

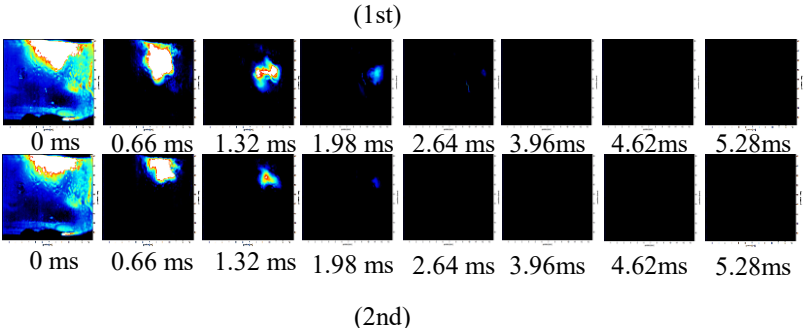

Figure 5.7: Flame kernel generation and propagation of two unsuccessful ignition events at 1500 Hz

5.1.5 Preliminary numerical investigation of the ignition process – comparison with the experimental data

The University of Florence has carried out simulations to support the experimental investigation. The commercial CFD solver CONVERGE [212] has been employed. The mesh is automatically refined in regions required by the efficient implementation of the AMR (Adaptive Mesh Refinement) algorithm [233]. Therefore, the total number of cells varied during the simulation allowing a higher local mesh resolution and reduced computational effort. The numerical domain is depicted in Figure 5.8 (a), where the prescribed mass flow rate and static pressure outlet have been imposed to reproduce the experimental conditions of the reference operating point (0.64 bar – T_{ref}). URANS with k-ε RNG turbulent model has been adopted, and AMR has been triggered based on temperature and velocity field (see Figure 5.8 (b), Figure A. 5 - Appendix A.5).

The standard Langrangian method is employed to track the atomized liquid fuel, and the SAGE direct chemistry solver is used to simulate the combustion and evaporation process. SAGE computes the reaction rates of each species, which subsequently are included as a source term in their transport equation [234]. The employed reaction mechanism has been reported in the literature by the Combustion research group of UC San Diego, involving 49 species and 262 reactions [235], while the spark is mimicked through the energy deposition model.

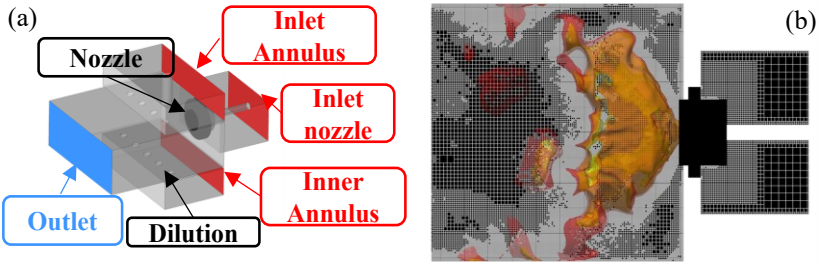

Figure 5.8: (a) numerical domain and (b) section of the combustion chamber with AMR [212]

In Figure 5.9, the evolution of a single ignition event is depicted. The ignition sequence revealed similar behavior to the experimental observation under the same imposed global operating conditions. Initially (see Figure 5.9 (a)), a small amount of fuel vapor rises following the energy deposition. Subsequently (see Figure 5.9 (b), (c), (d)), during the "black period", the fuel evaporation and the first combustion activity are apparent in the region near the walls of the combustion chamber. Moreover (see Figure 5.9 (e)), the evaporated fuel is sucked into the inner recirculation zone in which the second ignition stage occurs (see Figure 5.9 (f)) with the recirculation of the hot combustion products heating

the incoming mixture, which enhances the evaporation rate and therefore the reactivity (see Figure 5.9 (g), (h), (i)). Finally (see Figure 5.9 (j)), the flame development and stabilization conclude the ignition sequence.

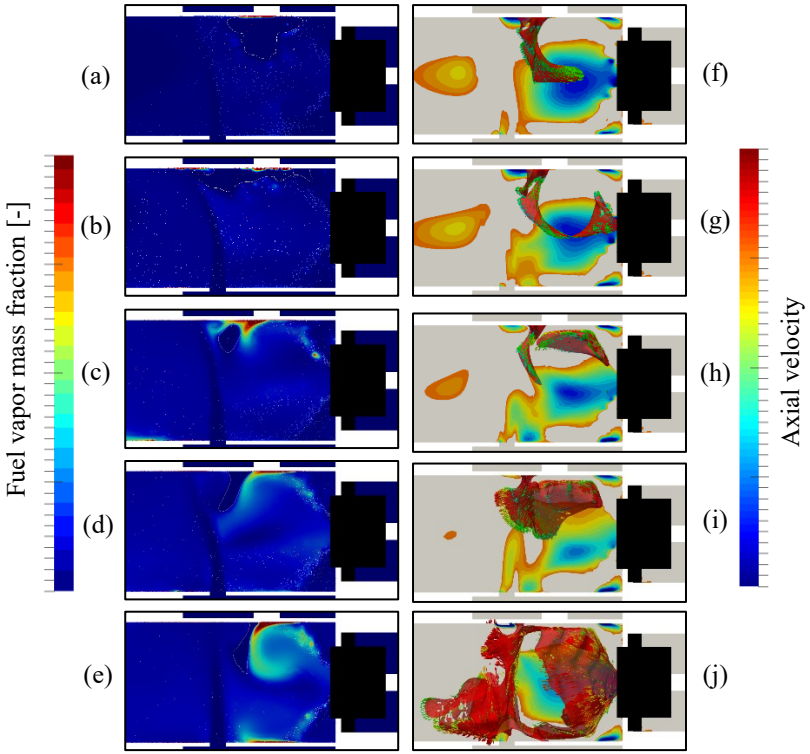

Figure 5.9: Numerical simulation of the flame kernel generation and propagation – 0.64 bar, T_{ref}

Furthermore, a similar minimum FAR has been detected in both experimental and CFD analysis. The experimental minimum FAR was measured 80% of the reference FAR for the reference operating condition. Simulations have been

performed at both 85% and 70% percent of reference FAR, and results indicated that a successful ignition event was identified in the first case, while in the latter, a stable flame could not be established.

5.2 High altitude relight capability with effusion cooling

5.2.1 High altitude relight probability and FAR determination

In the second configuration, effusion cooling is introduced. Detailed information concerning the liner's layout has been mentioned in Section 3.1.1. In Figure 5.10, the high altitude relight capability at fixed fuel mass flow (same as the configuration without effusion cooling) with effusion cooling is illustrated. The different behavior of the ignition probability between both configurations is evident. The ignitability of the configuration with effusion cooling is enhanced, leading to 100% (4 out of 4) successful ignition events. The latter is attributed to the additional air flowing parallel to the liners, creating favorable ignition conditions (see Section 5.3.7).

Moreover, Figure 5.10 depicts the minimum FAR based on the injector's mass flow for 100% ignition probability. Testing of the actual engines requires the latter information. Therefore, this approach has been implemented to increase the technical relevance of the study. However, measurements have also been performed to compare both configurations for 100 % ignition probability without effusion cooling. Similar to the first configuration, the poor performance of the airblast atomizer, with increased altitude, is compensated by creating richer mixtures in the primary zone.

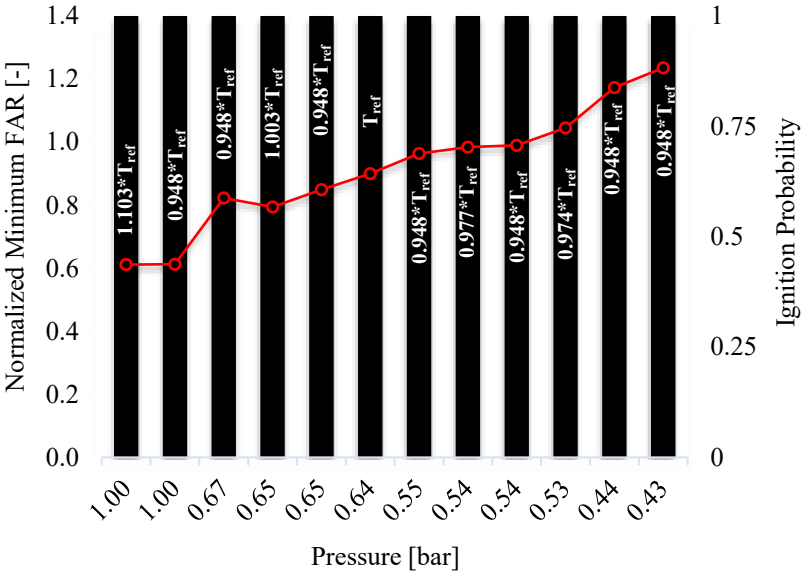

Figure 5.10: Ignition probability with constant fuel mass flow with respect to pressure and normalized temperature – minimum FAR determination (red curve) [226]

5.2.2 Minimum FAR comparison of the two configurations

As mentioned afore, the minimum FAR measurements for 100% probability have been carried out likewise without effusion cooling to achieve comparability between both configurations. In Figure 5.11, the normalized minimum FAR comparison with or without cooling interaction is illustrated. It is clear that even though both configurations exhibit a similar trend, with effusion cooling, the minimum FAR is lower, confirming that the additional air in the region of the spark aids the ignition process. The four operating conditions, shown in Figure 5.11, consist of two sets of pressure and temperature ranges. It is evident that even points with almost the same altitude exhibit a significant

increase in the minimum FAR due to the increased droplet diameter. The empirical correlation proposed by El-Shanawany & Lefebvre (see Eq. (3.20)) was employed to calculate the normalized predicted SMD. The SMD variation explains the significant increase in the minimum FAR among operating conditions with similar performance data.

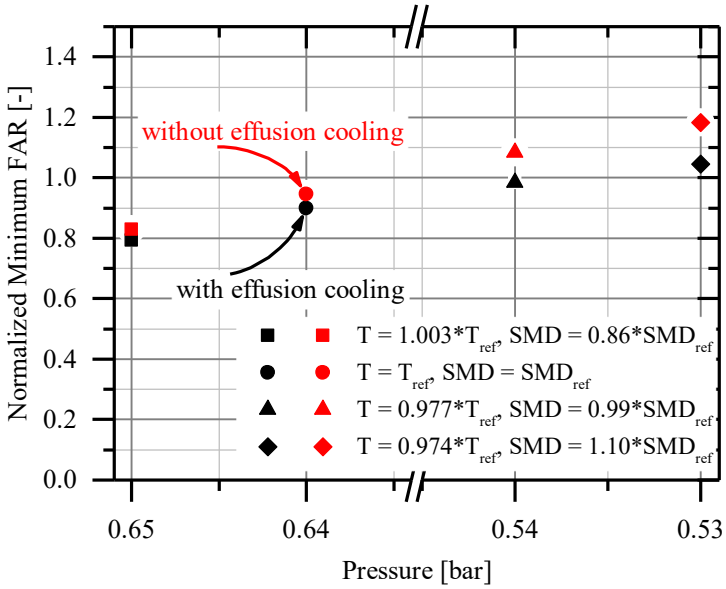

Figure 5.11: Direct comparison of the two configurations with respect to minimum FAR [226]

5.2.3 Ignition timing

Figure 5.12, Figure 5.13, and Figure 5.14 depict the ignition timing of the configuration with effusion cooling. It is conspicuous that, on average, the time

interval between the first spark and the onset of the flame increases with increased altitude, following the same behavior compared to the results of the first configuration (see Section 5.1.3).

The generated favorable conditions significantly reduce ignition timing compared to the previous configuration (see Figure 5.5 and Figure 5.14) under the same operating conditions. The increased ignitability of the second configuration is expressed by the higher ignition probability within 10 seconds, detected throughout the conduct of the second experimental campaign.

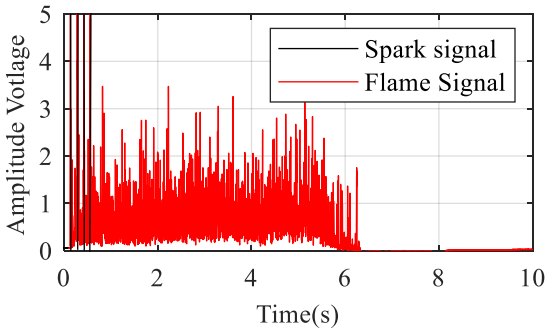

Figure 5.12: Ignition timing – 1 bar and 1.103*T_{ref} [226]

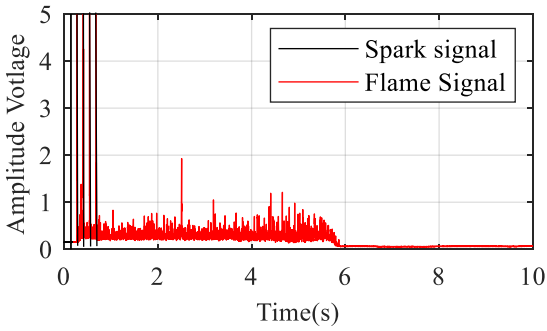

Figure 5.13: Ignition timing at 0.64 bar and T_{ref} [226]

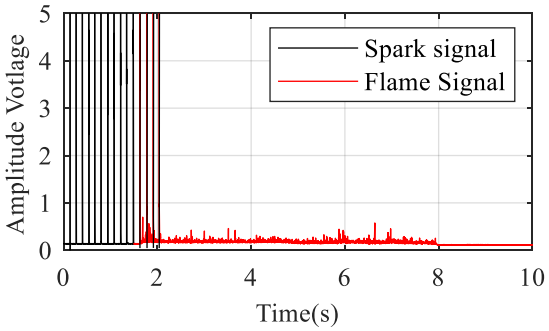

Figure 5.14: Ignition timing at 0.44 bar and 0.948*T_{ref} [226]

5.2.4 Analysis with ALETHO code

The total intensity variation measured by the high-speed camera appraises the combustion activity. A preliminary analysis used these data to characterize the effect of altitude on the ignition timescales and reveal the subsequent behavior of the stabilized flame. The recovery times assigned to individual ignition trials at sea level and high altitude are illustrated in Figure 5.15 and Figure 5.16, respectively. The high-intensity initial signal due to the spark decays to a low level within approximately 10 ms, approaching the black period, also detected in the previous configuration (see Figure 5.6). Subsequently, it grows and develops by emitting low intensity, following the same behavior captured without effusion cooling by flame visualization (see Figure 5.6). The flame recovery represents the period following the spark when the signal rises for the first time to exceed a threshold value of 2×10^4 counts (see red line in Figure 5.15 and Figure 5.16). After evaluating most of the ignition recordings, the self-adaptive threshold has been extracted. A curve fitting was applied to the mean behavior of the raw data acquired experimentally. This threshold corresponds

to the total intensity count of the mean raw data at which the second derivative of the fitted curve is zero, for the first time after the “black-period”; Therefore, it indicates the moment that the flame has recovered and is transitioning to the stable burning configuration (see Figure 5.18). Figure 5.17 depicts the typical behavior of an unsuccessful ignition event. The intensity never exceeds the threshold value during a failure, but it always recovers considerably after having exceeded it during a successful event. By taking into account the individual ignition trial for each operating condition, it is conspicuous that the recovery time increases with increased simulated altitude, as shown in Figure 5.15 and Figure 5.16, respectively.

The latter is attributed to flame kernel propagation rather than flame kernel generation. To validate the assertion above, the MIE of the test matrix’s reference operating condition (see Table 3.1) has been calculated with Eq. (2.123) and compared with the realistic ignition energy of a typical commercial ignition exciter. Therefore, a steady-state, quasi-one-dimensional flame simulation has been conducted by employing the Aachen combustion mechanism [59] (see Section 3.1.2). Hence, the adiabatic flame temperature and the equilibrium composition as a function of the corresponding equivalence ratio of the test matrix’s reference operating condition (0.64 bar, T_{ref} – see Table 3.1) have been computed (see Table 5.1).

Parameter	*Value*	*Comment*
T_{exh} [K]	1077.1	Cantera's equilibrium solver
M_{exh} [kgkmol^{-1}]	21.465	Cantera's equilibrium solver
R_{exh} [Jkg^{-1} k^{-1}]	387.35	R/ M_{exh}
a [m^2 s^{-1}]	2.79e-5	Brutscher [141] (0.64 bar, T_{ref})
S_L [ms^{-1}]	0.0153	(see Figure 3.17 - (0.64 bar, T_{ref}))
p [Nm^{-2}]	0.64e5	Global operating condition
T/Tref [-]	1.00	Global operating condition
C_p [Jkg^{-1} k^{-1}]	1529.9	Cantera's equilibrium solver
FAR/FAR_{ref}	1.00	(see Table 3.1Figure 3.17 - (0.64 bar, T_{ref}))

Table 5.1: Flame simulation parameters employed for the MIE calculation

The calculated MIE is 75mJ, which pertains to the adverse conditions (i.e., low pressure and temperature, extremely rich conditions). It is essential to mention that the same calculation for FAR/FAR_{ref} = 0.6 (i.e., still rich mixture) yields MIE of around 4mJ. The energy delivered into the system of a commercial ignition exciter is in the order of Joules, being significantly higher than the required MIE, even under these adverse conditions. The latter stipulates that the kernel generation is always successfully generated within the scope of this experimental activity, and the ignition process's evolution is not determined by the latter. Furthermore, experimental investigations have shown that the predicted MIE by the models is significantly greater than the corresponding

experimental one [12], suggesting that there is an additional redundancy between the energy delivered into the system and the minimum required one. Therefore, the focus of this experimental activity is the second phase of the ignition process (i.e., flame kernel propagation).

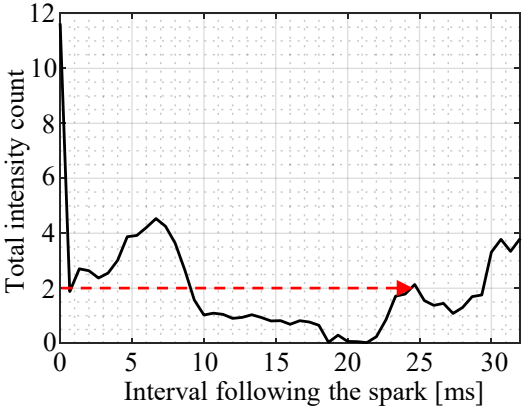

Figure 5.15: Flame recovery at sea level [226]

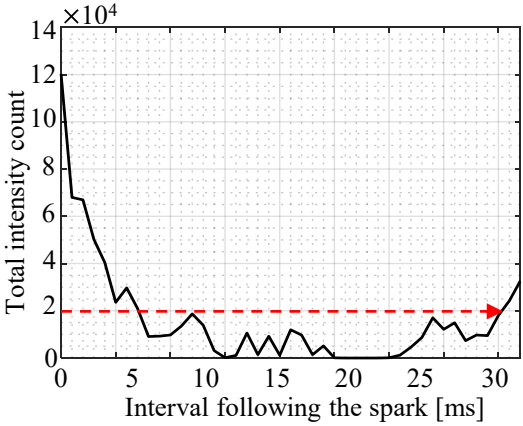

Figure 5.16: Flame recovery at 0.44 bar and 0.948*T_{ref} [226]

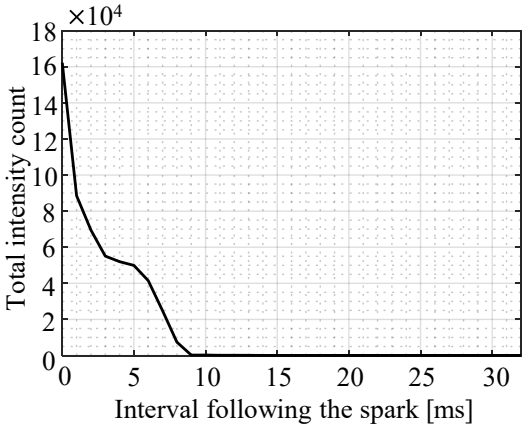

Figure 5.17: Typical behavior of an unsuccessful ignition event [226]

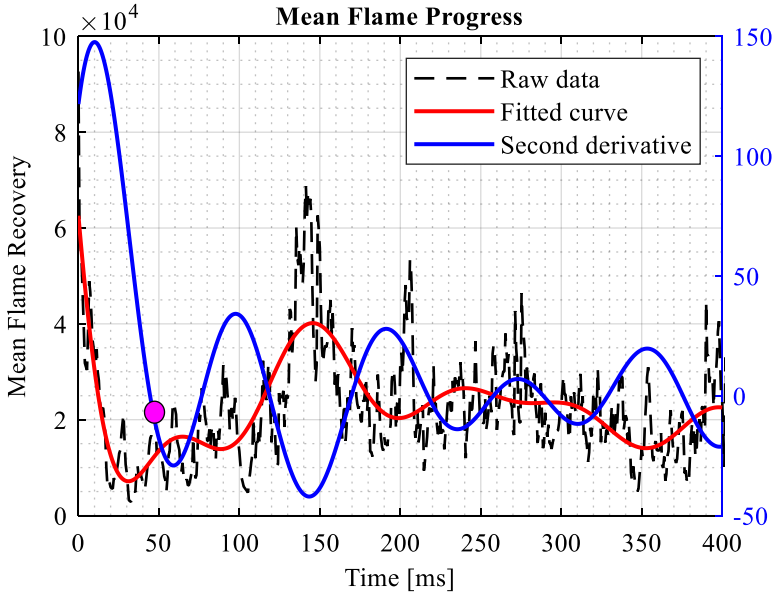

Figure 5.18: Application of the self-adoptive threshold

Furthermore, Figure 5.19 (a) & (b) illustrates the mean flame recovery and the subsequent flame progress out of four ignition trials together with the standard deviation. It is conspicuous that the flame kernel generation and propagation are very stochastic. Due to this randomness, performing four experiments per operating condition provides an indication, but it is an inadequate amount of data to correlate the flame's recovery time with the global operating conditions. Moreover, following the flame recovery, the stabilized flame fluctuates approximately sinusoidal with a peak frequency of 55 Hz (0.44 bar 0.948*T_{ref}) as the FFT of the signal indicates (see Figure A. 2 – Appendix A.3). The latter confirms Read's investigation [14], which states that stabilized flames (under the imposed conditions) demonstrate maximum power spectral densities of less than 60 Hz .

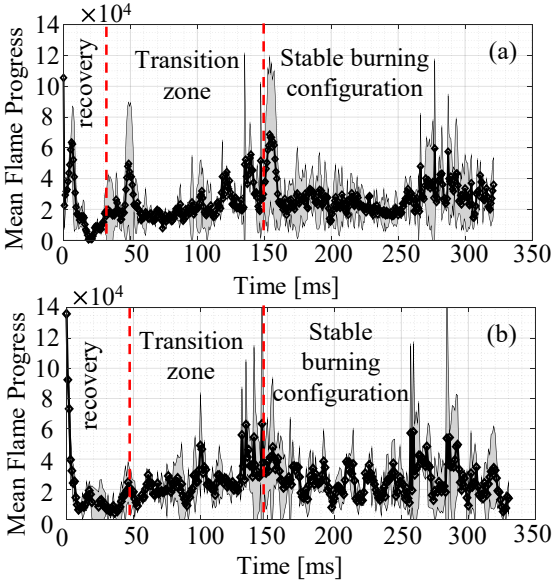

Figure 5.19: Mean flame progress – (a) Sea level – (b) 0.44 bar and 0.948*T_{ref} [226]

In Figure 5.20, the mean (out of 4 ignition trials - reference operating condition) movement of the flame's luminosity center in different periods is illustrated. The boundaries of the graphs represent the interrogation window of the high-speed camera assigned in this configuration. The initial activity, below the igniter, is depicted with the star (see Figure 5.20 (a)). Each subsequent movement is illustrated with red, whereas black represents the movement already established in the previous time scales. The flame kernel travels upstream towards the nozzle exit. Subsequently, it develops substantially in the upper upstream quadrant of the combustion chamber. After the "black-period" (not shown in this figure), the recovery occurs, and the flame propagates in the IRZ, which was also captured by the flame visualization of the configuration without effusion cooling (see Figure 5.6). In Figure 5.21, the average flame trajectory map for the stored recordings is depicted. The plot is color-coded concerning time, starting from dark blue to dark red for 0 ms and 500 ms, respectively. It is conspicuous that following the displacement in the IRZ, the flame spreads and occupies a significant proportion of the combustion chamber. From approximately 150 ms (light blue) until the end of the recording, the luminosity center does not fluctuate substantially. Therefore, the flame has already reached the stable burning configuration. The flame trajectory for both configurations is similar, while the time scale of the flame's evolution is slightly shorter for the case with effusion cooling. The latter is attributed to the reduced residence time resulting from the higher air mass flow employed in the configuration with effusion cooling.

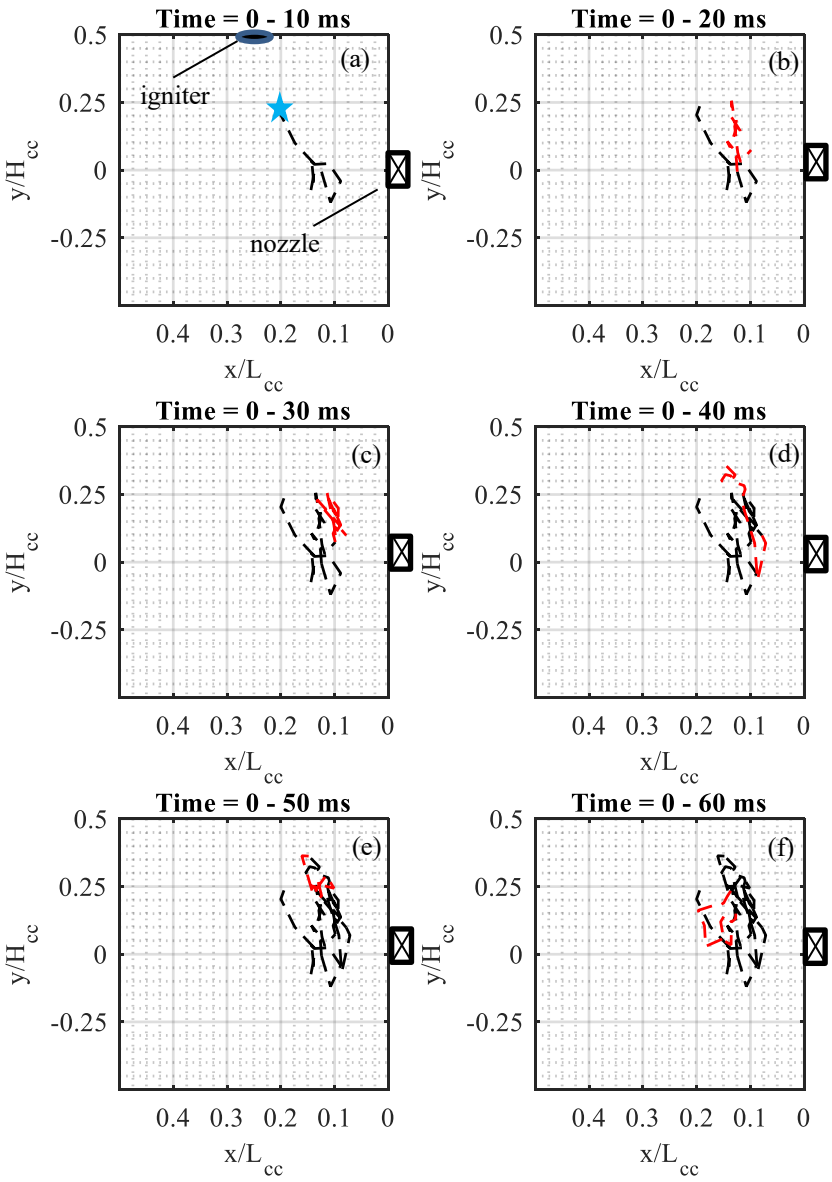

Figure 5.20: Tracking of the flame's luminosity center, flow direction from right to left

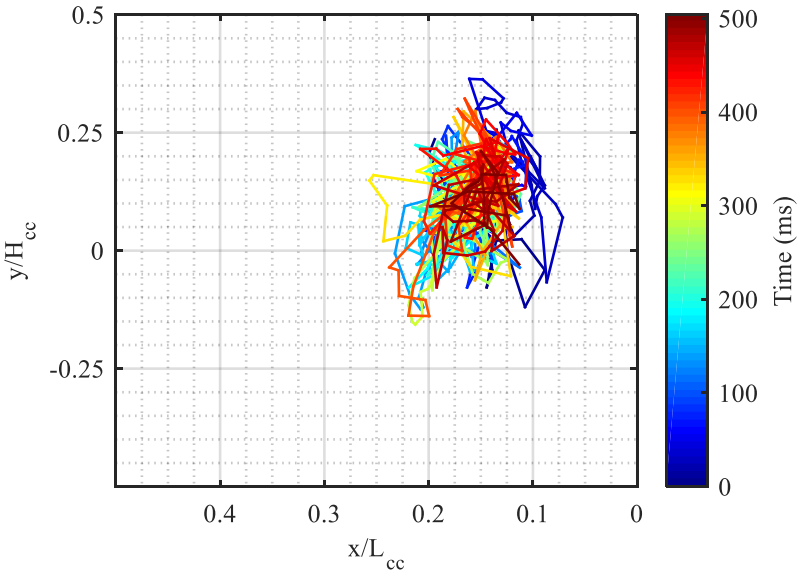

Figure 5.21: Color-coded movement of flame's luminosity center, flow direction from right to left [226]

The axial and the total velocity of the flame kernel are illustrated in Figure 5.22 and Figure 5.23 (according to Section 3.4.1.2), respectively. It is conspicuous that the flame kernel exhibits a strong interaction with the generated flow field. Therefore, the displacement of the flame's luminosity kernel is attributed to convection due to the imposed flow characteristics. The latter confirms the investigation of Read [14], who concluded that the generated cold flow plays a dominant role in predicting the ignition evolution, and its knowledge is more crucial compared to the minimum ignition energy.

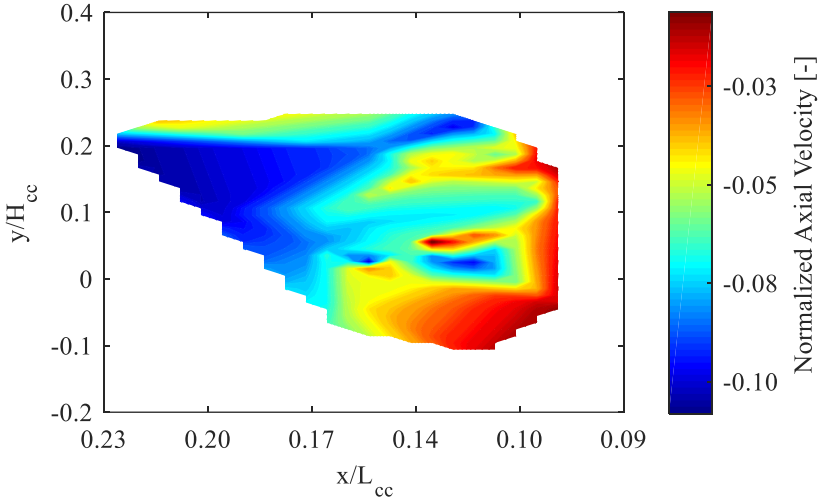

Figure 5.22: Axial velocity of the flame kernel, t = 0-25ms – scaled with maximum axial velocity in CFD

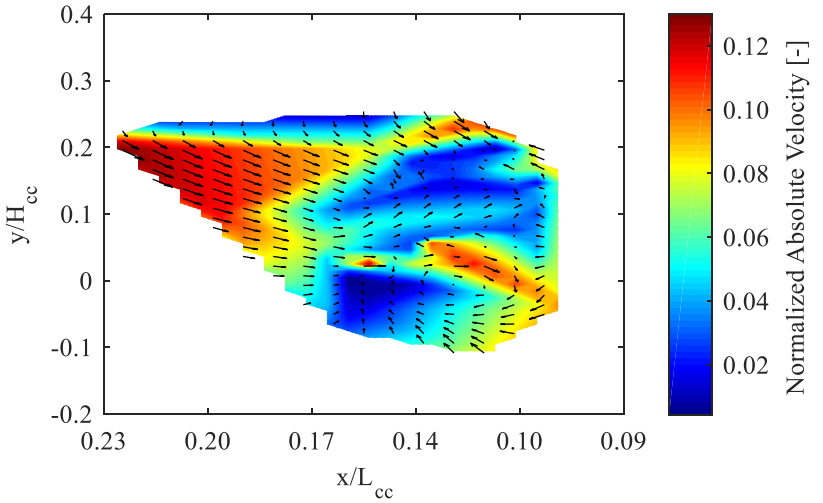

Figure 5.23: Velocity magnitude of the flame kernel, t = 0-25ms – scaled with the maximum velocity of the CFD

5.3 Spray characterization under high altitude conditions

The quality of the atomization appears to be of importance for predicting of the ignition performance. A thorough experimental investigation of the kerosene's Jet-A1 atomization under sub-atmospheric condition have been conducted to enhance and support the understanding/knowledge concerning the high altitude relight of the jet engine. To the best of the author's knowledge, this investigation is unique, and it has shed considerable light on the relevant phenomena governing the high attitude relight capability. Detailed results have been reported in the literature [196], and the most prominent of them are presented in the following sections.

5.3.1 Velocity Influence

In Figure 5.24, the influence of the varying air velocity on the SMD, according to Section 3.5.6.1 - Table 3.3, is illustrated. The results have been normalized by the maximum value detected throughout the conduct of the experimental campaign.

The applicability of the already existing correlations regarding the SMD calculation has not been validated under high-altitude conditions. The generic correlation corresponding to Eq. (3.20) may be written as follows:

$$SMD = D_h(1+FAR)\left[B\left(\frac{\sigma_l}{\rho_a {U_a}^2 D_P}\right)^{0.6}\left(\frac{\rho_l}{\rho_a}\right)^{0.1} + C\left(\frac{{\mu_l}^2}{\sigma\rho_l D_p}\right)^{0.5}\right] \quad (5.1)$$

where B and C are constants directly linked with the film thickness of the liquid on the pre-filmer. According to El-Shanawany and Lefebvre [220], the calibration of these parameters is essential because the film thickness directly affects the atomization quality. The latter parameter determination requires complex experimental set-ups, but it depends highly on the geometry of the nozzle. Therefore, a modified model, denoted as SMD-EBI based on Eq. (3.20), is proposed. This specific model is derived by employing a different B coefficient than the original model suggests. The SMD-EBI correlation exhibits a considerable good agreement with the experimentally obtained data acquired by the analyzed pre-filming airblast atomizer and may be written as follows:

$$SMD = D_h(1+FAR)\left[0.77\left(\frac{\sigma_l}{\rho_a {U_a}^2 D_P}\right)^{0.6}\left(\frac{\rho_l}{\rho_a}\right)^{0.1} + 0.068\left(\frac{{\mu_l}^2}{\sigma\rho_l D_p}\right)^{0.5}\right] \tag{5.2}$$

It is conspicuous that an increase in the air velocity, as expected, leads to the reduction of the normalized SMD. The higher relative velocity between the liquid and the gas phase generates higher shear stresses, better liquid breakup, and smaller droplets. It is essential to mention that the already existing correlations, albeit they did not predict the magnitude, captured the experimental trend, indicating that the physical phenomena governing the atomization process maintain the same under high altitude conditions.

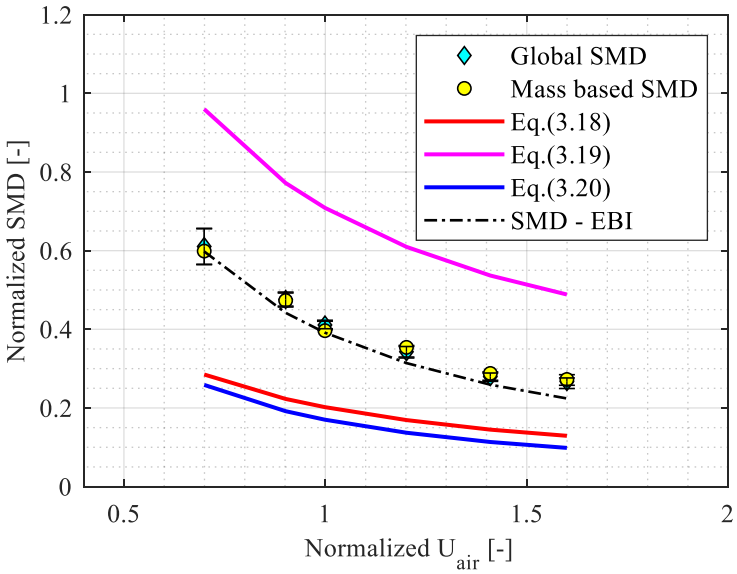

Figure 5.24: Influence of air velocity on SMD, p=0.64 bar – T_{norm} = 1.003 - ALR_{norm}= 1 – Kerosene

The Euler-Euler approach, employed usually for simulations of multiphase flows, was implemented to extract further information concerning the spray properties, such as the spray distribution, the droplet's velocity, and the spay angle [236]. The extracted information appears meaningful and has been used as input in a two-phase simulation (see Section 5.4) revealing the optimum igniter location. Based on this technique, the initial measurement volume is discretized into a finite number of control volumes. Subsequently, the average of properties, such as the absolute and axial velocity, the SMD of the droplets, and the relative mass flux contained within each control volume, is obtained. Therefore, a perspective of the average spray is revealed. However, the average behavior of the spray depends strongly on the grid size selection. The latter

arises because the number of droplets in the control volume alters. Therefore, the actual value being averaged varies. Three different mesh studies have been employed: a fine one whose results are presented in this investigation, an intermediate, and a coarse one whose results have been reported in the literature [196]**.** A qualitative evaluation of the obtained results indicated that the average behavior of the spray is maintained the same. However, as expected, a quantitative difference among the different grids was detected.

In Figure 5.25, the normalized (to the maximum detected value) droplet SMD distributions are illustrated. Results of the minimum (left) and the maximum (right) pressure drop imposed are presented for the sake of interpretation. Except for the previously analyzed lower detected SMD, additional information has been revealed by evaluating the SMD distribution with a higher relative velocity between the liquid and the gas phase. More specifically, larger droplets, apparently emanating directly from the pressure atomizer, are located in the middle plane of the nozzle ($y/H_{cc}=0$). Moreover, to maintain the ALR of both cases constant, the fuel mass flow of the low-pressure drop case (left) decreased, leading to lower pressure in the fuel line, further deteriorating the pressure atomizer's performance. Smaller droplets are contained in the measurement volume that overlaps with the high-velocity near the region of the nozzle's exit.

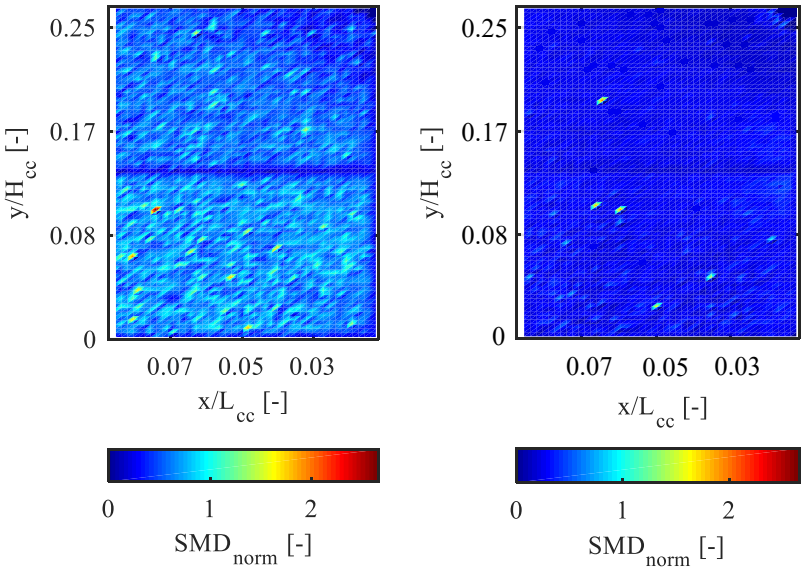

Figure 5.25: Normalized droplet SMD distribution: (left) - $(\Delta p/p)_{norm}$=0.35, (right) - $(\Delta p/p)_{norm}$=1.81 – p=0.64 bar - T_{norm}=1.003, flow direction from right to left

In Figure 5.26, the normalized (to the highest detected) droplet absolute velocity is illustrated. It is conspicuous that higher pressure drops, thus higher velocity at the exit of the nozzle, induce higher droplet velocity. Moreover, the strong interaction of the small droplets with the high-velocity regions is evident. The latter arises from their low Stokes number attributed to the small droplets generated from the atomization lip of the prefilmer. The small droplets follow the streamlines of the primary jet, whereas the larger droplets located close to the middle plane deviate due to their high inertia.

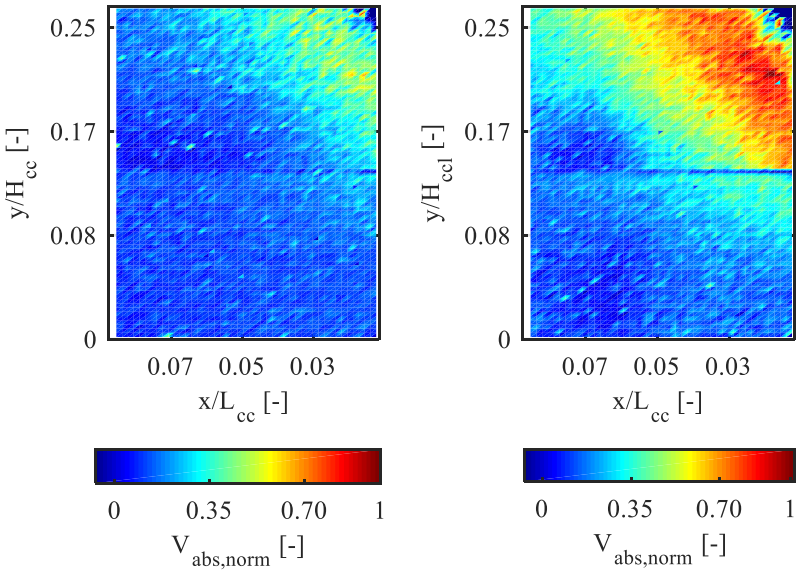

Figure 5.26: Normalized droplet absolute velocity distribution: (left) - $(\Delta p/p)_{norm}$=0.35, (right) - $(\Delta p/p)_{norm}$=1.81 – p=0.64 bar - T_{norm}=1.003, flow direction from right to left

In Figure 5.27, the normalized droplet axial velocity distribution is depicted. Droplets near the nozzle's middle axis exhibit negative axial velocity due to their interaction with the strong inner recirculation zone (IRZ) generated in this region (shown in Section 4.2).

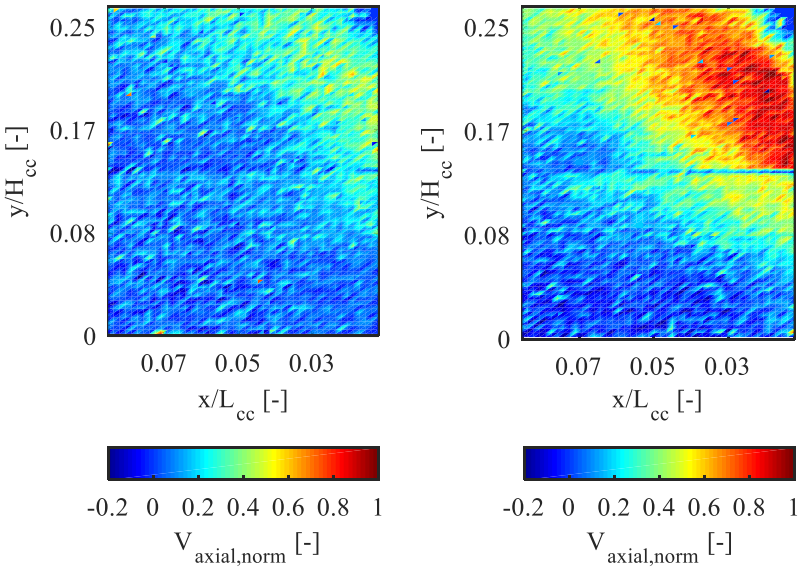

Figure 5.27: Normalized droplet axial velocity distribution: (left) - $(\Delta p/p)_{norm}$=0.35, (right) - $(\Delta p/p)_{norm}$=1.81 – p=0.64 bar - T_{norm}=1.003, flow direction from right to left

Evaluating the local FAR distribution inside the combustor constitutes a piece of essential information related to the combustion process. By employing the Euler-Euler approach, a qualitative distribution of the relative mass-flow across the measurement volume was feasible. The relative mass flow was calculated with the following correlation:

$$M_{rel,k} = \frac{\sum_{i=1}^{m} \rho_i Vol_i u_i}{\sum_{j=1}^{N} \rho_j Vol_j u_j} \tag{5.3}$$

where $M_{rel,k}$ denotes the relative mass flow of the mesh grid k, in which m droplets are contained, and N is the total number of droplets detected in each specific measurement. As shown in Figure 5.28, the highest relative fuel mass

flow was detected around y/H_{cc}=0.17 in both cases, while its maximum is subsequently transported with the main jet stream. This behavior is more evident in the high-pressure drop case (right) than the corresponding low-pressure drop (left) due to the higher droplet velocity relative to the air velocity. In the low-pressure drop case, the relative fuel mass flow is less uniform, caused by the poor performance of the airblast atomizer under the imposed conditions, generating larger droplets that tend to deviate by the streamlines of the carrier.

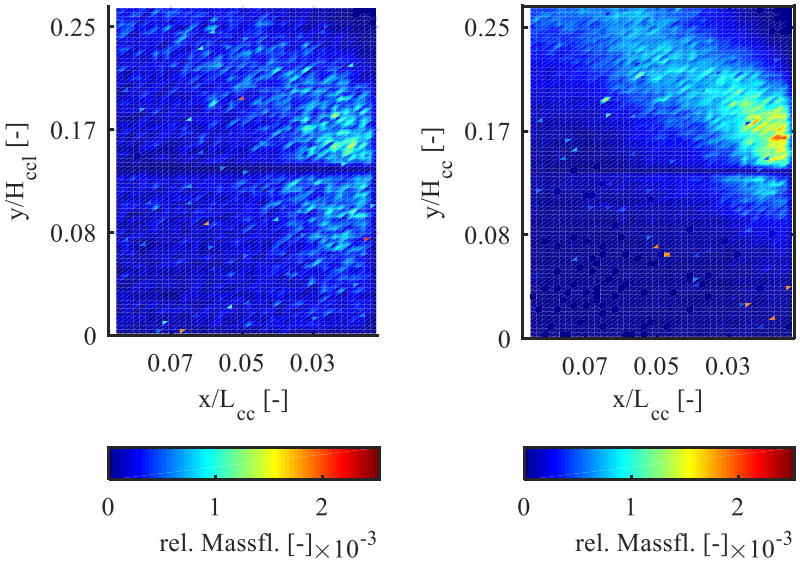

Figure 5.28: Relative mass flow distribution: (left) - $(\Delta p/p)_{norm}$=0.35, (right) - $(\Delta p/p)_{norm}$=1.81 – p=0.64 bar - T_{norm}=1.003, flow direction from right to left

As mentioned before (see Section 2.5.3), calculating the droplet distribution of the generated spray by a correlation constitutes a valuable tool. Usually, experimental investigations are expensive and time-consuming. Thus, correlations expressing essential information, such as the droplet dispersion across the

chamber, are used as input in the numerical simulations. Consequently, in the frame of this research activity, the Rosin-Rammler and the Rosin-Rammler modified performance has been validated by the experimentally obtained data. By employing Eq. (2.142) and Eq. (2.144), a fitting of the distributions obtained for all the values of the parametric analysis (see Section 3.7) has been performed. The parameters q and D_{632} and their 95% confidence interval have been stored for each operating condition. Except for the velocity, the effect of the different parameters governing the atomization process on the obtained mathematical distribution has been thoroughly investigated, and detailed results have been reported in the literature [196] but are irrelevant to the study.

On account of interpretation, only the effect of the velocity variation on the droplet dispersion and D_{632} is presented and shown in Figure 5.29 and Figure 5.30, respectively. An increase in the velocity leads to a D_{632} reduction. The latter indicates that 63.2% of the total liquid volume and the distribution peak have been shifted towards smaller droplets. However, an increase in the velocity decreases the q parameter, which indicates that the distribution becomes less uniform. The latter implies that the velocity exhibits a counter effect to both parameters

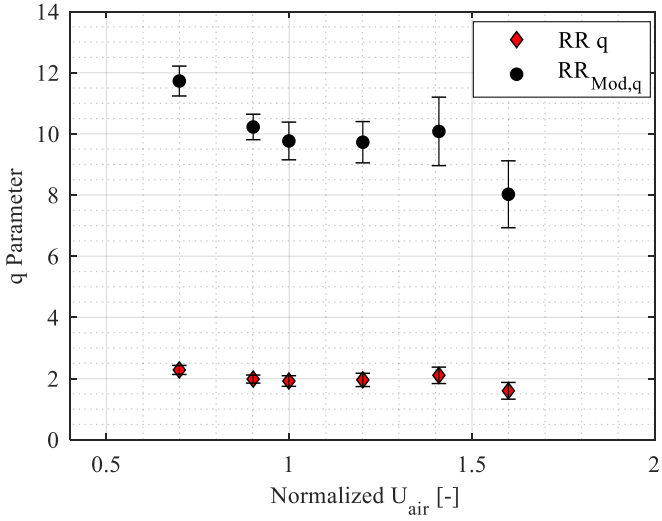

Figure 5.29: Velocity influence on q parameter

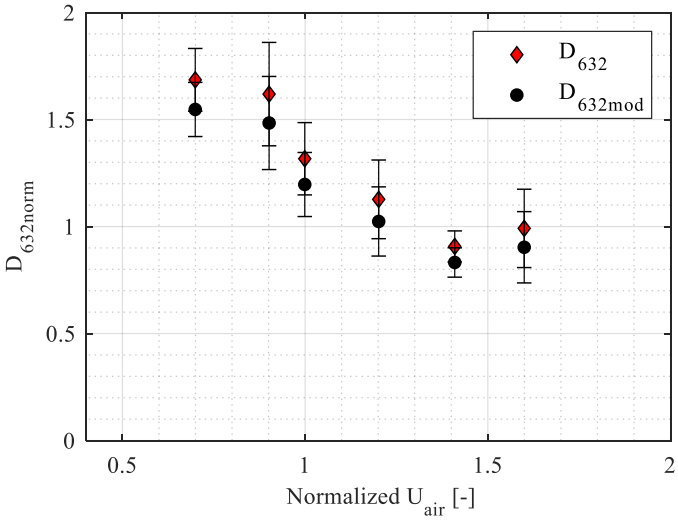

Figure 5.30: Velocity influence on D_{632}

Nevertheless, in Figure 5.31 and Figure 5.32, it is conspicuous that the effect of D_{632} is prominent, and a more uniform distribution is generated in the high-velocity case. The peak distribution, based on Rosin Rammler Mod, was observed at around $1.4 \cdot SMD$ (see Figure 5.32), in which the maximum relative volume fraction is 3.5%. In contrast, in Figure 5.31, the low-velocity case exhibits a peak distribution of 2.9% at around $1.6 \cdot SMD$. However, it is important to mention that the peak distribution depends highly on the droplet interval ΔD (see Section 2.5.3) selection. Additionally, the Rosin-Rammler modified exhibited a better fitting to the measured distributions for all the operating conditions.

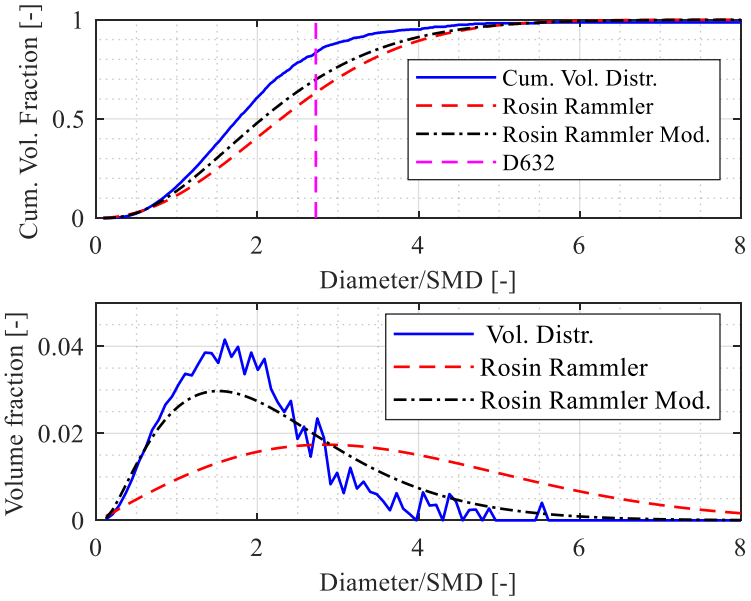

Figure 5.31: Droplet distribution; $(\Delta p/p)_{norm}$=0.35 – p=0.64 bar - T_{norm}=1.003 - D_{632} based on Rosin Rammler Mod.

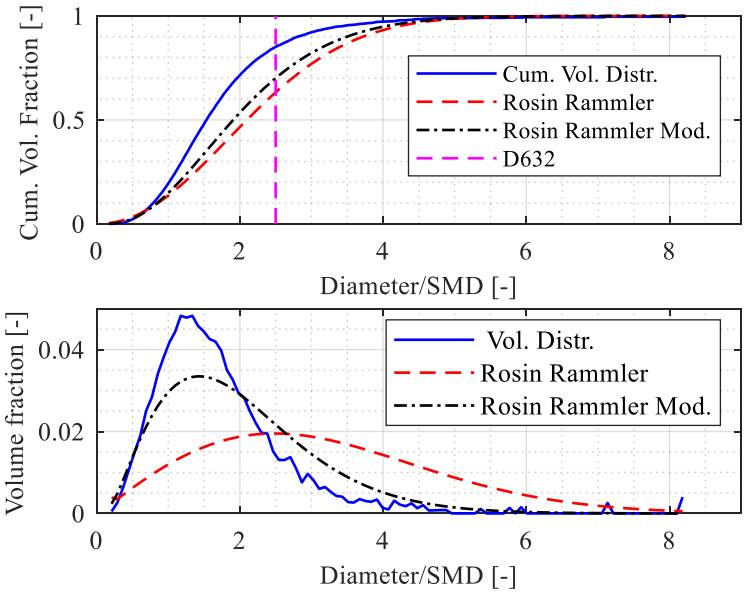

Figure 5.32: Droplet distribution; $(\Delta p/p)_{norm}$=1.81 – p=0.64 bar - T_{norm}=1.003- D_{632} based on Rosin Rammler Mod.

Therefore, the Rosin Rammler Mod. has been selected to model the droplet distribution in the two-phase numerical simulation conducted to support the optimum igniter location investigation (see Section 5.4).

5.3.2 Pressure influence

A variation in the operating pressure (see Table 3.4) affects the system's density, and the subsequent effect on atomization quality has been investigated. In Figure 5.33, it is evident that an increase in the system's pressure decreases the SMD. The breakup process is directly affected by the shear forces, which are proportional to the air density. Therefore, reducing the operating pressure hampers the atomization process and vice versa.

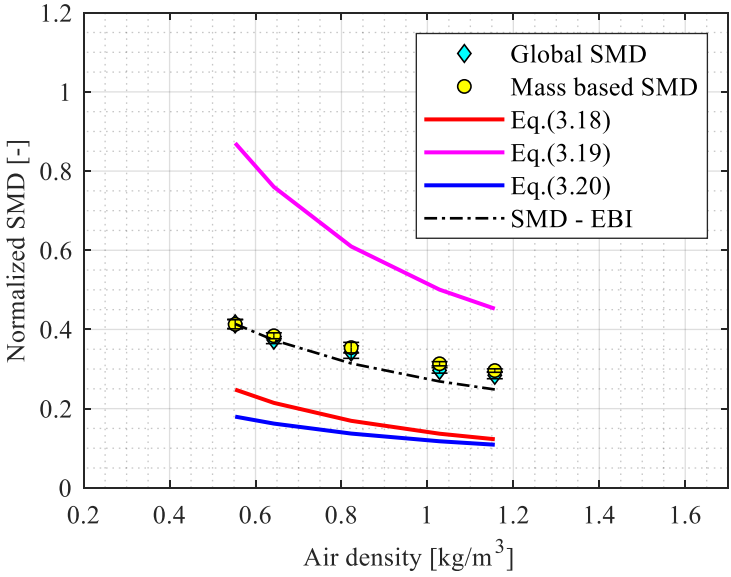

Figure 5.33: Influence of air pressure on SMD, Δp_{norm}=0.96 – T_{norm} = 1.003 - ALR_{norm}=1 – Kerosene

5.3.3 Constant We influence

The influence of constant We number (see Eq. (3.14)) on the SMD has been investigated. The operating conditions that allowed maintaining the ratio of the convective forces to the surface tension forces constant while varying the air density are shown in Table 3.6. This analysis aids in identifying potential influences that affect the droplet breakup rather than the ones imposed by the Weber number. As shown in Figure 5.34, no significant variation of the SMD was detected. It is conspicuous that only Eq. (3.20) predicts a similar trend from the already existing correlations. The consistency of this correlation with the experimental results led to its selection as the basis for developing the proposed SMD-EBI model.

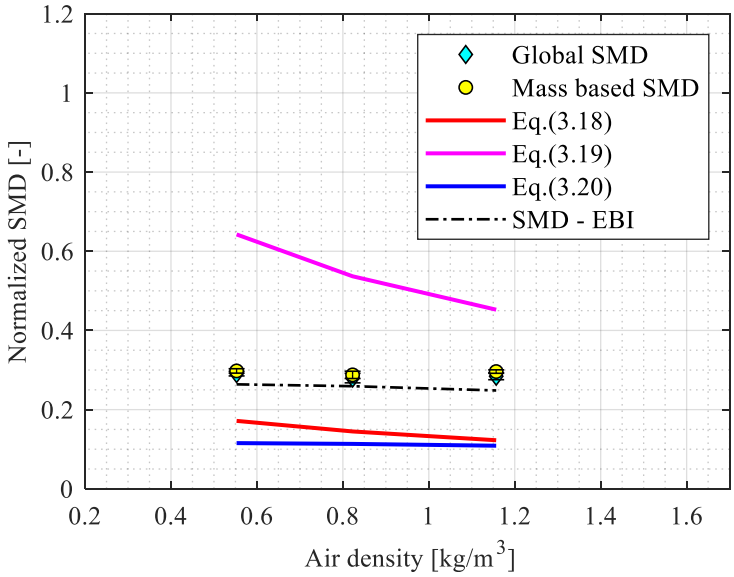

Figure 5.34: Influence of air density on SMD at We=const

5.3.4 ALR influence

In Figure 5.35, the influence of ALR on the SMD is depicted. For these measurements, the fuel mass flow was varying while maintaining the global operating conditions constant. Reducing the amount of injected fuel into the chamber leads to an improvement in the atomization quality. However, the latter effect is not prominent with increased ALR. A potential explanation of this behavior pertains to the different amount of fuel impinging on the pre-filmer, which affects the film thickness and atomization quality. The film thickness reaches its optimum value at some point, and no improvement is obtained by solely reducing the fuel flow rate.

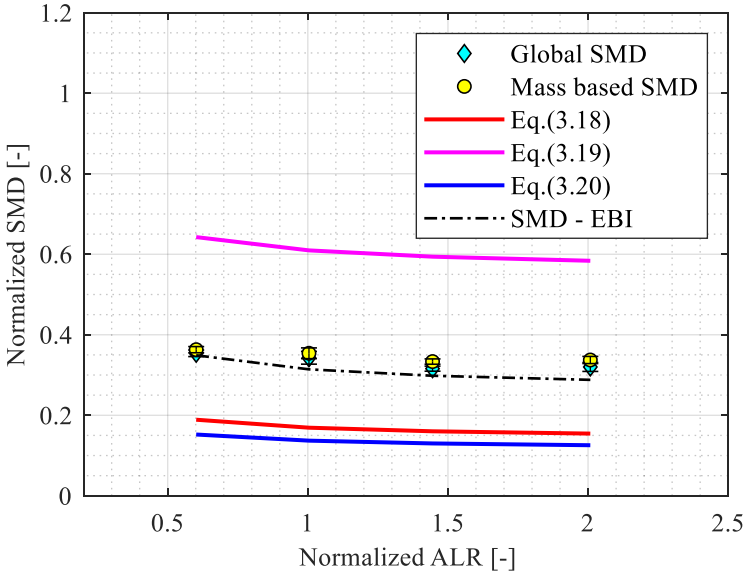

Figure 5.35: Influence of ALR on SMD, p=0.64 bar – T_{norm} = 1.003 - Δp_{norm}=0.96 – Kerosene

5.3.5 Water measurements

In the frame of the research activity, measurements with water under varying air velocity have been performed. These experiments have been conducted to verify whether the effect of the viscous forces on the atomization process maintains the same by employing a different fuel. Several issues have been encountered during the water measurements, with the most prominent being the different surface tension and the freezing point of the water. Droplets were attached and accumulated on the window, reducing the light intensity and significantly disturbing the acquired image's quality. Furthermore, to avoid the fuel's piping system icing, measurements have been conducted at a higher temperature (i.e., 1.048*T_{ref}). In Figure 5.36, the effect of the air velocity on the

SMD is depicted. It is conspicuous that the SMD-EBI correlation again agrees with the experimental results.

Moreover, the SMD with water is higher than the corresponding with kerosene due to the higher surface tension, lower viscosity, and therefore higher Ohnesorge and lower Weber numbers of the water, which affects the breakup process. Also, at lower air velocity associated with larger droplets, a deviation (also higher confidence interval) from the experimental results with the proposed model is observed. As mentioned before, water droplets were attached and accumulated on the windows. The subsequent image distortion created issues in the particle identification process, and this effect was more apparent when larger droplets were involved.

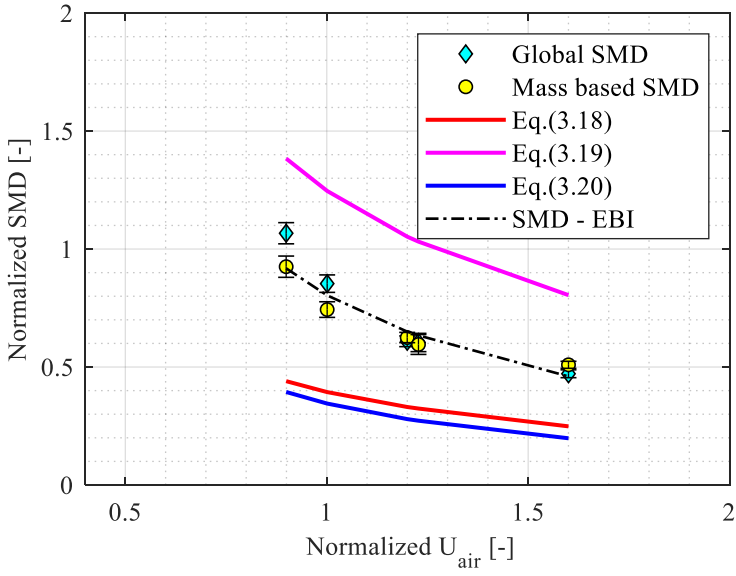

Figure 5.36: Influence of air velocity on SMD, p=0.64 bar – T_{norm} = 1.048 - ALR_{norm} = 1 – Fuel: Water

5.3.6 SMD at the igniter location

Spray measurements have also been performed at the igniter location to evaluate the SMD distribution across the combustion chamber (see Figure 3.38). More specifically, the effect of air velocity, air density, and ALR has been captured, and it is presented in this section. For comparison purposes, the already existing correlations, together with the proposed SMD-EBI model that predict the SMD well at the exit of the nozzle, are also depicted with the experimentally obtained data. As shown in Figure 5.37, Figure 5.38, and Figure 5.39, the extracted out of the experimental data SMD exhibit higher values than the exit of the nozzle. However, a similar behavior attributed to the influence of each parameter separately is captured. Two different reasons have been excelled regarding the higher SMD values at the location of the igniter. Both reasons might have acted simultaneously or individually. The first reason pertains to the exact location of the measurement. As shown in Figure 3.38, at this location is possible that large droplets, which deviate from the streamlines due to their high inertia, are located within the measurement area. The second reason is attributed to the impingement of the droplets against the combustor's liners. Hence, a second liquid film is created at the walls of the liners, and potentially larger droplets are generated, which immerse into the measurement area due to gravitational forces.

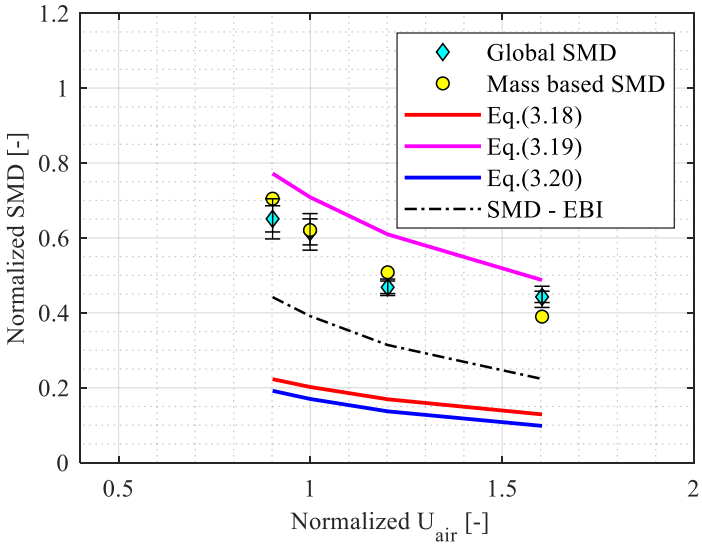

Figure 5.37: Air velocity influence on SMD – Igniter location

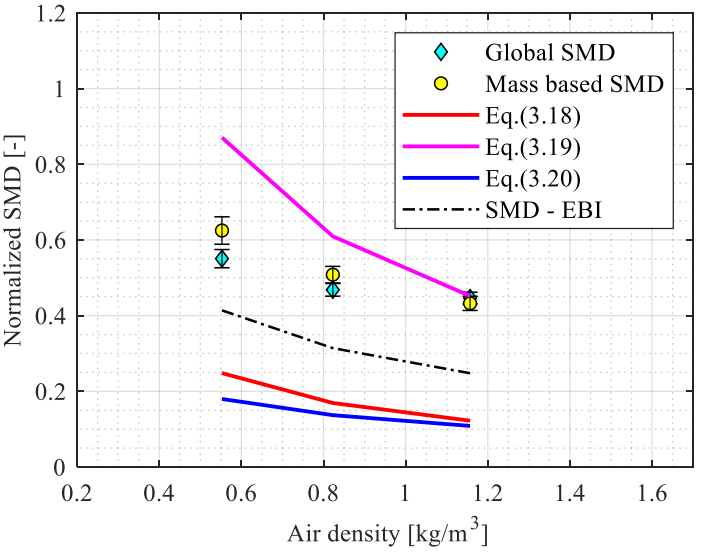

Figure 5.38: Air density influence on SMD – Igniter location

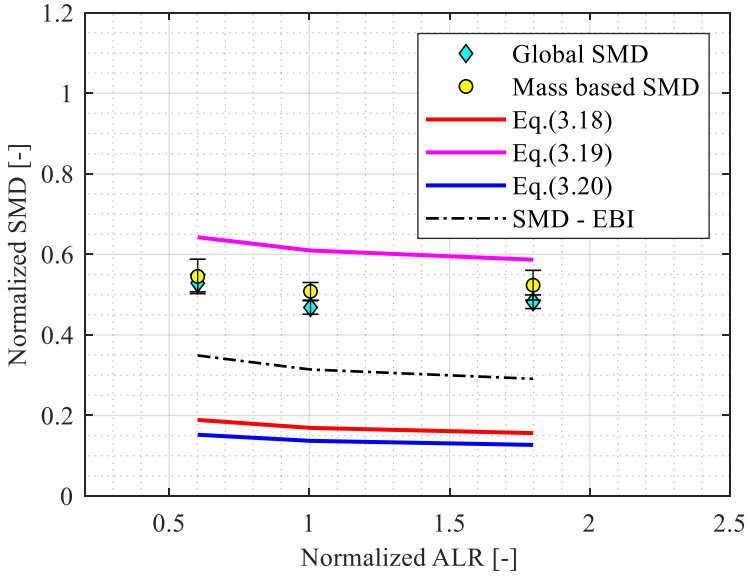

Figure 5.39: ALR influence on SMD – Igniter location

5.3.7 SMD comparison with and w/o effusion cooling

Measurements have shown that the integration of liners with effusion cooling enhances the ignitability of the combustion chamber under the same imposed operating conditions [226]. The quality of atomization might be the dominant factor in the latter behavior. Therefore, measurements to reveal the influence of the effusion cooling on the atomization quality have been carried out to support the aforementioned experimental outcome.

In Figure 5.40, the comparison of the global SMD obtained with and without effusion cooling is illustrated. The mean values of both configurations are similar, with the obtained value by employing effusion cooling being slightly

higher. However, a t-student test showed a high probability that both configurations exhibit the same mean value.

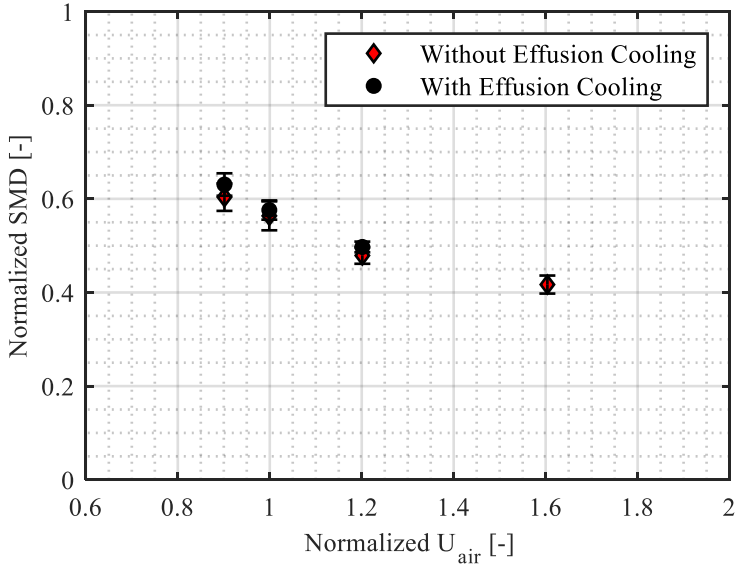

Figure 5.40: Normalized SMD comparison with and without effusion cooling, p=0.64 bar - T_{norm} = 1.003 – Kerosene

The Euler-Euler approach has been employed to reveal any potential difference that the SMD value cannot explain. In Figure A. 6 (see Appendix A.6), the SMD distribution for both configurations is depicted. There is no significant difference between both configurations, which is also the case for the relative mass flow distribution (see Figure A. 7 – Appendix A.6). However, a remarkable difference is observed in the absolute velocity of the droplets (see Figure 5.41), which is higher with effusion cooling holes. The latter indicates some interaction between the spray and the additional air, which flows into the combustion chamber through the effusion cooling holes. However, measurements

at this location have not revealed differences between both configurations to elucidate their different ignition behavior.

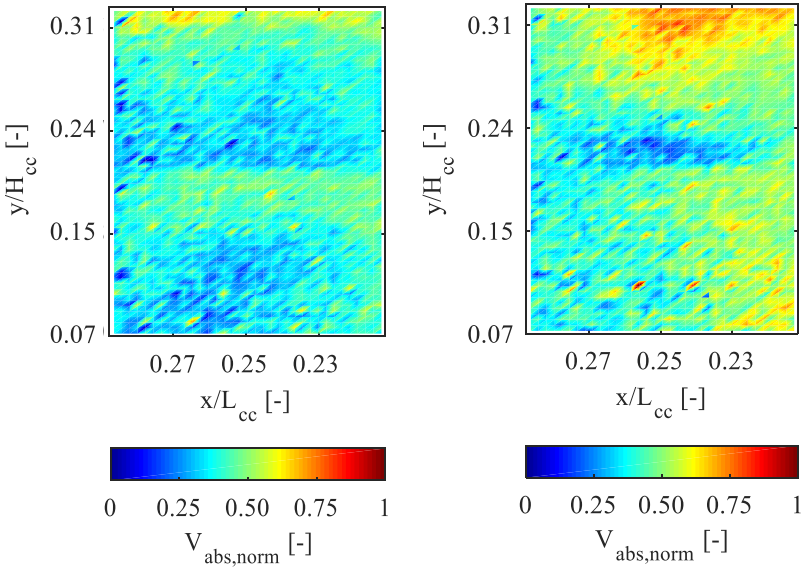

Figure 5.41: Normalized droplet absolute velocity distribution: (right) – with effusion cooling, (left) – without effusion cooling $(\Delta p/p)_{norm}$=1.04 – p=0.64 bar - T_{norm}=1.003, flow direction from right to left

Therefore, measurements have been performed closer to the liner (see Figure 3.38 – green dashed rectangular). This location was not selected initially due to the significant proportion of the lost optical access, which pertains to the round shape of the extension (see Figure 3.37). Even though the optical access reduction might have affected the thorough analysis conducted in Section 5.3.6, it is sufficient to compare both configurations. A closer look at the Euler-Euler approach of this measurement volume revealed significant differences between both configurations that could explain the higher ignitability of the

effusion cooling configurations. More specifically, even though, as shown in Figure 5.42, no significant SMD difference has been observed, it depicts clearly that no droplet could be detected above y/H_{cc}=0.36 for both measurements due to the reduced optical access mentioned above. However, with effusion cooling, the software identified a higher number of droplets above y/H_{cc}=0.34. The latter pertains to the software algorithm, which considers only droplets and not ligaments in the calculation. A qualitative analysis of the acquired images indicated that ligaments close to the liner were more prominent without than with effusion cooling (see Figure 5.46).

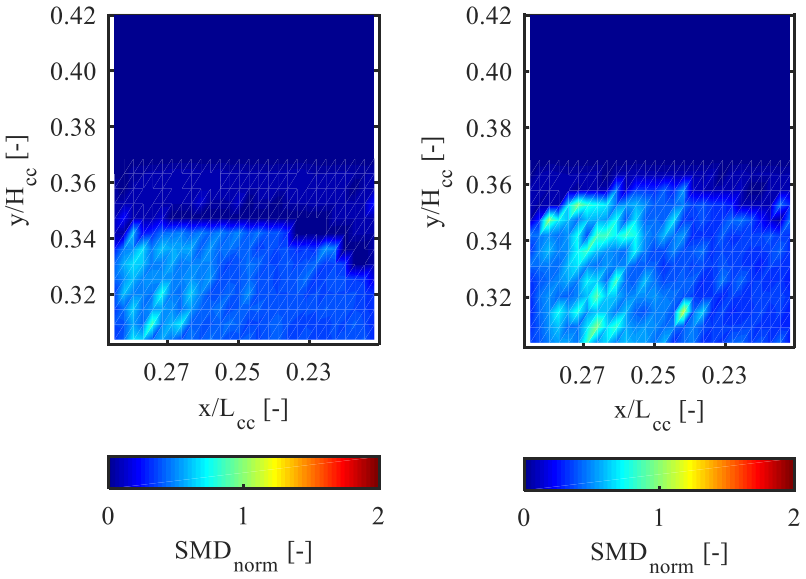

Figure 5.42: Normalized SMD distribution comparison: (left) without effusion cooling, (right) with effusion cooling – p=0.64 bar - T_{norm} = 1.003 - Δp_{norm}= 1.041 – Kerosene - flow direction from right to left

The normalized absolute and axial droplet velocities are illustrated in Figure 5.43 and Figure 5.44, respectively. As mentioned before, the droplets of the

effusion cooling configuration exhibit higher absolute and axial velocity, which confirms the strong interaction of the droplets with the additional air injected through the effusion cooling holes.

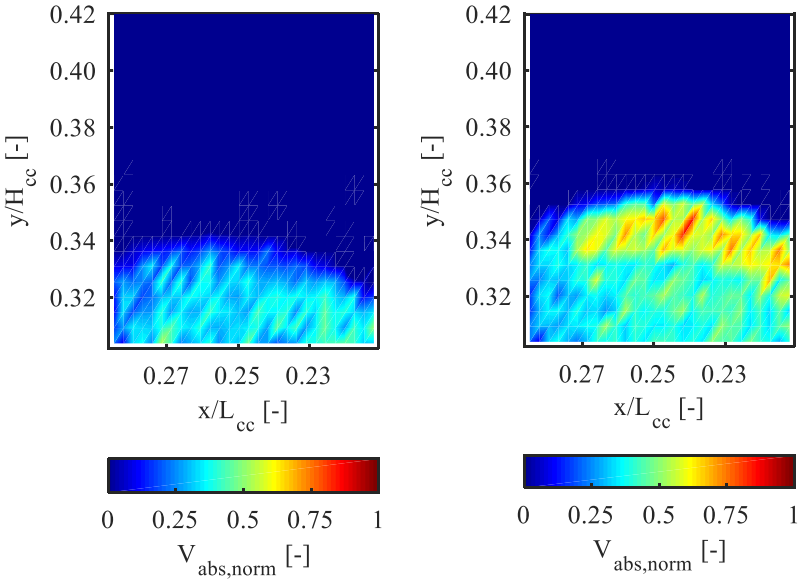

Figure 5.43: Normalized absolute velocity distribution comparison: (left) without effusion cooling, (right) with effusion cooling – p=0.64 bar - T_{norm} = 1.003 - - Δp_{norm}= 1.041 – Kerosene - flow direction from right to left

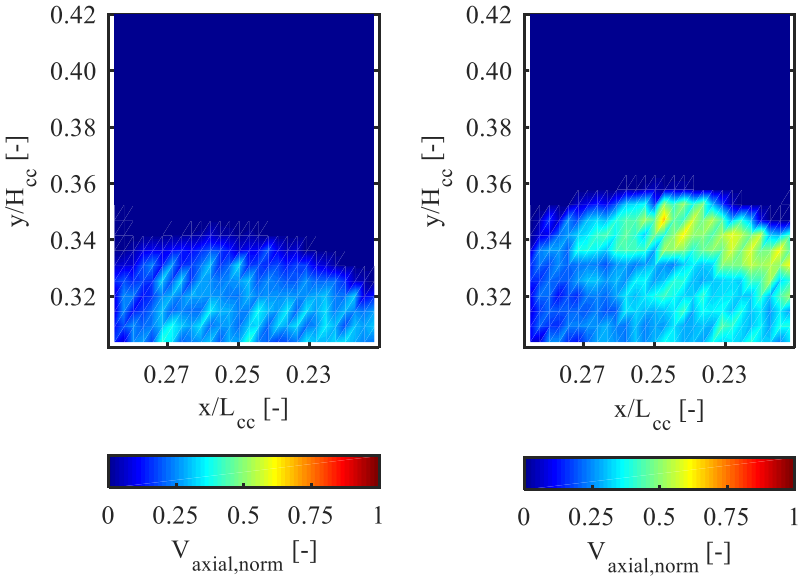

Figure 5.44: Normalized axial velocity distribution comparison: (left) without effusion cooling, (right) with effusion cooling – p=0.64 bar - T_{norm} = 1.003 - - Δp_{norm}= 1.041 – Kerosene - flow direction from right to left

As shown in Figure 5.45, the additional air, which flows parallel to the liner, carries a significant number of droplets closer to the igniter region when the configuration with effusion cooling is employed. It seems that when the spray impinges against the liner, a second liquid film is generated that is subsequently disintegrated by the relative velocity of the liquid phase with the injected air. The latter leads to a higher number and closer to the liner of detected droplets than in the configuration without effusion cooling, where the presence of ligaments plays a dominant role.

Therefore, the higher relative mass flow of kerosene droplets creates a more reactive mixture at the instant of the spark. Due to the ignition nature, which

depends highly on the probability of finding a flammable mixture in the spark region, the ignition probability with effusion cooling increases.

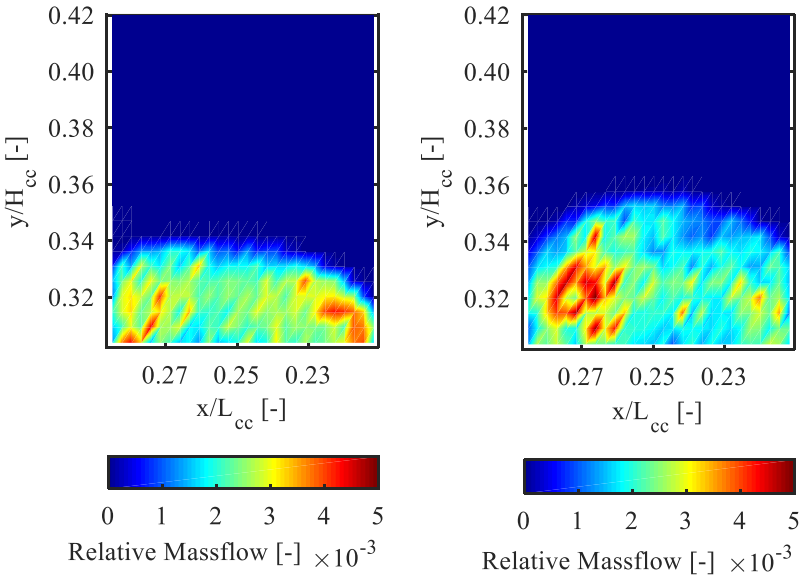

Figure 5.45: Normalized relative fuel mass flow distribution comparison: (left) without effusion cooling, (right) with effusion cooling – p=0.64 bar - T_{norm} = 1.003 - Δp_{norm}= 1.041 – Kerosene - flow direction from right to left

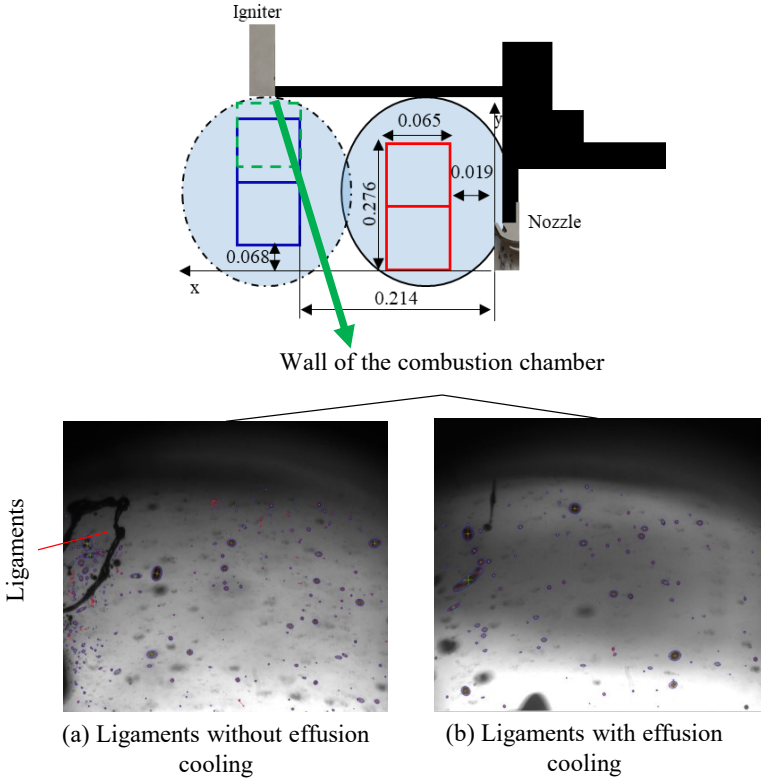

Figure 5.46: Detected ligaments – p=0.64 bar - T_{norm} = 1.003 - - Δp_{norm}= 1.041 – Kerosene - flow direction from right to left

5.4 Influence of igniter position on the ignition performance

In the frame of the SOPRANO EU Project, two-phase flow simulations have been carried out by the University of Florence [237]. The focus is to extract numerically spark plug locations, which reveal the influence of the igniter location on the ignition performance. Detailed information concerning the two-

phase flow simulation can be found in the literature, while a summary is given in Appendix A.2. The simulations and the experiments were conducted at 0.43 bar with slightly different cold temperatures (i.e., 0.963*T_{ref} for the experimental investigation and 0.948*T_{ref} for the simulation). In Figure 5.47, the normalized mass flow rate of the particles impinging onto the combustion chamber's liner per unit of surface is illustrated. Most of the droplets hit the liner slightly upstream from the nominal location of the spark plug. This computation removes the droplets from the simulation after impacting against the liner. However, in reality, they accumulate, creating a liquid film. he liquid film initialized in the dark red area is transported towards the spark plug and, most likely, downstream. However, the latter is not resolved by this simulation.

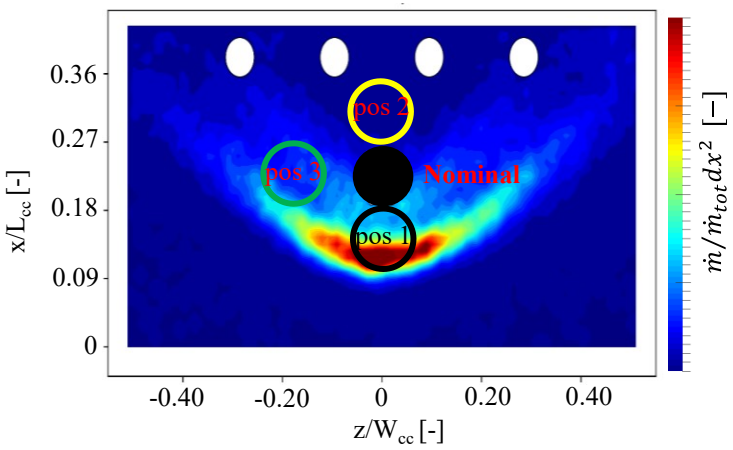

Figure 5.47: Non-dimensional mass flow rate per unit of surface on the droplets reaching the region of the spark – 0.43 bar, 0.948*T_{ref} [237]

In Figure 5.47, positions 1 to 3 represent the igniter locations of interest extracted by the experimental and numerical data (SBES Simulation). Table 5.2 presents the summary of the experimental results. It is conspicuous that position 1 is located in the region where the spark plug directly contacts the hollow cone spray. This location exhibits inferior ignition performance compared to the nominal. Ignition was not sensitive to FAR variations within a wide range of adjusted fuel mass flow. All the ignition trials have been reported unsuccessful, confirming investigations conducted in the past [238,239]. In this position, two effects might have created the latter outcome. The first one is attributed to the accumulation of cold liquid fuel on the surface of the igniter. It deteriorates the performance of the spark plug (reduces the deposited energy) while exhibiting a quenching action. This phenomenon is prominent under the imposed high-altitude conditions. The second one pertains to the effect of fluid dynamics. As shown in Figure 4.3, position 1 is located within the region of the high-velocity jet. The high turbulent strain rate imposed at this location may lead to the quenching of the flame kernel [100]. Both effects significantly weaken the flame kernel, enhancing the convective heat losses during the flame kernel generation, which is detrimental to the ignition evolution.

Comment		Global conditions				Results	
Fixed fuel mass flow		P_3	$T_{3,norm}$	$(\Delta p/p)_{nzl,norm}$	Ignition	Probability	$FAR_{min,norm}$
Location	Attempt	bar	[-]	[-]	Y/N	%	[-]
pos 1	1A	0.43	0.963	1.17	N	0%	not detected
	1B	-	-	-	N		
	1C	-	-	-	N		
	1D	-	-		N		
pos 2	2A	0.43	0.963	1.17	N	0%	1.489
	2B	-	-	-	N		
	2C	-	-	-	N		
	2D	-	-		N		
pos 3	3A	0.43	0.963	1.17	N	25%	1.443
	3B	-	-	-	N		
	3C	-	-	-	Y		
	3D	-	-		N		

Table 5.2: Summary of the igniter optimization activity

Figure 5.48 depicts the average flame's luminosity displacement. The high-velocity jet provides the flame kernel less time to propagate [240]. It is conspicuous that the weak kernel does not penetrate regions that promote the upstream propagation and is swept downstream after the spark's initial activity. The latter affects the ignition process immensely since the downstream propagation constitutes the "groundwork" of a successful ignition event. Under the imposed conditions, none of the ignition recordings at this location showed any combustion activity after 20 ms.

Figure A. 4 illustrates the ignition sequence with lower fuel injected at this location. It is interesting to note that under this condition, the ignition failure was reached faster than in the case with a higher amount of fuel presented afore, again confirming the sensitivity of the ignition process to the adjusted FAR.

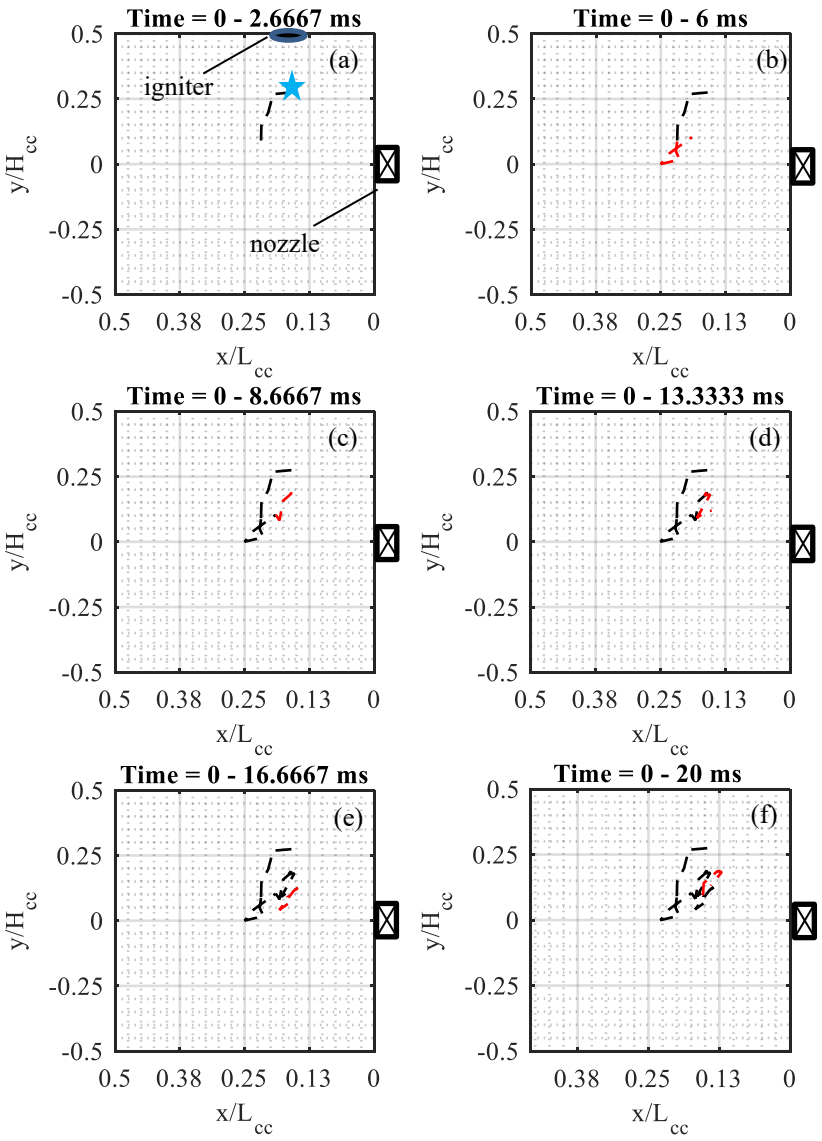

Figure 5.48: Average (out of 5 sparks) flame's luminosity movement – Igniter location: pos 1 (close to the nozzle)

The mean axial and mean total velocity of the flame kernel are illustrated in Figure 5.49 and Figure 5.50, respectively. The mean axial flame kernel velocity predicted by the ALETHO algorithm is around $0.1V_{x,norm}$ (light red), while the calculated by the CFD value lies in the same range see Figure 4.3). The directional component confirms that the flame kernel is convected away, initially exposed to conditions that extract energy out of it. Moreover, it moves upstream with low thermal energy, insufficient to heat the incoming mixture and sustain a stable flame. Therefore, it blows off.

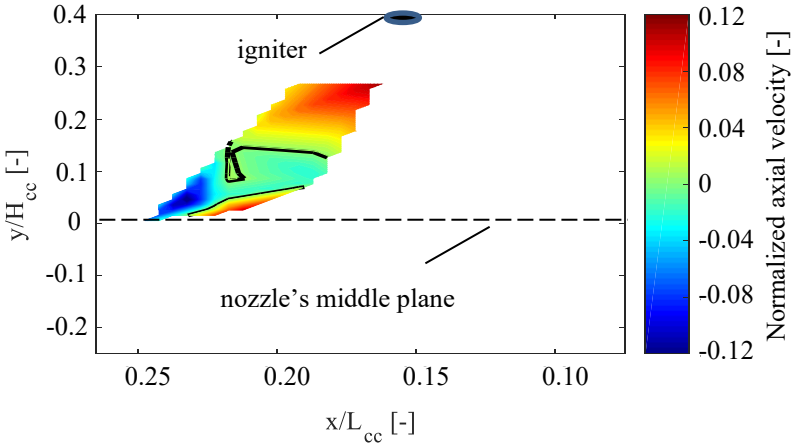

Figure 5.49: Normalized Axial velocity (pos 1) of the hot gases, black iso-line represents axial velocity V_x=0, Δt = 0-6 ms – normalization with $V_{x,max}$ extracted by CFD under similar conditions (Cold case see Table 4.1)

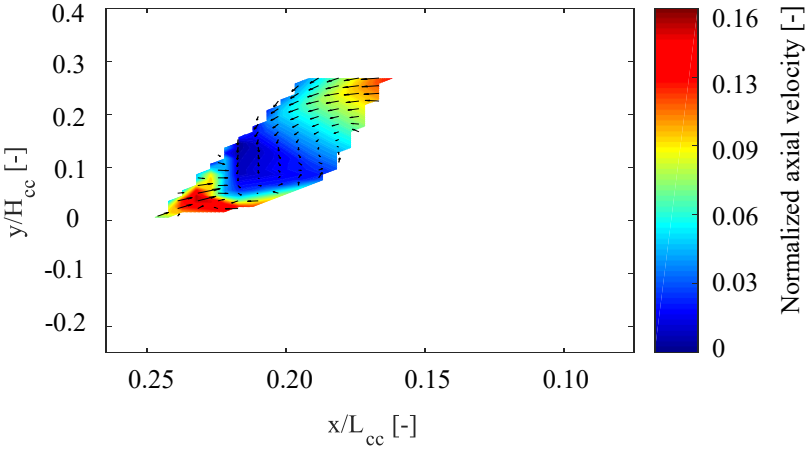

Figure 5.50: Normalized Total velocity (pos 1) of the hot gases - Δt = 0-6 ms – normalization with $V_{tot,max}$ extracted by CFD under similar conditions (Cold case see Table 4.1)

Even though the boundary conditions between the model and the experiments were not identical, a useful comparison, indicating that the flame's kernel movement is dominated by convection, is obtained.

As shown in Figure 5.47, the simulation predicts a negligible amount of fuel accumulated in pos 2. In reality, a fuel's proportion is transported through the interaction with the carrier phase, though very lean conditions are created. Therefore, all the ignition trials were reported unsuccessful when adjusting the fixed fuel mass flow. However, increasing the fuel mass flow leads to richer conditions, and a self-sustained flame kernel that propagates towards the exit of the nozzle is obtained (see Figure 5.51). Hence a minimum FAR (100 % - i.e., 4/4 successful ignition events) has been detected, which is higher than the nominal position (extrapolated value of min FAR = 1.429).

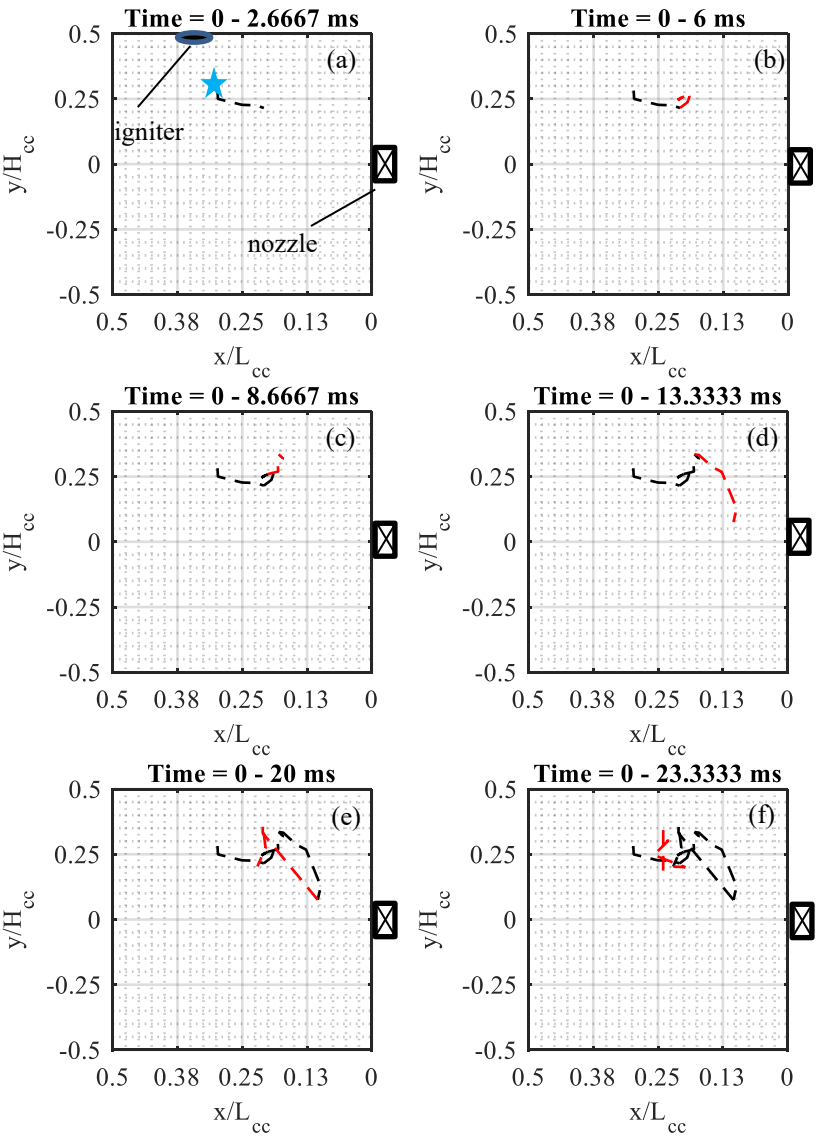

Figure 5.51: Average (out of 4 experiments) flame movement – Igniter location: pos 2 (far from the nozzle) – $FAR_{min.norm}$=1.489

As shown in Figure 5.47, position 3 has the exact axial but different radial distance than the nominal. The ignition performance revealed similar characteristics with the nominal position concerning the ignition probability with fixed fuel mass flow (both 25 %) and minimum FAR determination (approximately 1% difference). The latter indicates that the axial distance of the nominal position exhibit the best ignition performance. In this location, which lies between very rich (upstream) and very lean (downstream) conditions, the probability of finding a flammable mixture increases.

The flame kernel follows a reactive path that enables heating of a primary zone's significant proportion (see Figure 5.52). The latter raises the reactivity of the mixture leading to a stable burning configuration. For comparison purposes, the mean displacement of the flame's luminosity center is presented for position 3 within the first 23 ms. Figure A. 4 (see Appendix A.3) depicts the complete recording at this location under the imposed conditions.

The experimental results obtained in this research activity frame confirm that locations within flammable zones, which promote the upstream propagation of the hot gases towards the nozzle, have to be selected. The latter seems dominant since the former is compensated by injecting more fuel into the chamber.

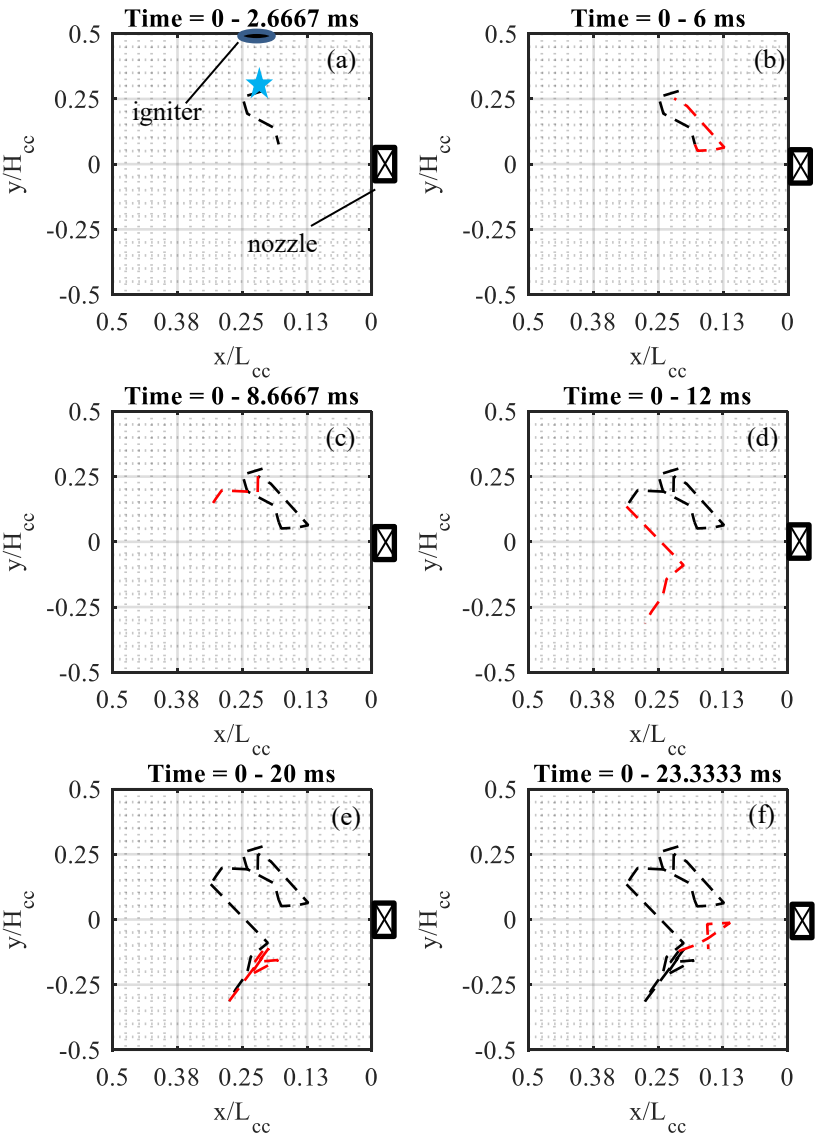

Figure 5.52 Average (out of 4 experiments) flame movement – Igniter location: pos 3 (far from the nozzle) – $FAR_{min.norm}$=1.445

5.5 Influence of higher air mass flows on the ignition performance

The quality of the atomization and the residence time of the mixture in the primary zone constitute the most crucial parameters that predict the ignition evolution. On the one hand, the improvement of the atomization quality leads to smaller droplets, which subsequently exhibit a higher evaporation rate, increases flame propagation, and, therefore, the stability of the flame. Moreover, it reduces due to better mixing with the oxidant. On the other hand, the increased air-flow rate associated with the improvement of the atomization's quality reduces the residence time and increases the turbulent strain rate that both impair the ignition process. Having commented on the effect of the aerodynamic strain (see Section 5.4), the residence time of the mixture within the combustion chamber must be long enough to ensure sufficient heat release, promoting flame stabilization.

5.5.1 Residence time distribution

As mentioned before, calculations concerning the residence time of the mixture in the primary zone and the spark plug region have been carried out. Table 5.3 demonstrates the normalized residence time of the mixture, calculated with three different approaches for the examined operating conditions listed in Table 4.1. The residence time of Case 3 is the largest, as expected, due to the lowest air volumetric flows in the primary zone. The value determined by Eq. (4.1) represents the order of magnitude for a perfectly stirred reactor. A significant variance among the different approaches is evident. More specifically, the estimated residence time with the transport equation is approximately half

the corresponding value calculated with the particle tracking. The latter pertains to the different computational domains associated with each different approach.

	Case 1	*Case 2*	*Case 3*
Residence time Eq. (4.1)	0.509	0.568	1.00
Transport equation	0.166	0.197	0.428
τ_{artf}	0.323	0.411	0.614

Table 5.3: Normalized residence time in the primary zone obtained, normalization based on Case 3 [229]

Figure 5.53 depicts the mass-specific residence time as a scalar quantity. As expected, Case 3 exhibits the largest residence time due to the lowest volumetric flows. The air penetrating the primary zone through the cooling holes of the igniter and the dilution hole affects the spatial distribution of the residence time. In the current configuration, the amplest residence time is accumulated in the upper section of the combustor's primary zone, which is beneficial to the ignition process.

Although the transport equation resembles the residence time given by the turbulent convection-diffusion and provides reasonable results, it fails to provide the mean residence time of the primary zone since it is quite sensitive to the applied source term in the region of interest (primary zone). In the current case, the source term outside the primary zone is set to zero. Therefore, the residence time in the inner recirculation reduces significantly since it mixes with the secondary air, whose assigned flow time is zero.

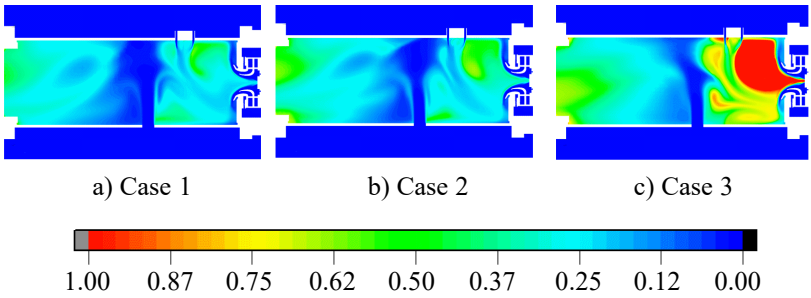

Figure 5.53: Residence time in the combustion chamber obtained by the transport equation, scaling based on Case 3, flow direction from right to left [229]

The particle tracking method is employed to solve the aforementioned shortcoming. With this method, a large number of massless particles are injected into the primary zone, released from four different inlets (nozzle, igniter cooling holes, inner and outer dilution holes) that were treated separately. The trajectories of the fluid particles are determined based on the RANS simulations, and therefore a random walk model is applied (see Section 4.3.2) to account for the effects of the turbulent mixing. According to this approach, the residence time distribution is obtained. Therefore, the mean value that a particle spends on the track in the primary zone is estimated.

In Figure 5.54 and Figure 5.55, only 25 particle paths (out of 20000) are illustrated for simplicity. When particles are injected through the nozzle (see Figure 5.54), the effect of increased volumetric flow on the residence time in the primary zone is evident. As expected, Case 3 exhibits the longest residence time due to the lowest air volumetric flows.

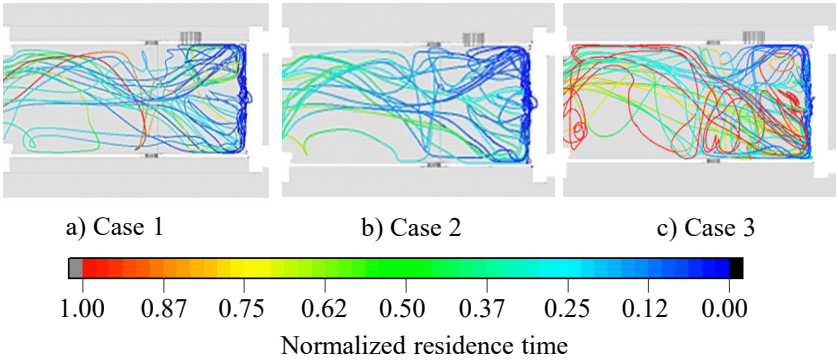

Figure 5.54: Normalized residence time along the characteristic particle paths – particle injection at the outlet of the nozzle, normalization based on Case 3, flow direction from right to left

The strong interaction of the secondary air with the recirculation zone is evident in Figure 5.55. Outer injection stands for particles emanating from the igniter's cooling holes and the dilution holes of the outer liner. A proportion of these particles is involved with the primary zone of the combustion chamber. Especially in Case 2 and Case 3, the particles accumulate and recirculate in the upper section of the combustion chamber, while from Case 3 to Case 1, fewer and fewer particle paths are accumulated in the igniter region. If particles are injected from the inner liner, the phenomenon of particles interacting with the IRZ is more prominent in the high-velocity cases due to the stronger reversed flow, which is not hindered by the air emanating from the cooling holes of the igniter.

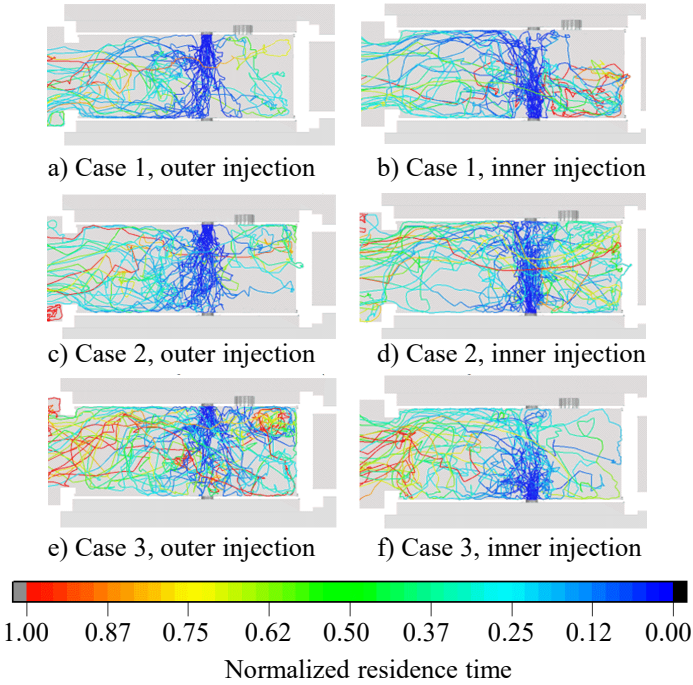

Figure 5.55: Normalized residence time along the characteristic paths – particle injection, left side: (a,c,e) outer dilution zone, right side: (b,d,f) inner dilution zone and igniter's cooling holes, normalization based on Case 3, flow direction from right to left

An artificial particle residence time has been determined to account for the volumetric flow difference through each inlet according to the following correlation:

$$\tau_{artf} = \frac{\dot{V}_{nzl}}{\dot{V}_{pmz}}\tau_{nzl} + \frac{\dot{V}_{igniter}}{\dot{V}_{pmz}}\tau_{igniter} + \frac{\dot{V}_{dilution}}{\dot{V}_{pmz}}\tau_{dilution} \qquad (5.4)$$

where the volumetric flow of the primary zone may be written as follows:

$$\dot{V}_{pmz} = \dot{V}_{nzl} + \dot{V}_{igniter\_holes} + \dot{V}_{dilutio\_holes} \qquad (5.5)$$

The volumetric flow entering the primary zone from the dilution holes $\dot{V}_{dilutio\_holes}$ is estimated by the mass balance in the control volume of the primary zone. The latter provides relative flexibility in setting the boundary conditions, especially in cases with multiple inlets. However, a shortcoming arises in the inaccurate weighting of the residence time for the different inlets. This method neglects the fluid flow that crosses the boundaries multiple times.

An estimation of the average time interval that a particle spends within an infinitesimally small volume (i.e., a mesh cell - ca. 80 mesh cells are located in the adjacent region of the spark) in the spark region has been carried out. As mentioned before, the particle tracking method provides a more precise overview of the residence time and has been employed to conduct this analysis. According to the following correlation, results were obtained by calculating the residence in a specified mesh grid located near the igniter.

$$\tau_{cell} = t_{out} - t_{in} \tag{5.6}$$

where t_{out} and t_{in} represent the time of outflow and inflow of a particle in the examined cell.

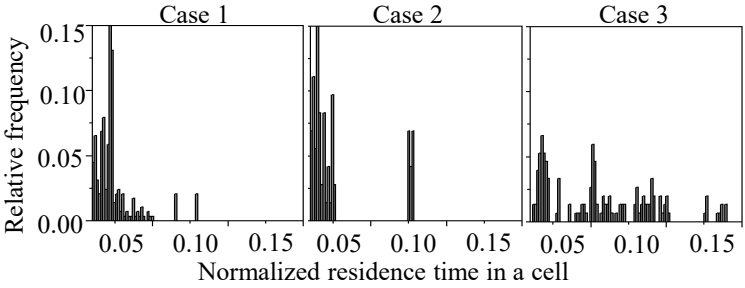

Figure 5.56: Normalized averaged residence time distribution in the region of the spark – obtained by the particle tracking method, normalization based on Case 3 (see Table 5.3) [229]

Table 5.4 illustrates the effect of increased volumetric flow on the residence time in the igniter region. The analysis has been conducted for a limited volume, and therefore the number of particles involved is also limited. However, it is evident that the residence time of the mixtures decreases up to 60 % within the practical operating range of the jet engine's combustion chamber. The latter would significantly hamper the ignition process, especially under adverse conditions (low pressure and temperature).

	Particle Tracking
Case 1	0.0229
Case 2	0.0246
Case 3	0.0554

Table 5.4: Normalized residence time of a cell in the igniter region, normalization based on Case 3 (see Table 5.3) [229]

5.5.2 Ignition performance

Figure 5.57 illustrates the effect of the atomization and the residence time on the minimum FAR under different imposed operating conditions. The effect of pressure on the ignition performance has been isolated, while the system's temperature was initially maintained constant at 1.06*Tref. Measurements have been carried out for three simulated altitudes, 0.8 km, 3.6 km, and 6.6 km (from the ground), corresponding to 0.9 bar, 0.64 bar, and 0.43 bar, respectively. Since temperature remains constant, pressure determines the reactivity of the mixture, and high altitudes (low pressure) are associated with slow reaction rates [241].

Moreover, a pressure drop variation from $(\Delta p/p)_{norm}$=0.45 to $(\Delta p/p)_{norm}$=1.83 has been imposed to represent the practical operating envelope of a jet engine. The latter directly affects the residence time of the mixture in the primary zone (see Section 5.5.1). It is conspicuous that the ignition performance responds differently to the air load variation as long as the simulated altitude increases. The outcome of this investigation lies in an air load at which the residence time becomes dominant over the atomization's quality. This point is shifted towards lower pressure drops with increased simulated altitude across the nozzle.

At low altitudes (i.e., 0.8 km), the influence of atomization is more prominent than the one of residence time. An air load increase decreases the residence time of the mixture. However, the small chemical kinetic time scales associated with low altitude, ensure adequate residence time for sufficient heat release. Therefore, the ignition process is atomization-driven since the better atomization quality enhances the evaporation rate and, subsequently, the overall mixture's reactivity. The latter confirms the enhanced stability limit of the flame associated with increased air load presented in Figure 3.16. Evidently, this trend (i.e., lower minimum FAR with increased air load) changes with the increase of the simulated altitude. The reaction rate is significantly slower at a higher simulated altitude (i.e., 3.6 km) since it is proportional to the system's pressure at a constant temperature [241]. Hence, under adverse conditions within the combustion chamber, high velocities hurt the ignition process immensely since the chemical time scales are large. The latter effect overcomes the faster evaporation associated with increased air load, and thus, the residence time becomes insufficient (i.e., smaller than the required chemical time scale) to ensure ignition. It is evident that at 3.6 km, from $(\Delta p/p)_{norm}$=0.91 to $(\Delta p/p)_{norm}$=1.83, although the atomization's quality is improved, the minimum

FAR does not exhibit a decreasing trend. This behavior is remarkably prominent at 6.6 km, where ignition was not feasible at a higher pressure drop than $(\Delta p/p)_{norm}$=1.37, although a wide range of fuel's mass flow variation towards rich conditions has been examined.

The outline is that the lowest pressure drop exhibits the highest minimum FAR associated with successful ignition events at all investigated simulated altitudes. The latter pertains to unfavorable atomization characteristics (i.e., at low pressure drops, ignition is an atomization-driven process). Whether the atomization's influence is dominant over the corresponding residence's time (or vice versa) with increased air load depends on the altitude.

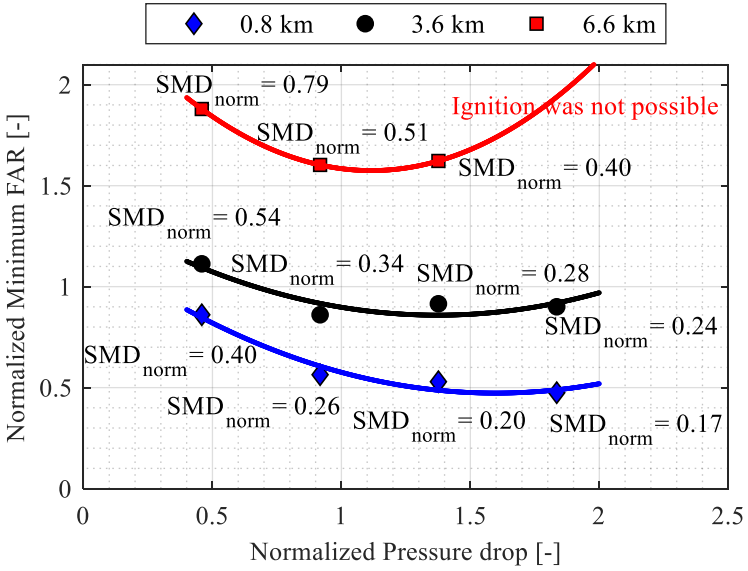

Figure 5.57: Effect of atomization and residence time on the ignition performance, SMD calculation carried out with Eq. (5.2)

Measurements have been conducted at 3.6 km and 0.985*T_{ref} to capture the effect of temperature on the ignition performance. The obtained results are compared with the corresponding at 1.066*T_{ref} (see Figure 5.58). It is noticeable at low temperatures that the minimum FAR increases while keeping a similar trend, which lies in several parameters, such as the fuel properties and, more prominently, the evaporation rate. With adverse conditions, the fuel pipes are exposed to lower temperatures. Hence, the heat transfer from the cold air decreases the temperature of the fuel and, therefore, the viscosity increases. Thus, the produced spray has a slightly lower quality, which leads to larger droplets. In combination with the lower temperature, the latter reduces the evaporation rate significantly. Therefore, leaner mixtures are formed due to the local FAR (concerning fuel vapor) variation, which is overcome by injecting higher fuel mass flows in the combustion chamber.

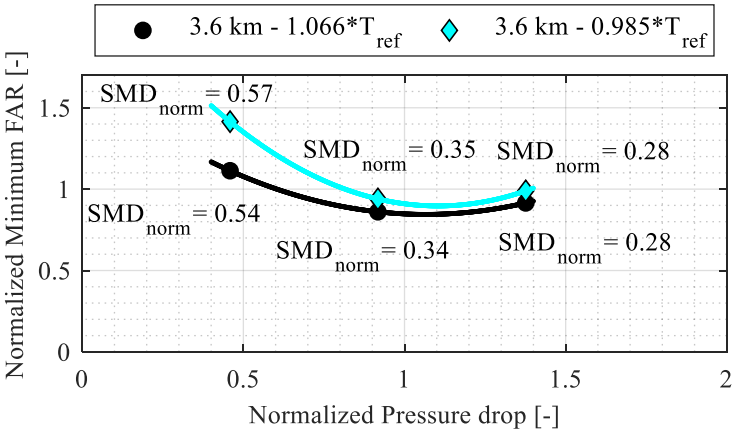

Figure 5.58: Temperature effect on the ignition performance

Figure 5.59 to Figure 5.64 depict the normalized mean axial and total velocity of the flame's luminosity center at the corresponding minimum FAR for each

operating condition. The generation of a strong IRZ within the primary zone is responsible for transporting the hot gases towards the exit of the nozzle. The velocity magnitude is significantly higher than the maximum turbulent flame speed of kerosene droplets in air reported in previous experimental investigations [242]. Combined with the exhibited similarity of the hot gases' flow pattern with the estimated cold-flow CFD, the latter confirms that the displacement is attributed to convection rather than propagation [14]. It is conspicuous that the velocity of the flame's luminosity center, for similar operating conditions, is in good agreement with the predicted velocity of the CFD to both magnitude and direction. More specifically, the flame kernel propagates upstream with an axial velocity $-0.1V_{x,norm}$, which is close to the predicted value from the CFD (light blue region in Figure 4.6 (c))

Moreover, increased pressure drops across the nozzle lead to stronger recirculation zones confirming investigations already reported in the literature [243]. Therefore, the velocity of the hot gases, propagating upstream, increased with increased air load. The latter indicates that prior knowledge of the generated flow field within the combustion chamber is crucial to ensure and optimize the jet engine's relight event.

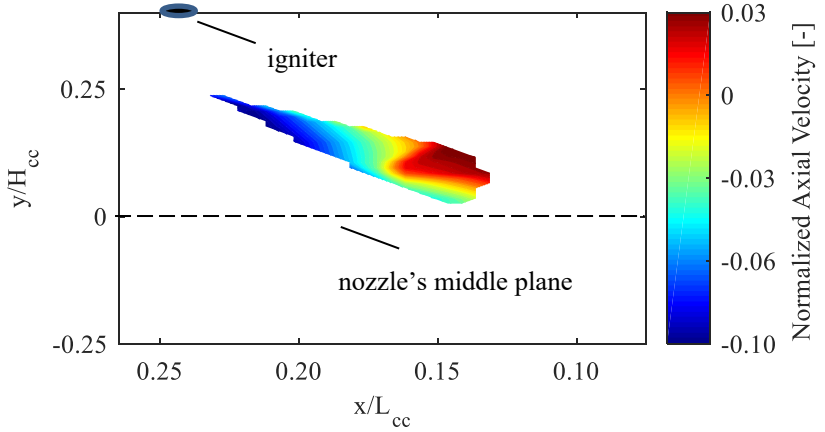

Figure 5.59: Normalized Axial velocity of the flame's luminosity center, Δt = 0-10 ms – normalization with $V_{x,max}$ extracted by CFD under the imposed conditions (Case 3 see Table 4.1) – 0.64 bar, $(\Delta p/p)_{norm}$= 0.458, flow direction from right to left – minimum FAR_{norm} = 1.112

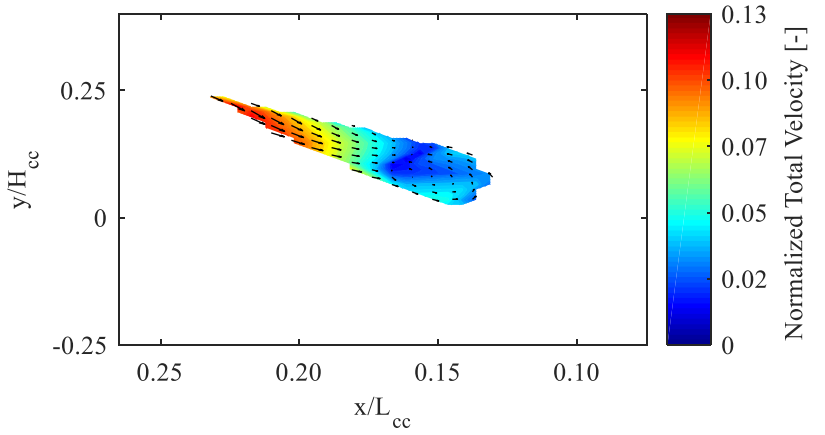

Figure 5.60: Normalized Total velocity of the flame's luminosity center, Δt = 0-10 ms – normalization with $V_{tot,max}$ extracted by CFD under the imposed conditions (Case 3 see Table 4.1) – 0.64 bar, $(\Delta p/p)_{norm}$= 0.917 flow direction from right to left, minimum FAR_{norm} = 1.112

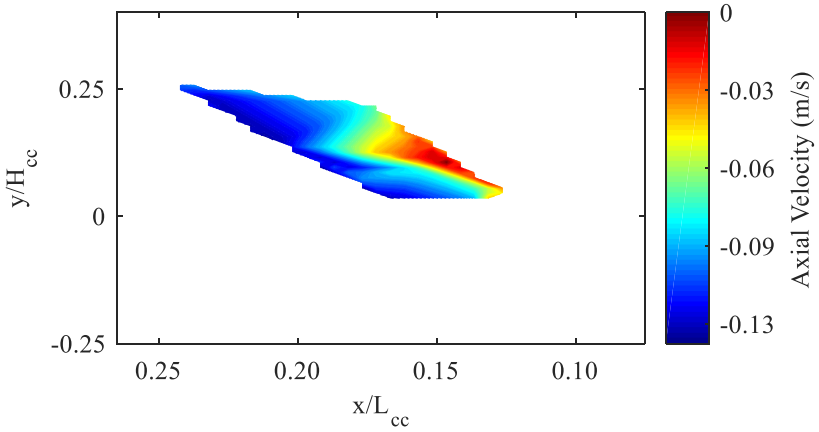

Figure 5.61: Normalized Axial velocity of the flame's luminosity center, Δt = 0-10 ms – normalization with $V_{x,max}$ extracted by CFD (Case 3 see Table 4.1) – 0.64 bar, $(\Delta p/p)_{norm}$= 0.917, flow direction from right to left – minimum FAR_{norm} = 0.860

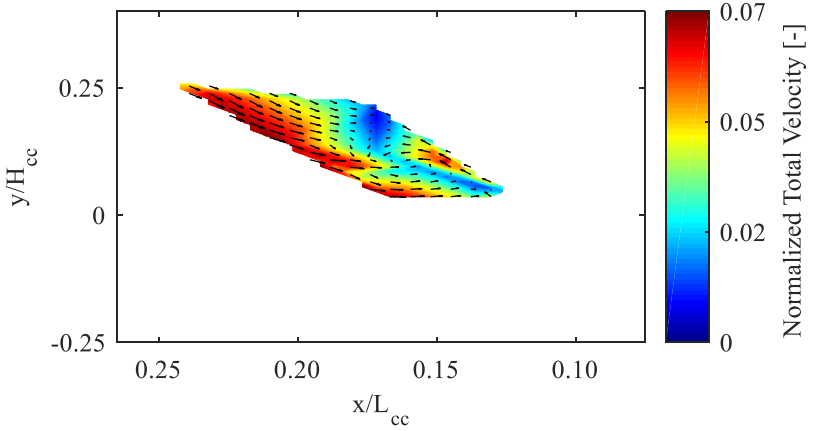

Figure 5.62: Normalized Total velocity of the flame's luminosity center, Δt = 0-10 ms – normalization with $V_{tot,max}$ extracted by CFD (Case 3 see Table 4.1) – 0.64 bar, $(\Delta p/p)_{norm}$= 0.917, flow direction from right to left, minimum FAR_{norm} = 0.860

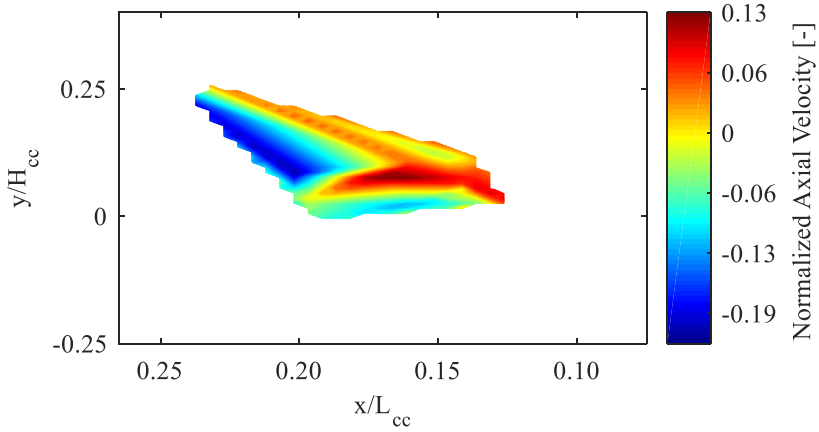

Figure 5.63: Normalized Axial velocity of the flame's luminosity center, Δt = 0-10 ms – normalization with $V_{x,max}$ extracted by CFD (Case 3 see Table 4.1) – 0.64 bar, $(\Delta p/p)_{norm}$=1.834, flow direction from right to left – minimum FAR_{norm} = 0.900

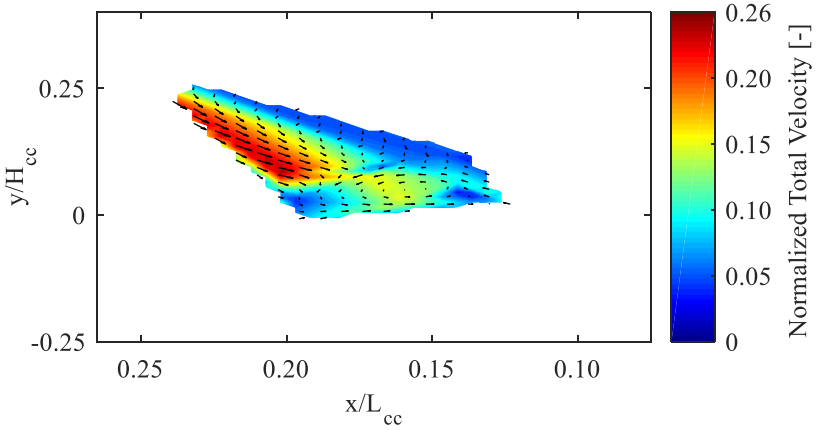

Figure 5.64: Normalized Total velocity of the flame's luminosity center, Δt = 0-10 ms – normalization with $V_{tot,max}$ extracted by CFD (Case 3 see Table 4.1) – 0.64 bar, $(\Delta p/p)_{norm}$= 1.834

5.5.2.1 Ignition map

In the frame of this research activity, the ignition limit that defines the transition from unsuccessful to successful ignition events has been determined. Due to the binary nature of the experimental outcome ("Ignition" or "No Ignition"), a classification algorithm known as regularized logistic regression has been developed to estimate how the varied imposed operating conditions affect the probability of a successful ignition event. The hypothesis of the logistic regression is defined as follows:

$$h_\theta(x) = g(\theta^T x) \tag{5.7}$$

where θ denotes a vector of length n and is adjusted based on m training examples. Moreover, the length n indicates the number of features involved in the classification algorithm, and x is the value of each feature. The parameter m is the number of experiments conducted under different pressure drops, and g is the sigmoid function that may be written:

$$g(z) = \frac{1}{1 + e^{-z}} \tag{5.8}$$

In this specific algorithm the hypothesis was formulated as follows:

$$h_\theta(x) = g(\theta_0 + \theta_1 x_1 + \theta_2 x_1^2 + \theta_3 x_1^2 x_2 + \theta_3 x_1^2 x_2^2) \tag{5.9}$$

Based on the hypothesis of Eq. (5.9) the prediction's cost function of the regularized logistic regression algorithm is defined by the following correlation:

$$J(\theta) = \frac{1}{m}\sum_{i=1}^{m}\left[-y^{(i)}\log\left(h_\theta\left(x^{(i)}\right)\right) - \left(1-y^{(i)}\right)\log\left(h_\theta\left(x^{(i)}\right)\right)\right] + \frac{\lambda}{2m}\sum_{j=1}^{n}\theta_j^2 \tag{5.10}$$

where the first term of the right-hand side is associated with the prediction cost of the hypothesis h_θ from the actual value y, while the second term controls any potential underfitting or overfitting of the data. The latter is feasible through the regularization parameter λ since high values lead to less complicated decision boundaries and vice versa. However, there is not such an issue of complexity in the current configuration.

Therefore, the objective is to minimize the cost function based on the optimum θ parameters, given a fixed dataset of features x and values y. The latter optimization has been conducted with Matlab by employing a quasi-newton algorithm with a maximum of 1000 iterations. In Figure 5.65 to Figure 5.68, the influence of the pressure drop across the nozzle on the ignition limit (nonlinear decision boundary) is illustrated. The prediction of the classifier has been calculated on an evenly spaced mesh grid generated within the boundaries of the graphs. Subsequently, the algorithm identifies and draws (black dash-dotted line) the contour plot precisely at the transition from “No Ignition” to “Ignition” regime.

The essential observations are listed below:

- The pressure drop affects the decision boundary strongly.
- From Δp_{norm}=0.45 to Δp_{norm}=0.91, the residence time in the primary zone is sufficient to ensure the stability of the flame. By adding the

effect of the atomization's improvement, the decision boundary is shifted towards leaner global equivalent ratios.

- From Δp_{norm}=0.91 to Δp_{norm}=1.37, at low simulated altitudes associated with faster reaction rates, an improvement on the atomization's quality shifts further the decision boundary towards leaner equivalence ratios. However, at higher altitudes, no reduction of the global equivalence ratio is evident, albeit the atomization's improvement.
- Due to the adverse imposed operating conditions at high altitudes, high-velocity regions, associated with an increase of pressure drop (Δp_{norm}=1.83), hurt immensely the ignition evolution. As a result, at the simulated altitude of 6.6 km (see Figure 5.68), no stabilized flame could be achieved for a wide range of equivalence ratios, up to the corresponding maximum with respect to the test facility's safe operation.

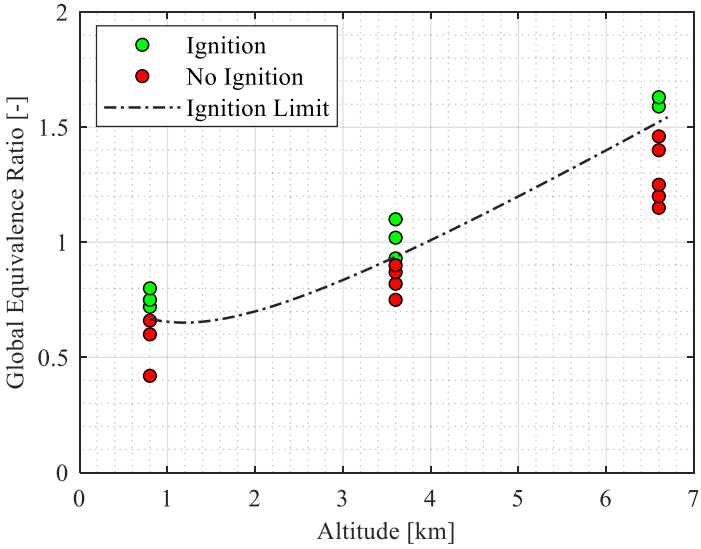

Figure 5.65: Ignition boundary at Δp_{norm}=0.45, T_{norm}=1.06

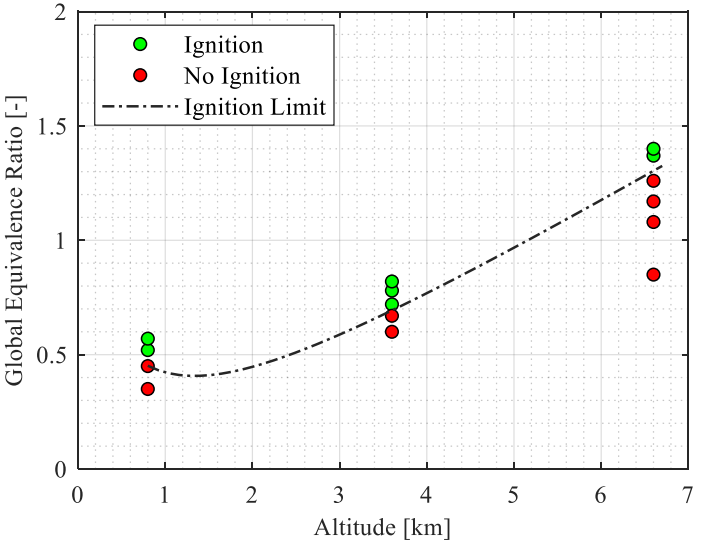

Figure 5.66: Ignition boundary at Δp_{norm}=0.91, T_{norm}=1.06

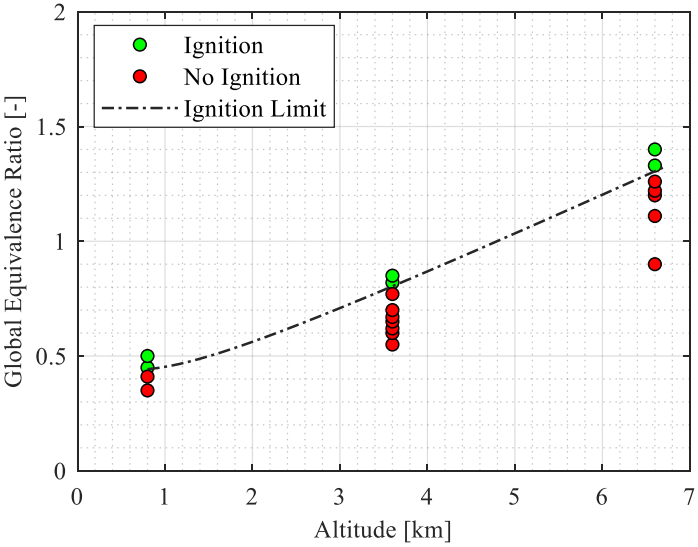

Figure 5.67: Ignition boundary at Δp_{norm}=1.37, T_{norm}=1.06

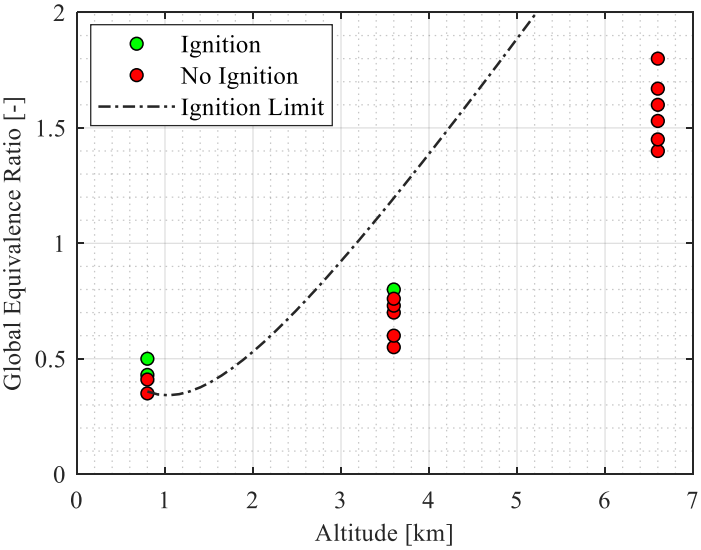

Figure 5.68: Ignition boundary at Δp_{norm}=1.83, T_{norm}=1.06

6 Summary

An investigation has been conducted concerning the ignition of flowing kerosene (Jet A-1)-air mixtures under high altitude conditions (low temperature and pressure). The influence of varying simulated altitudes on the ignition capability for two different liner configurations (without and with effusion cooling) was obtained. Moreover, CFD-RANS simulations and spray measurements under the imposed operating conditions have been conducted to support the ignition investigation and enhance the understanding/knowledge concerning the phenomena governing the high-altitude relight of a jet engine.

High-altitude relight capability with and without effusion cooling

More specifically, results indicated that in the configuration without effusion cooling, the pressure dominates the probability of having a successful ignition event for the specified maximum time of spark production due to the substantially limited temperature variations in the investigated test matrix. The general trend indicates that an increased simulated altitude decreases the ignition probability at a constant fuel mass flow. Low pressure and temperature conditions hamper several essential mechanisms governing the relight process. The most pronounced effects are the atomization's quality and the reaction rate, which can be detrimental to ignition, especially under adverse operating conditions.

The configuration with effusion cooling was not sensitive to pressure and temperature variations and exhibited higher ignitability than the former. The latter contradicts the initial speculation, which, based solely on the mixture's residence time (shorter in this case due to increased mass flow in the chamber),

predicted lower ignitability. A thorough analysis of the spray characteristics at the spark region for both configurations indicated that the additional air injected in the primary zone via the effusion cooling holes, flowing parallel to the liners, disintegrates ("secondary atomization") the liquid film and the ligaments created upon the spray impingement against the chamber's liner. Therefore, the higher relative mass flow of kerosene droplets at the instant of the spark created favorable conditions since it forms a more reactive mixture than the former configuration, where the presence of ligaments is dominant. Thus, the ignitability with effusion cooling is significantly enhanced, especially at high altitudes, resulting in a 100% ignition probability for each operating condition of the test matrix.

Moreover, the minimum FAR for a successful ignition event was determined. The minimum FAR showed an increasing trend in both configurations with increased simulated altitude. Low temperature and pressure create adverse conditions for the atomized fuel, producing larger droplets and lower evaporation rates. The latter leads to variations of the local FAR towards leaner mixtures, which is overcome by increasing the injected fuel in the primary zone. A direct comparison of the two configurations indicated a lower minimum FAR with effusion cooling, confirming this configuration's aforementioned enhanced ignitability. The effect of poor atomization is more prominent for operating conditions with almost the same simulated altitude. The ones with higher predicted SMD also experienced an increase in the minimum FAR.

Furthermore, measurements of the time interval between the first spark and the onset of the flame were carried out. On average, an increase in the simulated altitude leads to a slower ignition timing for both configurations. Randomness was apparent in both configurations since there was no clear trend among the

successful ignition events of the same operating conditions, confirming the ignition process's highly stochastic nature. Comparing both configurations indicated that the ignition timing was significantly faster with effusion cooling, which was also expressed by the higher probability of a successful ignition detection within 10 seconds.

Finally, an in-house image processing code was developed to extract information from the high-speed recordings' analysis systematically. Qualitative analysis showed that the reacting gas movement from the spark region to the inner recirculation zone is essential for stabilizing the flame. Additionally, quantitative spatial information of the flame's luminosity center displacement was derived. It was evident that the flame's luminosity center follows a similar pathway for both configurations, while with effusion cooling, the time scale of the flame's evolution is shorter due to the shorter flow residence time in this case. The latter is associated with the higher mass flow employed for effusion cooling.

Spray measurements under high-altitude conditions

A thorough investigation of the air and fuel properties' influence on the atomization quality of a pre-filmer airblast atomizer under high-altitude conditions has been conducted in the current research activity. To the author's knowledge, this experimental investigation is unique and focuses on generating an atomization database under adverse conditions. The experimental data have been obtained with the shadowgraphy measurement technique. The effect of the essential parameters governing the atomization process, such as the air velocity, density, ALR, and the fuel's viscosity, has been captured. Measurements have been carried out at the nozzle exit and the igniter location.

The SMD value has been extracted for each measurement point by employing a temporal and a spatial approach. However, the nozzle's exit measurements revealed no significant difference between both configurations. A comparison of the experimentally obtained results with the predicted values based on the already existing correlations related to the atomization of airblast atomizers was conducted. Results indicated that the mechanisms governing the atomization process (effect of Weber and Ohnesorge numbers) under atmospheric conditions are applicable under high-altitude conditions since the trend of the experimentally extracted data was similar to the one predicted by the existing correlations. Furthermore, the Rosin-Ramler and Rosin-Ramler Modified distributions were derived using the droplet cumulative distribution and droplet volume distributions for each measurement point. The Rosin-Ramler Modified distribution fitted better to the experimentally acquired droplet distribution, and this information can be used as input to future numerical simulations.

As mentioned before, a similar spray characterization has been conducted at the region of the igniter. It was evident that this location possessed a higher SMD than the corresponding values at the exit of the nozzle. The latter pertains to the deviation of the larger droplets from the carrier's streamlines, while due to their high inertia, they can travel across the combustion chamber.

Based on the Euler-Euler approach, usually employed in the numerical simulations of multiphase flows, the SMD, the droplet velocity, and the relative mass flow distributions have been constructed. Results indicated that the spray emanated from the prefilmer's lip is associated with the highest velocities, the smallest droplet sizes, and the highest, more uniform relative mass-flows. Larger droplets, less uniformly distributed, emanating from the pressure atomizer are located near the middle axis of the nozzle, and this phenomenon is

more prominent when reducing the atomization air (lower quality of atomization).

Effect of igniter location on the ignition performance

Based on the experimental data obtained related to the atomization quality under the imposed operating conditions, the droplet distribution and the SMD have been provided as inputs for two-phase flow simulations conducted in the frame of the EU SOPRANO Project. According to the simulations, three different locations have been selected, and while comparing their high-altitude relight capability with each other and the nominal location, essential information was revealed. Results showed that the ignition process is strongly dependent on the igniter's location. The position associated with the direct liquid impact and high-velocity jet exhibited the worst ignitability. The latter pertains to the effect of the cold liquid and the excessive strain rate, which enhance the convective heat losses during the flame's kernel generation and immensely hurt the ignition process. Positions promoting the flame's kernel penetration in the IRZ exhibited higher ignitability depending on the local FAR.

Effect of increased air load on the ignition performance at varied simulated altitudes

Increasing the air load (air emanating from the nozzle) exhibits a countereffect on the ignition process. On the one hand, it improves the atomization's quality significantly since the relative velocity between the gas and the liquid phase increases. On the other hand, as shown by the CFD simulations, it substantially reduces the residence time of the mixture in the primary zone. However, the latter should be long enough to exceed the evaporation, turbulent mixing, and

chemical kinetics time scales to ensure sufficient heat release and a subsequent stable flame. Results indicated that the air load increase benefited the ignition process at low simulated altitude, associated with a better atomization quality. This trend was reversed with increased simulated altitude, where reducing the residence time combined with the slow reaction rate associated with low pressure is detrimental to the ignition process. By employing the ALETHO algorithm, the velocity and the direction of the hot gases were calculated. A comparison with the predicted gas velocity magnitude and direction by the CFD under similar operating conditions showed the strong interaction of the hot gases with the imposed flow field (i.e., suction of the hot gases in the IRZ, velocity of hot gases significantly higher than the turbulent flame speed). The latter indicates that the flame's kernel displacement is attributed to convection rather than flame propagation. Therefore, an in-advantage knowledge of cold CFD is beneficial for the future development of combustion chambers concerning high-altitude relight. Since low-order ignition models are mainly based on the cold flow field, the experimental data extracted by this research activity might be the basis for their validation.

Moreover, measurements have been conducted for the same simulated altitude and different temperatures (Figure 5.58). Results show that higher FAR is required at lower temperatures since it hampers essential ignition mechanisms, such as the evaporation rate, leading to leaner mixtures than expected. Finally, a classification algorithm was trained based on the experimental data to identify the air load's effect under different simulated altitudes. The ignition limit has been defined in the transition from unsuccessful to successful ignition events.

Evaluation of the existing correlation for the prediction of the relight capability

This research activity revealed the pronounced effect of two parameters on the ignition performance, which are not considered in Eq. (1.1), or the way they are presented could be wrongfully interpreted. The igniter's location is associated with the former category, suggesting that a more sophisticated correlation, capable of precisely predicting the relight process, should include this parameter. Moreover, the correlation implies that an increased air mass flow deteriorates the ignition characteristics. However, the latter does not constitute a general rule since the increase in air mass flow also alters the spray properties. Therefore, by employing the correlation proposed by Lefebvre, the relight process can be predicted only for geometrically similar combustion chambers and identical SMD distributions.

Outlook:

Future investigations should address the following topics:

- The experimental data related to the high-altitude relight capability should be employed to validate low-order models that predict the ignition probability, and up to this date, they have never been used under these operating conditions. The latter will aid engineers in the early design of the combustion chamber, contributing to reducing the design iterations.
- The effect of the Markstein number on the laminar burning velocity and the consequent minimum FAR behavior for different operating conditions should be investigated in the future. The latter will confirm

whether the FAR trend also pertains to a chemical effect, such as the increased laminar burning velocity due to the induced flame stretch.

- The scientific community should support the growing interest of the aviation industry in alternative fuels that could replace fossil fuels. The high-altitude relight capability of these fuels would be beneficial to their integration into commercial aviation.
- Spray measurements exactly at the liner should be conducted to reveal the behavior of the spray impinging against the liner. Information, such as whether the droplets are rebounding into the chamber or creating a liquid film, could be used to improve numerical simulations.
- The uniqueness of the ISCAR test facility should be exploited by investigating novel combustion concepts that could constitute a breakthrough, facilitating the smooth transition towards the ambitious goal of zero-emission flights until 2050.

A Appendix

A.1 Effective area definition

Calculating the mass flow that passes through an orifice by employing the continuity equation based on the geometrical area adds a significant error in the predicted value. This difference arises from the fact that the continuity equation assumes a homogeneous exit velocity distribution. However, the internal shape of the orifice, or nozzle, affects significantly the shape of the exit velocity profile. Smoother geometrical features impose less pressure losses compare to sudden contractions, which form strong re-circulation zone. Therefore, in the former case, more air will flow through the orifice assuming same operating conditions between both configurations.

To attribute for the aforementioned effect, the so-called effective area is defined, which represents an equivalent to the geometrical area with a bulk exit velocity profile. Therefore, the actual mass flux is determined as follows:

$$\dot{m} = \rho A_{eff} u \tag{A.1.1}$$

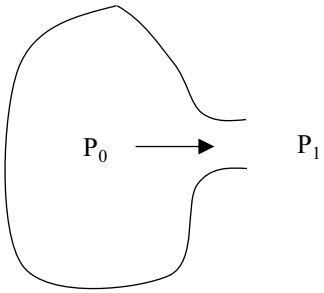

Figure A.1: Schematic representation of a flux through an orifice

According to the differential form of the Euler equation, derived by the momentum balance of a volume element across a line the following correlation applies:

$$\frac{\mathrm{dp}}{\mathrm{d\rho}} + gdz + udu = 0 \tag{A.1.2}$$

By assuming that the path from 0 to 1 (see Figure A.1) is an isentropic process, the relation between pressure and specific volume is expressed as follows:

$$p_0\theta_0^{\kappa} = p_1\theta_1^{\kappa} \tag{A.1.3}$$

where κ is the specific heat capacity of the gas and θ denotes the specific volume. By replacing the specific volume with density, the following applies:

$$\mathrm{dp} = p_1\rho_1^{-\kappa}\kappa\rho_0^{\kappa}\mathrm{d\rho} \tag{A.1.4}$$

By combining Eq. (A.1.4) and Eq. (A.1.2) yields:

$$\frac{\kappa}{\kappa-1}\frac{p_0}{\rho_0^{\kappa}}[\rho_1^{\kappa-1} - \rho_0^{\kappa-1}] + \left[\frac{u_1^2}{2} - \frac{u_0^2}{2}\right] \tag{A.1.5}$$

Assuming that the velocity in 0 is zero, and solving with respect to u_2 implies:

$$u_2 = \sqrt{\frac{2\kappa}{\kappa-1}\frac{p_0}{p_1}\left[1-\left(\frac{p_1}{p_0}\right)^{\kappa-1/\kappa}\right]} \tag{A.1.6}$$

By applying Eq. (A.1.6) into Eq. (A.1.1) and solving with respect to the effective area, the following correlation is derived:

$$A_{eff} = \frac{\dot{m}}{\rho_1 u_1} = \frac{\dot{m}}{\rho_1\sqrt{\frac{2\kappa}{\kappa-1}\frac{p_0}{\rho_0}\left[1-\left(\frac{p_1}{p_0}\right)^{\kappa-1/\kappa}\right]}} \tag{A.1.7}$$

By employing the ideal gas equation, and the relation between the specific heat and the ideal gas constant, the final form for the effective area calculation is derived.

$$A_{eff} = \frac{\dot{m}\sqrt{T_1}\frac{1}{p_0}}{\left(\frac{p_1}{p_0}\right)^{1/\kappa}\sqrt{\frac{2\kappa}{(\kappa-1)R}\left[1-\left(\frac{p_1}{p_0}\right)^{\kappa-1/\kappa}\right]}} \tag{A.1.8}$$

A.2 Two-phase simulation

A summary of the two-phase flow filed simulation conducted in the frame of this research activity is presented. Detailed information have been reported in the literature [237]:

Regarding the gaseous flow field:

- Solver ANSYS Fluent 2019R1
- Hybrid RANS-LES approach, known as Stress-Blended Eddy Simulation (SBES)

- Concerning the RANS contribution, a k-ω Shear Stress Transport (SST) has been employed
- Concerning the LES contribution, a WALE sub-grid scale model has been employed

Regarding the spray simulation:

- A standard Lagrangian framework has been employed to track the liquid dispersion.
- No secondary breakup
- Liquid injection has been carried out using a Rosin-Ramler distribution fitted to the experimental data (see Section 5.3)
- The SMD has been determined according to the model extracted by this research activity (see Eq. (5.2))
- No liquid film modeling has been applied
- Liquid evaporation has been overlooked to reduce the computational effort

A.3 FFT of the mean flame recovery signal at 0.44 bar and 0.948*T_{ref}

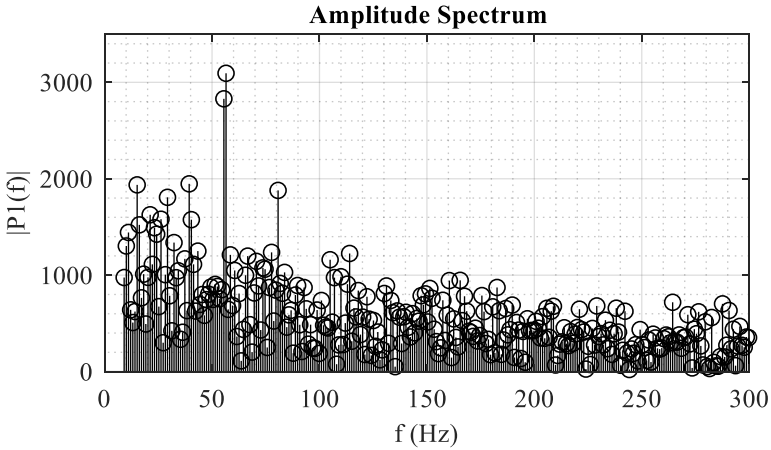

Figure A. 2: FFT – 0.43 bar, 0.963*T_{ref}

A.4 Complete recordings – influence of the igniter location

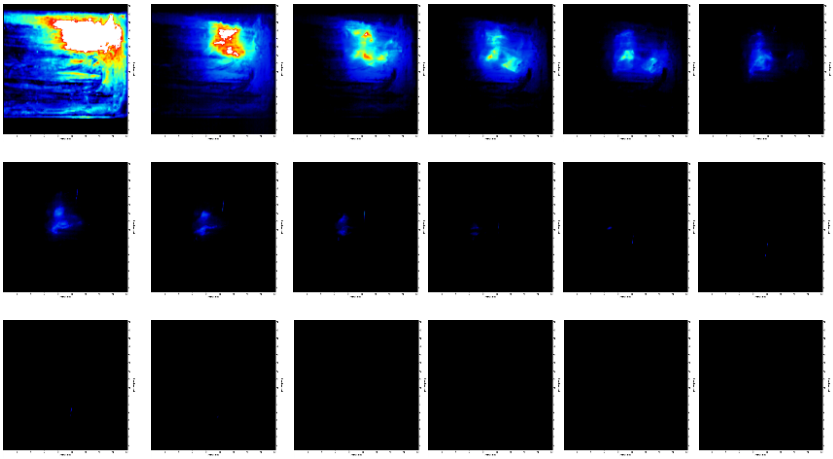

Figure A. 3: Unsuccessful ignition recording – 0.43 bar, 0.963*T_{ref} – Igniter location: pos 1 (close to the nozzle), flow direction from right to left, 1500 Hz

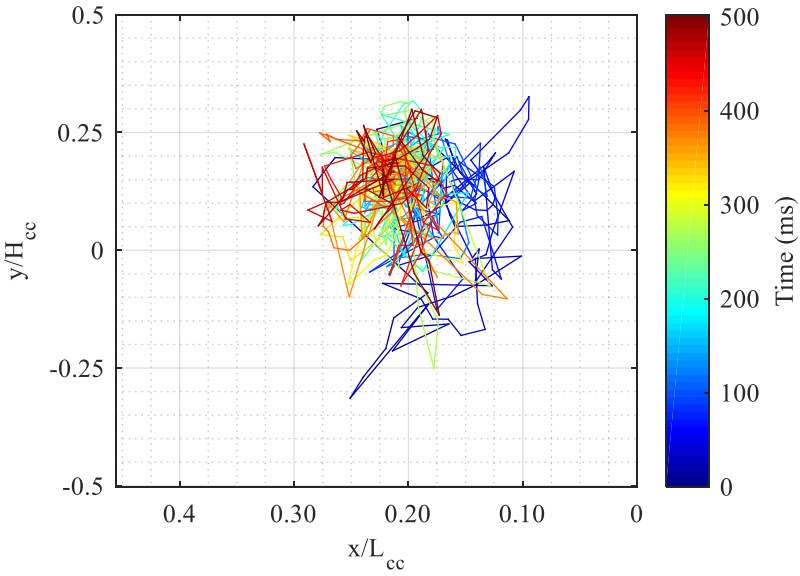

Figure A. 4: Color-coded movement of flame's luminosity center – 0.43 bar, 0.963*T_{ref} – Igniter location: pos 3, flow direction from right to left

A.5 Mesh refinement

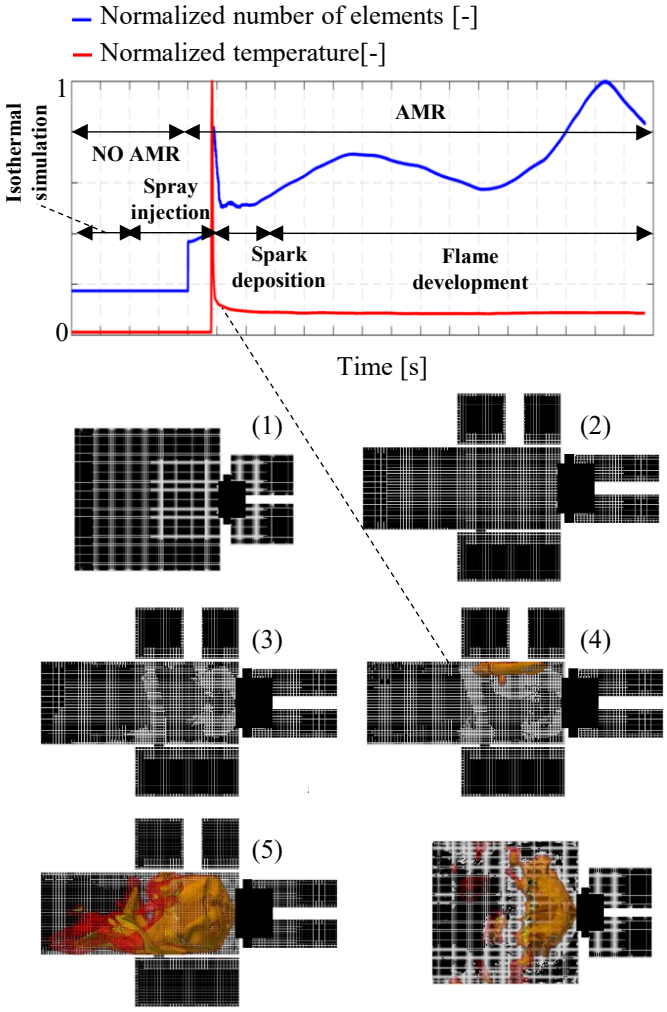

Figure A. 5: Automatic Mesh Refinement

A.6 Spray measurements

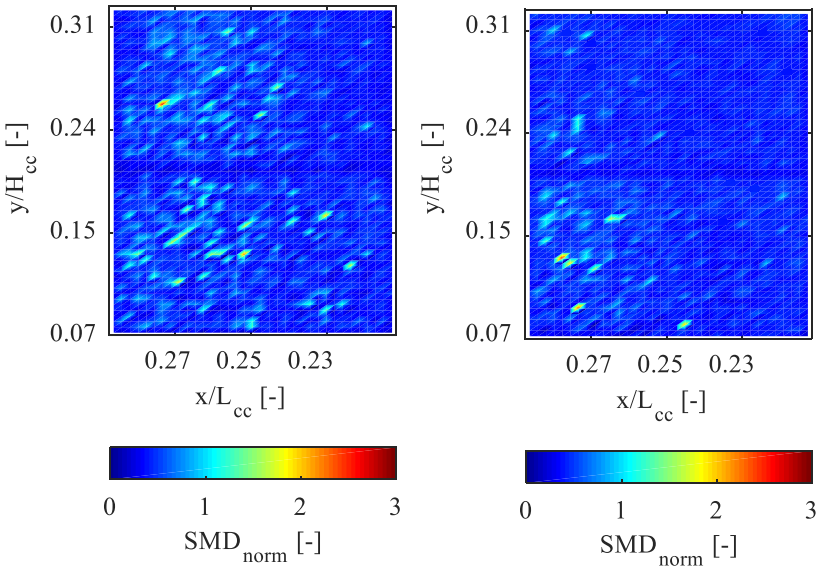

Figure A. 6: Normalized droplet SMD distribution: (left) -with effusion cooling, (right) – without effusion cooling - $(\Delta p/p)_{norm}$=1.04 – p=0.64 bar - T_{norm}=1.003, flow direction from right to left

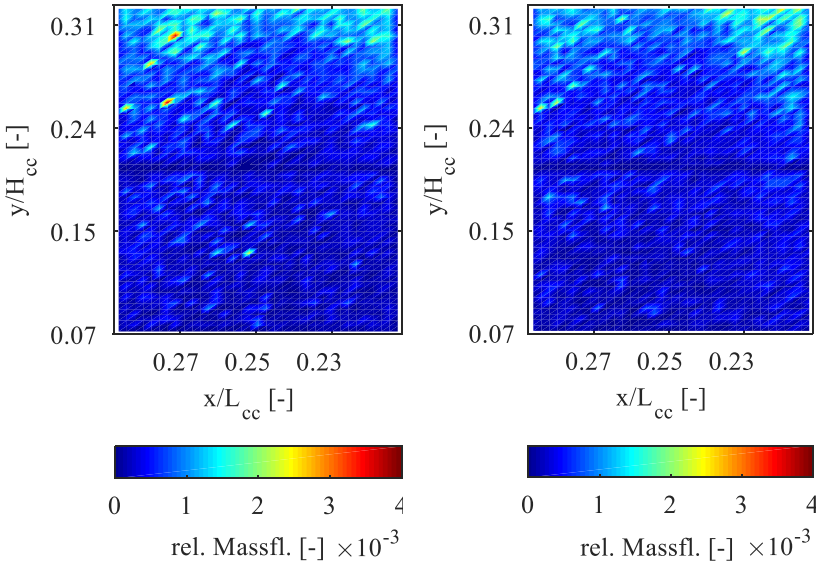

Figure A. 7: Relative mass flow distribution: (left) -with effusion cooling, (right) – without effusion cooling - $(\Delta p/p)_{norm}$=1.04 – p=0.64 bar - T_{norm}=1.003, flow direction from right to left

References

[1] E.A.S. Agency, Certification Specifications for Engines CS-E (2010) 1–166.

[2] Federal Aviation Administration, Aviation Rulemaking and Advisory Committe - Transport Airplane and Engine Issues -- New Tasks, 1998.

[3] T. Mosbach, R. Sadanandan, W. Meier, R. Eggels, in: Volume 2: Combustion, Fuels and Emissions, Parts A and B, 2010.

[4] S.K. Aggarwal, A review of spray ignition phenomena, Progress in Energy and Combustion Science 24 (1998) 565–600.

[5] S. Ahmed, R. Balachandran, T. Marchione, E. Mastorakos, Spark ignition of turbulent nonpremixed bluff-body flames, Combustion and Flame 151 (2007) 366–385.

[6] S. Ahmed, R. Balachandran, E. Mastorakos, Measurements of ignition probability in turbulent non-premixed counterflow flames, Proceedings of the Combustion Institute 31 (2007) 1507–1513.

[7] T. Marchione, S. Ahmed, E. Mastorakos, Ignition of turbulent swirling n-heptane spray flames using single and multiple sparks, Combustion and Flame 156 (2009) 166–180.

[8] D.R. Ballal, A.H. Lefebvre, A general model of spark ignition for gaseous and liquid fuel-air mixtures, Symposium (International) on Combustion 18 (1981) 1737–1746.

[9] S. Aggarwal, Ignition and flame propagation in dilute polydisperse sprays - Importance of d32 and d20, Journal of Propulsion and Power - J PROPUL POWER 4 (1988) 14–21.

[10] S. Aggarwal, Single droplet ignition, Progress in Energy and Combustion Science 45 (2014), doi:10.1016/j.pecs.2014.05.002.

[11] M.J. Denton, S.B. Tambe, S.M. Jeng, Experimental investigation into the high altitude relight of a three-cup combustor sector, Proceedings of the ASME Turbo Expo 4B-2018 (2018) 1–12.

[12] M. Majcherczyk, N. Zarzalis, F. Turrini, in: Volume 4A: Combustion, Fuels and Emissions, ASME, 2014, V04AT04A019.

[13] R.W. Read, J.W. Rogerson, S. Hochgreb, Planar Laser-Induced Fluorescence Fuel Imaging During Gas-Turbine Relight, Journal of Propulsion and Power 29 (2013) 961–974.

[14] R.W. Read, Experimental Investigations into High-Altitude Relight of a Gas Turbine, 2008.

[15] D.R. Ballal, A.H. Lefebvre, Ignition of liquid fuel sprays at subatmospheric pressures, Combustion and Flame 31 (1978) 115–126.

[16] A. Neophytou, E.S. Richardson, E. Mastorakos, Spark ignition of turbulent recirculating non-premixed gas and spray flames, Combustion and Flame 159 (2012) 1503–1522.

[17] J.M. Boyde, P. Le Clercq, M. Di Domenico, M. Rachner, G.C. Gebel, T. Mosbach, M. Aigner, Numerical Investigation of the Parameter Governing the Ignitability of a Spray Flame, Journal of Engineering for Gas Turbines and Power 135 (2012), doi:10.1115/1.4007377.

[18] A.H. Lefebvre, Gas turbine combustion, Second Edition, Taylor & Francis, Philadelphia, 1999.

[19] J.Y. Murthy, Numerical Methods in Heat Mass and Momentum Transfer, Lecture (2002) 1–196.

[20] J.P. Holman, J.R. Lloyd, J.D. Anderson, COMPUTATIONAL FLUID DYNAMICS McGraw-Hill Series in Mechanical Engineering Consulting Editors McGraw-Hill Series in Aeronautical and Aerospace Engineering Consulting Editor, 1995.

[21] O. Reynolds, On the Dynamical Theory of Incompressible Viscous Fluids and the Determination of the Criterion, Philosophical Transactions of the Royal Society of London. A 186 (1895) 123–164.

[22] O. Reynolds, An Experimental Investigation of the Circumstances Which Determine Whether the Motion of Water Shall Be Direct or Sinuous, and of the Law of Resistance in Parallel Channels. [Abstract], Proceedings of the Royal Society of London 35 (1883) 84–99.

[23] A.N. Kolmogorov, The Local Structure of Turbulence in Incompressible Viscous Fluid for Very Large Reynolds Numbers, Proceedings: Mathematical and Physical Sciences 434 (1991) 9–13.

[24] D.C. Wilcox, Turbulence Modeling for CFD, DCW Industries, 2006.

[25] S.B. Pope, Turbulent Flows, Cambridge University Press, 2000.

[26] L.F. Richardson, Weather Prediction by Numerical Process, 2nd ed., Cambridge University Press, Cambridge, 2007.

[27] T. Kalmár-Nagy, B.D. Bak, An intriguing analogy of Kolmogorov's scaling law in a hierarchical mass–spring–damper model, Nonlinear Dynamics 95 (2019) 3193–3203.

[28] G.I. Taylor, Statistical Theory of Turbulence, Proceedings of the Royal Society of London Series A 151 (1935) 421–444.

[29] J. Boussinesq, Théorie de l'écoulement tourbillonnant et tumultueux des liquides dans les lits, 1897.

[30] B.I. Davydov, On the Statistical Dynamics of an Incompressible Turbulent Fluid, Soviet Physics Doklady 4 (1960) 769.

[31] K. Hanjalic, Two-dimensional asymmetric turbulent flow in ducts, 1970.

[32] W.P. Jones, B.E. Launder, The prediction of laminarization with a two-equation model of turbulence, International Journal of Heat and Mass Transfer 15 (1972) 301–314.

[33] B.E. Launder, B.I. Sharma, Application of the energy-dissipation model of turbulence to the calculation of flow near a spinning disc, Letters in Heat and Mass Transfer 1 (1974) 131–137.

[34] D.C. Wilcox, Multiscale model for turbulent flows, AIAA Journal 26 (1988) 1311–1320.

[35] D.C. Wilcox, Formulation of the k-w Turbulence Model Revisited, AIAA Journal 46 (2008) 2823–2838.

[36] M. Kern, Modellierung kinetisch kontrollierter, turbulenter Flammen für Magerbrennkonzepte, KIT Scientific Publishing, Karlsruhe, 2013.

[37] C. Kraus, Experimental and Numerical Investigation of the Influence of Multiple-Burner Arrangements on Combustion Instabilities in Turbulent Swirl-Stabilized Flames, KIT, Karlsruhe, 2014.

[38] Stephen R. Turns, An Introduction to Combustion Concepts and Applications, McGraw Hill Higher Education, 2011.

[39] S. Arrhenius, Über die Reaktionsgeschwindigkeit bei der Inversion von Rohrzucker durch Säuren, Zeitschrift für Physikalische Chemie 4U (1889).

[40] T.M. Baust, Entwicklung eines Verbrennungsmodells für wasseremulgierte Flüssigbrennstoffe, KIT Scientific Publishing, Karlsruhe, 2019.

[41] T. Poinsot, D. Veynante, Theoretical and numerical combustion, [Eigenverl. Poinsot], [Toulouse, 2012.

[42] N. Manson, Some notes on the first theories of the flame velocity in gaseous mixtures, Combustion and Flame 71 (1988) 179–187.

[43] S.H. Chung, C.K. Law, An invariant derivation of flame stretch, Combustion and Flame 55 (1984) 123–125.

[44] B. Karlovitz, D.W. Denniston, D.H. Knapschaefer, F.E. Wells, Studies on Turbulent flames, Symposium (International) on Combustion 4 (1953) 613–620.

[45] C.K. Law, Dynamics of stretched flames, Symposium (International) on Combustion 22 (1989) 1381–1402.

[46] M. MATALON, On Flame Stretch, Combustion Science and Technology 31 (1983) 169–181.

[47] G.K. Giannakopoulos, A. Gatzoulis, C.E. Frouzakis, M. MATALON, A.G. Tomboulides, Consistent definitions of “Flame Displacement Speed” and “Markstein Length” for premixed flame propagation, Combustion and Flame 162 (2015) 1249–1264.

[48] C.K. Law, P. Cho, M. Mizomoto, H. Yoshida, Flame curvature and preferential diffusion in the burning intensity of bunsen flames, Symposium (International) on Combustion 21 (1988) 1803–1809.

[49] T.C. Lieuwen, Unsteady Combustor Physics, Cambridge University Press, Cambridge, 2012.

[50] E. Machover, E. Mastorakos, Spark ignition of annular non-premixed combustors, Experimental Thermal and Fluid Science 73 (2016) 64–70.

[51] G.H. MARKSTEIN, Experimental and Theoretical Studies of Flame-Front Stability, Journal of the Aeronautical Sciences 18 (1951) 199–209.

[52] F.N. Egolfopoulos, N. Hansen, Y. Ju, K. Kohse-Höinghaus, C.K. Law, F. Qi, Advances and challenges in laminar flame experiments and implications for combustion chemistry, Progress in Energy and Combustion Science 43 (2014) 36–67.

[53] P. Dagaut, M. Cathonnet, The ignition, oxidation, and combustion of kerosene, Progress in Energy and Combustion Science - PROG ENERG COMBUST SCI 32 (2006) 48–92.

[54] E. Ranzi, A. Frassoldati, R. Grana, A. Cuoci, T. Faravelli, A.P. Kelley, C.K. Law, Hierarchical and comparative kinetic modeling of laminar flame speeds of hydrocarbon and oxygenated fuels, Progress in Energy and Combustion Science 38 (2012) 468–501.

[55] V. Vukadinovic, P. Habisreuther, N. Zarzalis, Influence of pressure and temperature on laminar burning velocity and Markstein number of kerosene Jet A-1, Fuel 111 (2013) 401–410.

[56] C.T. Chong, S. Hochgreb, Measurements of laminar flame speeds of liquid fuels, Proceedings of the Combustion Institute 33 (2011) 979–986.

[57] X. Hui, A. Das, K. Kumar, C.-J. Sung, S. Dooley, F. Dryer, Laminar Flame Speeds and Extinction Stretch Rates of Selected Aromatic Hydrocarbons, Fuel 97 (2012) 695–702.

[58] X. Hui, C.-J. Sung, Laminar flame speeds of transportation-relevant hydrocarbons and jet fuels at elevated temperature and pressures, Fuel 109 (2013) 191–200.

[59] S. Honnet, K. Seshadri, U. Niemann, N. Peters, A Surrogate Fuel for Kerosene, Proceedings of The Combustion Institute - PROC COMBUST INST 32 (2009) 485–492.

[60] D. Bradley, S.E.-D. Habik, S.A. El-Sherif, A generalization of laminar burning velocities and volumetric heat release rates, Combustion and Flame 87 (1991) 336–345.

[61] G. Damköhler, Der Einfluss der Turbulenz auf die Flammengeschwindigkeit in Gasgemischen, Zeitschrift für Elektrochemie und angewandte physikalische Chemie 46 (1940) 601–626.

[62] I. Glassman, R. A. Yetter, Combustion, Academic Press, 2008.

[63] N. Peters, Laminar flamelet concepts in turbulent combustion, Symposium (International) on Combustion 21 (1988) 1231–1250.

[64] R. Borghi, in: C. Casci, C. Bruno (Eds.), Recent Advances in the Aerospace Sciences: In Honor of Luigi Crocco on His Seventy-fifth Birthday, Springer US, Boston, MA, 1985, pp. 117–138.

[65] H.-P. Schmid, Ein Verbrennungsmodell zur Beschreibung der Wärmefreisetzung von vorgemischten turbulenten Flammen, 1995.

[66] H.-P. Schmid, Ein Verbrennungsmodell zur Beschreibung der Wärmefreisetzung von vorgemischten turbulenten Flammen, 1995.

[67] N. Peters, Turbulent Combustion, Cambridge University Press, Cambridge, 2000.

[68] C.K. LAW, H.K. LAW, in: F.A. WILLIAMS, A.K. OPPENHEIM, D.B. OLFE, M. LAPP (Eds.), Modern Developments in Energy, Combustion and Spectroscopy, Pergamon, Oxford, 1993, pp. 29–48.

[69] G.A.E. Godsave, Studies of the combustion of drops in a fuel spray—the burning of single drops of fuel, Symposium (International) on Combustion 4 (1953) 818–830.

[70] M. GOLDSMITH, S.S. PENNER, On the Burning of Single Drops of Fuel in an Oxidizing Atmosphere, Journal of Jet Propulsion 24 (1954) 245–251.

[71] D.B. Spalding, The combustion of liquid fuels, Symposium (International) on Combustion 4 (1953) 847–864.

[72] N. Zarzalis, Mass Transfer and Reaction Kinetics: Lecture, KIT, 2020.

[73] N. Zarzalis, Angewandte Verbrennungstechnick: Vorlesung, KIT, 2020.

[74] W.A. Sirignano, Fluid Dynamics and Transport of Droplets and Sprays, 2nd ed., Cambridge University Press, Cambridge, 2010.

[75] K. Annamalai, W. Ryan, Interactive processes in gasification and combustion. Part I, Progress in Energy and Combustion Science 18 (1992) 221–295.

[76] P. Jenny, D. Roekaerts, N. Beishuizen, Modeling of turbulent dilute spray combustion, Progress in Energy and Combustion Science 38 (2012) 846–887.

[77] G.M. Faeth, Evaporation and combustion of sprays, Progress in Energy and Combustion Science 9 (1983) 1–76.

[78] G.M. Faeth, Mixing, transport and combustion in sprays, Progress in Energy and Combustion Science 13 (1987) 293–345.

[79] E.M. TWARDUS, T.A. BRZUSTOWSKI, An Experimental Study of Flame Spread and Burning in Arrays of Monosize Hydrocarbon Droplets, Combustion Science and Technology 17 (1978) 215–225.

[80] N.A. Chigier, C.G. McCreath, Combustion of droplets in sprays, Acta Astronautica 1 (1974) 687–710.

[81] S. William, Advances in droplet array combustion theory and modeling, Progress in Energy and Combustion Science 42 (2014), doi:10.1016/j.pecs.2014.01.002.

[82] M. LABOWSKY, D.E. ROSNER, in: Evaporation—Combustion of Fuels, AMERICAN CHEMICAL SOCIETY, 1978, pp. 63–79.

[83] H.H. Chiu, H.Y. Kim, E.J. Croke, Internal group combustion of liquid droplets, Symposium (International) on Combustion 19 (1982) 971–980.

[84] N. Zarzalis, Design of a Jet engine combustion chamber: Lecture, KIT, 2020.

[85] K. Merkle, Einfluss gleich- und gegensinniger Drehrichtung der Verbrennungsluftströme auf die Stabilisierung turbulenter Deppeldrall-Diffusionsflammen, 2006.

[86] P. Kasabov, Experimentelle Untersuchungen an abgehobenen Flammen unter Druck, 2014.

[87] K. Doebbeling, Experimentelle und theoretische Untersuchungen an stark verdrallten, turbulenten isothermen Stroemungen, 1990.

[88] F. Holzaepfel, K. Doebbeling, B. Lenze, in: In: High intensity combustors - steady isobaric combustion. Final report of the Collaborative Research Centre 167. Ed.: S. Wittig. Weinheim 2002. S. 135-155, 2002.

[89] N.A. Chigier, J.M. Bee´r, Velocity and Static-Pressure Distributions in Swirling Air Jets Issuing From Annular and Divergent Nozzles, J. Basic Eng 86 (1964) 788–796.

[90] R. Günther, H. Wilhelmi, G. Janisch, R. Kleine, H. Tietze, Verbrennung und Feuerungen, Springer Berlin Heidelberg, 1974.

[91] A.H. Lefebvre, D.R. Ballal, Gas turbine combustion: Alternative fuels and emissions, Taylor & Francis, Boca Raton, 2010.

[92] K. Prieur, D. Durox, G. Vignat, T. Schuller, S. Candel, in: 2018.

[93] E.S. Richardson, E. Mastorakos, Numerical investigation of forced ignition in laminar counterflow non-premixed methane-air flames, Combustion Science and Technology 179 (2007) 21–37.

[94] J.B. Greenberg, L.S. Kagan, G.I. Sivashinsky, A numerical study of polydisperse spray flame ignition and extinction fronts in a mixing layer, Combustion Theory and Modelling 17 (2013) 1053–1066.

[95] N. Chakraborty, H. Hesse, E. Mastorakos, Numerical investigation of edge flame propagation behavior in an igniting turbulent planar jet, Combustion Science and Technology 182 (2010) 1747–1781.

[96] N. Chakraborty, E. Mastorakos, Direct numerical simulations of localised forced ignition in turbulent mixing layers, Flow, Turbulence and Combustion 80 (2008) 155–186.

[97] N. Chakraborty, E. Mastorakos, R.S. Cant, Effects of turbulence on spark ignition in inhomogeneous mixtures, Combustion Science and Technology 179 (2007) 293–317.

[98] A.P. Wandel, Influence of scalar dissipation on flame success in turbulent sprays with spark ignition, Combustion and Flame 161 (2014) 2579–2600.

[99] A.P. Wandel, N. Chakraborty, E. Mastorakos, Direct numerical simulations of turbulent flame expansion in fine sprays, Proceedings of the Combustion Institute 32 II (2009) 2283–2290.

[100] S.F. Ahmed, E. Mastorakos, Spark ignition of lifted turbulent jet flames, Combustion and Flame 146 (2006) 215–231.

[101] C. Letty, E. Mastorakos, A.R. Masri, M. Juddoo, W. O'Loughlin, Structure of igniting ethanol and n-heptane spray flames with and without swirl, Experimental Thermal and Fluid Science 43 (2012) 47–54.

[102] D.J. Beerer, V.G. McDonell, Autoignition of Hydrogen and Air Inside a Continuous Flow Reactor With Application to Lean Premixed Combustion, J. Eng. Gas Turbines Power 130 (2008), doi:10.1115/1.2939007.

[103] C. Markides, E. Mastorakos, An experimental study of hydrogen autoignition in a turbulent co-flow of heated air, Proceedings of the Combustion Institute 30 (2005) 883–891.

[104] J.U. Steinle, E.U. Franck, High Pressure Combustion – Ignition Temperatures to 1000 bar, Berichte der Bunsengesellschaft für physikalische Chemie 99 (1995) 66–73.

[105] I.A.B. Reid, C. Robinson, D.B. Smith, Spontaneous ignition of methane, Symposium (International) on Combustion 20 (1985) 1833–1843.

[106] C. Robinson, D.B. Smith, The auto-ignition temperature of methane, Journal of Hazardous Materials 8 (1984) 199–203.

[107] M. Caron, M. Goethals, G. de Smedt, J. Berghmans, S. Vliegen, E. Van't Oost, A. van den Aarssen, Pressure dependence of the auto-ignition temperature of methane/air mixtures, Journal of Hazardous Materials 65 (1999) 233–244.

[108] L. Ye, Y. Pan, J. Jiang, W. Zhang, A numerical study of the auto-ignition temperatures of CH4-Air, C3H8-Air, CH4-C3H8-Air and CH4-CO2-Air mixtures, Journal of Loss Prevention in the Process Industries 29 (2014), doi:10.1016/j.jlp.2014.02.005.

[109] R. Bounaceur, P.-A. Glaude, B. Sirjean, R. Fournet, P. Montagne, M. Vierling, M. Molière, Prediction of Auto-Ignition Temperatures and Delays for Gas Turbine Applications, J. Eng. Gas Turbines Power 138 (2015), doi:10.1115/1.4031264.

[110] F. Norman, F. van den Schoor, F. Verplaetsen, Auto-ignition and upper explosion limit of rich propane–air mixtures at elevated pressures, Journal of Hazardous Materials 137 (2006) 666–671.

[111] M.R. Chandraratna, J.F. Griffiths, Pressure and concentration dependences of the autoignition temperature for normal butane + air mixtures in a closed vessel, Combustion and Flame 99 (1994) 626–634.

[112] A. Gupta, C. Markides, An experimental study of the autoignition of polydispersed liquid-fuel droplets in a confined high-temperature turbulent coflow, 2017.

[113] L.J. Spadaccini, J.A. Tevelde, Autoignition characteristics of aircraft-type fuels, Combustion and Flame 46 (1982) 283–300.

[114] V. Babrauskas, Ignition handbook database, Fire Science Pub, [Place of publication not identified], 2003.

[115] M.G. Zabetakis, Flammability Characteristics of Combustible Gases and Vapors, U.S. Department of the Interior, Bureau of Mines, 1965.

[116] N.N. Semenov, I.I. Frenkel, Chemical kinetics and chain reactions, Clarendon Press, Oxford, 1935.

[117] D.A. FRANK-KAMENETSKII, N. Thon, Diffusion and Heat Exchange in Chemical Kinetics, Princeton University Press, 1955.

[118] V. Babrauskas, Ignition Handbook, 2003.

[119] A.L. Furno, A.C. Imhof, J.M. Kuchta, Effect of pressure and oxidant concentration on auto-ignition temperatures of selected combustibles in various oxygen and dinitrogen tetroxide atmospheres, Journal of Chemical & Engineering Data 13 (1968) 243–249.

[120] J.M. Kuchta, R.G. Clodfelter, in: 1985.

[121] C.E. Frank, Blackham, Angus U. & Swarts, Donald E., Investigation of spontaneous ignition temperatures of organic compounds with particular emphasis on lubricants (1952).

[122] J.F. Griffiths, B.F. Gray, Fundamentals of Autoignition of Hydrocarbons and Other Organic Substrates in the Gas Phase, 24th Loss Prevention Symp; AIChe (1990).

[123] T.J. Snee, J.F. Griffiths, Criteria for spontaneous ignition in exothermic, autocatalytic reactions, Combustion and Flame 75 (1989) 381–395.

[124] L.H. Coweli, A.H. Lefebvre, in: SAE International, 1986.

[125] S. IKURA, T. KADOTA, H. HIROYASU, Ignition Delay of Fuel Sprays in a Constant Volume Bomb, Transactions of the Japan Society of Mechanical Engineers 41 (1975) 1559–1568.

[126] B.P. Mullins, The spontaneous combustion of fuels injected into a hot gas stream, Symposium on Combustion and Flame, and Explosion Phenomena 3 (1948) 704–713.

[127] B.P. Mullins, Spontaneous Ignition of Liquid Fuels, on behalf of the Advisory Group for Aeronautical Research and Development, North Atlantic Treaty Organization, 1955.

[128] J.C. Livengood, P.C. Wu, Correlation of autoignition phenomena in internal combustion engines and rapid compression machines, Symposium (International) on Combustion 5 (1955) 347–356.

[129] W.R. LASTER, K. ANNAMALAI, IGNITION DELAY OF DROPLET CLOUDS, Chemical Engineering Communications 105 (1991) 201–219.

[130] M. Mawid, S.K. Aggarwal, Ignition of a Fuel Spray by Hot Surfaces in a Constant Volume Combustor, Journal of Non-Equilibrium Thermodynamics 15 (1990) 369–382.

[131] S.K. Aggarwal, Ignition behavior of a multicomponent fuel spray, Combustion and Flame 76 (1989) 5–15.

[132] W.A. Noyes, The Kinetics of Chemical Change (Hinshelwood, C. N.), Journal of Chemical Education 17 (1940) 552.

[133] J.B. Zeldowitsch, G.I. Barenblatt, V.B. Librovich, G.M. Makhviladze, The Mathematical theory of combustion and explosions, Consultants Bureau, New York, 1985.

[134] M. Pelucchi, M. Bissoli, C. Cavallotti, A. Cuoci, T. Faravelli, A. Frassoldati, E. Ranzi, A. Stagni, Improved Kinetic Model of the Low-Temperature Oxidation of n-Heptane, Energy & Fuels 28 (2014) 7178–7193.

[135] A. Cuoci, A.E. Saufi, A. Frassoldati, D.L. Dietrich, F.A. Williams, T. Faravelli, Flame extinction and low-temperature combustion of isolated fuel droplets of n-alkanes, Proceedings of the Combustion Institute 36 (2017) 2531–2539.

[136] H.K. Ciezki, G. Adomeit, Shock-tube investigation of self-ignition of n-heptane-air mixtures under engine relevant conditions, Combustion and Flame 93 (1993) 421–433.

[137] S.W. Benson, The kinetics and thermochemistry of chemical oxidation with application to combustion and flames, Progress in Energy and Combustion Science 7 (1981) 125–134.

[138] NASA Glenn Research Center, Cool Flames - Perspectives on their Importance in Combustion Systems.

[139] E.L. Litchfield, Minimum Ignition-energy Concept and Its Application to Safety Engineering, U.S. Department of the Interior, Bureau of Mines, 1960.

[140] D.R. Ballal, A.H. Lefebvre, Ignition and Flame Quenching in Flowing Gaseous Mixtures, Proceedings of the Royal Society of London. Series A, Mathematical and Physical Sciences 357 (1977) 163–181.

[141] T. Brutscher, Experimentelle und theoretische Untersuchungen zur Entflammung und Flammenausbreitung bei funkengezündeten Brenngas-Luft-Gemischen unter besonderer Berücksichtigung bevorzugter Diffusion, 2003.

[142] D.R. Ballal, A. Lefebvre, in: 1975.

[143] M.V. Blanc, P.G. Guest, G. von Elbe, B. Lewis, Ignition of Explosive Gas Mixtures by Electric Sparks. I. Minimum Ignition Energies and Quenching Distances of Mixtures of Methane, Oxygen, and Inert Gases, The Journal of Chemical Physics 15 (1947) 798–802.

[144] C.C. Swett, Spark Ignition of Flowing Gases, NACA-TR 1287 (1956).

[145] Y. Ko, R.W. Anderson, V.S. Arpaci, Spark ignition of propane-air mixtures near the minimum ignition energy, Combustion and Flame 83 (1991) 75–87.

[146] P.S. Tromans, R.M. Furzeland, An analysis of lewis number and flow effects on the ignition of premixed gases, Symposium (International) on Combustion 21 (1988) 1891–1897.

[147] H.L. Olsen, R.B. Edmonson, E.L. Gayhart, Microchronometric Schlieren Study of Gaseous Expansion from an Electric Spark, Journal of Applied Physics 23 (1952) 1157–1162.

[148] D.R. Ballal, A.H. Lefebvre, The influence of spark discharge characteristics on minimum ignition energy in flowing gases, Combustion and Flame 24 (1975) 99–108.

[149] T. Kravchik, E. Sher, Numerical modeling of spark ignition and flame initiation in a quiescent methane-air mixture, Combustion and Flame 99 (1994) 635–643.

[150] M. THIELE, J. Warnatz, A. Dreizler, S. LINDENMAIER, R. Schießl, U. Maas, A. GRANT, P. Ewart, Spark ignited hydrogen/air mixtures, Combustion and Flame - COMBUST FLAME 128 (2002) 74–87.

[151] D. Thévenin, O. Gicquel, J. de Charentenay, R. Hilbert, D. Veynante, Two- versus three-dimensional direct simulations of turbulent methane flame kernels using realistic chemistry, Proceedings of the Combustion Institute 29 (2002) 2031–2039.

[152] E. Mastorakos, Ignition of turbulent non-premixed flames, Progress in Energy and Combustion Science 35 (2009) 57–97.

[153] H.F. Calcote, C.A. Gregory, C.M. Barnett, R.B. Gilmer, Spark Ignition. Effect of Molecular Structure, Industrial & Engineering Chemistry 44 (1952) 2656–2662.

[154] J.B. Fenn, Lean Flammability Limit and Minimum Spark Ignition Energy. Commercial Fluids and Pure Hydrocarbons, Industrial & Engineering Chemistry 43 (1951) 2865–2869.

[155] Lewis, B and Von Elbe, G, Combustion, flames and explosions of gases. Third edition, United States, 1987.

[156] M. Champion, B. Deshaies, G. Joulin, K. Kinoshita, Spherical flame initiation, Combustion and Flame 65 (1986) 319–337.

[157] D. Bradley, F.K.-K. Lung, Spark ignition and the early stages of turbulent flame propagation, Combustion and Flame 69 (1987) 71–93.

[158] C.C. Huang, S.S. Shy, C.C. Liu, Y.Y. Yan, A transition on minimum ignition energy for lean turbulent methane combustion in flamelet and distributed regimes, Proceedings of the Combustion Institute 31 (2007) 1401–1409.

[159] A.D. Birch, D.R. Brown, M.G. Dodson, Ignition probabilities in turbulent mixing flows, Proc. Combust. Inst. 18 (1981) 1755–1780.

[160] W.P. Jones, V.N. Prasad, LES-pdf simulation of a spark ignited turbulent methane jet, Proceedings of the Combustion Institute 33 (2011) 1355–1363.

[161] G. Lacaze, E. Richardson, T. Poinsot, Large eddy simulation of spark ignition in a turbulent methane jet, Combustion and Flame 156 (2009) 1993–2009.

[162] U. Maas, J. Warnatz, Ignition processes in hydrogen oxygen mixtures, Combustion and Flame 74 (1988) 53–69.

[163] C.-S. WANG, M. SIBULKIN, Comparison of Minimum Ignition Energy for Four Alkanes, Combustion Science and Technology 91 (1993) 163–178.

[164] A. FRENDI, M. SIBULKIN, Dependence of Minimum Ignition Energy on Ignition Parameters, Combustion Science and Technology 73 (1990) 395–413.

[165] T.M. Sloane, Ignition and Flame Propagation Modeling With an Improved Methane Oxidation Mechanism, Combustion Science and Technology 63 (1989) 287–313.

[166] Y. Wu, Z. Huang, T. Xiong, The numerical solution of governing equations for ignition by a sphere of burned gas or spark, Symposium (International) on Combustion 20 (1985) 151–159.

[167] C.E. Polymeropoulos, S. Das, The effect of droplet size on the burning velocity of kerosene-air sprays, Combustion and Flame 25 (1975) 247–257.

[168] S.D. WEHE, N. ASHGRIZ, Ignition Probability and Absolute Minimum Ignition Energy in Fuel Sprays, Combustion Science and Technology 86 (1992) 45–65.

[169] D.L. Dietrich, N.P. Cernansky, M.B. Somashekara, I. Namer, Spark ignition of a bidisperse, n-decane fuel spray, Symposium (International) on Combustion 23 (1991) 1383–1389.

[170] A.M. Danis, I. Namer, N.P. Cernansky, Droplet size and equivalence ratio effects on spark ignition of monodisperse N-heptane and methanol sprays, Combustion and Flame 74 (1988) 285–294.

[171] D.R. Ballal, A.H. Lefebvre, Ignition and Flame Quenching of Quiescent Fuel Mists, Proceedings of the Royal Society of London. Series A, Mathematical and Physical Sciences 364 (1978) 277–294.

[172] H.N.S. RAO, A.H. Lefebvre, Ignition of Kerosine Fuel Sprays in a Flowing Air Stream, Combustion Science and Technology 8 (1973) 95–100.

[173] A.K. Singh, C.E. Polymeropoulos, Spark ignition of aerosols, Symposium (International) on Combustion 21 (1988) 513–519.

[174] D.R. Ballal, A.H. Lefebvre, Ignition and flame quenching of flowing heterogeneous fuel-air mixtures, Combustion and Flame 35 (1979) 155–168.

[175] C.B. Graves, Y.L. Tang, J.G. Skifstad, Ignition of a fuel spray by a hot surface, AIAA Journal 24 (1986) 1994–2001.

[176] S.K. Aggarwal, W.A. Sirignano, Ignition of fuel sprays, Symposium (International) on Combustion 20 (1985) 1773–1780.

[177] J.B. Greenberg, Finite-rate evaporation and droplet drag effects in spherical flame front propagation through a liquid fuel mist, Combustion and Flame 148 (2007) 187–197.

[178] D.R. Ballal, A.H. Lefebvre, Flame propagation in heterogeneous mixtures of fuel droplets, fuel vapor and air, Symposium (International) on Combustion 18 (1981) 321–328.

[179] H. Nomura, I. Kawasumi, Y. Ujiie, J.'i. Sato, Effects of pressure on flame propagation in a premixture containing fine fuel droplets, Proceedings of the Combustion Institute 31 (2007) 2133–2140.

[180] A. Neophytou, E. Mastorakos, R.S. Cant, The internal structure of igniting turbulent sprays as revealed by complex chemistry DNS, Combustion and Flame 159 (2012) 641–664.

[181] T. NIIOKA, FLAME PROPAGATION IN SPRAYS AND PARTICLE CLOUDS OF LESS VOLATILE FUELS, Combustion Science and Technology 177 (2005) 1167–1182.

[182] M. Boileau, G. Staffelbach, B. Cuenot, T. Poinsot, C. Bérat, LES of an ignition sequence in a gas turbine engine, Combustion and Flame 154 (2008) 2–22.

[183] W. Jones, A. Tyliszczak, Large Eddy Simulation of Spark Ignition in a Gas Turbine Combustor, Flow, Turbulence and Combustion 85 (2010) 711–734.

[184] T. Lancien, K. Prieur, D. Durox, S. Candel, R. Vicquelin, Large Eddy Simulation of Light-Round in an Annular Combustor With Liquid Spray Injection and Comparison With Experiments, Journal of Engineering for Gas Turbines and Power 140 (2017), doi:10.1115/1.4037827.

[185] F. Collin-Bastiani, J. Marrero-Santiago, E. Riber, G. Cabot, B. Renou, B. Cuenot, A joint experimental and numerical study of ignition in a spray burner, Proceedings of the Combustion Institute 37 (2019) 5047–5055.

[186] L. Hervo, J.-M. Senoner, A. Biancherin, C. Benedicte, Large-Eddy Simulation of Kerosene Spray Ignition in a Simplified Aeronautic Combustor, Flow, Turbulence and Combustion 101 (2018), doi:10.1007/s10494-018-9924-4.

[187] L. Bayvel, Liquid Atomization, Taylor and Francis Group, New York, 1993.

[188] A.H. Lefebvre, V.G. McDonell, Atomization and sprays, 2nd ed., Boca Raton, FL CRC Press, Taylor and Francis Group, 2017.

[189] K. Masters, Spray drying handbook, 1991.

[190] Batarseh F.Z.M., Spray generated by an airblast atomizer: atomization, propagation and aerodynamic instability, PhD thesis, Technische Universität Darmstadt, 2009.

[191] G.M. Faeth, Spray combustion phenomena, Symposium (International) on Combustion 26 (1996) 1593–1612.

[192] J.O. Hinze, Fundamentals of the hydrodynamic mechanism of splitting in dispersion processes, AIChE Journal 1 (1955) 289–295.

[193] W.R. Lane, Shatter of Drops in Streams of Air, Industrial & Engineering Chemistry 43 (1951) 1312–1317.

[194] R.S. Brodkey, The Phenomena of Fluid Motions, Brodkey Publishing, 2004.

[195] L.-P. Hsiang, G.M. Faeth, Drop deformation and breakup due to shock wave and steady disturbances, International Journal of Multiphase Flow 21 (1995) 545–560.

[196] D.M. Aguirre Bermudez, Spray measurements in a laboratory RQL combustion chamber under high altitude relight conditions, Master's thesis, Karlsruhe Institute of Technology, 2020.

[197] Rayleigh, On The Instability Of Jets, Proceedings of the London Mathematical Society s1-10 (1878) 4–13.

[198] R. Reitz, F. Bracco, Mechanisms of breakup of round liquid jets, Encyclopedia of Fluid Mechanics 3 (1986).

[199] G. Wozniak, Zerstäubungstechnik: Prinzipien, Verfahren, Geräte, 1st ed., Springer-Verlag Berlin Heidelberg, 2003.

[200] C. Weber, Zum Zerfall eines Flüssigkeitsstrahles, Z. angew. Math. Mech. 11 (1931) 136–154.

[201] N.K. Rizk, A.H. Lefebvre, The Influence of Liquid Film Thickness on Airblast Atomization, J. Eng. Power 102 (1980) 706–710.

[202] S. Gepperth, A. Müller, R. Koch, H.-J. Bauer, Ligament and Droplet Characteristics in Prefilming Airblast Atomization: ICLASS 2012, 12th Triennial International Conference on Liquid Atomization and Spray Systems, 2012.

[203] N.K. Rizk, A.H. Lefebvre, Drop-size distribution characteristics of spill-return atomizers, Journal of Propulsion and Power 1 (1985) 16–22.

[204] R.W Read, Experimental Investigations into High-Altitude Relight of a Gas Turbine, PhD, Cambridge, 2008.

[205] Federal Aviation Administration, Aviation Rulemaking and Advisory Committe - Transport Airplane and Engine Issures -- New Tasks (1998).

[206] P.P. Walsh, P. Fletcher, Gas Turbine Performance, Wiley, 2008.

[207] W. Naegeli D, Dodge, L, G, Ignition Study in a Gas Turbine Combustor, Combustion Science and Technology 80 (1991) 165–184.

[208] S. Mosier, R. Pierce, Advanced combustion systems for stationary gas turbine engines: Volume I. Review and preliminary evaluation, Washington, D.C.

[209] R.J. Shaw, S. Gilkey, R. Hines (Eds.), Engine technology challenges for a 21st Century High-Speed Civil Transport, 1993, NASA TM-106216.

[210] T.J. Rosfjord, F.C. Padget, Experimental Assessment of the Emissions Control Potential of a Rich/Quench/Lean Combustor for High Speed Civil Transport Aircraft Engines, United Technologies Research Center East Hartford, CT United States, 2001, NASA CR—2001-210613.

[211] A. Andreini, G. Caciolli, B. Facchini, L. Tarchi, H. Xiao, K.A. Sallam, Experimental Evaluation of the Density Ratio Effects on the Cooling Performance of a Combined Slot/Effusion Combustor Cooling System, ISRN Aerospace Engineering 2013 (2013) 423190.

[212] A. Martinos, L. Palanti, S. Harth, A. Andreini, N. Zarzalis, D. Trimis, I. Vitale (Eds.), Analysis of ignition processes at combustors for aero engines at high altitude conditions [in press]: Proceedings of the European Combustion Meeting – 2019, April 14-17, Lisboa, Portugal, 2019.

[213] E. Mastorakos, Forced ignition of turbulent spray flames, Proceedings of the Combustion Institute 36 (2017) 2367–2383.

[214] E. Mayhew, C.M. Mitsingas, V. Coburn, J. Temme, C.-B. Kweon, in: AIAA Scitech 2020 Forum, American Institute of Aeronautics and Astronautics, 2020.

[215] X. Yang, X. Shen, J. Long, H. Chen, An Improved Median-based Otsu Image Thresholding Algorithm, AASRI Procedia 3 (2012) 468–473.

[216] Lavision GmbH, Product Manual, ParticleMaster Shadow (2016).

[217] G. Brenn, F. Durst, C. Tropea, Monodisperse Sprays for Various Purposes — Their production and characteristics, Part. Part. Syst. Charact. 13 (1996) 179–185.

[218] G. Brenn, T. Helpiö, F. Durst, A new apparatus for the production of monodisperse sprays at high flow rates, Chemical Engineering Science 52 (1997) 237–244.

[219] D.F. Rutland, G.J. Jameson, A non-linear effect in the capillary instability of liquid jets, Journal of Fluid Mechanics 46 (1971) 267–271.

[220] M.S. El-Shanawany, A.H. Lefebvre, Airblast Atomization, Journal of Energy 4 (1980) 184–189.

[221] A.H. Lefebvre, Airblast atomization, Progress in Energy and Combustion Science 6 (1980) 233–261.

[222] A.A. Rizkalla, A.H. Lefebvre, The Influence of Air and Liquid Properties on Airblast Atomization, J. Fluids Eng 97 (1975) 316–320.

[223] A.K. Jasuja, Atomization of Crude and Residual Fuel Oils, J. Eng. Power 101 (1979) 250–258.

[224] B.N. Caines, R.A. Hicks, C.W. Wilson, Influence of sub-atmospheric conditions on the performance of an airblast atomiser, 37th Joint Propulsion Conference and Exhibit (2001), doi:10.2514/6.2001-3573.

[225] M. Rachner, Die Stoffeigenschaften von Kerosin Jet A-1, DLR-Mitteilungen 98-01 (1998).

[226] A.D. Martinos, N. Zarzalis, S.R. Harth (Eds.), Analysis of Ignition Processes at Combustors for Aero Engines at High Altitude Conditions With and Without Effusion Cooling: Proceedings of the ASME Turbo Expo 2020, GT2020-16173, 2020.

[227] M. Gruber, Bewertung verschiedener laseroptischer Spraymesstechniken hinsichtlich der Zerstäubung von fluiden unterschiedlicher Viskosität mittels einer außenmischenden zweistoffdüse, Master thesis, Karlsruhe Institute of Technology, 2013.

[228] D.C. Montgomery, G.C. Runger, Applied statistics and probability for engineers, 2014.

[229] A. Fomina, CFD simulation of a laboatory RQL combustion chamber under high altitude relight conditions, Master thesis, Karlsruhe Institute of Technology, 2020.

[230] Blesinger.G., Flammenrückschlag durch verbrennungsinduziertes Wirbelaufplatzen Ähnlichkeitsanalyse unter Berücksichtigung von Baugröße und Brennstoffeigenschaften, PhD thesis, 2021.

[231] R. Stachler, J. Lefkowitz, J. Heyne, S. Stouffer, T. Ombrello, J. Miller, The impact of residence time on ignitability and time to ignition in a toroidal jet-stirred reactor, Proceedings of the Combustion Institute 37 (2018), doi:10.1016/j.proci.2018.09.009.

[232] G. Li, A. Mukhopadhyay, C.-Y. Cheng, y. Dai, Various Approaches to Compute Fluid Residence Time in Mixing Systems, American Society of Mechanical Engineers, Fluids Engineering Division (Publication) FEDSM 1 (2010), doi:10.1115/FEDSM-ICNMM2010-30771.

[233] G. Kumar, S.A. Drennan, A CFD Investigation of Multiple Burner Ignition and Flame Propagation with Detailed Chemistry and Automatic

Meshing, 52nd AIAA/SAE/ASEE Joint Propulsion Conference (2016) 1–13.

[234] P.K. Senecal, E. Pomraning, K.J. Richards, T.E. Briggs, C.Y. Choi, R.M. McDavid, M.A. Patterson, Multi-Dimensional Modeling of Direct-Injection Diesel Spray Liquid Length and Flame Lift-off Length using CFD and Parallel Detailed Chemistry, 2003.

[235] S.C. Li, B. Varatharajan, F.A. Williams, Chemistry of JP-10 Ignition, AIAA Journal 39 (2001) 2351–2356.

[236] M. Wörner, A compact introduction to the numerical modeling of multiphase flows, 2003.

[237] A. Andreini, L. Palanti, SOPRANO Deliverable D3.8: Two phase flow field CFD simulation (2020).

[238] Armstrong, J, C, H.D. Wilsted, Investigation of several techniques for improving altitude starting limits of turbojet engines, Washington, D.C., 1952.

[239] J. Odgers, A. Coban, in: 1977.

[240] C.C. Clyde, Spark ignition of flowing gases using long-duration discharges, Symposium (International) on Combustion 6 (1957) 523–532.

[241] J.L. Kerrebrock, Aircraft Engines and Gas Turbines, The MIT Press, Cambridge, Massachusetts, 1977.

[242] G.A. Richards, A.H. Lefebvre, Turbulent flame speeds of hydrocarbon fuel droplets in air, Combustion and Flame 78 (1989) 299–307.

[243] I. M. s. a, M.N. Mohd Jaafar, Effect of Velocity Variation at High Swirl on Axial Flow Development inside a Can Combustor, Jurnal Teknologi 71 (2014), doi:10.11113/jt.v71.3716.